International Journal of
Molecular Sciences

Special Issue Reprint

The Chitosan Biomaterials

Advances and Challenges—2nd Edition

Edited by
Lacramioara Popa, Mihaela Violeta Ghica and Cristina Elena Dinu-Pirvu

mdpi.com/journal/ijms

MDPI

The Chitosan Biomaterials: Advances and Challenges—2nd Edition

The Chitosan Biomaterials: Advances and Challenges—2nd Edition

Guest Editors

Lacramioara Popa
Mihaela Violeta Ghica
Cristina Elena Dinu-Pirvu

MDPI

Basel • Beijing • Wuhan • Barcelona • Belgrade • Novi Sad • Cluj • Manchester

Guest Editors

Lacramioara Popa
Physical and Colloidal Chemistry Department
University of Medicine and Pharmacy Carol Davila
Bucharest
Romania

Mihaela Violeta Ghica
Department of Physical and Colloidal Chemistry
"Carol Davila" University of Medicine and Pharmacy
Bucharest
Romania

Cristina Elena Dinu-Pirvu
Physical and Colloidal Chemistry Department
University of Medicine and Pharmacy Carol Davila
Bucharest
Romania

Editorial Office
MDPI AG
Grosspeteranlage 5
4052 Basel, Switzerland

This is a reprint of the Special Issue, published open access by the journal *International Journal of Molecular Sciences* (ISSN 1422-0067), freely accessible at: https://www.mdpi.com/journal/ijms/special_issues/3EYU0FJ94L.

For citation purposes, cite each article independently as indicated on the article page online and as indicated below:

Lastname, A.A.; Lastname, B.B. Article Title. *Journal Name* **Year**, *Volume Number*, Page Range.

ISBN 978-3-7258-5423-3 (Hbk)
ISBN 978-3-7258-5424-0 (PDF)
https://doi.org/10.3390/books978-3-7258-5424-0

Contents

About the Editors . . . . . **vii**

Preface . . . . . **ix**

Lăcrămioara Popa, Mihaela Violeta Ghica and Cristina-Elena Dinu-Pîrvu
Chitosan Biomaterials: Advances and Challenges—2nd Edition
Reprinted from: *Int. J. Mol. Sci.* **2025**, *26*, 4836, https://doi.org/10.3390/ijms26104836 . . . . . **1**

Karolina Kulka-Kamińska, Patrycja Brudzyńska, Mayuko Okura, Tatsuyuki Ishii, Marco Skala, Russel J. Reiter, et al.
Melatonin/Chitosan Biomaterials for Wound Healing and Beyond: A Multifunctional Therapeutic Approach
Reprinted from: *Int. J. Mol. Sci.* **2025**, *26*, 5918, https://doi.org/10.3390/ijms26135918 . . . . . **6**

Anjana Aravind, Kristina Seliverstova, Kaitlin K. K. Kammerlander, Thomas Henle and Eike Brunner
Processing α-Chitin into Stable Composite Materials for Heavy Metal Adsorption
Reprinted from: *Int. J. Mol. Sci.* **2025**, *26*, 3149, https://doi.org/10.3390/ijms26073149 . . . . . **28**

Roxana Popescu, Cristina-Elena Dinu-Pîrvu, Mihaela Violeta Ghica, Valentina Anuța and Lăcrămioara Popa
Physico-Chemical Characterization and Initial Evaluation of Carboxymethyl Chitosan–Hyaluronan Hydrocolloid Systems with Insulin Intended for Intranasal Administration
Reprinted from: *Int. J. Mol. Sci.* **2024**, *25*, 10452, https://doi.org/10.3390/ijms251910452 . . . . . **41**

Andreea Miron, Tanta-Verona Iordache, Artur J. M. Valente, Luisa Maria Rocha Durães, Andrei Sarbu, Georgeta Ramona Ivan, et al.
Chitosan-Based Beads Incorporating Inorganic–Organic Composites for Copper Ion Retention in Aqueous Solutions
Reprinted from: *Int. J. Mol. Sci.* **2024**, *25*, 2411, https://doi.org/10.3390/ijms25042411 . . . . . **62**

Verginica Schröder, Daniela Gherghel, Manuela Rossemary Apetroaei, Cristiana Luminița Gîjiu, Raluca Isopescu, Daniel Dinculescu, et al.
α-Chitosan and β-Oligochitosan Mixtures-Based Formula for In Vitro Assessment of Melanocyte Cells Response
Reprinted from: *Int. J. Mol. Sci.* **2024**, *25*, 6768, https://doi.org/10.3390/ijms25126768 . . . . . **78**

Pawel Poznanski, Abdullah Shalmani, Marcin Bryla and Waclaw Orczyk
Salicylic Acid Mediates Chitosan-Induced Immune Responses and Growth Enhancement in Barley
Reprinted from: *Int. J. Mol. Sci.* **2024**, *25*, 13244, https://doi.org/10.3390/ijms252413244 . . . . . **106**

Corneliu-George Coman, Alexandru Anisiei, Sandu Cibotaru, Daniela Ailincai, Sorin Aurelian Pasca, Caroline Chabot, et al.
Chitosan-Electrospun Fibers Encapsulating Norfloxacin: The Impact on the Biochemical, Oxidative and Immunological Profile in a Rats Burn Model
Reprinted from: *Int. J. Mol. Sci.* **2024**, *25*, 12709, https://doi.org/10.3390/ijms252312709 . . . . . **129**

Julio César López-Velázquez, Soledad García-Morales, Gloria Paola López-Sánchez, Mayra Itzcalotzin Montero-Cortés, Alberto Uc-Várguez and Joaquín Alejandro Qui-Zapata
High-Density Chitosan Induces a Biochemical and Molecular Response in *Coffea arabica* during Infection with *Hemileia vastatrix*
Reprinted from: *Int. J. Mol. Sci.* **2023**, *24*, 16165, https://doi.org/10.3390/ijms242216165 . . . . . **148**

About the Editors

Lacramioara Popa

Lacramioara Popa is a Professor, PhD, Dr. Habil. in Pharmacy, Department of Physical and Colloidal Chemistry, Faculty of Pharmacy, Carol Davila University of Medicine and Pharmacy, Bucharest, Romania; Researcher, Innovative Therapeutic Structures R&D Center, and President of the Ethics and Quality Assurance Commission, Faculty of Pharmacy, at the same university; 32 years' expertise in integration of the Quality by Design strategy in the development of drug delivery systems; surface characterization of raw materials and pharmaceutical systems; biopolymer chitosan in medical applications; over 75 ISI articles; H index-21.

Mihaela Violeta Ghica

Mihaela Violeta Ghica is a Professor, PhD, Dr. Habil. in Pharmacy, Department of Physical and Colloidal Chemistry, Faculty of Pharmacy, Carol Davila University of Medicine and Pharmacy, Bucharest, Romania; Researcher, Innovative Therapeutic Structures R&D Center, at the same university; Master's in Physical Chemistry and Applied Radiochemistry, Faculty of Chemistry, University of Bucharest; 23 years' expertise in developing biomaterials for precision treatment, advanced topical formulations, statistical experimental design for drug delivery systems, and biotechnological process optimization; over 100 ISI articles; H index-25.

Cristina Elena Dinu-Pirvu

Cristina Elena Dinu-Pirvu is a Professor, PhD, Dr. Habil. in Pharmacy, Department of Physical and Colloidal Chemistry, Faculty of Pharmacy, Carol Davila University of Medicine and Pharmacy, Bucharest, Romania; Director of the Innovative Therapeutic Structures R&D Center, and Director of the Doctoral School, at the same university; 32 years' expertise in design and development of bioactive compound delivery systems for personalized medicine; functionalized nanoparticulate systems for theranostic purposes; valorization of the biopharmacological potential of medicinal and aromatic plants; more than 100 ISI articles; H index-27.

Preface

Chitosan remains an essential biopolymer within materials science and biomedical engineering, valued for its distinct physicochemical and biological characteristics, including biocompatibility, biodegradability, antimicrobial properties, and notable chemical versatility. Its range of applications encompasses drug delivery, wound healing, tissue engineering, and various environmental technologies.

Engineering, valued for its distinct physicochemical and biological characteristics, including biocompatibility, biodegradability, antimicrobial properties, and notable chemical versatility. Its range of applications encompasses drug delivery, wound healing, tissue engineering, and various environmental technologies.

This volume presents selected papers from the Special Issue "Chitosan Biomaterials: Advances and Challenges, 2nd Edition", published in the International Journal of Molecular Sciences. The articles in this collection reflect recent progress in chitosan modification, nanoparticle systems, hybrid composites, injectable hydrogels, and advanced biological evaluation techniques.

The studies included here not only advance our understanding of chitosan-based materials but also address key challenges such as improving mechanical performance, targeting drug release, and scaling up production for clinical or industrial translation.

We thank all authors and reviewers for their contributions to this Special Issue. This compilation is intended to provide information for researchers, clinicians, and engineers who are investigating and developing the applications of chitosan in science and technology.

Lacramioara Popa, Mihaela Violeta Ghica, and Cristina Elena Dinu-Pirvu

Guest Editors

International Journal of
Molecular Sciences

MDPI

Editorial

Chitosan Biomaterials: Advances and Challenges—2nd Edition

Lăcrămioara Popa [1,2], Mihaela Violeta Ghica [1,2,*] and Cristina-Elena Dinu-Pîrvu [1,2]

[1] Department of Physical and Colloidal Chemistry, Faculty of Pharmacy, "Carol Davila" University of Medicine and Pharmacy, 020956 Bucharest, Romania; lacramioara.popa@umfcd.ro (L.P.); cristina.dinu@umfcd.ro (C.-E.D.-P.)
[2] Innovative Therapeutic Structures Research and Development Centre (InnoTher), "Carol Davila" University of Medicine and Pharmacy, 020956 Bucharest, Romania
* Correspondence: mihaela.ghica@umfcd.ro

Obtained via the partial deacetylation of chitin, the naturally occurring polysaccharide chitosan is known for its biodegradability, biocompatibility, bioabsorbability, and non-toxicity [1–3]. Reactive amino and hydroxyl functional groups mean that it can easily be chemically functionalised and processed to create a wide range of biomaterials, including films, sponges, hydrogels, and nanofibres. These qualities have facilitated its extensive use in many fields, including biomedicine, pharmacology, agriculture, environmental protection, the food sector, and cosmetics [4–8]. Beyond these basic properties, chitosan shows a wide spectrum of intrinsic biological activity, including antibacterial, antifungal, antioxidant, haemostatic, immunostimulatory, anti-inflammatory, and anti-cancer action [9–13]. Many chitosan derivatives with improved physicochemical characteristics and therapeutic potential have been developed thanks to the synergy between their broad range of biological activities and chemical flexibility.

This Special Issue outlines recent developments in chitosan-based biomaterials and emphasises both the expected results and currently unsolved issues in this and related fields. These studies show innovation in a range of application fields, and show promise in helping to overcome current limitations.

In biomedical and pharmaceutical research, chitosan has been intensively investigated as a fundamental component in drug delivery systems, tissue engineering scaffolds, and strategies for wound healing and vaccine adjuvants [14,15]. Its capacity to produce hydrogels, nanofibres, and membranes has led to creative ideas in skin regeneration, controlled medication release, and chronic wound care.

Being highly adaptable, chitosan has shown promise in several domains, including cancer and tissue engineering. Its haemostatic, antibacterial, and mucoadhesive characteristics allow it to be used in wound dressings, as it can be processed into films, sponges, or nanofibres that tightly attach to the extracellular matrix and provide a moist environment ideal for tissue healing [16,17].

Our objective in curating this Special Issue, "Chitosan Biomaterials: Advances and Challenges—2nd Edition", was to compile innovative research on the design, synthesis, characterisation, and use of chitosan-based biomaterials. The published contributions offer a comprehensive view of current advancements, while highlighting challenges and suggesting future perspectives.

Several original studies have explored innovative biomedical applications of chitosan. Chitosan-based hydrogel systems for nasal insulin delivery have demonstrated significant potential in crossing biological barriers to target the central nervous system [18]. Popescu et al. designed and characterised novel hydrocolloid systems based on carboxymethyl

chitosan and hyaluronan, optimised for insulin delivery via the intranasal route, in an evaluation of carboxymethyl chitosan–hyaluronan hydrocolloid systems with insulin [18]. Their research demonstrated improved biocompatibility and bioavailability, paving the way for advancements in non-invasive diabetic therapies.

Regarding chitosan electrospun fibres, one contribution to this Special Issue showed encouraging results, including the development of chitosan–norfloxacin sheets that showed rapid and effective wound-healing effects by enhancing antioxidant defences and modulating inflammation. In a rat burn model, Coman et al. evaluated the biochemical and immunological effects of electrospun chitosan fibres loaded with the antibiotic norfloxacin [19]. Their results showed fast wound healing, decreased oxidative stress, and improved immunological responses, highlighting the therapeutic possibilities of chitosan–antibacterial systems.

In terms of cosmetic and dermatological applications, thanks to its moisturising, film-forming, and antimicrobial properties, chitosan is increasingly being utilised in skin care formulations, anti-ageing products, and hair treatments [20].

For their research article for this Special Issue, Schröder et al. explored the biological effects of α-chitosan and β-oligochitosan combinations on melanocyte cells. Their findings suggest the potential for chitosan-based formulas in regenerative medicine and therapies targeting skin conditions, including melanoma [21].

In the field of agriculture, chitosan functions as a natural inducer of plant immune responses and growth promoters. Its capacity to enhance plant resistance to pathogens while promoting biomass accumulation renders it a valuable tool in sustainable agriculture. In a study, Poznanski et al. demonstrated that treatment with partially deacetylated chitosan triggered immune responses and promoted biomass production in barley through salicylic acid-mediated pathways. This finding supports the use of chitosan as a natural elicitor in sustainable agriculture [22]. Furthermore, López-Velázquez et al. investigated how well high-density chitosan might prevent coffee leaf rust. Their study demonstrated higher disease resistance in Coffea arabica by stimulating a greater activation of defence enzymes and phytoalexin accumulation [23]. Novel chitosan-based beads that incorporate inorganic–organic composites effectively remove heavy metal ions from contaminated waters, demonstrating potential in environmental applications. These findings reinforce the role of chitosan as a promising green material in environmental remediation.

Chitosan's important affinity for heavy metals and organic pollutants positions it as an efficient material for water purification in the field of environmental protection. It has also been shown that chitosan-based composites can help greatly in removing pollutants from aqueous solutions, suggesting reasonably priced and sustainable solutions for raising water quality. Aravind et al. designed stable α-chitin-based composite materials for effective heavy metal ion adsorption from aqueous solutions through the processing of α-chitin into stable composite materials for heavy metal adsorption [24]. These composites show excellent adsorption capabilities and physicochemical stability, suggesting environmentally benign methods for wastewater treatment. Miron et al. developed chitosan-based beads using inorganic–organic composites for effective copper ion removal from polluted water using ecological methods. Their findings suggest a feasible path for environmentally friendly water treatment [25].

In the food sector, chitosan is employed both as a natural preservative and as a biodegradable packaging material. Chitosan coatings extend the shelf life of fresh produce by providing antimicrobial protection, while chitosan-based films offer eco-friendly alternatives to synthetic plastics [26–28].

All of this research is invaluable in clarifying how best to maximise chitosan materials for use in many different fields. Still, some important issues still need to be resolved if

we are to achieve the full potential of chitosan: firstly, especially in relation to molecular weight and degree of deacetylation, it is imperative that we standardise the description of chitosan derivatives; secondly, further study is required to improve the mechanical and biological characteristics of chitosan via creative functionalizing techniques; thirdly, the development and scaling of environmentally friendly industrial techniques are still of great importance; and fourthly, informed targeted uses depend on a better knowledge of the molecular processes behind the biological actions of chitosan. Ultimately, increasing the acceptance and impact of chitosan depends on the facilitation of the clinical and industrial transfer of chitosan-based innovations.

The ongoing development and application of chitosan in the scientific and industrial sectors depend on further explorations of these research topics.

Chitosan innovation could help shape the future and highlight a number of important topics for further research (Table 1).

Table 1. Priority areas for future research.

Priority Area	Research Focus
Advanced Functionalization	Design of chitosan derivatives for specific applications
Sustainable Production	Green extraction and eco-friendly processing
Mechanistic Insights	Elucidation of biological interactions
Standardisation and Regulation	Development of international quality standards
Smart Biomaterials	Integration into multifunctional systems

Chitosan's unique characteristics and natural source place it at the forefront of technological innovation, environmental sustainability, and human health. Chitosan-based materials will become more and more significant as the world pursues better solutions and more successful treatments.

The developments reported in this Special Issue highlight the current dynamic changes in chitosan research. They show not only the extent of development in this field but also the currently untapped potential.

As a naturally occurring, flexible, widely applicable biomaterial, we believe that chitosan will keep inspiring creativity in biomedicine, environmental science, and sustainable technology.

Although the field of chitosan innovation is one that is still emerging, it shows significant potential for transformation and innovation across many fields of science.

Author Contributions: Conceptualization, L.P. and M.V.G.; methodology, C.-E.D.-P.; software, L.P.; validation, L.P., M.V.G. and C.-E.D.-P.; formal analysis, C.-E.D.-P.; investigation, M.V.G.; resources, C.-E.D.-P.; data curation, M.V.G.; writing—original draft preparation, L.P.; writing—review and editing, L.P.; visualization, L.P. and M.V.G.; supervision, C.-E.D.-P.; project administration, L.P.; funding acquisition, C.-E.D.-P. All authors have read and agreed to the published version of the manuscript.

Acknowledgments: We acknowledge the support of "Carol Davila" University of Medicine and Pharmacy, Bucharest, Romania, through Contract No. CNFIS-FDI-2025-F-0646.

Conflicts of Interest: The authors declare no conflicts of interest.

References

1. Hong, K.; Meyers, S.P. Preparation and characterization of chitin and chitosan—A review. *J. Aquat. Food Prod. Technol.* **1995**, *4*, 27–52.
2. Younes, I.; Rinaudo, M. Chitin and Chitosan Preparation from Marine Sources. Structure, Properties and Applications. *Mar. Drugs* **2015**, *13*, 1133–1174. [CrossRef] [PubMed]

3. Yadav, M.; Kaushik, B.; Rao, G.K.; Srivastava, C.M.; Vaya, D. Advances and Challenges in the Use of Chitosan and Its Derivatives in Biomedical Fields: A Review. *Carbohydr. Polym. Technol. Appl.* **2023**, *5*, 100323. [CrossRef]
4. Jiménez-Gómez, C.P.; Cecilia, J.A. Chitosan: A Natural Biopolymer with a Wide and Varied Range of Applications. *Molecules* **2020**, *25*, 3981. [CrossRef]
5. Thambiliyagodage, C.; Jayanetti, M.; Mendis, A.; Ekanayake, G.; Liyanaarachchi, H.; Vigneswaran, S. Recent Advances in Chitosan-Based Applications—A Review. *Materials* **2023**, *16*, 2073. [CrossRef]
6. Ngo, D.-H.; Kim, S.-K. Antioxidant Effects of Chitin, Chitosan, and Their Derivatives. In *Advances in Food and Nutrition Research*; Kim, S.-K., Ed.; Academic Press: Cambridge, MA, USA, 2014; Volume 73, pp. 15–31. [CrossRef]
7. Kumar, S.; Mukherjee, A.; Dutta, J. Chitosan Based Nanocomposite Films and Coatings: Emerging Antimicrobial Food Packaging Alternatives. *Trends Food Sci. Technol.* **2020**, *97*, 196–209. [CrossRef]
8. Román-Doval, R.; Torres-Arellanes, S.P.; Tenorio-Barajas, A.Y.; Gómez-Sánchez, A.; Valencia-Lazcano, A.A. Chitosan: Properties and Its Application in Agriculture in Context of Molecular Weight. *Polymers* **2023**, *15*, 2867. [CrossRef]
9. Kou, S.G.; Peters, L.; Mucalo, M. Chitosan: A Review of Molecular Structure, Bioactivities and Interactions with the Human Body and Micro-Organisms. *Carbohydr. Polym.* **2022**, *282*, 119132. [CrossRef]
10. Aranaz, I.; Alcántara, A.R.; Civera, M.C.; Arias, C.; Elorza, B.; Heras Caballero, A.; Acosta, N. Chitosan: An Overview of Its Properties and Applications. *Polymers* **2021**, *13*, 3256. [CrossRef]
11. Ding, J.; Guo, Y. Recent Advances in Chitosan and Its Derivatives in Cancer Treatment. *Front. Pharmacol.* **2022**, *13*, 888740. [CrossRef]
12. Pu, S.; Li, J.; Sun, L.; Zhong, L.; Ma, Q. An In Vitro Comparison of the Antioxidant Activities of Chitosan and Green Synthesized Gold Nanoparticles. *Carbohydr. Polym.* **2019**, *211*, 161–172. [CrossRef] [PubMed]
13. Sarkar, S.; Das, D.; Dutta, P.; Kalita, J.; Wann, S.B.; Manna, P. Chitosan: A Promising Therapeutic Agent and Effective Drug Delivery System in Managing Diabetes Mellitus. *Carbohydr. Polym.* **2020**, *247*, 116594. [CrossRef]
14. Desai, N.; Rana, D.; Salave, S.; Gupta, R.; Patel, P.; Karunakaran, B.; Sharma, A.; Giri, J.; Benival, D.; Kommineni, N. Chitosan: A Potential Biopolymer in Drug Delivery and Biomedical Applications. *Pharmaceutics* **2023**, *15*, 1313. [CrossRef]
15. Rodríguez-Vázquez, M.; Vega-Ruiz, B.; Ramos-Zúñiga, R.; Saldaña-Koppel, D.A.; Quiñones-Olvera, L.F. Chitosan and Its Potential Use as a Scaffold for Tissue Engineering in Regenerative Medicine. *Biomed. Res. Int.* **2015**, *2015*, 821279. [CrossRef]
16. Jha, R.; Mayanovic, R.A. A Review of the Preparation, Characterization, and Applications of Chitosan Nanoparticles in Nanomedicine. *Nanomaterials* **2023**, *13*, 1302. [CrossRef]
17. Madni, A.; Kousar, R.; Naeem, N.; Wahid, F. Recent Advancements in Applications of Chitosan-Based Biomaterials for Skin Tissue Engineering. *J. Bioresour. Bioprod.* **2021**, *6*, 11–25. [CrossRef]
18. Popescu, R.; Dinu-Pîrvu, C.-E.; Ghica, M.V.; Anuța, V.; Popa, L. Physico-Chemical Characterization and Initial Evaluation of Carboxymethyl Chitosan–Hyaluronan Hydrocolloid Systems with Insulin Intended for Intranasal Administration. *Int. J. Mol. Sci.* **2024**, *25*, 10452. [CrossRef]
19. Coman, C.-G.; Anisiei, A.; Cibotaru, S.; Ailincai, D.; Pasca, S.A.; Chabot, C.; Gardikiotis, I.; Mititelu-Tartau, L. Chitosan-Electrospun Fibers Encapsulating Norfloxacin: The Impact on the Biochemical, Oxidative and Immunological Profile in a Rats Burn Model. *Int. J. Mol. Sci.* **2024**, *25*, 12709. [CrossRef] [PubMed]
20. Kulka, K.; Sionkowska, A. Chitosan Based Materials in Cosmetic Applications: A Review. *Molecules* **2023**, *28*, 1817. [CrossRef]
21. Schröder, V.; Gherghel, D.; Apetroaei, M.R.; Gîjiu, C.L.; Isopescu, R.; Dinculescu, D.; Apetroaei, M.-M.; Enache, L.E.; Mihai, C.-T.; Rău, I.; et al. α-Chitosan and β-Oligochitosan Mixtures-Based Formula for In Vitro Assessment of Melanocyte Cells Response. *Int. J. Mol. Sci.* **2024**, *25*, 6768. [CrossRef]
22. Poznanski, P.; Shalmani, A.; Bryla, M.; Orczyk, W. Salicylic Acid Mediates Chitosan-Induced Immune Responses and Growth Enhancement in Barley. *Int. J. Mol. Sci.* **2024**, *25*, 13244. [CrossRef] [PubMed]
23. López-Velázquez, J.C.; García-Morales, S.; López-Sánchez, G.P.; Montero-Cortés, M.I.; Uc-Várguez, A.; Qui-Zapata, J.A. High-Density Chitosan Induces a Biochemical and Molecular Response in *Coffea arabica* during Infection with *Hemileia vastatrix*. *Int. J. Mol. Sci.* **2023**, *24*, 16165. [CrossRef]
24. Aravind, A.; Seliverstova, K.; Kammerlander, K.K.K.; Henle, T.; Brunner, E. Processing α-Chitin into Stable Composite Materials for Heavy Metal Adsorption. *Int. J. Mol. Sci.* **2025**, *26*, 3149. [CrossRef]
25. Miron, A.; Iordache, T.-V.; Valente, A.J.M.; Durães, L.M.R.; Sarbu, A.; Ivan, G.R.; Zaharia, A.; Sandu, T.; Iovu, H.; Chiriac, A.-L. Chitosan-Based Beads Incorporating Inorganic–Organic Composites for Copper Ion Retention in Aqueous Solutions. *Int. J. Mol. Sci.* **2024**, *25*, 2411. [CrossRef]
26. Stefanowska, K.; Woźniak, M.; Dobrucka, R.; Ratajczak, I. Chitosan with Natural Additives as a Potential Food Packaging. *Materials* **2023**, *16*, 1579. [CrossRef]

27. Ferreira, D.C.M.; de Souza, A.L.; da Silveira, J.V.W.; Marim, B.M.; Giraldo, G.A.G.; Mantovan, J.; Mali, S.; Pelissari, F.M. Chitosan Nanocomposites for Food Packaging Applications. In *Multifunctional Hybrid Nanomaterials for Sustainable Agri-Food and Ecosystems*; Abd-Elsalam, K.A., Ed.; Elsevier: Amsterdam, The Netherlands, 2020; pp. 393–435. [CrossRef]
28. Priyadarshi, R.; Rhim, J.-W. Chitosan-Based Biodegradable Functional Films for Food Packaging Applications. *Innov. Food Sci. Emerg. Technol.* **2020**, *62*, 102346. [CrossRef]

International Journal of
Molecular Sciences

MDPI

Review

Melatonin/Chitosan Biomaterials for Wound Healing and Beyond: A Multifunctional Therapeutic Approach

Karolina Kulka-Kamińska [1], Patrycja Brudzyńska [1], Mayuko Okura [2], Tatsuyuki Ishii [2], Marco Skala [3], Russel J. Reiter [4], Andrzej T. Slominski [5,6], Kazuo Kishi [2], Kerstin Steinbrink [3], Alina Sionkowska [1,*] and Konrad Kleszczyński [3,*]

[1] Laboratory for Biomaterials and Cosmetics, Nicolaus Copernicus University in Toruń, Gagarin Str. 7, 87-100 Toruń, Poland; kkulka@doktorant.umk.pl (K.K.-K.); patrycja.brudzynska@umk.pl (P.B.)
[2] Department of Plastic and Reconstructive Surgery, Keio University School of Medicine, Tokyo 160-8582, Japan; mayuko.okura@keio.jp (M.O.); ttsyksh@keio.jp (T.I.); kkishi@keio.jp (K.K.)
[3] Department of Dermatology, University of Münster, Von-Esmarch-Str. 58, 48149 Münster, Germany; uni@skalamarco.eu (M.S.); kerstin.steinbrink@ukmuenster.de (K.S.)
[4] Department of Cell Systems and Anatomy, Long School of Medicine, UT Health, San Antonio, TX 78229, USA; reiter@uthscsa.edu
[5] Department of Dermatology, Comprehensive Cancer Center, Cancer Chemoprevention Program, University of Alabama at Birmingham, Birmingham, AL 35294, USA; aslominski@uabmc.edu
[6] VA Medical Center, Birmingham, AL 35294, USA
* Correspondence: alinas@umk.pl (A.S.); konrad.kleszczynski@ukmuenster.de (K.K.)

Abstract: Chitosan is increasingly utilized in combination with melatonin in novel formulations for a wide range of therapeutic applications. As a biocompatible and biodegradable polymer, chitosan exhibits notable properties, including antioxidant, antimicrobial, moisturizing, and absorption capabilities, in addition to a high potential for chemical modification due to its functional groups. These characteristics make it a valuable material in biomedical, pharmaceutical, cosmetic, food packaging, and environmental applications. Melatonin, an indoleamine primarily synthesized in the pineal gland but also found in various peripheral organs and in diverse organisms—including plants, bacteria, and fungi—has been extensively investigated for its antioxidant, anti-apoptotic, and anti-inflammatory activities, as well as its roles in immunomodulation, mitochondrial function, and melanin biosynthesis. This review summarizes recent advances in the combined use of chitosan and melatonin, with emphasis on their synergistic effects in wound healing, anti-cancer therapies, tissue engineering (i.e., skin and bone regeneration), and drug delivery systems. Additional potential applications are discussed in the context of cosmetology, aesthetic medicine, and veterinary practice.

Keywords: chitosan; melatonin; biomaterials; wound healing; anti-cancer therapy; drug delivery systems

1. Introduction

To reduce our environmental impact and dependence on fossil fuels, efforts are increasingly focused on the use of biodegradable materials, particularly those derived from natural sources. Among these, biopolymers stand out for their significant biodegradability and biocompatibility. In recent years, chitosan—a derivative of chitin composed of *β*-(1,4)-*D*-glucosamine and *β*-(1,4)-*N*-acetyl-*D*-glucosamine units—has gained considerable popularity [1,2]. Over the past two decades, chitosan has become a widely used raw material across numerous fields due to its unique properties. Its primary advantages include

its proven safety and non-toxicity [3], along with its notable antioxidant and antimicrobial activities. Additionally, chitosan exhibits excellent moisturizing and adsorption capabilities, and its functional groups allow for versatile chemical modifications [4]. However, its application is somewhat limited by its poor solubility in neutral and basic solutions [5]. Chitosan is primarily characterized by two key parameters: molecular weight and degree of deacetylation. The latter should be at least 60% for chitosan to exhibit desirable properties. These parameters significantly influence the physicochemical characteristics of the biopolymer, including its viscosity and solubility—factors that are crucial for its bioactivity, antibacterial and antioxidant properties, biodegradability, toxicity, and biocompatibility [6–8]. Low-molecular-weight chitosan typically exhibits better solubility and lower viscosity compared to its high-molecular-weight counterpart. Additionally, it can form denser structures, which may enhance the mechanical properties of materials. According to the literature, low-molecular-weight chitosan also demonstrates improved biodegradability and biocompatibility, lower toxicity, and greater bioactivity than chitosan with a higher molecular weight. Its antioxidant and antimicrobial activities are likewise more pronounced. Therefore, both molecular weight and degree of deacetylation should be carefully considered when designing chitosan-based materials for specific applications [9–11]. This biopolymer is widely used across various fields, including medical sciences, pharmacy, cosmetology, and the food and food packaging industries, as well as environmental pollution control [2,12]. It has been approved as a safe substance for use in food and medicine by the United States Food and Drug Administration (US FDA) [4]. Chitosan is particularly valuable as a drug delivery system due to its mucoadhesive properties and enhanced absorption, which stem from its polycationic nature. These characteristics make chitosan an effective matrix for drug encapsulation and delivery [13]. As a carrier, chitosan protects active substances, such as drugs, from oxidation and other environmental factors. For substances sensitive to external conditions, a protective delivery system is essential. Moreover, chitosan-based carriers enable the controlled release of active compounds, a feature that is highly important in many medical treatments. Chitosan is increasingly used in combination with melatonin (*N*-acetyl-5-methoxytryptamine), an indoleamine neurohormone synthesized predominantly in the pineal gland. Melatonin plays a key role in regulating circadian rhythms and a wide range of physiological functions [14]. Its secretion peaks at night but naturally declines with age, a change associated with neurodegenerative processes [15]. Beyond the pineal gland, melatonin is also synthesized in peripheral organs as a protective response against endogenous and exogenous stressors [16,17]. It regulates numerous physiological processes [17] and is found not only in animals but also in plants, bacteria, fungi, and other unicellular organisms [18,19], as well as in several natural products, including honey [20]. Melatonin participates in various cellular processes, exhibiting antioxidant, anti-apoptotic, and anti-inflammatory activities. It also regulates immune responses, mitochondrial homeostasis, and pigmentation [21]. Thanks to its amphiphilic nature, melatonin can act in both lipid and aqueous environments within cells, effectively reducing oxidative stress. It influences glutathione synthesis and the activity of glutathione reductase. Moreover, melatonin has demonstrated potential in anti-cancer strategies [22], and as a promising agent in anti-aging skincare, particularly in mitigating the harmful effects of UV radiation [17,23,24]. However, melatonin has a short half-life and low bioavailability, which limits its therapeutic effectiveness. Encapsulation using biopolymeric carriers such as chitosan offers a promising solution to these limitations [25]. In most applications, chitosan functions as a carrier that protects melatonin until it reaches its target site. Due to its broad biological activity, melatonin is used far beyond sleep regulation, with applications spanning medicine, the food industry, and more. This review compiles and summarizes the scientific findings on the combined use of chitosan and melatonin,

focusing on their applications in wound healing, cancer therapy, tissue engineering, drug delivery, and food chemistry, with additional insight into potential uses in cosmetology, veterinary medicine, and agriculture (Figure 1).

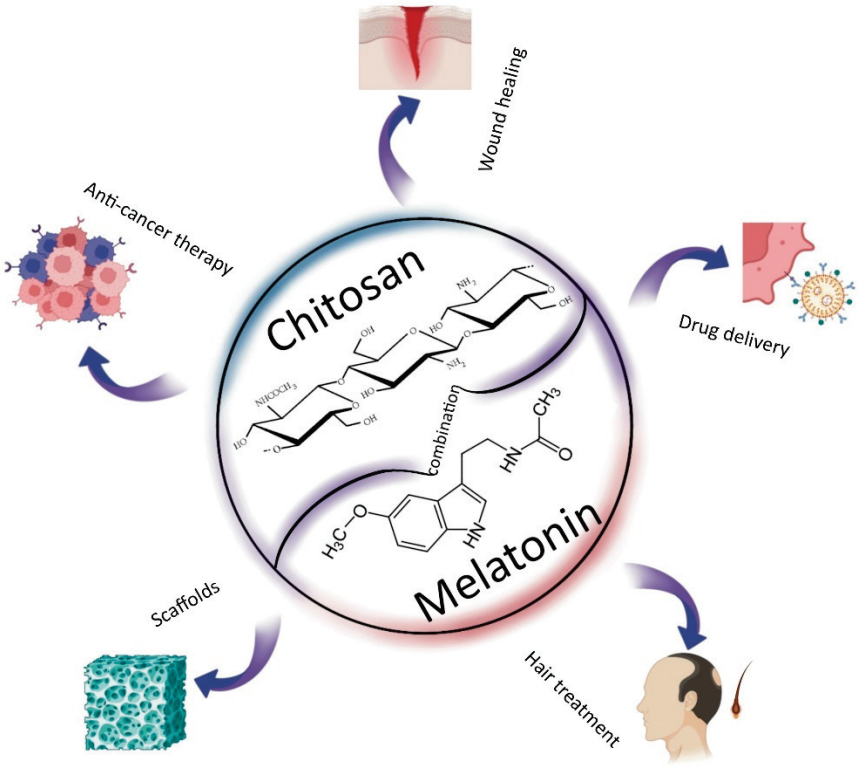

Figure 1. Applications of chitosan and melatonin combinations.

2. Synergistic Applications of Chitosan and Melatonin

2.1. Wound Healing

Human skin is constantly exposed to environmental factors and serves as the primary self-regulating barrier against such stressors [17,26]. Beyond its protective function, the skin plays multiple roles, including roles in thermoregulation, vitamin D synthesis, sensory perception, and various secretory functions [27–30]. As such, any disruption to the skin—such as a wound—can pose a significant threat to human health or, in severe cases, life. Even minor wounds may lead to undesirable outcomes such as scarring. A wound is defined as a disruption of tissue continuity and can be classified based on its cause, type, and treatment duration [27,31]. Wound healing is a complex biological process aimed at restoring the structural and functional integrity of damaged tissue. It occurs through four overlapping phases: hemostasis, inflammation, proliferation, and dermal remodeling [28,32]. This process is tightly regulated and involves dynamic communication between various cell types [33]. Wound dressings play a critical role in supporting and guiding the healing process [25]. The characteristics of an ideal wound dressing include gas permeability, a barrier against external contaminants, absorption and removal of excess exudate, maintenance of optimal moisture levels, and the controlled release of active substances [31,34] (Figure 2). Dressings made from biopolymers are especially promising due to their beneficial properties, including non-toxicity, biodegradability, biocompatibility, and their structural similarity to macromolecules naturally recognized by the human body [31,35].

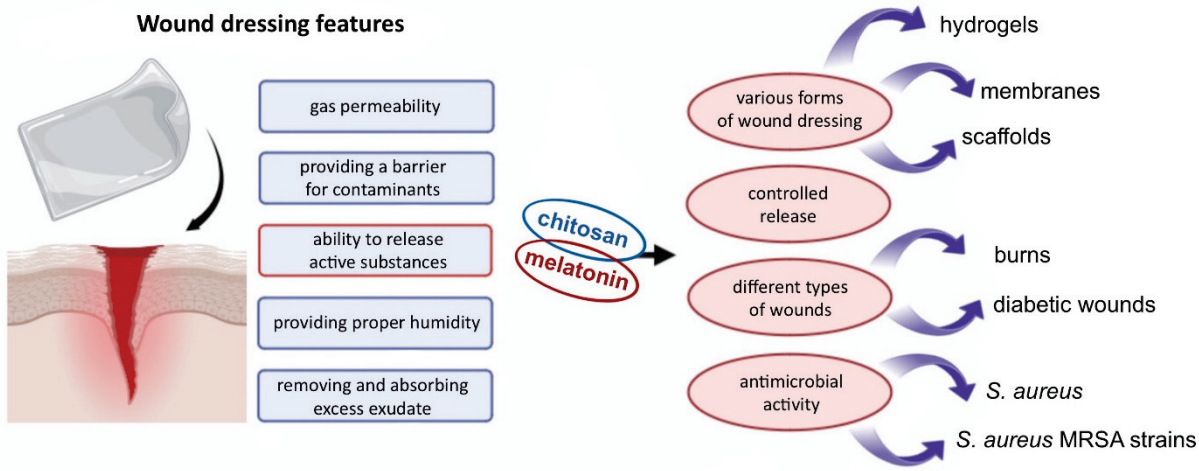

Figure 2. The potential of a chitosan/melatonin combination as a wound-healing agent.

Modern wound dressings based on biopolymers are designed in various forms, but their primary goal remains the same: to enhance healing efficiency. In this context, nano- and microtechnological solutions have gained considerable interest, particularly those involving microspheres, nanoparticles, and nanofibers. For example, Romic et al. [36] developed melatonin-loaded chitosan-based microspheres as a dry powder formulation suitable for wound dressings. Upon contact with wound exudate, the powder rapidly forms a hydrogel. The encapsulation of melatonin within chitosan/Pluronic F127 microspheres significantly enhanced the antimicrobial activity of chitosan against *Staphylococcus aureus*, including five clinical isolates of methicillin-resistant *S. aureus* (MRSA) strains. These microspheres were also shown to be biocompatible with epidermal keratinocytes and dermal fibroblasts at concentrations relevant to antimicrobial activity against planktonic bacteria. Additionally, the hydrogel formed from these microspheres maintained a favorable water vapor transmission rate (WVTR), ranging from 2357 to 2421 $g/m^2/day$, depending on the pH level. This range falls within the optimal WVTR for maintaining wound moisture without dehydration, typically between 2000 and 2500 $g/m^2/day$ [36]. Chronic, non-healing wounds remain a significant global health challenge. Melatonin has demonstrated potential in promoting diabetic wound healing and supporting corneal regeneration. In a subsequent study, Romic et al. [37] evaluated two types of melatonin-loaded chitosan microspheres. The research included full characterization of the microspheres, stability testing, and assessment of their wound-healing potential. Results showed that the chitosan microspheres effectively protected melatonin from degradation, even after six months of storage. The wound-healing properties of the formulations were evaluated using an in vitro scratch assay with human dermal fibroblasts. While both microsphere systems exhibited good stability, the inclusion of lipids enhanced their wound-healing efficacy [37]. Romic et al. [38] developed a hybrid wound-dressing system composed of nanostructured lipid carrier (NLC)-loaded, chitosan-based microspheres containing melatonin in dry powder form. This advanced formulation is designed to form a hydrogel layer upon contact with wound exudate, providing a modern approach to wound care. Nanostructured lipid carriers serve as an effective matrix for active substances, enabling controlled drug release. The preparation process involved two key steps: first, melatonin-loaded NLCs were produced using a hot homogenization technique; second, the final dry powder was obtained through spray drying. The release profile of melatonin from this hybrid system followed a biphasic pattern characterized by an initial burst release followed by a sustained-release phase. This dual-phase release is beneficial for wound healing, as it allows for immediate antimicrobial action while maintaining therapeutic levels of the drug over an extended period. The

formulation demonstrated biocompatibility with human keratinocytes and fibroblasts, indicating its safety for topical use. Moreover, the system exhibited antimicrobial activity against *Staphylococcus aureus* and MRSA strains [38,39]. Cytotoxicity studies further confirmed the safety of the nanoparticle-based system, showing no membrane damage or reduction in cell viability even at concentrations up to 200 μg/mL.

Melatonin is considered a strong candidate for transdermal delivery due to its low molecular weight, amphiphilic chemical nature, and short plasma half-life. Topical application of melatonin is also desirable because of its anti-inflammatory and antioxidant properties [39]. In a study by Blazevic et al. [40], an alternative strategy was developed involving the use of nanocarriers to locally deliver melatonin for wound-healing purposes. Lecithin/chitosan nanoparticles were prepared using four different types of chitosan, all in the form of hydrochloride salts with varying molecular weights and degrees of deacetylation. Two of the types of chitosan had molecular weights ranging from 50 to 150 kDa, while the other two ranged from 150 to 400 kDa. The degree of deacetylation was either between 75 and 90% or greater than 90%. An in vitro scratch assay was used to evaluate the wound epithelialization potential. Nanoparticles derived from chitosan with a molecular weight of 50–150 kDa and a deacetylation degree above 90% demonstrated the highest wound-healing efficacy. However, the differences compared to other samples were not statistically significant. Therefore, it can be concluded that the various types of chitosan used in nanoparticle formulation have comparable effects on keratinocyte proliferation and migration. The key factor enhancing wound epithelialization appears to be the combination of chitosan and melatonin within the nanoparticle suspension, which may exert a synergistic effect [40]. Kaczmarek-Szczepańska et al. [41] developed biomimetic hybrid scaffolds based on a biopolymer matrix containing not only chitosan but also collagen—a valuable material for tissue engineering—enriched with melatonin for potential wound-dressing applications. The prepared scaffolds significantly enhanced cell viability in reference melanoma cells, dermal fibroblasts, and epidermal keratinocytes. Materials containing melatonin demonstrated accelerated re-epithelialization, increased water retention, and reduced wound-healing duration. Furthermore, the presence of this biologically active compound did not adversely affect the thermal stability of the scaffolds [41]. As previously mentioned, wound care in diabetic patients is a critical global health concern, often leading to amputations and even death. Correa et al. [42] developed an in vivo animal model to evaluate the wound-healing potential of lecithin/chitosan nanoparticles loaded with melatonin in the context of diabetes. The nanoparticles exhibited a positive surface charge due to the presence of chitosan—an important characteristic for wound dressings, as it facilitates interaction with cells in the wound environment. In a rat wound-healing model, treatment with melatonin-loaded nanoparticles for three days significantly stimulated fibroblast proliferation and increased the number of blood vessels, indicating that this formulation promotes healing at the early proliferative phase. Similar results were observed after seven days of treatment. Additionally, an increase in collagen content was noted in the rats treated with the melatonin-loaded chitosan nanoparticles. This formulation effectively protected encapsulated melatonin and ensured its controlled delivery to the wound site. The nanoparticle structure enabled sustained release of the active biomolecule, contributing to the angiogenesis process [42].

Burn wounds are a distinct type of skin injury that require targeted treatment to prevent infections and minimize scarring. Traditional burn treatments often rely on silver-based formulations due to their antimicrobial properties; however, the cytotoxicity of silver compounds can delay the healing process. Melatonin, known for its antioxidant and anti-inflammatory properties, presents a promising alternative for this application. In a study conducted by Soriano et al. [43], a nanogel formulation based on hyaluronic acid, chitosan,

and poloxamer, with the addition of melatonin, was developed. This formulation was compared with a commercially available silver-based preparation. Cytotoxicity assays revealed that the melatonin-containing nanogel was non-toxic and exhibited excellent physicochemical and wound-healing properties while also being biocompatible with healthy skin [43]. A different approach was proposed by Mirmajidi et al. [44], who developed a more complex multilayered wound dressing using the electrospinning technique. The dressing consisted of three layers: the outer and inner layers were composed of polycaprolactone/chitosan, and the middle layer was made of poly(vinyl alcohol) containing melatonin. The resulting nanofiber dressing was found to be nearly hydrophilic, a characteristic not affected by melatonin concentration. This hydrophilicity is advantageous for maintaining a moist wound environment, which supports the healing process. The multilayer dressing functioned as both a reservoir and a matrix for drug release. It exhibited an initial burst release of melatonin during the first 14 h, followed by a sustained release over time—an ideal profile for wound patches intended to remain in place for several days. In vivo studies confirmed the dressing's positive impact on wound healing, showing enhanced collagen synthesis and improved regeneration of the epithelial layer [44].

In addition to their proven efficacy in wound healing, systems combining chitosan and melatonin offer another significant advantage: the protection of melatonin during storage prior to application. Hafner et al. [45] investigated the stability of lecithin/chitosan nanoparticles loaded with melatonin following a freeze-drying process. The study evaluated the effects of different types of lecithin and various cryoprotectants, including glucose and trehalose. The results demonstrated that trehalose was the more effective cryoprotectant, enabling the storage of melatonin-loaded chitosan-based nanoparticles for up to seven months at 4 °C without significant changes in appearance, physicochemical properties, or melatonin content [45]. Melatonin release behavior is a critical factor in many biomedical applications. Pancescu et al. [46] conducted a detailed analysis of melatonin release through chitosan/sEPDM (sulfonated ethylene/propylene/diene terpolymer) composite membranes under various conditions. Compared to pure sEPDM membranes, the composite membranes exhibited a faster melatonin release rate. The authors suggested that this system may be particularly suitable for sports-related applications, where rapid drug action is essential [46]. Beyond wound dressings, the combination of chitosan and melatonin is showing increasing promise in biomedical engineering, particularly in the development of scaffolds for tissue regeneration and repair.

2.2. Scaffolds and Hydrogels

According to the World Health Organization, only 10% of the global demand for tissues and organs is currently met, representing a significant public health challenge [47]. Advances in regenerative medicine and tissue engineering offer promising solutions to address this shortage. The primary goals of tissue engineering include restoring, replacing, maintaining, or enhancing the function of various types of biological tissues [48]. With the rapid progress in this field, scaffolds have gained considerable attention, particularly those made from natural polymers. Chitosan is one such biopolymer widely used in scaffold construction for applications such as bone regeneration [48–50], oral bone repair [51], cardiovascular treatments [52,53], and skin regeneration [54,55]. Recently, chitosan-based scaffolds combined with melatonin have emerged as a novel and promising approach in tissue engineering. Bone regeneration relies on multiple factors, with bone morphogenetic proteins (BMPs) playing a crucial role. Among them, BMP-2 is the most well-known and potent osteoinductive agent. However, the use of high doses of BMP-2 in bone treatment can lead to undesirable side effects, such as osteoclast activation.

In a study conducted by Jarrar et al. [56], scaffolds composed of chitosan and hydroxyapatite were developed with the addition of BMP-2 and melatonin, with the latter being used as an osteoclast-inhibiting agent at a concentration of 800 μM. This concentration of melatonin effectively attenuated osteoclast differentiation induced by a high dose of BMP-2, suggesting that the designed scaffolds hold significant promise for bone regeneration therapies [56]. In a subsequent study by the same research group [57], the focus was on evaluating the osteogenic activity of pre-osteoblastic MC3T3-E1 cells in response to the prepared scaffolds. The tested material consisted of a chitosan/hydroxyapatite scaffold loaded with polylactic-co-glycolic acid (PLGA) microparticles encapsulating both melatonin and BMP-2. These microparticles were synthesized using a double emulsion solvent evaporation method, resulting in a dual-release scaffold system. The study demonstrated that the synergistic effect of the combined release of melatonin and BMP-2 significantly enhanced the osteogenic activity of pre-osteoblasts in vitro, compared to single-agent systems containing either melatonin or BMP-2 alone. The dual system notably increased the expression of early osteogenic markers and promoted osteoblast formation [57,58].

As previously mentioned, melatonin has demonstrated anti-cancer properties, including anti-proliferative effects and the ability to inhibit tumor promotion and progression. One study investigated the formation of melatonin inclusion complexes by incorporating melatonin into the hydrophobic cavity of cyclodextrins, a strategy aimed at enhancing melatonin's solubility. Cell culture experiments were conducted using three types of chitosan-based scaffolds: a plain chitosan scaffold, a scaffold loaded with melatonin, and a scaffold loaded with the melatonin/cyclodextrin inclusion complex. The cumulative release of melatonin from the inclusion complex was higher than from the scaffold containing pure melatonin. In vitro studies showed that approximately 5.1 mM of melatonin was released from the melatonin-loaded scaffold, whereas 9.3 mM was released from the inclusion complex scaffold. A melatonin concentration of 9 mM was sufficient to induce significant cell growth inhibition, while a 5 mM concentration initially caused some cell death, but surviving cells resumed proliferation over the remainder of the study period [58]. Another research group proposed a scaffold-based device incorporating melatonin for osteosarcoma therapy, evaluating its dual activities. First, a rapid release of melatonin at high concentration was intended to exert anti-cancer effects, then a sustained low-concentration release was intended to promote bone regeneration. To investigate the first approach, the effect of a melatonin/2-hydroxypropyl-β-cyclodextrin (HPβCD) inclusion complex on MG-63 human osteosarcoma cells was assessed. Melatonin was rapidly released within 5 h, leading to inhibited cell proliferation by arresting cells in the G0/G1 phase. The second approach involved incorporating melatonin into poly(lactic-co-glycolic acid) (PLGA) microparticles. Both delivery systems were then loaded into chitosan/hydroxyapatite scaffolds, enabling controlled melatonin release characterized by an initial burst within 24 h followed by sustained release over 40 days at concentrations ranging approximately from 40 to 70 μM. In this sustained-release scenario, melatonin significantly increased the expression of osteogenic differentiation markers compared to controls. This scaffold system thus exhibits both anti-cancer and osteoinductive properties, making it a promising therapeutic option for osteosarcoma patients, particularly post-surgery, to eliminate residual cancer cells and promote new bone formation [59]. In a related study, Huang et al. [60] aimed to prepare melatonin-loaded chitosan microparticles with osteoinductive and osteoconductive potential. Two fabrication methods were employed: ionic cross-linking and an oil-in-water emulsion technique. The in vitro release profiles of melatonin were comparable between the two types of microparticles, and mineralization matrix formation assays were conducted. Results demonstrated that this sustained-release system effectively induced osteogenic differentiation in vitro. Alkaline phosphatase, an early osteoblast differ-

entiation marker, was activated through continuous melatonin administration, which also promoted calcium deposition. This controlled-release platform may thus offer beneficial effects for bone tissue regeneration [60].

In the study by Kaczmarek-Szczepańska et al. [61], 3D skin scaffolds composed of chitosan and collagen and loaded with melatonin were developed. Glyoxal was used as a cross-linking agent to achieve optimal porosity, as well as favorable physicochemical and mechanical properties. Various biopolymer ratios were prepared, both with and without glyoxal. The results demonstrated that melatonin enhanced cell proliferation regardless of whether the cross-linker was present. Increased growth rates were observed in human keratinocytes, fibroblasts, and melanoma cells. Melatonin contributed to maintaining mitochondrial homeostasis, protecting cells against reactive oxygen species, and supporting the skin's barrier function by stimulating the expression of involucrin and keratins. The porous structure of the scaffolds was a critical feature, allowing oxygen flow and thereby accelerating tissue repair. Overall, the melatonin-loaded chitosan/collagen scaffolds showed promise as safe and effective materials for skin restoration applications [61].

2.3. Cosmetology/Dermatology (Hair Treatment)

Melatonin has also been explored for its potential applications in cosmetics and dermatology, particularly in the treatment of androgenic alopecia. This genetically predisposed, chronic condition is characterized by a shortened anagen phase and a prolonged telogen phase within the hair growth cycle. Hair loss associated with androgenic alopecia can significantly impact quality of life and self-esteem. Currently, the U.S. Food and Drug Administration (FDA) has approved two treatments: orally administered finasteride and topically applied minoxidil [62]. However, both agents are associated with adverse effects and often demonstrate limited efficacy, prompting the need for alternative therapies. Melatonin emerges as a promising candidate in this context. Human skin and hair follicles contain melatonin receptors, which play a role in regulating cellular proliferation and differentiation [16,62]. Moreover, melatonin and its metabolites exert bioregulatory effects through nuclear receptors such as the aryl hydrocarbon receptor (AhR) and peroxisome proliferator-activated receptor gamma (PPARγ) [63]. The skin also possesses the enzymatic machinery required to synthesize melatonin from tryptophan via a series of enzymatic reactions [16]. Melatonin contributes not only to hair growth regulation but also to hair pigmentation [64]. Additionally, the skin's endogenous melatoninergic antioxidant system offers protection against UV-induced damage [16,65]. A study by Fischer et al. [64] investigated the topical application of melatonin in patients with androgenic alopecia (AGA) or general hair loss. Results demonstrated a significant reduction in the severity of alopecia after 30 and 90 days of once-daily application. Importantly, topical melatonin did not affect endogenous serum melatonin levels. The authors concluded that the melatonin solution presents a viable treatment option for AGA [62]. Melatonin's efficacy in treating alopecia is attributed to its antioxidant properties and biochemical activity at the levels of corneocytes and hair follicles. However, melatonin is susceptible to photodegradation and oxidation, which can limit its effectiveness. To address this, Elshall et al. [66] encapsulated melatonin in Pickering emulsions stabilized with chitosan/dextran sulfate nanoparticles. The formulation was compared with minoxidil, the standard drug used for alopecia treatment. These chitosan/dextran sulfate-based emulsions enhanced the photostability of melatonin and preserved its antioxidant activity [66].

Overall, formulations combining chitosan and melatonin offer a promising alternative for the treatment of androgenic alopecia, with potential advantages in stability, biocompatibility, and therapeutic efficacy.

2.4. Anti-Cancer Therapy

Cancer remains one of the most prevalent diseases worldwide, resulting from uncontrolled cellular proliferation [67,68]. A variety of treatment modalities are currently employed, including chemotherapy, radiation therapy, immunotherapy, targeted therapies, and surgical resection [67,68]. While conventional treatments such as chemotherapy can be effective, cancer-related mortality rates remain high. Major limitations of these therapies include a lack of specificity, poor drug solubility, and significant cytotoxicity to healthy tissues [68]. Emerging anti-cancer strategies rooted in precision medicine are increasingly based on nanotechnology [69]. Nanoparticles offer several advantages over traditional therapies, including localized activity that reduces systemic side effects. In addition, they are typically non-toxic, biodegradable, biocompatible, and non-immunogenic, and they can facilitate the delivery of poorly soluble drugs [69]. Researchers are also actively exploring natural substances as potential anti-cancer agents [70]. Among these, melatonin has gained significant interest due to its multifaceted biological activity [22]. Although further studies are needed to fully elucidate its mechanisms of action in cancer treatment [71], melatonin is recognized for its anti-cancer potential through various pathways. These include modulation of cell signaling pathways, antioxidant effects, protection of genomic integrity, inhibition of cancer cell migration, and suppression of the inflammatory processes associated with carcinogenesis [72–74]. The combination of chitosan nanoparticles and melatonin is gaining increasing attention in cancer research, as illustrated in Figure 3.

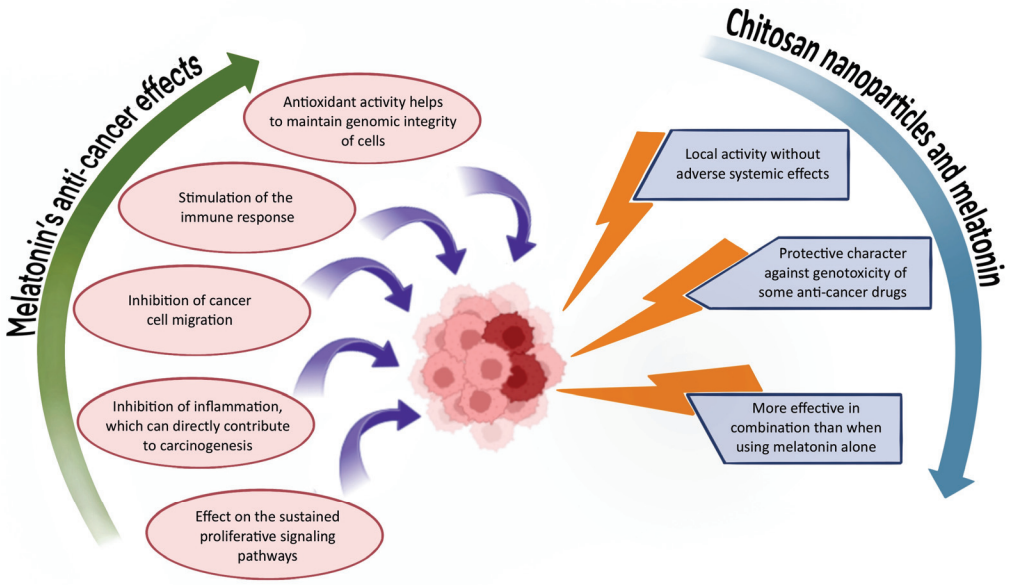

Figure 3. Overview of the properties and benefits of the chitosan/melatonin combination in anti-cancer therapy.

Breast cancer is the second most common type of cancer among women worldwide. Although various treatment options are available, resistance to therapy remains a significant clinical challenge. A novel approach was proposed by Jafari et al. [75], who developed composite nanoparticles incorporating melatonin for potential use in breast cancer therapy. The polymer matrix consisted of chitosan and hydroxypropyl methylcellulose, cross-linked with tripolyphosphate. The release profile of melatonin from the matrix varied depending on the pH of the environment, with significantly higher cumulative release observed at pH 5.5 compared to pH 7.5. Both free and encapsulated melatonin demonstrated cytotoxicity toward MDA-MB-231 breast cancer cells; however, encapsulated melatonin showed enhanced toxicity. These findings suggest that the proposed composite nanoparticle system may be more effective in acidic tumor microenvironments [75]. Another research

group, led by Yadav et al. [76], developed chitosan nanoparticles loaded with melatonin as a potential anti-cancer therapy. The nanoparticles were prepared using the ionic gelation method with a tripolyphosphate solution. Cytotoxicity studies were conducted using the U87MG cell line, a human glioblastoma model. After 24 h of incubation, melatonin-loaded nanoparticles reduced cell viability to 22%, a significantly better outcome compared to the control. To assess safety for healthy cells, the HEK293T cell line was used, and the results indicated very low cytotoxicity. Furthermore, co-culture experiments with both HEK293T and U87MG cells demonstrated moderate overall cytotoxicity. These findings highlight the potential of this nanoparticle system for glioblastoma treatment [76].

Melatonin is recognized not only for its anti-cancer properties but also for its role as an organ protectant during cancer pharmacotherapy [22]. Shokrzadeh et al. [77] conducted studies demonstrating melatonin's protective effect against genotoxicity induced by etoposide—a potent chemotherapeutic agent known for its side effects, including vomiting, alopecia, and DNA damage in healthy tissues. In this study, the protective effects of both free melatonin and melatonin in nanoparticle form were evaluated using human HepG2 hepatoma cells. Melatonin was encapsulated in nanoparticles using chitosan and sodium tripolyphosphate. The results showed that both forms of melatonin conferred protection against etoposide-induced genotoxicity, but the nanoparticle formulation was more effective. A concentration of 100 μmol/L significantly reduced DNA fragmentation in the treated cells [77]. In another study by the same research group, Shokrzadeh et al. [25] investigated the protective properties of chitosan/tripolyphosphate nanoparticles loaded with melatonin against the genotoxic effects of doxorubicin, another widely used chemotherapeutic drug. Melatonin was utilized for its known genoprotective and antioxidant effects. The results revealed that melatonin significantly reduced doxorubicin-induced genotoxicity, lowered intracellular reactive oxygen species levels, and increased glutathione content in HepG2 cells. These findings suggest that melatonin-loaded nanoparticles, prepared via the ionotropic gelation method, offer substantial protective effects against chemotherapy-induced cellular damage [25].

Overall, numerous studies underscore the broad potential of chitosan-based systems enriched with melatonin in addressing cancer-related challenges, both as therapeutic agents and as supportive protective strategies.

2.5. Drug Delivery Systems

Chitosan is a chemically stable compound that is biocompatible with a wide range of tissues and cells [78]. Owing to its beneficial properties—including its antimicrobial, antioxidant, anti-inflammatory, and mucoadhesive effects, as well as its ability to facilitate controlled drug release, in situ gelation, and enhanced permeation—it is considered a highly suitable biopolymer for use in drug delivery systems. These favorable characteristics are primarily attributed to the presence of primary amino groups, which confer chitosan's cationic nature [79]. Chitosan can be utilized via various delivery routes, including nasal, oral, transdermal, pulmonary, ocular, vaginal, and ophthalmic routes, depending on its formulation [78,80]. Among these, nanoparticles are the most commonly used form in drug delivery applications. Chitosan nanoparticles are advantageous due to their effectiveness, ease of preparation, and enhanced stability [80]. Methods for producing chitosan nanoparticles include ionic cross-linking, covalent cross-linking, the reverse micellar method, precipitation, and the emulsion-droplet coalescence method [80,81]. Importantly, chitosan nanoparticles are generally considered safe and exhibit low toxicity. However, some studies have reported that the toxicity of unmodified chitosan may increase with higher charge density and a greater degree of deacetylation [82,83]. Overall, chitosan

serves as a versatile drug carrier which is particularly suitable for transporting sensitive pharmaceutical substances, such as melatonin, that require protection from external factors.

In the study conducted by Hafner et al. [84], two types of nanocarriers were developed for ocular drug delivery of melatonin. The first formulation consisted of lecithin/chitosan nanoparticles, while the second involved Pluronic 127/chitosan micelles. The nanoparticles were larger in size and exhibited a higher surface charge compared to the micelles. The mucoadhesive properties of the lecithin/chitosan nanoparticles were also evaluated, as these characteristics are critical for prolonging drug residence time on the ocular surface. Chitosan-based nanoparticles demonstrated enhanced mucoadhesive capabilities, which correlated with their higher surface charge. Cytotoxicity was assessed using HCE-T cells treated with chitosan concentrations ranging from 2.5 to 20 μg/mL. Cell viability assays indicated that the chitosan-based nanosystems were safe, showing no significant toxic effects. Notably, chitosan incorporated into nanocarriers was less cytotoxic than chitosan in solution form, highlighting the advantage of nanoparticle formulation. In vitro tests using a corneal epithelial model showed that lecithin/chitosan nanoparticles provided a prolonged release of melatonin compared to both the micelle system and melatonin solution. These properties are promising for ocular applications, offering improved bioavailability and potential for intraocular pressure reduction [84].

Novel hydrogel materials based on chitosan, incorporating melatonin or propolis as antioxidant agents along with other active substances, were evaluated for use in stomatology by Perchyok et al. [85]. The antioxidants, including melatonin, were microencapsulated. The stability of these antioxidants within the system was assessed after 24 h and again after 6 months of storage using a cupric ion (Cu^{2+}) reducing strength assay. The results showed over 95% stability, indicating effective protection by the microcarriers. Additionally, the presence of chitosan enhanced the antioxidant activity, suggesting a synergistic effect between the biopolymer and the antioxidants. The proposed hydrogel material also improved dentin adhesive bond strength and positively influenced drug release behavior [85].

Excessive reactive oxygen species (ROS) can impair oocyte maturation, often due to insufficient antioxidant defenses. In a study by Tawfik et al. [86], melatonin supplementation was used in maturation media to investigate its antioxidant effects on the cytoplasmic and nuclear maturation of porcine oocytes. Melatonin also acted as a cytoprotective agent, preventing nitrosative damage. However, its clinical application is challenged by its short half-life and low water solubility. Nanocapsules offer a promising solution for effective melatonin delivery. The study revealed significant differences in gene expression profiles among the groups treated with melatonin-loaded chitosan nanoparticles, free melatonin, and the control. Encapsulated melatonin nanoparticles proved to be the most effective in enhancing oocyte maturation [86].

Chitosan nanoparticles have been used as carriers for melatonin due to its anti-inflammatory properties. In a study by Soni et al. [87], melatonin-loaded chitosan nanoparticles were evaluated for their potential in treating inflammatory bowel disease (IBD). The primary goal was to enhance the drug release profile and assess the therapeutic efficacy of the formulation. The synthesized nanoparticles demonstrated improved anti-inflammatory activity in both in vitro and in vivo IBD models, confirming their protective and therapeutic effects. Consequently, the therapeutic efficacy of melatonin was enhanced [87]. In a separate study, Mohanbhai et al. [88] also investigated the use of melatonin and chitosan for IBD treatment. Given melatonin's poor water solubility, the researchers developed chitosan nanoparticles coated with a colon-targeting polymer (Eudragit S-100) to enhance its delivery. The formulation enabled prolonged and targeted release of melatonin in the colon, resulting in improved therapeutic effectiveness [88]. Additionally, chitosan was employed as a nanocarrier for the co-delivery of melatonin and tretinoin using a self-assembly

method. Aghaz et al. [89] evaluated the antioxidant activity of this dual-drug system in a mouse oocyte and embryo model. The results indicated that the combination effectively reduced ROS levels and exhibited synergistic antioxidant effects. Taken together, the existing literature demonstrates that chitosan is an effective carrier for melatonin, enhancing its stability, bioavailability, and therapeutic potential across various biomedical applications.

2.6. Other Applications

Melatonin has a wide range of applications beyond medicine and dermatology, including uses in jet lag treatment, food technology, and agriculture. Jet lag is a condition characterized by disturbances in the sleep–wake cycle which is often accompanied by fatigue, impaired cognitive performance, daytime sleepiness, and gastrointestinal discomfort. These symptoms result from rapid transitions across time zones and can persist for several days, significantly affecting the quality of life of travelers and long-haul flight crews [90]. Melatonin supplementation, taken at times when it would naturally be released by the body, can facilitate adaptation to new time zones and alleviate jet lag symptoms [91]. In an effort to address this issue, Razali et al. [92] developed a multi-particulate delivery system incorporating both melatonin and caffeine. The objective of the study was to design a dual-release formulation: one that sustains the release of melatonin to promote sleep and another that delays the release of caffeine to support wakefulness after the sleep period. Various system configurations were evaluated, including pellets, compact forms, and a dome-shaped matrix. The most effective melatonin delivery system consisted of an alginate/chitosan matrix with a cushioning agent—low-viscosity hydroxypropyl methylcellulose—which enabled complete gastrointestinal release of melatonin within 8 h. For caffeine, the most promising delayed-release system included microcrystalline cellulose, high-viscosity hydroxypropylcellulose, and high-viscosity ethylcellulose. This combination successfully delayed caffeine release until approximately 8 h after melatonin administration, aligning with the desired timing for post-sleep alertness [92]. The applications of chitosan in food technology stem from its advantageous physicochemical properties, biological activity, and safety profile. Key areas of its utilization include shelf-life extension, functional food production, emulsification, and flocculation [1] (Figure 4). The extension of food shelf life is primarily attributed to chitosan's antioxidant, antimicrobial, and film-forming properties. Edible films and coatings made from chitosan represent a simple and effective packaging method, which can be further enhanced with the addition of flavorings, colorants, preservatives, and other active ingredients [1,93]. The combination of chitosan and melatonin in food-related applications offers synergistic effects, particularly in enhancing antioxidant potential. Melatonin plays a significant role in preserving the quality of food products by delaying chlorophyll degradation, reducing oxidative damage in freshly cut fruits, minimizing weight loss, and maintaining firmness in postharvest fruit products [94]. This combination presents a promising strategy for improving the quality and extending the shelf life of fresh produce.

Al-Quarashi et al. [95] proposed a postharvest dipping treatment for bananas that used 1% chitosan and 0.5 mM melatonin, applied both individually and in combination. The treatment delayed ripening by preserving a greener peel and greater firmness compared to the control group. Additionally, treated bananas exhibited higher total phenolic and flavonoid content, as well as enhanced antioxidant activity [95]. The same research group later evaluated the effects of a similar postharvest dipping treatment for mature green limes over a 20-day storage period. As limes undergo various metabolic changes during storage—such as color fading—the study investigated the effects of melatonin and chitosan both separately and together. Results demonstrated that these treatments enhanced the fruit's antioxidant system and helped retain quality for up to 16 days of shelf life. The

melatonin treatment preserved more vitamin C compared to the control; however, no synergistic benefits were observed when melatonin and chitosan were used in combination [96]. Similarly, Bal et al. [97] studied the effects of chitosan coatings enriched with melatonin on the storability of sweet cherries. Weekly assessments included assessment of parameters such as weight loss, firmness, and anthocyanin, phenolic, and antioxidant content. The results showed that the chitosan/melatonin composite coating reduced respiration rate and weight loss while preserving higher biochemical content and fruit firmness [97]. Zhao et al. [94] evaluated a chitosan-based melatonin coating applied to fresh-cut produce, including cucumber (*Cucumis sativus*), broccoli (*Brassica oleracea*), and melon (*Cucumis melo* var. *saccharinus*). The coating delayed chlorophyll degradation and improved antimicrobial and antioxidant properties [94].

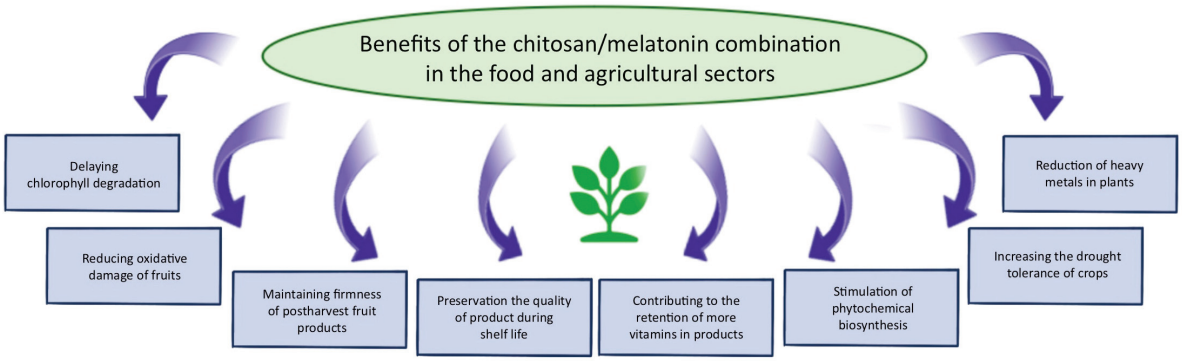

Figure 4. Summary of the benefits of using a chitosan/melatonin combination in the food industry and agriculture.

In another study, chitosan and melatonin were used to create a composite coating for pomegranate aril sacs to delay aging and maintain quality. The sacs were immersed in the coating solution, air-dried at room temperature, and stored at 5 °C for 21 days. The treatment reduced weight loss and respiration rate, and resulted in higher anthocyanin content, antioxidant activity, and chroma values. Moreover, it helped to minimize surface browning, indicating its effectiveness in preserving pomegranate aril quality [98]. Ullah et al. [99] investigated the use of chitosan and melatonin as elicitors in agitated shoot cultures of *Ajuga integrifolia*. Elicitors are agents that induce physiological stress to enhance phytochemical biosynthesis. Antioxidant activity was assessed using DPPH, ABTS, and FRAP assays. Melatonin significantly enhanced antioxidant activity and stimulated the biosynthesis of several phytochemicals, including chlorogenic acid, rosmarinic acid, apigenin, and quercetin. Chitosan also showed notable effects, particularly on anti-inflammatory activity [99]. In agriculture, melatonin is recognized for its role in enhancing plant drought tolerance. To protect melatonin from environmental degradation, Zhou et al. [100] encapsulated it in hybrid particles composed of chitosan, sodium tripolyphosphate, and pectin. These particles, designed to release melatonin gradually, were tested on wheat seedlings. SEM imaging revealed that the particle surfaces were rougher than pure melatonin, and photodegradation was significantly reduced. While chitosan did not affect seedling growth, the encapsulated melatonin increased dry weight, root length, and peroxidase activity, demonstrating improved drought resistance [100]. Cadmium accumulation in crops poses a global agricultural challenge. Chen et al. [101] developed a foliar spray delivery system using mesoporous silica nanoparticles and chitosan/mesoporous silica nanoparticles to administer melatonin. Both carriers enabled controlled release, but the chitosan-modified system performed better in vitro. In rice plants, this nano-delivery system significantly reduced cadmium accumulation, increased antioxidant enzyme activity, and enhanced photosynthetic efficiency, outperforming free melatonin and melatonin

with silica alone [101]. Additionally, Tabassum et al. [102] studied the effects of chitosan foliar treatment on two accessions of *Pisum sativum* L. The biopolymer treatment improved antioxidant activity, plant growth, and inorganic ion accumulation, and also stimulated endogenous melatonin synthesis in the tested plants [102].

Chitosan and melatonin have also found promising applications in veterinary medicine. López-Valverde et al. [103] evaluated bone density around dental implants in canine jaws, comparing standard etched implant surfaces with those coated with chitosan and melatonin. After 12 weeks, no statistically significant differences were found in bone density between the groups. This lack of difference may be attributed to the mechanical instability of the surface coatings, which might have been lost during implantation due to low mechanical resistance [103]. A more successful application was demonstrated by Abdelrasoul et al. [104], who developed a composite hydrogel composed of alginate, chitosan, and β-tricalcium phosphate loaded with melatonin. The hydrogel's regenerative capacity was tested in six dogs with periodontal defects. After eight weeks, the melatonin-loaded scaffold enhanced bone formation and supported complete periodontal regeneration. The newly formed bone showed quality comparable to native compact bone [104]. In a subsequent study, Abdelrasoul et al. [105] further assessed the hydrogel's systemic toxicity, physical effects on bone defects, and regenerative performance using a rabbit model. Both the melatonin-loaded and unloaded scaffolds were found to be biocompatible, with no signs of systemic toxicity. While both groups showed reductions in defect depth, volume, and area size, the overall rate of regeneration was similar between scaffolds with and without melatonin over an 8-week period [105]. Beyond biological and clinical applications, chitosan has shown potential as a functional material in melatonin detection systems. Chitosan, in combination with nano-carbon acetylene black, has been used to construct a sensor capable of the simultaneous detection of melatonin and serotonin in biological samples [106]. In another study, a screen-printed carbon electrode modified with nano-ceria and chitosan enhanced electrochemical sensitivity, providing a selective, fast, and sensitive method for melatonin determination [107]. Similarly, a composite sensor based on a glassy carbon electrode modified with chitosan and carboxylated multi-walled carbon nanotubes enabled simultaneous detection of melatonin, serotonin, and dopamine in human saliva samples [108].

These studies highlight the versatility of chitosan/melatonin-based materials, which not only serve in wound healing, bone regeneration, and disease treatment in both human and veterinary medicine but also show promise as components in analytical tools for hormone detection. The broad spectrum of applications is summarized in Table 1.

Table 1. Chitosan/melatonin-based materials and their applications.

Chitosan/Melatonin Combination				
Application	**Matrix Composition**	**Form/System**	**Year**	**Reference**
Wound healing	chitosan/Pluronic® F127	microspheres	2016	[36]
	chitosan/Pluronic® F127	microspheres enriched with nanostructured lipid carriers	2019	[37,38]
	lecithin/chitosan	nanoparticles	2011	[39]
	lecithin/chitosan	nanoparticles	2016	[40]
	chitosan/collagen	scaffold	2021	[41]
	lecithin/chitosan	nanoparticles	2020	[42]
	Poloxamer407/chitosan/ hyaluronic acid	nanogel	2020	[43]

Table 1. *Cont.*

Chitosan/Melatonin Combination				
Application	**Matrix Composition**	**Form/System**	**Year**	**Reference**
Wound healing	chitosan–polycaprolactone/ polyvinyl alcohol–melatonin/ chitosan–polycaprolactone	three-layer nanofiber	2021	[44]
	lecithin/chitosan	nanoparticles	2011	[45]
	chitosan/sulfonated ethylene-propylene-diene terpolymer (sEPDM)	membrane	2023	[46]
Scaffolds and hydrogels	chitosan/hydroxyapatite (HAp)	scaffold	2021	[57]
	chitosan	scaffold	2015	[58]
	chitosan/hydroxyapatite (HAp)	scaffold	2019	[59]
	chitosan	microparticles	2020	[60]
	collagen/chitosan	scaffold	2022	[61]
Cosmetology/ dermatology	chitosan/dextran sulphate	nanoparticles for Pickering emulsion stabilization	2023	[66]
Anti-cancer treatment	chitosan/tripolyphosphate	nanoparticles	2020	[25]
	chitosan/hydroxypropyl methylcellulose cross-linked in the presence of tripolyphosphate	nanoparticles	2021	[75]
	chitosan/tripolyphosphate	nanoparticles	2017	[76]
	chitosan/tripolyphosphate	nanoparticles	2018	[77]
Drug delivery systems	1. lecithin/chitosan; 2. Pluronic® F127/chitosan.	1. nanoparticles; 2. micelles.	2015	[84]
	chitosan	hydrogel	2013	[85]
	chitosan	nanoparticles	2023	[86]
	chitosan	nanoparticles	2021	[87]
	chitosan	nanoparticles	2022	[88]
	chitosan	amphiphilic nanocarrier (ACN)	2021	[89]
Others	Alginate/chitosan	pellets	2020	[92]
	chitosan/carboxymethyl chitosan + carboxymethyl cellulose	film	2020	[94]
	chitosan	solution/film	2024	[95]
	chitosan	solution/film	2023	[96]
	chitosan	solution/film	2023	[97]
	chitosan	solution/film	2022	[98]
	chitosan	solution/film	2023	[99]
	chitosan/sodium tripolyphosphate (TPP)/pectin	particles	2022	[100]
	mesoporous silica nanoparticles (MSN)/chitosan	particles	2022	[101]

Table 1. *Cont.*

Chitosan/Melatonin Combination				
Application	**Matrix Composition**	**Form/System**	**Year**	**Reference**
Others	chitosan	film-forming solution	2021	[103]
	alginate/chitosan/β-tricalcium phosphate	hydrogel	2023	[104]
	alginate/chitosan/β-tricalcium phosphate	hydrogel	2020	[105]

3. Conclusions and Perspectives

The health and life sciences sector is constantly evolving, driven by emerging challenges and the need for innovative therapeutic strategies. A common approach involves combining well-established bioactive compounds to enhance efficacy and broaden their applicability. A review of the Scopus database reveals that research on the chitosan/melatonin combination has been ongoing since the early 2020s. A keyword search for 'melatonin' and 'chitosan' yields 96 research articles published between 2002 and 2024 (Figure 5). Although this is not yet a widely explored topic, the growing number of publications indicates a rising interests in this synergistic pairing, likely due to its diverse range of potential applications. Melatonin, best known for its role in circadian rhythm regulation via pineal gland secretion, is also synthesized in peripheral organs where it exerts various local regulatory functions. Its therapeutic versatility—including antioxidant, anti-inflammatory, immunomodulatory, and anti-cancer activities—makes it a valuable candidate for treating neurodegenerative disorders, immune-related conditions, and malignancies. Despite its biocompatibility and safety, melatonin's instability and rapid degradation in physiological environments necessitate the use of protective delivery systems, particularly at the nanoscale [109]. Chitosan, a natural polysaccharide derived from chitin, offers multiple advantages as a carrier for melatonin, including mucoadhesive properties, enzymatic resistance, and inherent antimicrobial and antioxidant activity. The functional versatility of chitosan enables the development of innovative delivery platforms that enhance melatonin's stability and bioavailability. The scientific evidence reviewed in this article demonstrates that chitosan can effectively serve as a carrier or enhancer for melatonin, enabling both systemic and topical therapeutic applications. The integration of melatonin with chitosan has opened up new possibilities in tissue engineering, wound healing, cancer treatment, veterinary medicine, food preservation, and cosmetics (Table 1). Although research on chitosan/melatonin formulations is still in its early stages, preliminary findings are very promising. This combination represents a compelling frontier in biotechnology, with significant potential for expansion. The recent increase in related publications suggests a growing recognition of this pairing's utility. Future advancements are likely to focus on surface-functionalized biomaterials and nanotechnology-based delivery platforms. As the field matures, novel and currently unforeseen applications are expected to emerge, further solidifying the role of chitosan/melatonin systems in advanced therapeutic and industrial innovations.

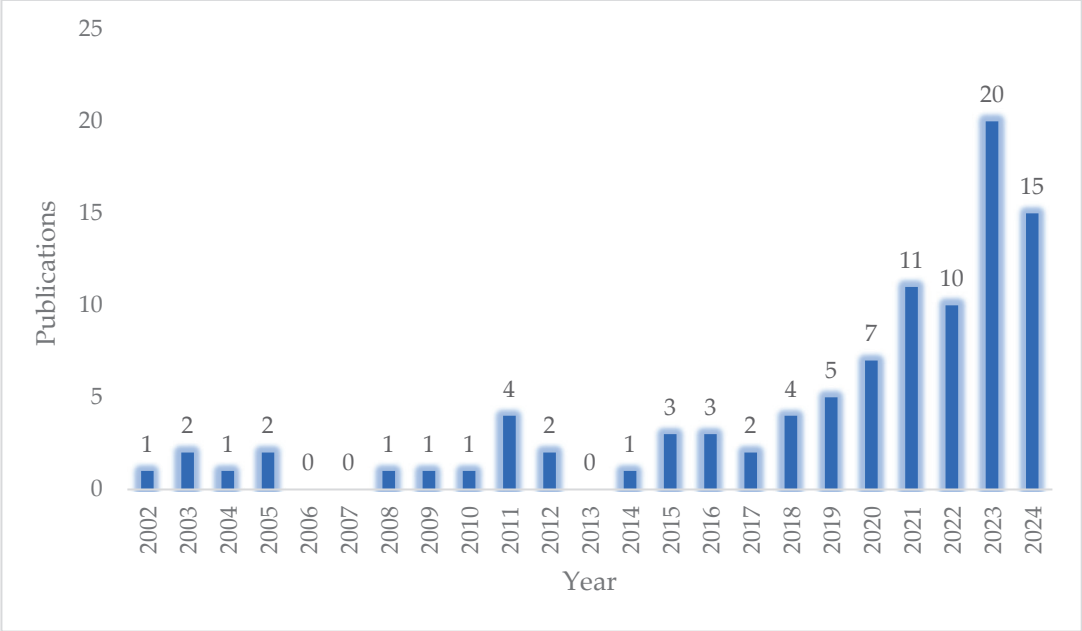

Figure 5. Publications on the subjects of melatonin and chitosan over the years (search for words "melatonin" and "chitosan" in the title, abstract, and keywords). The figure is based on data from the Scopus database [accessed on 12 December 2024].

Author Contributions: Conceptualization and writing—original draft preparation, K.K.-K., P.B., K.K. (Konrad Kleszczyński) and A.S.; supervision, A.S. and K.K. (Konrad Kleszczyński); revision and approval of the final version of the manuscript, K.K.-K., P.B., M.O., T.I., M.S., R.J.R., A.T.S., K.K. (Kazuo Kishi), K.S., A.S. and K.K. (Konrad Kleszczyński). All authors have read and agreed to the published version of the manuscript.

Funding: The author(s) declare financial support was received for the research, authorship, and/or publication of this article. This research was supported in part by the German Research Foundation (Deutsche Forschungsgemeinschaft, DFG), grant number KL2900/3-1 (to K.K. (Konrad Kleszczyński)), TR156/C05-246807620, SFB1009/B11-194468054, SFB1066/B06-213555243, and SFB1450/C06-431460824 (to K.S.), by NIH grants 1R01AR073004 and R01AR071189, VA merit 1I01BX004293-01A1, and DOD grant W81XWH2210689 (to A.S.), and by the Rowe-Smith Foundation Grant (to R.R.).

Conflicts of Interest: The authors declare no conflicts of interest.

References

1. Kabanov, V.L.; Novinyuk, L.V. Chitosan application in food technology: A review of recent advances. *Food Syst.* **2020**, *3*, 10–15. [CrossRef]
2. Kulka, K.; Sionkowska, A. Chitosan Based Materials in Cosmetic Applications: A Review. *Molecules* **2023**, *28*, 1817. [CrossRef] [PubMed]
3. Matica, M.A.; Aachmann, F.L.; Tondervik, A.; Sletta, H.; Ostafe, V. Chitosan as a Wound Dressing Starting Material: Antimicrobial Properties and Mode of Action. *Int. J. Mol. Sci.* **2019**, *20*, 5889. [CrossRef] [PubMed]
4. Wang, W.; Meng, Q.; Li, Q.; Liu, J.; Zhou, M.; Jin, Z.; Zhao, K. Chitosan Derivatives and Their Application In Biomedicine. *Int. J. Mol. Sci.* **2020**, *21*, 487. [CrossRef]
5. Aranaz, I.; Alcantara, A.R.; Civera, M.C.; Arias, C.; Alorza, B.; Caballero, A.H.; Acosta, N. Chitosan: An Overview of Its Properties and Applications. *Polymers* **2021**, *13*, 3256. [CrossRef]
6. Bhatt, S.; Pathak, R.; Punetha, V.D.; Punetha, M. Chitosan Nanocomposites as a Nano-Bio Tool in Phytopathogen Control. *Carbohydr. Polym.* **2024**, *331*, 121858. [CrossRef]
7. Harugade, A.; Sherje, A.P.; Pethe, A. Chitosan: A Review on Properties, Biological Activities and Recent Progress in Biomedical Applications. *React. Funct. Polym.* **2023**, *191*, 105634. [CrossRef]

8. Nasaj, M.; Chehelgerdi, M.; Asghari, B.; Ahmadieh-Yazdi, A.; Asgari, M.; Kabiri-Samani, S.; Sharifi, E.; Arabestani, M. Factors Influencing the Antimicrobial Mechanism of Chitosan Action and its Derivatives: A Review. *Int. J. Biol. Macromol.* **2024**, *277*, 134321. [CrossRef]
9. Suryani, S.; Chaerunisaa, A.Y.; Joni, I.M.; Ruslin, R.; Ramadhan, L.O.A.N.; Wardhana, Y.W.; Sabarwati, S.H. Production of Low Molecular Weight Chitosan Using a Combination of Weak Acid and Ultrasonication Methods. *Polymers* **2022**, *14*, 3417. [CrossRef]
10. Choi, J.; Hwang, D.S.; Lim, C.; Lee, D.W. Interaction Mechanism Between Low Molecular Weight Chitosan Nanofilm and Functionalized Surfaces in Aqueous Solutions. *Carbohydr. Polym.* **2024**, *324*, 121504. [CrossRef]
11. Román-Doval, R.; Torres-Arellanes, S.P.; Tenorio-Barajas, A.Y.; Gómez-Sánchez, A.; Valencia-Lazcano, A.A. Chitosan: Properties and Its Application in Agriculture in Context of Molecular Weight. *Polymers* **2023**, *15*, 2867. [CrossRef] [PubMed]
12. Pellis, A.; Guebnitz, G.M.; Nyanhongo, G.S. Chitosan: Sources, Processing and Modification Techniques. *Gels* **2022**, *8*, 393. [CrossRef]
13. Rodrigues, S.; Dionisio, M.; Lopez, C.R.; Grenha, A. Biocompatibility of Chitosan Carriers with application in Drug Delivery. *J. Funct. Biomater.* **2012**, *3*, 615–641. [CrossRef]
14. Fowler, S.; Hoedt, E.C.; Talley, N.J.; Keely, S.; Burns, G.L. Circadian Rhythms and Melatonin Metabolism in Patients With Disorders of Gut-Brain Interactions. *Front. Neurosci.* **2022**, *16*, 825246. [CrossRef]
15. Ismaili, L.; Romero, A.; do Carmo Carreiras, M.; Marco-Contelles, J. Multitarget-Directed Antioxidants as Therapeutic Agents: Putting the Focus on the Oxidative Stress. In *Design of Hybrid Molecules for Drug Development*; Decker, M., Ed.; Elsevier Ltd.: Amsterdam, The Netherlands, 2017; pp. 5–46. [CrossRef]
16. Slominski, A.; Wortsman, J.; Tobin, D.J. The cutaneous serotoninergic/melatoninergic system: Securing a place under the sun. *FASEB J.* **2005**, *19*, 176–194. [CrossRef] [PubMed]
17. Arnao, M.B.; Hernández-Ruiz, J. Chapter 11—Phytomelatonin: Searching for Plants with High Levels for Use as a Natural Nutraceutical. In *Studies in Natural Products Chemistry*; Atta-ur-Rahman, Ed.; Elsevier: Amsterdam, The Netherlands, 2015; pp. 519–545. [CrossRef]
18. Barba, F.J.; María, J.; Esteve, M.J.; Frígola, A. Chapter 11—Bioactive Components from Leaf Vegetable Products. In *Studies in Natural Products Chemistry*; Atta-ur-Rahman, Ed.; Elsevier: Amsterdam, The Netherlands, 2014; pp. 321–346. [CrossRef]
19. Kim, T.K.; Slominski, R.M.; Pyza, E.; Kleszczynski, K.; Tuckey, R.C.; Reiter, R.J.; Holick, M.F.; Slominski, A.T. Evolutionary formation of melatonin and vitamin D in early life forms: Insects take centre stage. *Biol. Rev.* **2024**, *99*, 1772–1790. [CrossRef] [PubMed]
20. Kim, T.K.; Atigadda, V.R.; Brzeminski, P.; Fabisiak, A.; Tang, E.K.Y.; Tuckey, R.C.; Reiter, R.J.; Slominski, A.T. Detection of Serotonin, Melatonin, and Their Metabolites in Honey. *ACS Food Sci. Technol.* **2021**, *1*, 1228–1235. [CrossRef]
21. Slominski, A.T.; Zmijewski, M.A.; Semak, I.; Kim, T.K.; Janjetovic, Z.; Slominski, R.M.; Zmijewski, J.W. Melatonin, mitochondria, and the skin. *Cell. Mol. Life Sci.* **2017**, *74*, 3913–3925. [CrossRef]
22. Reiter, R.J.; Rosales-Corral, S.A.; Tan, D.X.; Acuna-Castroviejo, D.; Qin, L.; Yang, S.F.; Xu, K. Melatonin, a Full Service Anti-Cancer Agent: Inhibition of Initiation, Progression and Metastasis. *Int. J. Mol. Sci.* **2017**, *18*, 843. [CrossRef]
23. Slominski, A.T.; Kim, T.K.; Janjetovic, Z.; Slominski, R.M.; Ganguli-Indra, G.; Athar, M.; Indra, A.K.; Reiter, R.J.; Kleszczyński, K. Melatonin and the Skin: Current Progress and Perspectives for Human Health. *J. Investig. Dermatol.* **2025**, *145*, 1345–1360.e2. [CrossRef]
24. Kleszczyński, K.; Fischer, T.W. Melatonin and human skin aging. *Dermatoendocrinology* **2012**, *4*, 245–252. [CrossRef] [PubMed]
25. Shokrzadeh, M.; Ashari, S.; Ghassemi-Barghi, N. Attenuation of Doxorubicin Induced Genotoxicity in HepG2 Cells: Effect of Melatonin Loading Chitosan-Tripolyphosphate Nanoparticles on Oxidative stress. *Int. J. Cancer Res. Ther.* **2020**, *5*, 35–42. [CrossRef]
26. Slominski, A.; Wortsman, J. Neuroendocrinology of the skin. *Endocr. Rev.* **2000**, *21*, 457–487. [CrossRef] [PubMed]
27. Tottili, E.M.; Dorati, R.; Genta, I.; Chiesa, E.; Pisani, S.; Conti, B. Skin Wound Healing Process and New Emerging Technologies for Skin Wound Care and Regeneration. *Pharmaceutics* **2020**, *12*, 735. [CrossRef]
28. Wilkinson, H.N.; Hardman, M.J. Wound healing: Cellular mechanism and pathological outcomes. *Open Biol.* **2023**, *10*, 200223. [CrossRef]
29. Bikle, D.D. Vitamin D: Newer concepts of Its metabolism and function at the basic and clinical level. *J. Endocr. Soc.* **2020**, *4*, bvz038. [CrossRef]
30. Slominski, R.M.; Raman, C.; Jetten, A.M.; Slominski, A.T. Neuro-immuno-endocrinology of the skin: How environment regulates body homeostasis. *Nat. Rev. Endocrinol.* **2025**, *in press*. [CrossRef]
31. Gardikiotis, I.; Cojocaru, F.-D.; Mihai, C.-T.; Balan, V.; Dodi, G. Borrowing the Features of Biopolymers for Emerging Wound Healing Dressings: A Review. *Int. J. Mol. Sci.* **2022**, *23*, 8778. [CrossRef]
32. Landen, N.X.; Li, D.; Stahle, M. Transition from inflammation to proliferation: A critical step during wound healing. *Cell. Mol. Life Sci.* **2016**, *73*, 3861–3885. [CrossRef]
33. Reinke, J.M.; Sorg, H. Wound repair and regeneration. *Eur. Surg. Res.* **2012**, *49*, 35–43. [CrossRef]

34. Boateng, J.S.; Metthews, K.H.; Stevens, H.N.E.; Eccleston, G.M. Wound Healing Dressing and Drug Delivery Systems: A Review. *J. Pharm. Sci.* **2008**, *97*, 2892–2923. [CrossRef] [PubMed]
35. Ndlovu, S.P.; Ngece, K.; Alven, S.; Aderibigbe, B.A. Gelatin-Based Hybrid Scaffolds: Promising Wound Dressings. *Polymers* **2021**, *13*, 2959. [CrossRef] [PubMed]
36. Romic, M.D.; Klaric, M.S.; Lovric, J.; Pepic, I.; Cetina-Cizmek, B.; Filipovic-Grcic, J.; Hafner, A. Melatonin-loaded chitosan/Pluronic F127 microspheres as in situ forming hydrogel: An innovative antimicrobial wound dressing. *Eur. J. Pharm. Biopharm.* **2016**, *107*, 67–79. [CrossRef]
37. Romic, M.D.; Susac, A. Evaluation of stability and in vitro wound healing potential of melatonin loaded (lipid enriched) chitosan microspheres. *Acta Pharm.* **2019**, *69*, 635–648. [CrossRef]
38. Romic, M.D.; Spoljaric, D.; Klaric, M.S.; Cetina-Cizmek, B.; Filipovic-Grcic, J.; Hafner, A. Melatonin loaded lipid enriched chitosan microspheres—Hybrid dressing for moderate exuding wounds. *J. Drug Deliv. Sci. Technol.* **2019**, *52*, 431–439. [CrossRef]
39. Hafner, A.; Lovric, J.; Pepic, I.; Filipovic-Grcic, J. Lecithin/chitosan nanoparticles for transdermal delivery of melatonin. *J. Microencapsul.* **2011**, *28*, 807–815. [CrossRef]
40. Blazevic, F.; Milekic, T. Nanopartcile-mediated interplay of chitosan and melatonin for improved wound epithelialization. *Carbohyd. Polym.* **2016**, *146*, 445–454. [CrossRef]
41. Kaczmarek-Szczepańska, B.; Ostrowska, J.; Kozłowska, J.; Szota, Z.; Brożyna, A.A.; Dreier, R.; Reiter, R.J.; Slominski, A.T.; Steinbrink, K.; Kleszczyński, K. Evaluation of polymeric matrix loaded with melatonin for wound dressing. *Int. J. Mol. Sci.* **2021**, *22*, 5658. [CrossRef]
42. Correa, V.; Martins, J.A.; de Souza, T.R.; Rincon, G.C.N.; Miguel, M.P.; de Menezes, L.B.; Amaral, A.C. Melatonin loaded lecithin-chitosan nanoparticles improved the wound healing in diabetic rats. *Int. J. Biol. Macromol.* **2020**, *162*, 1465–1475. [CrossRef]
43. Soriano, J.L.; Calpena, A.C.; Rincon, M.; Perez, N.; Halbut, L.; Rodriguez, M.J.; Clares, B. Melatonin nanogel promotes skin healing response in burn wounds of rats. *Nanomedicine* **2020**, *15*, 2133–2147. [CrossRef]
44. Mirmajidi, T.; Chogan, F.; Rezayan, A.H.; Sharifi, A.M. In vitro and in vivo evaluation of nanofiber wound dressing loaded with melatonin. *Int. J. Pharm.* **2021**, *596*, 120213. [CrossRef]
45. Hafner, A.; Durrigl, M. Short- and Long-Term Stability of Lyophilised Melatonin-Loaded Lecithin/Chitosan Nanoparticles. *Chem. Pharm. Bull.* **2011**, *59*, 1117–1123. [CrossRef]
46. Păncescu, F.M.; Rikabi, A.A.K.K.; Oprea, O.C.; Grosu, A.R.; Nechifor, A.C.; Grosu, V.-A.; Tanczos, S.-K.; Dumitru, F.; Nechifor, G.; Bungău, S.G. Chitosan-sEPDM and Melatonin—Chitosan—sEPDM Composite Membranes for Melatonin Transport and Release. *Membranes* **2023**, *13*, 282. [CrossRef]
47. Shabbirahmed, A.M.; Sekar, R.; Gomez, L.A.; Sekhar, M.R.; Hiruthyaswamy, S.P.; Basavegowa, N.; Somu, P. Recent Developments of Silk-Based Scaffolds for Tissue Engineering and Regenerative Medicine Applications: A Special Focus on the Advancement of 3D Printing. *Biomimetics* **2023**, *8*, 16. [CrossRef] [PubMed]
48. Sukpaita, T.; Chirachanchai, S.; Pimkhaokham, A.; Ampornaramveth, R.S. Chitosan-Based Scaffold for Mineralized Tissue Regeneration. *Mar. Drugs* **2021**, *19*, 551. [CrossRef] [PubMed]
49. Abbasi, N.; Hamlet, S.; Love, R.M.; Nguyen, N.T. Porous scaffolds for bone regeneration. *J. Sci. Adv. Mater. Devices* **2020**, *5*, 1–9. [CrossRef]
50. Lee, S.S.; Du, X.; Kim, I.; Ferguson, S.J. Scaffolds for bone-tissue engineering. *Matter* **2022**, *5*, 2722–2759. [CrossRef]
51. Lauritano, D.; Limongelli, I.; Moreo, G.; Favia, G.; Carinci, F. Nanomaterials for Periodontal Tissue Engineering Chitosan-Based Scaffolds. A Systemic Review. *Nanomaterials* **2020**, *10*, 605. [CrossRef]
52. Acosta, B.B.; Advincula, R.C.; Grande-Tovar, C.D. Chitosan-Based Scaffolds for the Treatment of myocardial Infraction: A Systemic Review. *Molecules* **2023**, *28*, 1920. [CrossRef]
53. Martins, A.M.; Eng, G.; Caridade, S.G.; Mano, J.F.; Reis, R.L.; Vunjak-Novakovic, G. Electrically Conductive Chitosan/Carbon Scaffolds for Cardiac Tissue Engineering. *Biomacromolecules* **2014**, *15*, 635–643. [CrossRef]
54. Pezeshki-Modaress, M.; Zandi, M.; Rajabi, S. Tailoring the gelatin/chitosan electrospun scaffold for application in skin tissue engineering: An in vitro study. *Prog. Biomater.* **2018**, *7*, 207–218. [CrossRef] [PubMed]
55. Sandri, G.; Rossi, S.; Bonferoni, M.C.; Miele, D.; Faccendini, A.; Favero, E.; Di Cola, E.; Cornaglia, A.I.; Boselli, C.; Luxbacher, T.; et al. Chitosan/glycosaminoglycan scaffolds for skin reparation. *Carbohydr. Polym.* **2019**, *220*, 219–227. [CrossRef] [PubMed]
56. Jarrar, H.; Altindal, D.C.; Gumusderelioglu, M. Effect of melatonin/BMP-2 co-delivery scaffold on the osteoclast activity. *J. Mater. Sci. Mater. Med.* **2021**, *32*, 32. [CrossRef]
57. Jarrar, H.; Çetin Altındal, D.; Gümüşderelioğlu, M. Scaffold-based osteogenic dual delivery system with melatonin and BMP-2 releasing PLGA microparticles. *Int. J. Pharm.* **2021**, *600*, 120489. [CrossRef] [PubMed]
58. Topal, B.; Altindal, D.C.; Gumusderelioglu, M. Melatonin/HPBCD complex: Microwave synthesis, integration with chitosan scaffolds and inhibitory effects on MG-63CELLS. *Int. J. Pharm.* **2015**, *496*, 801–811. [CrossRef]

59. Altindal, D.C.; Gumusderelioglu, M. Dual-functional melatonin releasing device loaded with PLGA microparticles and cyclodextrin inclusion complex for osteosarcoma therapy. *J. Drug Deliv. Sci. Technol.* **2019**, *52*, 586–596. [CrossRef]
60. Huang, R.-Y.; Hsiao, P.Y.; Mau, L.P.; Tsai, Y.W.C.; Cochran, D.L.; Weng, P.W.; Cheng, W.C.; Chung, C.H.; Huang, Y.C. Synthesis and Characterization of Melatonin-Loaded Chitosan Microparticles Promote Differentiation and Mineralization in Preosteoblastic Cells. *J. Oral Implantol.* **2020**, *46*, 562–570. [CrossRef]
61. Kaczmarek-Szczepańska, B.; Pin, J.M.; Zasada, L.; Sonne, M.M.; Reiter, R.J.; Slominski, A.T.; Steinbrink, K.; Kleszczyński, K. Assesment of Melatonin-Cultured Collagen/Chitosan Scaffolds Cross-Linked by a Glyoxal Solution as Biomaterials for Wound Healing. *Antioxidants* **2022**, *11*, 570. [CrossRef]
62. Fischer, T.W.; Hänggi, G.; Innocenti, M.; Elsner, P.; Trüeb, R. Topical Melatonin for Treatment of Androgenetic Alopecia. *Int. J. Trichology* **2012**, *4*, 236–245. [CrossRef]
63. Slominski, A.T.; Kim, T.K.; Slominski, R.M.; Song, Y.; Qayyum, S.; Placha, W.; Janjetovic, Z.; Kleszczynski, K.; Atigadda, V.; Song, Y.; et al. Melatonin and Its Metabolites Can Serve as Agonists on the Aryl Hydrocarbon Receptor and Peroxisome Proliferator-Activated Receptor Gamma. *Int. J. Mol. Sci.* **2023**, *24*, 15496. [CrossRef]
64. Fischer, T.W.; Slominski, A.; Tobin, D.J.; Paus, R. Melatonin and the hair follicle. *J. Pineal Res.* **2008**, *44*, 1–15. [CrossRef] [PubMed]
65. Fischer, T.W.; Sweatman, T.W.; Semak, I.; Sayre, R.M.; Wortsman, J.; Slominski, A. Constitutive and UV-induced metabolism of melatonin in keratinocytes and cell-free systems. *FASEB J.* **2006**, *20*, 1564–1566. [CrossRef]
66. Elshall, A.A.; Ghoneim, A.M.; Abd-Elmonsif, N.M.; Osman, R.; Shaker, D.S. Boosting hair growth through follicular delivery of melatonin through lecithin-enhanced Pickering emulsion stabilized by chitosan-dextran nanoparticles in testosterone induced androgenic alopecia rat model. *Int. J. Pharm.* **2023**, *639*, 122972. [CrossRef] [PubMed]
67. Mansouri, V.; Beheshitizadeh, N.; Gharibshahian, M.; Sabouri, L.; Varzandeh, M.; Rezaei, N. Recent advances in regenerative medicine strategies for cancer treatment. *Biomed. Pharmacother.* **2021**, *141*, 111875. [CrossRef] [PubMed]
68. Cheng, Z.; Li, M.; Dey, R.; Chen, Y. Nanomaterials for cancer therapy: Current progress and perspectives. *J. Hematol. Oncol.* **2021**, *14*, 85. [CrossRef]
69. Mundekkad, D.; Cho, C.W. Nanoparticles in Clinical Translation for Cancer Therapy. *Int. J. Mol. Sci.* **2022**, *23*, 1685. [CrossRef]
70. Huang, M.; Lu, J.-J.; Ding, J. Natural Products in Cancer Therapy: Past, Present and Future. *Nat. Prod. Bioprospect.* **2011**, *11*, 5–13. [CrossRef]
71. Wang, L.; Wang, C.; Choi, W.S. Use of Melatonin in Cancer Treatment: Where Are We? *Int. J. Mol. Sci.* **2022**, *23*, 3779. [CrossRef]
72. Talib, W.H.; Alsayed, A.R.; Abuawad, A.; Daoud, S.; Mahmod, A.I. Melatonin in Cancer Treatment: Current Knowledge and Future Opportunities. *Molecules* **2021**, *26*, 2506. [CrossRef]
73. Talib, W.H. Melatonin and Cancer Hallmarks. *Molecules* **2018**, *23*, 518. [CrossRef]
74. Das, N.K.; Samanta, S. The potential anti-cancer effects of melatonin on breast cancer. *Explor. Med.* **2022**, *3*, 112–127. [CrossRef]
75. Jafari, H.; Hassanpour, M.; Akbari, A.; Rezie, J.; Gohari, G.; Reza, G.; Mahdavinia, E. Jabbari Characterization of pH-sensitive chitosan/hydroxypropyl methycellulose nanopartciles for delivery of melatonin in cancer therapy. *Mater. Lett.* **2020**, *282*, 128818. [CrossRef]
76. Yadav, S.K.; Srivastava, A.K.; Dev, A.; Kaundal, B.; Choudhury, S.R.; Karmakar, S. Nanomelatonin triggers superior anticancer functionality in a human malignant glioblastoma cell line. *Nanotechnology* **2017**, *28*, 365102. [CrossRef]
77. Shokrzadeh, M.; Ghassemi-Barghi, N. Melatonin Loading Chitosan-Tripolyphosphate Nanoparticles: Application in Attenuating Etoposide-Induced Genotooxicity in HepG2 Cells. *Pharmacology* **2018**, *102*, 74–80. [CrossRef]
78. Desai, N.; Rana, D.; Salave, S.; Gupta, R.; Patel, P.; Karunakaran, B.; Sharma, A.; Giri, J.; Benival, D.; Kommineni, N. Chitosan: A Potential Biopolymer in Drug Delivery and Biomedical Applications. *Pharmaceutics* **2023**, *15*, 1313. [CrossRef] [PubMed]
79. Bernkop-Schnürch, A.; Dünnhaupt, S. Chitosan-based drug delivery systems. *Eur. J. Pharm. Biophram.* **2012**, *81*, 463–469. [CrossRef] [PubMed]
80. Garg, U.; Chauhan, S.; Nagaich, U.; Jain, N. Current Advances in Chitosan Nanoparticles Based Drug Delivery and Targeting. *Adv. Pharm. Bull.* **2019**, *9*, 195–204. [CrossRef]
81. Li, J.; Cai, C.; Li, J.; Li, J.; Li, J.; Sun, T.; Wang, L.; Wu, H.; Yu, G. Chitosan-Based Nanomaterials for Drug Delivery. *Molecules* **2018**, *23*, 2661. [CrossRef]
82. Mohhamed, M.A.; Syeda, J.T.M.; Wasan, K.M.; Wasan, E.K. An Overview of Chitosan Nanoparticles and Its Application in Non-Parenteral Drug Delivery. *Pharmaceutics* **2017**, *9*, 53. [CrossRef]
83. Wang, J.J.; Zeng, Z.W.; Xiao, R.Z.; Xie, T.; Zhou, G.L.; Zhan, X.R.; Wang, S.L. Recent advances of chitosan nanoparticles as drug carriers. *Int. J. Nanomed.* **2011**, *6*, 765–774. [CrossRef]
84. Hafner, A.; Lovric, J.; Romić, M.D.; Juretic, M.; Pepic, I.; Cetina-Cizmek, B.; Filipovic-Grcic, J. Evaluation of cationic nanosystems with melatonin using an eye-related bioavailability prediction model. *Eur. J. Pharm. Sci.* **2015**, *75*, 142–150. [CrossRef] [PubMed]
85. Perchyonok, V.T.; Zhang, S.; Basson, N.J.; Grobler, S.; Oberholzer, T.; Massey, W. Insights into chitosan based gels as functional restorative biomaterials prototypes: In vitro approach. *Open J. Stomatol.* **2013**, *3*, 22–30. [CrossRef]

86. Tawfik, H.N.; Kandil, O.M.; Mansour, I.M.; El-Debaky, H.A.; Ali, K.A.; Ismail, E.A.; Abedelaziz, S.A. Effect of Melatonin-loaded Chitosan Nanoparticles (CMN) on Gene Expression of in vitro Matured Buffalo Oocyte. *J. Adv. Vet. Res.* **2023**, *13*, 656–663.
87. Soni, J.M.; Sardoiwala, M.N.; Choudhury, S.R.; Sharma, S.S.; Karmakar, S. Melatonin-loaded chitosan nanoparticles endows nitric oxide synthase 2 mediated anti-inflammatory activity in inflammatory bowel disease model. *Mater. Sci. Eng. C* **2021**, *124*, 112038. [CrossRef]
88. Mohanbhai, S.J.; Sardoiwala, M.N.; Gupta, S.; Shrimali, N.; Choudhury, S.R.; Sharma, S.S.; Guchhait, P.; Karmakar, S. Colon targeted chitosan-melatonin nanotherapy for preclinical Inflammatory Bowel Disease. *Biomater. Adv.* **2022**, *136*, 212796. [CrossRef] [PubMed]
89. Aghaz, F.; Vaisi-Raygani, A.; Khazaei, M.; Arkan, E.; Kashanian, S. Enhanced Synergistic-Antioxidant Activity of Melatonin and Tretinoin by Co-encapsulation into Amphiphilic Chitosan Nanocarriers: During Mice In Vitro Matured Oocyte/Morula-Compact Stage Embryo Culture Model. *Reprod. Sci.* **2021**, *28*, 3361–3379. [CrossRef] [PubMed]
90. Ruscitto, C.; Ogden, J.; Ellis, J.G. To what extent is circadian predictive of subjective jet lag in long-haul cabin crew pre- and post-trip? *Appl. Ergon.* **2023**, *106*, 103882. [CrossRef]
91. Chase, J.E.; Gidal, B.E. Melatonin: Therapeutic Use in Sleep Disorders. *Ann. Pharmacother.* **1997**, *31*, 1218–1226. [CrossRef]
92. Razali, S.; Bose, A.; Chong, P.W.; Benetti, C.; Colombo, P.; Wong, T.W. Design of multi-particulate "Dome matrix" with sustained-release melatonin and delayed-release caffeine for jet lag treatment. *Int. J. Pharm.* **2020**, *587*, 119618. [CrossRef]
93. Chen, Y.; Liu, Y.; Dong, Q.; Xu, C.; Deng, S.; Kang, Y.; Fan, M.; Li, L. Application of functionalized chitosan in food: A review. *Int. J. Biol. Macromol.* **2023**, *235*, 123716. [CrossRef]
94. Zhao, H.; Wang, L.; Belwal, T.; Jiang, Y.; Li, D.; Xu, Y.; Luo, Z.; Li, L. Chitosan-based melatonin bilayer coating for maintaining quality of fresh-cut products. *Carbohydr. Polym.* **2020**, *235*, 115973. [CrossRef] [PubMed]
95. Al-Quarashi, A.D.; Awad, M.A.; Elsayed, M.I.; Ali, M.A. Postharvest melatonin and chitosan treatments retain quality of 'Williams' bananas during ripening. *J. Food Sci. Technol.* **2023**, *61*, 84–96. [CrossRef]
96. Al-Qurashi, A.D.; Awad, M.A. Effect of exogenous melatonin and chitosan treatment of quality and chemical changes of 'Balady Banzahir' limes during shelf life. *J. Anim. Plant Sci.* **2023**, *33*, 310–319. [CrossRef]
97. Bal, E. Impact of Chitosan-Melatonin Composite Coating on Postharvest Quality of Sweet Cherry. *Appl. Fruit Sci.* **2023**, *66*, 763–770. [CrossRef]
98. Mwelase, S.; Opara, U.L.; Fawole, O.A. Effect of chitosan-based melatonin composite coating on the quality of minimally processed pomegranate aril-sacs during cold storage. *J. Food Process. Preserv.* **2022**, *46*, e17096. [CrossRef]
99. Ullah, M.A.; Gyl, F.Z.; Zaman, G.; Iqbal, J.; Drouhet, S.; Tungmunnithum, D.; Hano, C.; Abbasi, B.H. The influence of exogenous melatonin and chitosan on secondary metabolites production and biological activities of tissue extracts in agitated micro-shoot cultures of Ajuga integrifolia Buch. Ham. Ex D. Don. *Acta Physiol. Plant.* **2023**, *45*, 106. [CrossRef]
100. Zhou, B.; Yu, X.J.; Zhang, M.; Tian, H.Y.; Dong, J.J.; Guo, L.; Zhang, T.J. Melatonin chitosan microparticles decrease degradation and increase drought resistance properties of melatonin. *J. Plant Nutr. Fertil.* **2022**, *28*, 1308–1317. [CrossRef]
101. Chen, J.; Qin, H.; Zhang, B.; Mao, W.; Lou, L.; Shen, C.; Mao, J.; Lin, Q. Development of melatonin nano-delivery systems to reduce cadmium accumulation in rice (*Oryza sativa* L.) seedlings: Insights from photosynthetic efficiency, antioxidative response and gene expression. *Environ. Exp. Bot.* **2022**, *196*, 104822. [CrossRef]
102. Tabassum, M.; Noreen, Z.; Aslam, M.; Shah, A.N.; Usman, S.; Waqas, A.; Alsherif, E.A.; Korany, S.M.; Nazim, M. Chitosan modulated antioxidant activity, inorganic ions homeostasis and endogenous melatonin to improve yield of *Pisum sativum* L. accessions under salt stress. *Sci. Hortic.* **2024**, *323*, 112509. [CrossRef]
103. López-Valverde, N.; López-Valverde, A.; Aragoneses, J.M.; Martínez-Martínez, F.; González-Escudero, M.C.; Ramírez, J.M. Bone density around titanium dental implants coating tested/coated with chitosan or melatonin: An evaluation via microtomography in jaws of beagle dogs. *Coatings* **2021**, *11*, 777. [CrossRef]
104. Abdelrasoul, M.; El-Fattah, A.A.; Kotry, G.; Ramadan, O.; Essawy, M.; Kamaldin, J.; Kandil, S. Regeneration of critical-sized grade II furcation using a novel injectable melatonin-loaded scaffold. *Oral Dis.* **2023**, *29*, 3583–3598. [CrossRef] [PubMed]
105. Abdelrasoul, M.; Kamaldin, J.B.; Ooi, J.P.; El-Fattah, A.A.; Kotry, G.; Ramadan, O.; Kandil, S. An eight-week in vivo study on the clinical signs of systemic toxicity and bone regenerative performance of composites containing beta tricalcium phosphate, hydrogel and melatonin in adult New Zealand Rabbit (*Oryctolagus cuniculus*). *Malays. J. Med. Health Sci.* **2020**, *16*, 38–45.
106. Thomas, A.; Kumar, K.G. Acetylene black-chitosan mediated electro-oxidation of serotonin and melatonin: An efficient platform for simultaneous voltammetric sensing. *Ionics* **2019**, *25*, 2337–2349. [CrossRef]
107. Sunon, P.; Wongkaew, P.; Johns, J.; Johns, N. Characterization of cerium oxide-chitosan nanocomposite-modified screen printed carbon electrode and application in melatonin determination. *Int. J. GEOMATE* **2018**, *14*, 151–157. [CrossRef]

108. Tang, S.; Liang, A.; Liu, M.; Wang, W.; Zhang, F.; Luo, A. A glassy carbon electrode modified with a composite consisting of electrodeposited chitosan and carboxylated multi-walled carbon nanotubes for simultaneous voltammetric determination of dopamine, serotonin, and melatonin. *Carbon Lett.* **2023**, *33*, 2129–2139. [CrossRef]
109. Mirza-Aghazadeh-Attari, M.; Mihanfar, A.; Yousefi, B.; Majidinia, M. Nanotechnology-based advances in the efficient delivery of melatonin. *Cancer Cell Int.* **2022**, *22*, 43. [CrossRef]

International Journal of
Molecular Sciences

MDPI

Article

Processing α-Chitin into Stable Composite Materials for Heavy Metal Adsorption

Anjana Aravind [1,†], Kristina Seliverstova [2,†], Kaitlin K. K. Kammerlander [1], Thomas Henle [2] and Eike Brunner [1,*]

[1] Bioanalytische Chemie, Fakultät für Chemie und Lebensmittelchemie, TU Dresden, 01062 Dresden, Germany; anjana.aravind@tu-dresden.de (A.A.)
[2] Lebensmittelchemie, Fakultät für Chemie und Lebensmittelchemie, TU Dresden, 01062 Dresden, Germany; kristina.seliverstova@tu-dresden.de (K.S.); thomas.henle@tu-dresden.de (T.H.)
* Correspondence: eike.brunner@tu-dresden.de
† These authors contributed equally to this work.

Abstract: Water contamination by heavy metals, including radionuclides, is a major threat to human health and the environment. New methods for their removal are therefore needed. Adsorption is currently a common method for wastewater treatment. It depends on the physical and chemical interactions between heavy metal ions and adsorbents. The main characteristics of suitable adsorption methods are (i) a high adsorption efficiency and ability to remove different types of ions, (ii) a high retention time and cycle stability of adsorbents, and (iii) availability. Chitin is a commercially available biopolymer from marine waste that has several favourable properties: availability, low cost, high biocompatibility, biodegradability, and effective adsorption properties for metal ions. However, the processing of chitin into stable structures, such as chitin-based composites, is difficult due to its high chemical stability and extremely low solubility in most solvents. The central working hypothesis of the present work is that powdered α-chitin can be dissolved in the ionic liquid 1-butyl-3-methylimidazolium acetate and cross-linked with its monomer, N-acetyl-D-glucosamine, in a Maillard-like or caramelisation reaction to produce chitin-based composites. It is further hypothesised that such composites can be used as biosorbents for heavy metal ions. Eu(III) is chosen here as a non-radioactive representative and analogue for other f-elements.

Keywords: α-chitin; N-acetyl-D-glucosamine; ionic liquids; composite; characterisation; europium adsorption

1. Introduction

Mining activities as well as nuclear energy production lead to the risk of the release of heavy metals, including radionuclides, into the environment as well as food chains. Many heavy elements are toxic. Long-living radionuclides (actinides) are of further concern due to their radioactivity. Given their high toxicity and carcinogenicity, heavy elements and especially actinides pose severe risks to human health as well as ecosystems. There are several methods for their removal from aqueous solutions, such as solvent extraction, ion exchange, coagulation, electrodeposition, and reverse osmosis. Currently, adsorption attracts increasing attention due to its high efficiency, simplicity, and low cost [1–7]. Adsorption using functional materials has been demonstrated to be an efficient technique for removing heavy metals/radionuclides from water [8–12]. There is already a market for low-cost materials with a high adsorption capacity under intense environmental conditions to remove radionuclides.

Chitin $(C_8H_{13}O_5N)_n$ is the second most abundant biopolymer after cellulose. In the chemical sense, it is a polysaccharide consisting of β-1,4-linked N-acetyl-D-glucosamine (GlcNAc) units [13,14]. It is a primary component of the cell walls in fungi and of the exoskeletons in various invertebrates such as crustaceans and insects [13], and even in some marine sponges [15]. Chitin is also produced by several other living organisms in the lower plant and animal kingdoms, serving many functions like reinforcement/mechanical strength [16]. Chitin is well-suited for various applications due to its excellent biocompatibility, biodegradability, hydrophilicity, low toxicity, and availability from the aforementioned renewable resources. Depending on its source, chitin occurs as three allomorphs: the α, β, and γ forms, which can be differentiated, e.g., by attenuated total reflectance (ATR), Fourier transform infrared (FTIR), and solid-state nuclear magnetic resonance (NMR) spectroscopy, as well as X-ray diffraction [17]. α-chitin is the stable and most abundant form. It occurs in fungal and yeast cell walls, krill, lobster, crab tendons, shrimp shells, insect cuticles, and even in the skeletons of some marine sponge species [7]. Hence, α-chitin is a low-cost and easily available biopolymer. Its use as an eco-friendly material is thus desirable from the point of view of sustainability.

Chitin is also well-known for its favourable adsorption properties, especially with respect to various heavy metal ions from solutions, including uranium, cadmium, iron, nickel, copper, lead, and zinc [18–24]. This is due to suitable functionalities, especially carbonyl and hydroxyl groups. For example, Lin et al. [20] demonstrated efficient uranyl-carbonate removal from aqueous solutions by film-like chitin/polyethyleneimine (CH-PEI) biosorbents. Duan et al. [19] exploited a synergistic effect of chitin in combination with lignin, thus enabling more efficient adsorption of iron and copper. Boulaiche et al. [22] evaluated the effective biosorption of heavy metals such as copper, zinc, lead, and cadmium by chitin. However, the crystalline and stable α-chitin is unable to swell, and most of these functional groups are thus inaccessible for the metal ions in solution. Using a special, sponge-like form of α-chitin extracted from a marine sponge with a comparably high external surface area, very high adsorption capacities for uranyl ions from aqueous solutions could be obtained [18], which emphasises the need to enhance the external surface area. However, the primary sources of chitin are crab and shrimp shells. This material is commercially available as a powder consisting of α-chitin particles. The transformation of this commercially available material into stable chitin-based composites, sponge-like structures, or other composites would thus be highly desirable. However, chitin is hardly soluble by organic solvents or water due to its very stable, strongly hydrogen-bonded structure [17,25]. Dissolution of chitin is only feasible in very few solvents [17,26–28], which are, however, toxic, degradable, corrosive, scarce, or mutagenic. Therefore, most current uses of this natural resource are associated with chitosan, a soluble, partially or completely deacetylated derivative of chitin.

Recently, ionic liquids (ILs) have been documented to dissolve biopolymers and are considered as "green" solvents capable of substituting the volatile organic compounds (VOCs) generally used in different processing and synthesis industries. The pioneering work on the utilisation of ILs as solvents for polysaccharides was carried out by the group of Roger [25,29,30]. It was found that ILs could be employed as non-derivatising solvents for native cellulose. One of the ILs used in this work, 1-butyl-3-methylimidazolium chloride ([BMIM][Cl]), showed the best solvating capability. Up to 25 wt.% cellulose could be dissolved under microwave heating. That means, ILs obviously provide efficient access to this natural biopolymer and subsequently enable an entire product platform based on this renewable source, a significant step towards sustainability. Wu et al. [31] developed an approach to dissolve α-chitin in 1-butyl-3-methylimidazolium acetate [BMIM][OAc]. This IL was used for the dissolution processing of the biopolymer into a microsphere architecture.

Based on this preliminary work, the central working hypothesis of the present work is that powdered α-chitin can be dissolved in the ionic liquid 1-butyl-3-methylimidazolium acetate and can be cross-linked using its monomer, N-acetyl-D-glucosamine, in a Maillard-like or caramelisation reaction to produce chitin-based composites. It is also hypothesised that such composites can be used as mechanically stable adsorbents for heavy metal ions. Europium (Eu) is typically utilised as a non-radioactive analogue for other trivalent lanthanides and actinides because of its similar physicochemical properties [32]. The present study investigated the biosorption of trivalent Eu(III) on the processed chitin-based composites created from the commercially available biopolymer α-chitin. Their morphology, structure, and surface properties were analysed using FTIR, solid-state NMR spectroscopy, and SEM analysis methods. The biosorption of Eu(III) was quantified using inductively coupled plasma optical emission spectroscopy (ICP-OES).

2. Results and Discussion

2.1. Characterisation of Composites

The first step after the preparation and drying of the chitin-based composites (cf. Figure 1) was the visual inspection of the material (see Figure 2).

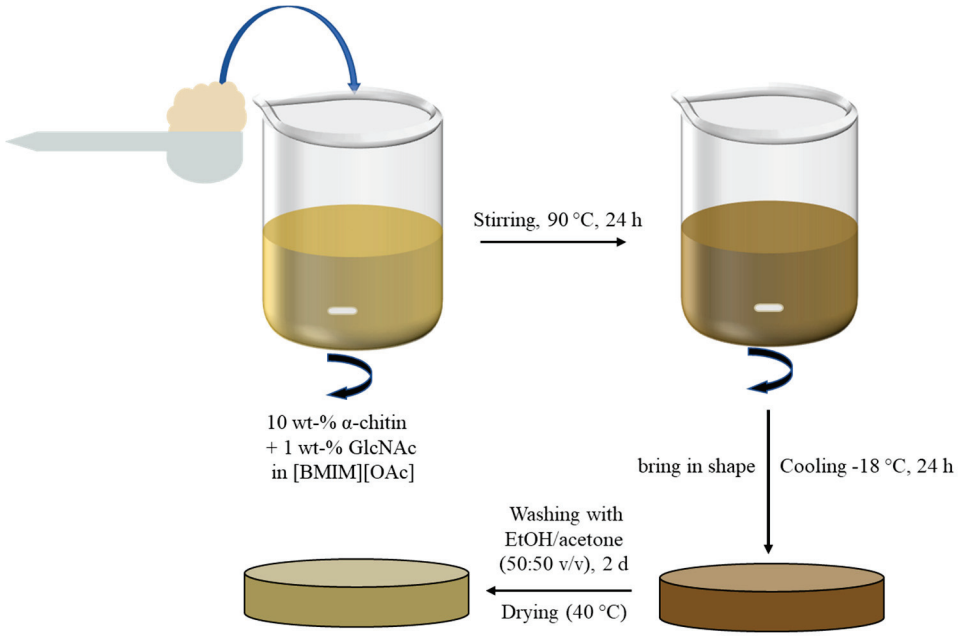

Figure 1. Experimental scheme of the synthesis procedure of chitin-based composites.

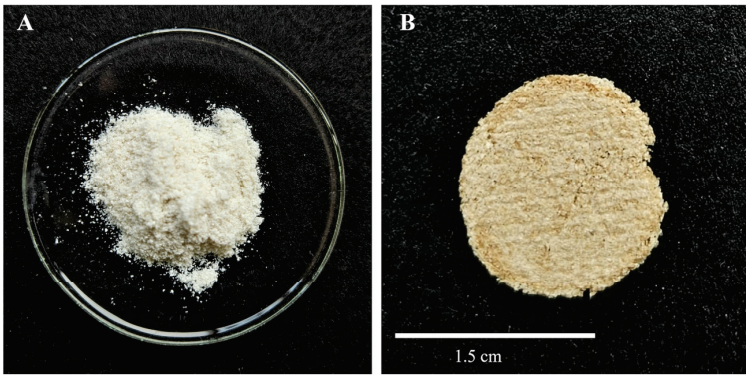

Figure 2. (**A**) Initial material (commercial α-chitin powder) and (**B**) prepared chitin-based composite after washing in EtOH/acetone and oven-drying.

Figure 2 shows the commercial α-chitin and the synthesised chitin-based composite. It can already be seen visually that the oven-dried, chitin-based composite has an amber colour. This is characteristic for the reaction of sugars in non-enzymatic browning reactions such as caramelisation or the Maillard reaction [33,34]. This principle was used here for the preparation of the composite, which is a novel contribution of the work presented.

In short, the reaction described by Louis-Camille Maillard in 1912 [35] is an amino-carbonyl reaction which is particularly important in processed food, such as baking bread or roasting coffee. Based on the above-mentioned examples, reducing sugars and amino components such as amino acids or proteins react with each other to produce a variety of odour- and taste-active products, as well as colouring components such as melanoidins and other "advanced glycation end products" (AGEs) [34]. The precursors of these end products include Amadori and Heyns products. Later dicarbonyls, e.g., methylglyoxal, are formed at different stages of the Maillard reaction. However, they can also be formed during the classical caramelisation of sugars [34]. The particular focus on such compounds is due to their potential as possible cross-linking agents. The idea is that the addition of the monomer GlcNAc can promote cross-linking between the individual polymer chains of chitin. This should lead to an increased stability but also flexibility of the composites. It is assumed that the reaction could lead to the formation of dicarbonyls, as well as to a reaction of the carbonyl group of the monomer with the partially diacetylated residues in the chitin. The latter would be described as a Maillard self-reaction [36,37]. The hypotheses for the formation of such cross-links are summarised in Figure 3.

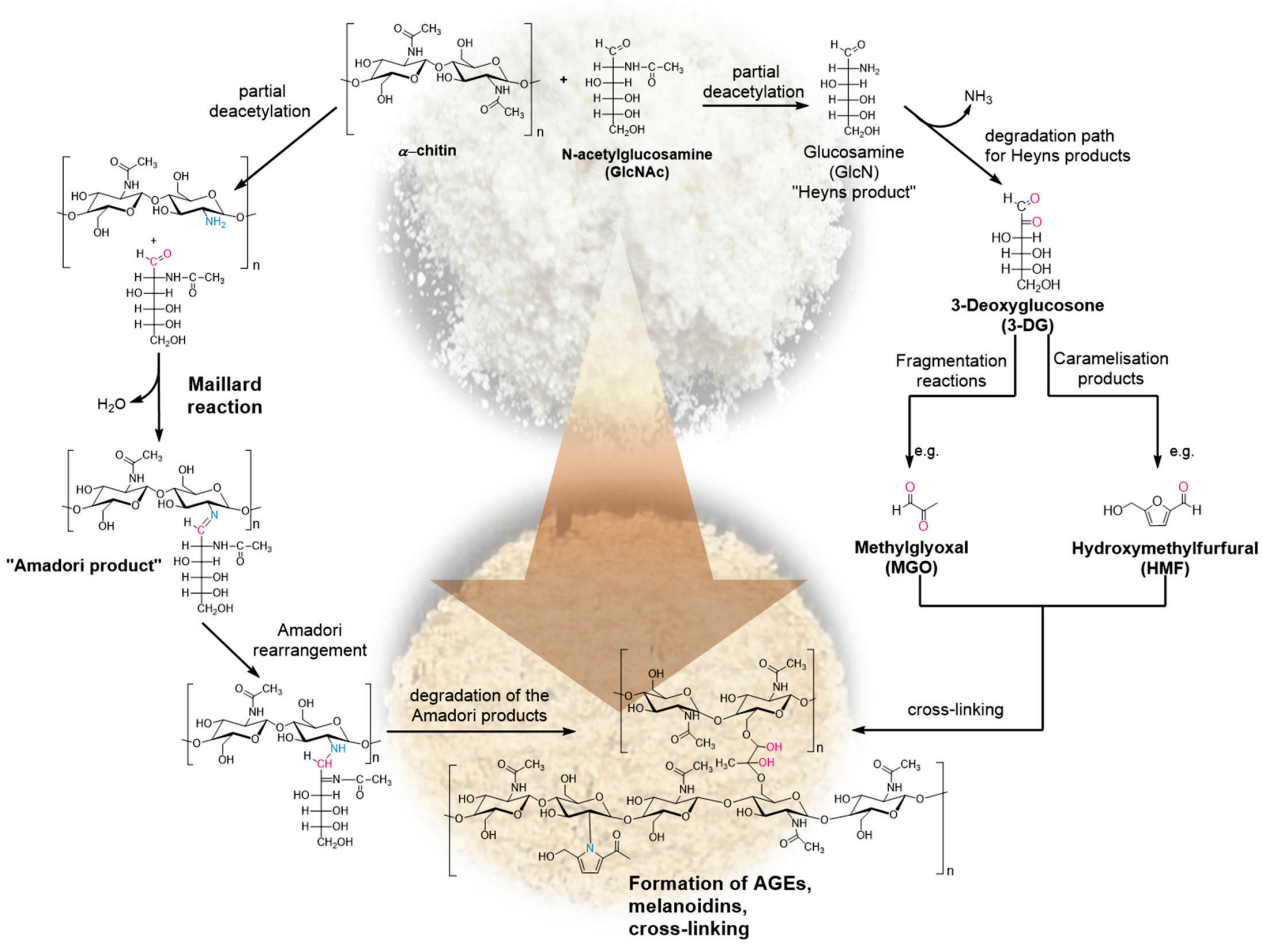

Figure 3. Proposed mechanism of interaction and cross-linking between α-chitin and GlcNAc via Maillard self-reaction and caramelisation processes.

Scanning electron microscopy was used for the morphological characterisation of the chitin-based composites. Figure 4 shows the images of commercial α-chitin compared to the prepared material. The structural difference is evident. While the native chitin powder has an uneven surface (A), the prepared composite appears to have a smooth and uniform surface with no visible particles (C). This indicates that chitin has been successfully dissolved and restructured during the manufacturing process. The lateral image of the fragments also shows a difference. The α-chitin has an unstructured, fibrous structure (B), whereas the chitin-based composite appears to have an ordered, layered structure (D). Similar observations were made by Wu et al. [31] for their composites obtained without the GlcNAc cross-linking agent.

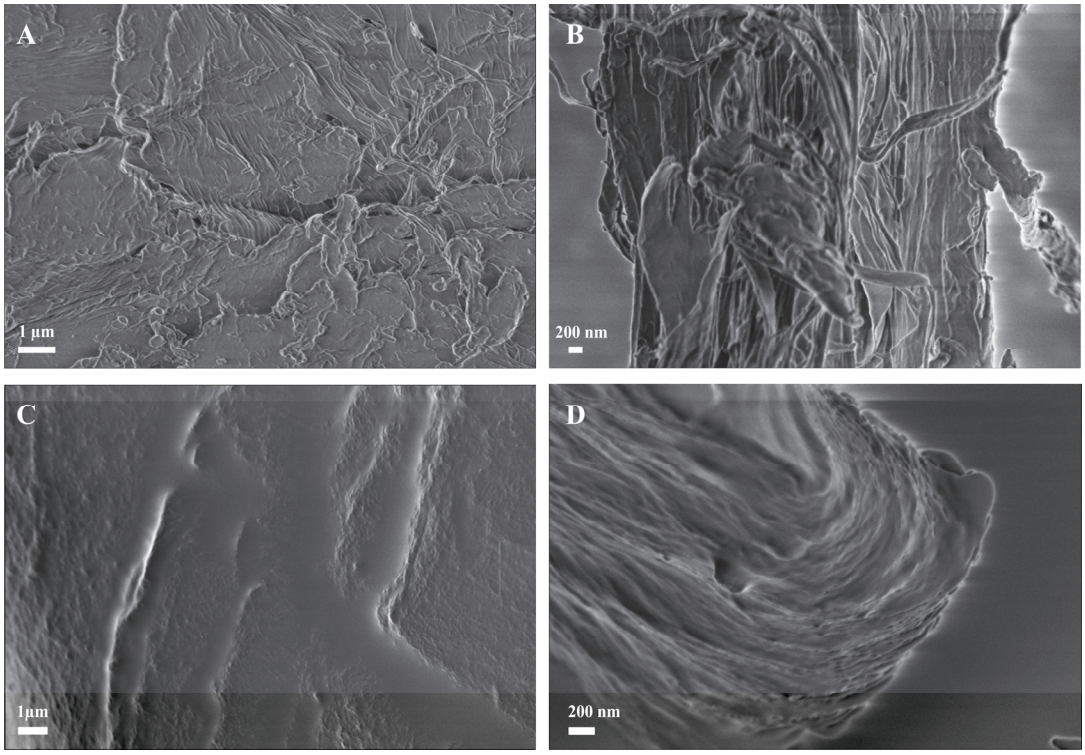

Figure 4. Morphological characterisation of the initial material (α-chitin) and produced chitin-based composites by SEM: (**A**) surface and (**B**) interior structure of dried α-chitin; (**C**) surface structure and (**D**) interior structure of formed and oven-dried, chitin-based composites.

In order to characterise the materials at the molecular level, ^{13}C cross-polarisation (CP) MAS NMR experiments were performed. Figure 5 shows the ^{13}C CP MAS NMR spectra of α-chitin, the chitin-based composite, and monomeric GlcNAc. The spectra of the samples show well-resolved signals from each expected carbon position (see structure inserted in Figure 5). The signal assignment for α-chitin following the literature [38] is given in Table S1 (ESI). The spectra measured for the α-chitin reference samples agree very well with previously published data [38–41]. Kameda et al. [39] demonstrated that the carbonyl ^{13}C NMR signal at room temperature consists of two lines due to different hydrogen bonds in α-chitin. At elevated temperature, these two signals merge into a single, symmetric peak, indicating an exchange between the carbonyl carbons involved in different hydrogen-bonding environments. The spectrum of α-chitin measured here at room temperature also shows the presence of these two components (Figure 5a). The C=O signal of N-acetyl-D-glucosamine (Figure 5c) exhibits a small splitting due to the residual dipolar coupling with the neighbouring quadrupolar ^{14}N nucleus (S = 1). The magnetic dipole–dipole interaction between a spin-1/2 nucleus and a nucleus carrying an electric quadrupole moment

(i.e., a spin with S > 1/2) can result in a characteristic residual dipolar broadening and splitting of the MAS NMR signals of the spin-1/2 nucleus [42,43]. The main difference between α-chitin and the chitin-based composites occurs in the region C=O carbon (see inserts in Figure 5a,b). The signal from chitin shifts to lower chemical shift values and becomes narrower. Note that the less intense peak at the higher chemical shift is likely due to the cross-linking of the monomer unit. This observation confirms the observations described above in the context of Figure 3: the cross-linking reaction takes place via caramelisation or the Maillard reaction [33,36,37], whereby the N-acetyl-D-glucosamine moiety seems to be the interaction site. Further support for this idea comes from the cross-polarisation (CP) kinetics of ^{1}H-^{13}C CP MAS NMR experiments [44,45]. Depending on the dipolar coupling strength, the ^{13}C NMR signals build up and decay at different rates. Mobility also affects the CP efficiency. The intensities of the ^{13}C CP MAS NMR signals were measured at different contact times ranging from 0.25 ms to 10 ms. The resonance peak intensity follows the function described in the literature (see, e.g., [46]). The variation in the contact time allows the determination of both the cross-polarisation build-up time (T_{CP}) and proton spin-lattice relaxation time in the rotating frame ($T_{1\rho}$). Figure 6 shows the intensity (peak area) of the ^{13}C CP MAS NMR signal of C=O as a function of the contact time for α-chitin and the composite. All the cross-polarisation build-up times T_{CP} and proton spin-lattice relaxation times $T_{1\rho}$ of α-chitin and the composite are given in Figure S3 (ESI). Significant differences between α-chitin and the composite occur selectively for the C=O signal, especially for $T_{1\rho}$. This observation further indicates that the cross-linking with the monomer mainly occurs via the GlcNAc moiety of chitin.

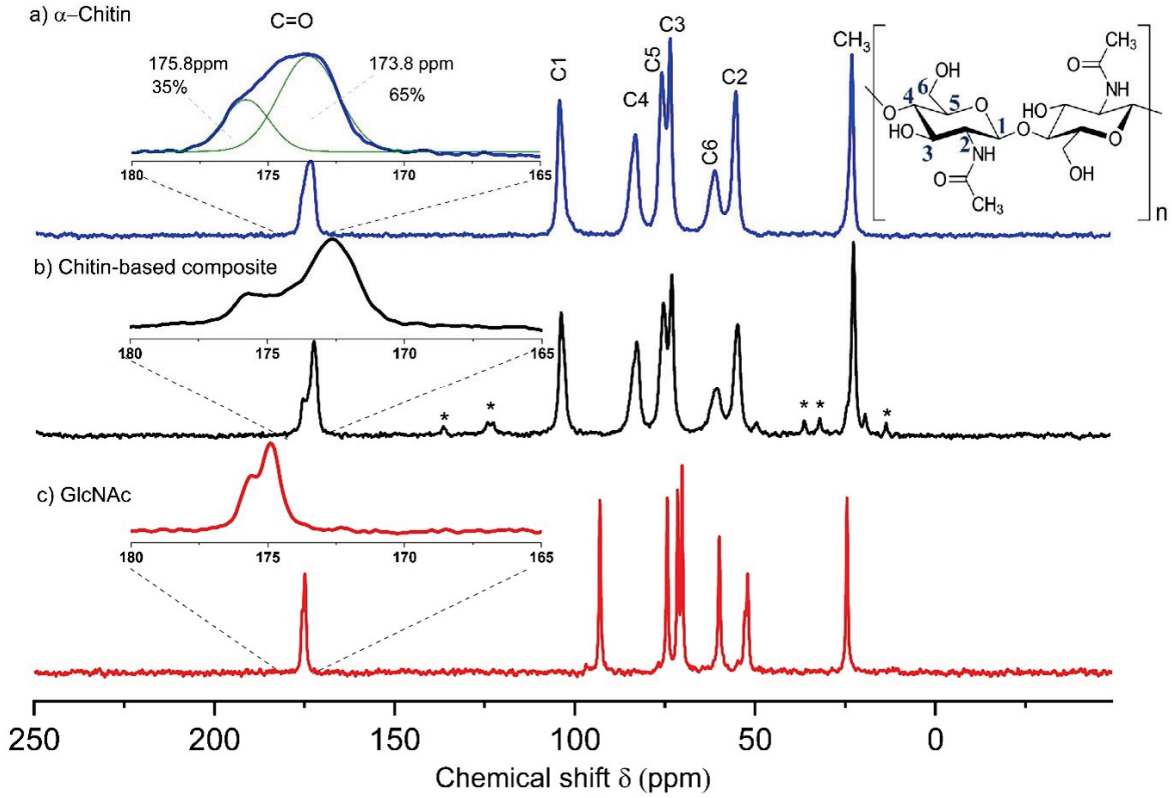

Figure 5. ^{13}C CP MAS NMR spectra of (**a**) α-chitin, (**b**) chitin-based composite, and (**c**) GlcNAc. CP contact time: 4 ms. The minor signals indicated by an asterisk in the composite spectrum are due to residual spurious amounts of the ionic liquid used for the processing. The insert in (**a**) shows the decomposition of the C=O signal into the two components discussed in text (green lines).

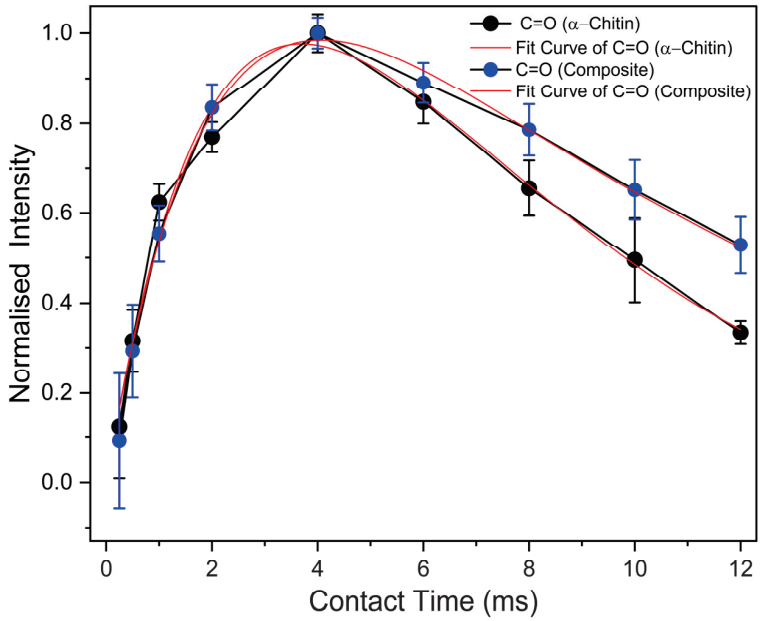

Figure 6. CP build-up curves for the C=O signal in α-chitin and the chitin-based composite measured at variable contact times of 0.25–12 ms. Furthermore, the fitted curves are shown, which allow the determination of T_{CP} and $T_{1\rho}$.

The infrared spectra are displayed in Figure 7. The bands are assigned based on the literature [13,15,47] (see Table S2 (ESI)). IR spectroscopy can distinguish the different chitin crystal structures (α or β) due to the influence of the different hydrogen bond patterns upon the spectra [13]. Two amide bands at 1653 and 1619 cm^{-1} [48] occur due to two different hydrogen bond states. The component at 1653 cm^{-1} is assigned to C=O groups hydrogen bonded only to NH groups, while the component at 1619 cm^{-1} should be ascribed to the similar group with another hydrogen bond to the side chain CH_2OH [49]. The existence of these inter-chain hydrogen bonds is responsible for the high chemical stability of the α-chitin structure [13]. In the chitin-based composites, these two bands are narrower and have slightly different relative intensities in line with the conclusions drawn above from the ^{13}C CP MAS NMR spectra.

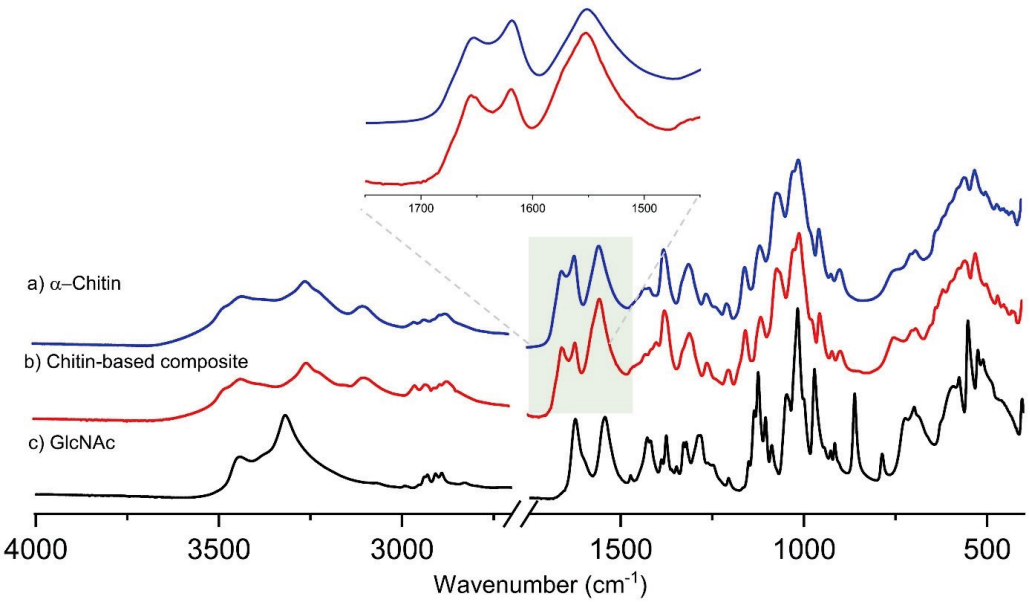

Figure 7. ATR-FTIR spectra of α-chitin (**a**), chitin-based composite (**b**), and GlcNAc monomer (**c**).

2.2. Characterisation of the Adsorbent After Eu Adsorption

The ICP-OES studies reveal (Figure 8) that the pure α-chitin adsorbed more europium than the composite for both initial Eu(III) concentrations in solution. With increasing time, the adsorption capacity increases for both materials.

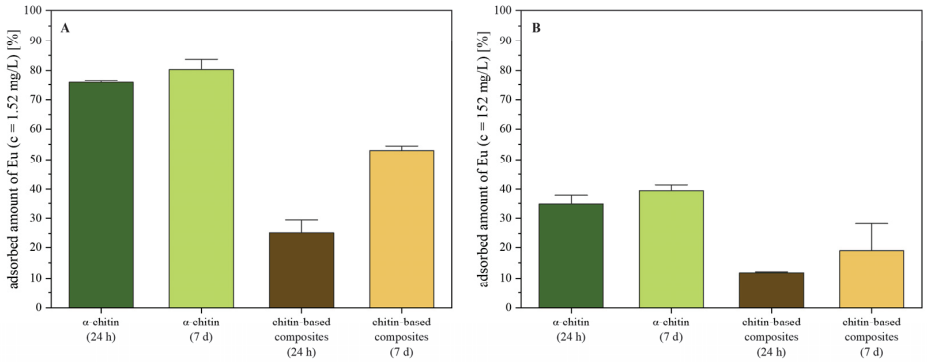

Figure 8. Characterisation of the europium adsorption on chitin and chitin-based composites by ICP-OES: (**A**) adsorbed europium amount after 24 h and 7 d [c($EuCl_3 \cdot 6H_2O$) = 10^{-5} M] and (**B**) adsorbed europium amount after 24 h and 7 d [c($EuCl_3 \cdot 6H_2O$) = 10^{-3} M].

Pure chitin is very efficient in adsorbing the small amount of Eu(III) dissolved in the solution with a 10^{-5} M concentration, which corresponds to only 1.52 mg/L. The composites are less efficient. Their decreased adsorption capacity is probably due to the partial blocking of adsorption sites by cross-linking with the monomers via the probable interaction sites, which are the C=O (see above). For the highly concentrated solution (10^{-3} M Eu(III) corresponding to 152 mg/L), the trend is similar. The adsorption capacity, i.e., the amount of Eu(III) adsorbed per gram of adsorbent material, is calculated using Equation (1). The adsorption capacity of α-chitin after 24 h and seven days and the 10^{-3} M solution was 33 mg/g (milligram europium per gram material) and 38 mg/g. For the composite, 11 mg/g and 18 mg/g europium loading are obtained after 24 h and seven days. The comparison shows that native α-chitin has a higher adsorption capacity for Eu(III) than the composites at both adsorption times.

To ensure the structural integrity of the adsorbents after europium sorption, we measured ^{13}C CP MAS NMR and ATR-IR spectra (see ESI, Figures S1 and S2) and compared them with the spectra of the unloaded samples discussed above (Figures 5 and 7). The adsorption of europium did not result in significant changes in the spectra apart from decent line broadening in the NMR spectra, which is likely due to the paramagnetic europium ions. This indicates that the europium ion is not covalently bound to chitin, as the formation of bonds should be visible in the NMR spectra in the form of measurable chemical shifts or signal splitting. The absence of observable changes in the measured spectra strongly implies that europium caused no chemical modification or destruction of the chitin. A probable interaction mechanism that may explain all these observations is the coordination of europium via the C=O groups. This may also involve the formation of hydrogen bonds between the hydroxyl groups of the different europium complexes and the polymer. Such weak interactions tend to favour the reversible reaction and the easy desorption of the metal. That means, the overall configuration of the polymer chain is maintained during the process.

3. Materials and Methods

3.1. Chemicals

The chitin materials used in this study include α-chitin from crab shells purchased from Carl Roth (Karlsruhe, Germany) of 400,000 g/mol molecular mass, respectively.

$EuCl_3 \cdot 6H_2O$ (99.99%) and N-acetyl-D-glucosamine (≥95%, MW: 221.2 g/mol) were purchased from Sigma Aldrich (St. Louis, MO, USA). The chitin and N-acetyl glucosamine were used directly without further purification. 1-Butyl-3-methyl-imidazolium acetate [BMIM][OAc] was purchased from Iolitech (Heilbronn, Germany) at ≥98% purity. Ethanol (EtOH) and acetone of high-performance liquid chromatography (HPLC) grade were obtained from Fisher Chemicals (Schwerte, Germany).

3.2. Sample Preparation

The preparation of the chitin-based composites follows a modified procedure inspired by the previous work of Wu et al. [31]. In contrast to previous studies, the monomer N-acetyl-D-glucosamine was added to α-chitin for the first time here as a cross-linker. A 10 wt.-% solution of α-chitin and 1 wt.-% of GlcNAc in IL was prepared by dissolving 0.3 g of chitin and 0.03 g of GlcNAc in 3 mL of [BMIM][OAc]. Chitin, GlcNAc, and IL were mixed and heated in an oil bath at 90 °C (±5 °C) for 24 h until full dissolution of the chitin. During heating and stirring, the solution became an amber colour. After 24 h, the hot solution was poured over a round-shaped Teflon form with an inner diameter of 17 mm and 2.3 mm depth. After shaping and cooling to room temperature, the composite was cooled overnight at −20 °C. Afterwards, the composites were placed in a solution of ethanol and acetone to remove the IL. After washing, the finished chitin-based composites were dried at 40 °C in a drying oven for 2 days. These treatment steps are schematically summarised in Figure 1.

3.3. Batch Eu(III) Sorption Experiments

A total of 15.5 mg (±0.3 mg) of the chitin and chitin-based composite was suspended in 10 mL of solution with either 10^{-3} mol/L or 10^{-5} mol/L $EuCl_3 \cdot 6H_2O$ in ultrapure water. Pure α-chitin was loaded with europium for comparison. The suspensions were shaken in total for 7 days; however, an aliquot was taken after 24 h. Since the central goal of our present work was to develop a synthesis procedure for stable composites that maintain the favourable biosorption properties of pure chitin at least partly, it was decided to evaluate the short-term behaviour after 24 h and the long-term behaviour after 7 days. Afterward the samples were centrifuged at 5000 rpm for 10 min, the supernatant was separated from the pellet and used for ICP-OES. The pellet of the sample was dried under air atmosphere, and the Eu(III) uptake (q) was calculated as follows [20]:

$$q = (C_0 - C_i) \cdot V / m \quad (1)$$

where C_0 and C_i (mg/L) are the concentrations of Eu(III) before and after adsorption, respectively; V is the volume of Eu(III) solution; and m is the weight of the adsorbent (α-chitin or chitin-based composite).

3.4. Scanning Electron Microscopy (SEM)

Scanning electron microscopy (SEM) was used to examine the sample morphologies. The surface morphology of chitin and chitin-based composites samples was recorded at room temperature using a scanning electron microscope, Oxford XMaxN 150—150 mm^2, (Oxford Instruments, Abingdon, UK) with an acceleration voltage of 50 kV, accessible through the Dresden Center for Nanoanalysis (DCN) at TU Dresden.

3.5. Fourier Transform Infrared (FTIR) Spectroscopy

The FTIR measurements were performed on a Thermo Scientific Nicolet iS5 spectrometer (Waltham, MA, USA) equipped with a broad-band mercury-cadmium-telluride detector. The spectra were acquired in the attenuated total reflection (ATR) mode using

single-reflection monolithic durable diamond ATR Specac's Golden Gate accessory (Orpington, UK). All spectra were acquired from a spot 2 mm in diameter on samples pressed against the diamond crystal. Spectra (500 scans at 2 cm^{-1} resolution) were collected in the 4000–400 cm^{-1} range.

3.6. Nuclear Magnetic Resonance (NMR)

Solid-state ^{13}C nuclear magnetic resonance (NMR) spectra were acquired using a Bruker Ascend 300 MHz NMR spectrometer at 75.47 MHz for ^{13}C using a commercial double-resonance 4 mm magic-angle spinning (MAS) NMR probe (Bruker Biospin, Ettlingen, Gemany). Approximately 15 mg of sample was packed into the rotors and spun at 15 kHz. Ramped cross-polarisation (CP) was used for all the samples spun at the magic angle of 15 kHz. A CP contact time of 4 ms and a recycle delay of 3 s were used. Free induction decays (FIDs) were accumulated (in total 26,000 scans) with a total acquisition time of 22 h. The spectral width was 30 kHz. Furthermore, CP build-up curves were acquired with a contact time variation between 0.25 and 10 ms. Spectra were referenced relative to tetramethylsilane (TMS) using adamantane with its well-known signals at 29.5 ppm and 18.5 ppm as the secondary standard.

3.7. Inductively Coupled Plasma Optical Emission Spectroscopy (ICP-OES)

To analyse the sorption properties of the chitin-based composites and the pure chitin, the supernatant from the batch adsorption tests was measured and compared with the initial concentration of the Eu(III) solution. Therefore, samples were diluted in HNO_3 (5%), respectively. The resulting liquids were analysed with an Optima 7000DV spectrometer (Perkin Elmer, Waltham, MA, USA) utilising the following parameters: high frequency power 1300 W, liquid flow 1.6 L/min, plasma gas flow 15 L/min, auxiliary gas flow 0.2 L/min, and nebuliser gas flow 0.65 L/min. The spectral line was 412.970 nm for the radial detection of europium.

4. Conclusions

The working hypothesis of the present study was confirmed: we have successfully established a novel method for processing commercially available powdered α-chitin into stable composites based on dissolution in the IL 1-butyl-3-methylimidazolium acetate and cross-linking with the added monomer N-acetyl-D-glucosamine at relatively low temperatures. After cooling these solutions to room temperature, gels remain, and the chitin-based composites are then obtained by ethanol/acetone coagulation. Cross-linking with GlcNAc in a Maillard-like or caramelisation reaction gives mechanically stable composites for applications such as filter materials. FTIR studies the structural integrity of the chitin after these processing steps. ^{13}C solid-state NMR experiments showed changes in the NMR parameters of the C=O signal induced by cross-linking with the GlcNAc monomer. This implies that the N-acetyl moiety of chitin is influenced by the cross-linking. The suitability of these composites for heavy metal biosorption was demonstrated using europium as an analogue for f-elements, confirming a second working hypothesis of our present work. Europium adsorption did not lead to any changes in the spectra indicative of chemical modifications of the chitin or the composites. The ICP-OES data showed that the original α-chitin biosorbed more Eu(III) than the chitin-based composites at different concentrations. It appears that the cross-linking monomer partially blocks the adsorption sites, which are probably the C=O groups.

In summary, commercially available chitin is successfully processed into mechanically and chemically stable composites with promising properties. Future work should focus on further improving the biosorption properties, e.g., by using other cross-linking agents that

do not block the C=O groups or—ideally—even providing other functional groups that provide additional interaction sites for metal ions to improve the adsorption properties.

Supplementary Materials: The following supporting information can be downloaded at: https://www.mdpi.com/article/10.3390/ijms26073149/s1.

Author Contributions: Conceptualisation, T.H. and E.B.; methodology, A.A., K.S. and K.K.K.K.; software, A.A., E.B. and K.K.K.K.; validation, A.A., K.S. and K.K.K.K.; formal analysis, A.A., K.S. and K.K.K.K.; investigation, A.A., K.S. and K.K.K.K.; resources, T.H. and E.B.; data curation, A.A. and K.S.; writing—original draft preparation, A.A. and K.S.; writing—review and editing, A.A. and K.S.; supervision, T.H. and E.B.; project administration, T.H. and E.B.; funding acquisition, T.H. and E.B. All authors have read and agreed to the published version of the manuscript.

Funding: This research was funded and supported by the project Planar Carbon Lattices, funded by the Deutsche Forschungsgemeinschaft (German Research Foundation) DFG GRK2861—491865171 and the Bundesministerium für Bildung und Forschung (Federal Ministry for Education and Research) BMBF FENABIUM 02NUK077A.

Institutional Review Board Statement: Not applicable.

Informed Consent Statement: Not applicable.

Data Availability Statement: The original contributions presented in this study are included in the article and Supplementary Materials. Further inquiries can be directed to the corresponding author.

Acknowledgments: The authors thank the Dresden Center for Nanoanalysis (DCN) facilities at the TU Dresden for technical guidance with the scanning electron microscopy and image analysis and Christiane Leudolph (TU Dresden) for the elemental analyses with ICP-OES.

Conflicts of Interest: The authors declare no conflicts of interest. The funders had no role in the design of the study; in the collection, analyses, or interpretation of data; in the writing of the manuscript; or in the decision to publish the results.

References

1. Bruggeman, C.; Maes, N. Uptake of Uranium(VI) by Pyrite under Boom Clay Conditions: Influence of Dissolved Organic Carbon. *Environ. Sci. Technol.* **2010**, *44*, 4210–4216. [CrossRef] [PubMed]
2. Cadogan, E.I.; Lee, C.-H.; Popuri, S.R.; Lin, H.-Y. Efficiencies of Chitosan Nanoparticles and Crab Shell Particles in Europium Uptake from Aqueous Solutions through Biosorption: Synthesis and Characterization. *Int. Biodeterior. Biodegrad.* **2014**, *95*, 232–240. [CrossRef]
3. Hao, Y.; Cui, Y.; Peng, J.; Zhao, N.; Li, S.; Zhai, M. Preparation of Graphene Oxide/Cellulose Composites in Ionic Liquid for Ce (III) Removal. *Carbohydr. Polym.* **2019**, *208*, 269–275. [CrossRef] [PubMed]
4. Li, Y.; Sheng, G.; Sheng, J. Magnetite Decorated Graphene Oxide for the Highly Efficient Immobilization of Eu (III) from Aqueous Solution. *J. Mol. Liq.* **2014**, *199*, 474–480. [CrossRef]
5. Lujanienė, G.; Novikau, R.; Karalevičiūtė, K.; Pakštas, V.; Talaikis, M.; Levinskaitė, L.; Selskienė, A.; Selskis, A.; Mažeika, J.; Jokšas, K. Chitosan-Minerals-Based Composites for Adsorption of Caesium, Cobalt and Europium. *J. Hazard. Mater.* **2024**, *462*, 132747. [CrossRef] [PubMed]
6. Nikiforova, T.; Kozlov, V.; Razgovorov, P.; Politaeva, N.; Velmozhina, K.; Shinkevich, P.; Chelysheva, V. Heavy Metal Ions(II) Sorption by a Cellulose-Based Sorbent Containing Sulfogroups. *Polymers* **2023**, *15*, 4212. [CrossRef]
7. Younes, I.; Rinaudo, M. Chitin and Chitosan Preparation from Marine Sources: Structure, Properties and Applications. *Mar. Drugs* **2015**, *13*, 1133–1174. [CrossRef]
8. Crini, G. Recent Developments in Polysaccharide-Based Materials Used as Adsorbents in Wastewater Treatment. *Prog. Polym. Sci.* **2005**, *30*, 38–70. [CrossRef]
9. Muzzarelli, R.A.A. Potential of Chitin/Chitosan-Bearing Materials for Uranium Recovery: An Interdisciplinary Review. *Carbohydr. Polym.* **2011**, *84*, 54–63. [CrossRef]
10. Rafatullah, M.; Sulaiman, O.; Hashim, R.; Ahmad, A. Adsorption of Methylene Blue on Low-Cost Adsorbents: A Review. *J. Hazard. Mater.* **2010**, *177*, 70–80. [CrossRef]
11. Vo, T.S.; Hossain, M.M.; Jeong, H.M.; Kim, K. Heavy Metal Removal Applications Using Adsorptive Membranes. *Nano Converg.* **2020**, *7*, 36. [CrossRef] [PubMed]

12. Qasem, N.A.A.; Mohammed, R.H.; Lawal, D.U. Removal of Heavy Metal Ions from Wastewater: A Comprehensive and Critical Review. *Npj Clean Water* **2021**, *4*, 27. [CrossRef]
13. Cárdenas, G.; Cabrera, G.; Taboada, E.; Miranda, S.P. Chitin Characterization by SEM, FTIR, XRD, and 13C Cross Polarization/Mass Angle Spinning NMR. *J. Appl. Polym. Sci.* **2004**, *93*, 1876–1885. [CrossRef]
14. Shahidi, F.; Arachchi, J.K.V.; Jeon, Y.-J. Food Applications of Chitin and Chitosans. *Trends Food Sci. Technol.* **1999**, *10*, 37–51. [CrossRef]
15. Brunner, E.; Ehrlich, H.; Schupp, P.; Hedrich, R.; Hunoldt, S.; Kammer, M.; Machill, S.; Paasch, S.; Bazhenov, V.V.; Kurek, D.V.; et al. Chitin-Based Scaffolds Are an Integral Part of the Skeleton of the Marine Demosponge *Ianthella basta*. *J. Struct. Biol.* **2009**, *168*, 539–547. [CrossRef] [PubMed]
16. Jayakumar, R.; Menon, D.; Manzoor, K.; Nair, S.V.; Tamura, H. Biomedical Applications of Chitin and Chitosan Based Nanomaterials—A Short Review. *Carbohydr. Polym.* **2010**, *82*, 227–232. [CrossRef]
17. Rinaudo, M. Chitin and Chitosan: Properties and Applications. *Prog. Polym. Sci.* **2006**, *31*, 603–632. [CrossRef]
18. Schleuter, D.; Günther, A.; Paasch, S.; Ehrlich, H.; Kljajić, Z.; Hanke, T.; Bernhard, G.; Brunner, E. Chitin-Based Renewable Materials from Marine Sponges for Uranium Adsorption. *Carbohydr. Polym.* **2013**, *92*, 712–718. [CrossRef]
19. Duan, Y.; Freyburger, A.; Kunz, W.; Zollfrank, C. Lignin/Chitin Films and Their Adsorption Characteristics for Heavy Metal Ions. *Polymers* **2021**, *13*, 2090. [CrossRef]
20. Lin, Z.; Chen, L.; Ye, Z.; Chen, X.; Wang, X.; Wei, Y. Film-Like Chitin/Polyethylenimine Biosorbent for Highly Efficient Removal of Uranyl-Carbonate Compounds from Water. *J. Environ. Chem. Eng.* **2021**, *9*, 105340. [CrossRef]
21. Karthik, R.; Meenakshi, S. Chemical Modification of Chitin with Polypyrrole for the Uptake of Pb(II) and Cd(II) Ions. *Int. J. Biol. Macromol.* **2015**, *74*, 51–59. [CrossRef]
22. Boulaiche, W.; Hamdi, B.; Trari, M. Removal of Heavy Metals by Chitin: Equilibrium, Kinetic and Thermodynamic Studies. *Appl. Water Sci.* **2019**, *9*, 39. [CrossRef]
23. Yousefi, N.; Jones, M.; Bismarck, A.; Mautner, A. Fungal Chitin-Glucan Nanopapers with Heavy Metal Adsorption Properties for Ultrafiltration of Organic Solvents and Water. *Carbohydr. Polym.* **2021**, *252*, 117175. [CrossRef]
24. Bartczak, P.; Klapiszewski, Ł.; Wysokowski, M.; Majchrzak, I.; Czernicka, W.; Piasecki, A.; Ehrlich, H.; Jesionowski, T. Treatment of Model Solutions and Wastewater Containing Selected Hazardous Metal Ions Using a Chitin/Lignin Hybrid Material as an Effective Sorbent. *J. Environ. Manage.* **2017**, *204 Pt 1*, 300–310. [CrossRef]
25. Swatloski, R.P.; Spear, S.K.; Holbrey, J.D.; Rogers, R.D. Dissolution of Cellulose Correction of Cellulose with Ionic Liquids. *J. Am. Chem. Soc.* **2002**, *124*, 4974–4975. [CrossRef] [PubMed]
26. Hu, X.; Du, Y.; Tang, Y.; Wang, Q.; Feng, T.; Yang, J.; Kennedy, J.F. Solubility and Property of Chitin in NaOH/Urea Aqueous Solution. *Carbohydr. Polym.* **2007**, *70*, 451–458. [CrossRef]
27. Ravi Kumar, M.N.V. A Review of Chitin and Chitosan Applications. *React. Funct. Polym.* **2000**, *46*, 1–27. [CrossRef]
28. Ravindra, R.; Krovvidi, K.R.; Khan, A.A. Solubility Parameter of Chitin and Chitosan. *Carbohydr. Polym.* **1998**, *36*, 121–127. [CrossRef]
29. Shamshina, J.L. Chitin in Ionic Liquids: Historical Insights into the Polymer's Dissolution and Isolation. A Review. *Green Chem.* **2019**, *21*, 3974–3993. [CrossRef]
30. Zhu, S.; Wu, Y.; Chen, Q.; Yu, Z.; Wang, C.; Jin, S.; Ding, Y.; Wu, G. Dissolution of Cellulose with Ionic Liquids and Its Application: A Mini-Review. *Green Chem.* **2006**, *8*, 325. [CrossRef]
31. Wu, Y.; Sasaki, T.; Irie, S.; Sakurai, K. A Novel Biomass-Ionic Liquid Platform for the Utilization of Native Chitin. *Polymer* **2008**, *49*, 2321–2327. [CrossRef]
32. Götzke, L.; Schaper, G.; März, J.; Kaden, P.; Huittinen, N.; Stumpf, T.; Kammerlander, K.K.; Brunner, E.; Hahn, P.; Mehnert, A.; et al. Coordination Chemistry of f-Block Metal Ions with Ligands Bearing Bio-Relevant Functional Groups. *Coord. Chem. Rev.* **2019**, *386*, 267–309. [CrossRef]
33. Gullón, B.; Montenegro, M.I.; Ruiz-Matute, A.I.; Cardelle-Cobas, A.; Corzo, N.; Pintado, M.E. Synthesis, Optimization and Structural Characterization of a Chitosan-Glucose Derivative Obtained by the Maillard Reaction. *Carbohydr. Polym.* **2016**, *137*, 382–389. [CrossRef] [PubMed]
34. Hellwig, M.; Henle, T. Baking, Ageing, Diabetes: A Short History of the Maillard Reaction. *Angew. Chem. Int. Ed.* **2014**, *53*, 10316–10329. [CrossRef]
35. Maillard, L.C. Formation d'Humus et de Combustibles Mineraux sans Intervention de l'Oxygene Atmospherique, des Microorganismes des Hautes Temperatures ou des Fortes Pressions. *C. R. Hebd. Seances Acad. Sci.* **1912**, *154*, 66–68.
36. Kraskouski, A.; Hileuskaya, K.; Nikalaichuk, V.; Ladutska, A.; Kabanava, V.; Yao, W.; You, L. Chitosan-Based Maillard Self-Reaction Products: Formation, Characterization, Antioxidant and Antimicrobial Potential. *Carbohydr. Polym. Technol. Appl.* **2022**, *4*, 100257. [CrossRef]
37. Hrynets, Y.; Ndagijimana, M.; Betti, M. Studies on the Formation of Maillard and Caramelization Products from Glucosamine Incubated at 37 °C. *J. Agric. Food Chem.* **2015**, *63*, 6249–6261. [CrossRef]

38. Belton, P.S.; Tanner, S.F.; Cartier, N.; Chanzy, H. High-Resolution Solid-State Carbon-13 Nuclear Magnetic Resonance Spectroscopy of Tunicin, an Animal Cellulose. *Macromolecules* **1989**, *22*, 1615–1617. [CrossRef]
39. Kameda, T.; Miyazawa, M.; Ono, H.; Yoshida, M. Hydrogen Bonding Structure and Stability of Alpha-Chitin Studied by 13C Solid-State NMR. *Macromol. Biosci.* **2005**, *5*, 103–106. [CrossRef]
40. Kono, H. Two-Dimensional Magic Angle Spinning NMR Investigation of Naturally Occurring Chitins: Precise ^{1}H and ^{13}C Resonance Assignment of Alpha- and Beta-Chitin. *Biopolymers* **2004**, *75*, 255–263. [CrossRef]
41. Brunner, E.; Richthammer, P.; Ehrlich, H.; Paasch, S.; Simon, P.; Ueberlein, S.; van Pée, K.-H. Chitin-Based Organic Networks: An Integral Part of Cell Wall Biosilica in the Diatom *Thalassiosira pseudonana*. *Angew. Chem. Int. Ed.* **2009**, *48*, 9724–9727. [CrossRef] [PubMed]
42. Olivieri, A.C. Quadrupolar Effects in the CPMAS NMR Spectra of Nuclei. *J. Magn. Reson. (1969)* **1989**, *81*, 201–205. [CrossRef]
43. Böhm, J.; Fenzke, D.; Pfeifer, H. Effects of Quadrupolar Nuclei on NMR Spectra of Nuclei in Magic-Angle Spinning Experiments. *J. Magn. Reson. (1969)* **1983**, *55*, 197–204. [CrossRef]
44. Voelkel, R. Possible Applications and Advantages of High-Resolution Solid State 13C NMR Spectroscopy in Polymers. *ChemInform* **1989**, *7*. [CrossRef]
45. Sullivan, M.J.; Maciel, G.E. Structural Resolution in the Carbon-13 Nuclear Magnetic Resonance Spectrometric Analysis of Coal by Cross Polarization and Magic-Angle Spinning. *Anal. Chem.* **1982**, *54*, 1606–1615. [CrossRef]
46. Kolodziejski, W.; Klinowski, J. Kinetics of Cross-Polarization in Solid-State NMR: A Guide for Chemists. *Chem. Rev.* **2002**, *102*, 613–628. [CrossRef]
47. Pearson, F.G.; Marchessault, R.H.; Liang, C.Y. Infrared Spectra of Crystalline Polysaccharides. V. Chitin. *J. Polym. Sci.* **1960**, *43*, 101–116. [CrossRef]
48. Focher, B.; Naggi, A.; Torri, G.; Cosani, A.; Terbojevich, M. Chitosans from *Euphausia superba*. 2: Characterization of Solid State Structure. *Carbohydr. Polym.* **1992**, *18*, 43–49. [CrossRef]
49. Miya, M.; Iwamoto, R.; Yoshikawa, S.; Mima, S.I.R. Spectroscopic Determination of CONH Content in Highly Deacylated Chitosan. *Int. J. Biol. Macromol.* **1980**, *2*, 323–324. [CrossRef]

International Journal of
Molecular Sciences

MDPI

Article

Physico-Chemical Characterization and Initial Evaluation of Carboxymethyl Chitosan–Hyaluronan Hydrocolloid Systems with Insulin Intended for Intranasal Administration

Roxana Popescu [1], Cristina-Elena Dinu-Pîrvu [1,2], Mihaela Violeta Ghica [1,2,*], Valentina Anuța [1,2] and Lăcrămioara Popa [1,2]

[1] Department of Physical and Colloidal Chemistry, Faculty of Pharmacy, "Carol Davila" University of Medicine and Pharmacy, 6 Traian Vuia Str., 020950 Bucharest, Romania; roxana_popescu@drd.umfcd.ro (R.P.); cristina.dinu@umfcd.ro (C.-E.D.-P.); valentina.anuta@umfcd.ro (V.A.); lacramioara.popa@umfcd.ro (L.P.)
[2] Innovative Therapeutic Structures Research and Development Centre (InnoTher), "Carol Davila" University of Medicine and Pharmacy, 020956 Bucharest, Romania
* Correspondence: mihaela.ghica@umfcd.ro

Abstract: The nasal route of administration can bypass the blood–brain barrier in order to obtain a higher concentration in the brain, thus offering a feasible alternative route of administration for diseases associated with the central nervous system. The advantages of the intranasal administration and the potential favorable therapeutic effects of intranasally administered insulin led to the formulation of carboxymethyl chitosan (CMC) and sodium hyaluronate (NaHA) hydrocolloidal systems with insulin for nasal administration, targeting nose-to-brain delivery and the initial assessment of these systems. The influence of the formulation variables on the response parameters defined as surface properties, rheology, and in vitro release of insulin were analyzed using experimental design and statistical programs (Modde and Minitab software). The systems recorded good wetting and adhesion capacity, allowing the spread of the hydrocolloidal systems on the nasal mucosa. The samples had a pseudoplastic flow and the rapid release of the insulin was according to our objective. According to the physico-chemical characterization and preliminary assessment, these formulations are appropriate for administration on the nasal mucosa, but further studies are necessary to demonstrate the beneficial therapeutic actions and the safety of using intranasal insulin.

Keywords: carboxymethyl chitosan; intranasal insulin; nose-to-brain delivery

1. Introduction

Among researchers, more interest is shown toward the intranasal route of administration from the point of view of the management of neurodegenerative diseases and brain disorders (brain tumors, cerebral ischemic injuries, stroke and others), and for the administration of substances that act at the brain level, because it avoids the blood–encephalic barrier (BBB), enzymatic degradation, hepatic metabolism, and gastrointestinal pH issues [1–4]. Nasal administration is not invasive and does not require the presence of qualified personnel, thus improving the patient's compliance with the treatment [1,5,6]. The nose-to-brain delivery of the active pharmaceutical ingredient is mostly achieved through the olfactory and trigeminal nerves, and also by systemic circulation, because the nasal mucosa is well vascularized [5,7–9].

For more over 100 years, insulin has been widely used for its hypoglycemic effect to treat diabetes [10,11], and lately the intranasal route has been studied for the administration of insulin [12]. People with Type 2 Diabetes Mellitus (T2DM) are more vulnerable to developing cognitive impairment [13,14], Alzheimer disease [15,16], or Parkinson disease [17,18].

To date, based on the information available on the clinicaltrials.gov website, there are studies that investigate the effectiveness of intranasal insulin administration for metabolic-, neurodegenerative- and central nervous system-associated diseases [19].

Currently, insulin is also being researched for its neuroprotective effect after intranasal administration, in addition to its use in the treatment of diabetes. Studies conducted have revealed the potential beneficial therapeutic action of insulin administered intranasal, by slowing the progression of neurodegenerative diseases, improving the cognitive impairments associated with T2DM, or stimulating the socio-communicative capacity of patients [20–22] (Alzheimer disease [23–25], Parkinson disease [26–28], eating disorders [29,30], but additional studies are still required.

It was shown that insulin can improve cognitive function by reducing amyloid plaques, influences tau phosphorylation, stabilizes microtubules, and enhances tubulin polymerization [1,31].

Even if the risk of hypoglycemia is lower after the administration of insulin intransally, compared with subcutaneous administration [32], there were some reported side effects during the clinical trials, such as flu-like symptoms, falls, hypoglycemia, dizziness, diarrhea [33], a slow decrease in blood glucose, nasal burning sensation [34], local nasal rhinitis [35], transient nasal stinging, nasal irritation, and unpleasant odor [36].

It was also observed that insulin may have a favorable impact on the management of addictions [37] and smoking behavior [38]. Based on a randomized study, 60 IU insulin was administered nasally daily to people who wanted to quit smoking, which showed a decrease in the need for nicotine, although the results are not yet conclusive. Also, adverse events like nasal irritation, sweating, confusion, watering eyes, anxiety, and others were reported [39,40].

The administration of a high cumulative nasal dose does not lead to an increase in the systemic concentration of insulin. Most of the studies carried out so far used a daily dose of 0.5–1.5 IU/body kg (or 10–160 IU/day) [41]. Studies conducted on small groups of people did not lead to serious adverse events, but at a dose higher than 160 IU/day, side effects may occur [15]. Further investigation needs to be performed to establish the therapeutic effect of insulin after intranasal administrations and its safety profile.

Carboxymethyl chitosan (CMC) is a derivative of chitosan obtained by introducing the carboxymethyl group into its structure, which can increase the water solubility of chitosan [42]. It is a biodegradable, biocompatible, non-toxic polymer [43,44]. Chitosan is very well studied because it has favorable mucoadhesion on the mucosa [45,46], but the mucoadhesive property of CMC is superior to chitosan [47] and acts as a permeation-enhancer adjuvant [48]. CMC has intrinsic actions, such as antibacterial [49], antioxidant, antifungal, anticancer, and antitumor [43].

Sodium hyaluronate (NaHA) (also known as hyaluronan) is the sodium salt of hyaluronic acid, a natural anionic polysaccharide and soluble in water. This substance possesses mucoadhesive properties, increases the viscosity of formulations, prolongs the contact time, and potentiates the absorption of proteins through the nasal mucosa [50,51]. It has the capacity to hydrate and protects against irritation [52] and also lubricates tissues [51].

It is necessary to consider the tight junction of the epithelium, the mucociliary clearance, and the optimal nasal pH for the formulation of the intranasal delivery systems. The factors that influence the release of the ingredient at the level of the olfactory area in the nasal cavity are surface tension, mucoadhesion, and viscosity [1].

Inspired by the potential therapeutic benefits of insulin administered intranasal, the aim of this study was the development and physico-chemical characterization of nasal systems based on CMC and NaHA with insulin, which would combine the mucoadhesive properties of the polymers and stimulate insulin absorption. We assessed the influence of formulation factors on surface properties, rheology, and in vitro release of insulin complementary using Design of Experiments strategies.

2. Results

2.1. Physico-Chemical Characterization of Hydrocolloidal Systems

2.1.1. Visual Aspect and pH

The hydrocolloidal systems were clear, transparent, and homogeneous, without any suspended particles or other instabilities. The pH of the formulations was between 6.57 and 6.72, as shown in Table 1, which is in the range of the nasal tolerability.

Table 1. Table of formulations and results for pH, contact angle, and surface tension.

System	X1 CMC (% *w*/*v*)	X2 CMC/NaHA Ratio	X3 Insulin (IU/mL)	pH	Contact Angle (°)	Surface Tension (mN/m)
S1	1	1/1	20	6.65	66.35 ± 0.64	57.19 ± 0.24
S2	2	1/1	20	6.57	65.48 ± 2.06	60.51 ± 0.05
S3	1	1/2	20	6.68	68.79 ± 1.56	58.85 ± 0.77
S4	2	1/2	20	6.64	64.68 ± 0.73	62.07 ± 0.71
S5	1	1/1	30	6.68	61.73 ± 0.75	60.91 ± 0.49
S6	2	1/1	30	6.62	64.10 ± 0.65	59.01 ± 0.32
S7	1	1/2	30	6.72	50.47 ± 0.26	59.65 ± 0.72
S8	2	1/2	30	6.65	58.43 ± 0.52	62.46 ± 0.30

where CMC is carboxymethyl chitosan and NaHA is sodium hyaluronate.

The pH values were similar, and we can conclude that the formulation parameters do not have an impact on the pH.

2.1.2. Contact Angle

The wetting capacity of the hydrocolloidal systems was characterized based on the contact angle (CA) determination. The average CA values were obtained from the left and right angle of the drop, at the contact with the solid surface. All the systems had the CA under 90°. The lowest contact angle was obtained for S7, 50.47 ± 0.26°, and the highest value was for S3, 68.79 ± 1.56°.

For the systems with a higher amount of insulin and the same CMC concentration and CMC/NaHA ratio, the CA is lower, especially for samples S3 and S7, where there is the most significant difference (18.32°), followed by the S4–S8 difference (6.25°).

2.1.3. Surface Tension

The values obtained for the ST parameter varied between 57.19 ± 0.24 mN/m for S1 and 62.46 ± 0.29 mN/m for S8. The concentration of the CMC had a slight influence on the ST parameter; the values were slightly lower for the systems with CMC 1% *w*/*v*, except for samples S5 and S6, where the S5 had the highest value, but the difference was non-significant (1.9 mN/m).

To have good system tolerability by the nasal mucosa, the surface tension of the products should be appropriate to the nasal mucosa superficial tension. Systems S1, S3, S6, and S7 demonstrated this requirement, but samples S2 and S5 were also close.

2.1.4. Work of Adhesion, Work of Cohesion, and Spreading Coefficient Based on Superficial Properties

The three parameters should be analyzed together because they are interconnected and offer information regarding the display and the adherence of the system on the nasal mucosa, indicated by a p value of 0.014. A high value of work of adhesion (Wa) combined with a lower work of cohesion (Wc) provide an optimal spreading coefficient (S).

For all the systems, the work of adhesion calculated based on the CA and ST was over 80 mN/m. The maximum value was for S7 (97.62 ± 1.1 mN/m), followed by S8

(95.17 ± 0.45 mN/m). The lowest value was determined for S3 (80.14 ± 2.75 mN/m), followed by S1 (82.84 ± 0.27 mN/m).

The weakest cohesion forces were recorded for S1 (114.38 ± 0.48 mN/m) and the strongest bonding was for S4 (124.14 ± 1.43 mN/m) and S8 (124.93 ± 0.23 mN/m).

Based on the results from Table 2, it can be stated that the formulations that have a better displaying capacity are the ones that have a spreading coefficient closer to zero: S7 (−21.68 ± 0.23 mN/m), S8 (−29.76 ± 0.21 mN/m), and S1 (−31.54 ± 0.7 mN/m).

Table 2. Work of adhesion, work of cohesion and spreading coefficient results.

System	Wa	Wc	S
S1	82.84 ± 0.27	114.38 ± 0.48	−31.54 ± 0.7
S2	85.62 ± 1.95	121.02 ± 0.1	−35.40 ± 2.02
S3	80.14 ± 2.75	117.7 ± 2.72	−37.56 ± 1.45
S4	88.62 ± 1.16	124.14 ± 1.43	−35.52 ± 0.88
S5	89.76 ± 0.26	121.83 ± 0.98	−32.06 ± 0.96
S6	84.79 ± 0.8	118.03 ± 1.31	−33.24 ± 0.57
S7	97.62 ± 1.1	119.3 ± 1.44	−21.68 ± 0.23
S8	95.17 ± 0.45	124.93 ± 0.23	−29.76 ± 0.21

where Wa is the work of adhesion (mN/m); Wc is the work of cohesion (mN/m), and S is the spreading coefficient (mN/m).

For the superficial parameters determined for the eight hydrocolloidal systems, we can emphasize that all systems have a good adhesion capacity and a satisfactory spreading capacity.

2.2. Rheology Analysis

The power law model is suitable to evaluate the polymeric material and was applied to analyze the rheological flow of the systems. This model describes the relationship between the shear stress, shear rate, and viscosity [53]. According to Table 3, the determination coefficient values were between 0.9926 and 0.9980. The power law model adequately and correctly fit the rheological analysis, since all the values were higher than 0.9900. The flow index values were less than 1, which means that all the systems had non-Newtonian pseudoplastic behavior.

Table 3. Power law model parameters for all eight systems.

Sample	S1	S2	S3	S4	S5	S6	S7	S8
K	0.261	0.841	1.054	1.187	0.393	0.475	0.897	1.095
n	0.611	0.539	0.526	0.549	0.670	0.620	0.576	0.546
R^2	0.9980	0.9926	0.9960	0.9952	0.9969	0.9953	0.9958	0.9954

where K is the consistency index ($Pa \cdot s^n$); n is the flow index, and R^2 is the determination coefficient.

The higher consistency index values were recorded for the hydrocolloid systems that had the higher CMC concentration for the same amount of insulin, and the same tendency was noticed at the same concentration of CMC and insulin with the CMC/NaHA ratio (S1 < S3 and S2 < S4 for the lower amount of insulin, respectively, S5 < S7 and S6 < S8).

The ascending flow curves of shear stress versus shear rate for all the systems are plotted in Figure 1, where the shear rate varies between 0.36 s^{-1} and 73.38 s^{-1}.

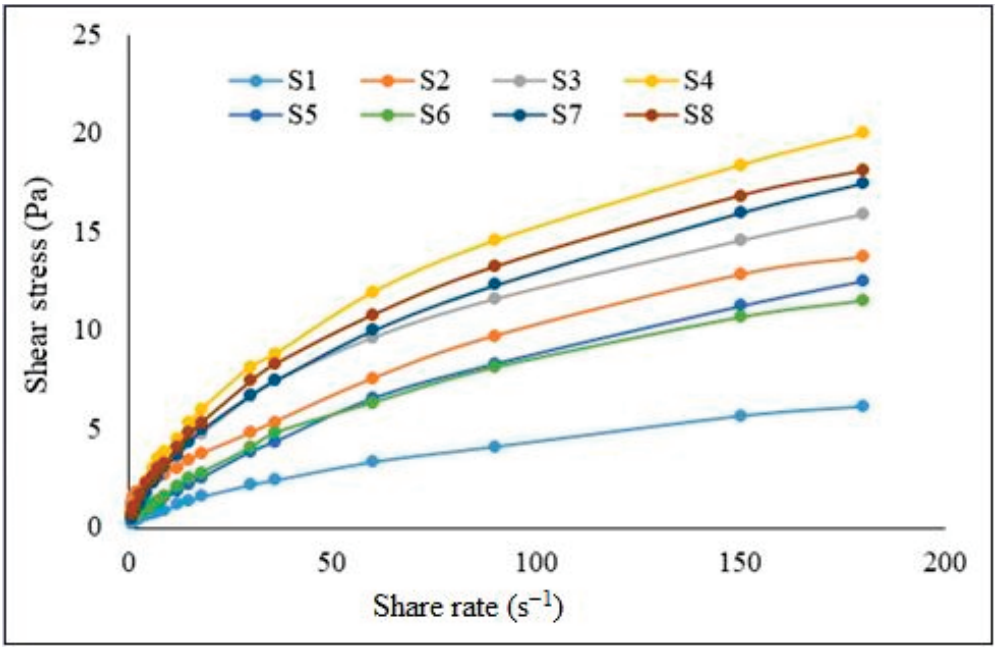

Figure 1. The flow curves representing the shear stress as function of shear rate.

All the formulations presented shear-thinning characteristics; the viscosity decreased when the shear rate increased. The rheogram viscosity as function of shear rate is presented in Figure 2 for each hydrocolloidal system.

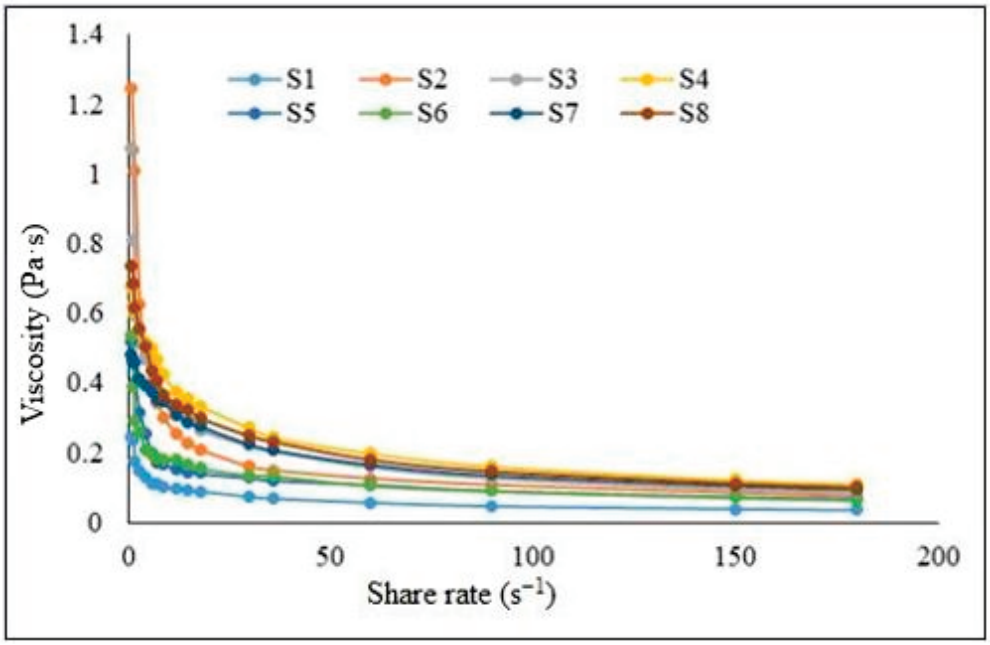

Figure 2. The influence of shear rate on the viscosity.

2.3. In Vitro Drug Release

The rapid release of the active pharmaceutical ingredient from the systems should be in accordance with the nasal characteristics. Different release kinetics models were applied (Higuchi, zero-order, and power law kinetic models), and the determination coefficients along with the kinetics parameters and the cumulative percentage of insulin release after 3 h are shown in Table 4. From the comparison of R^2, the mathematical model that fit the experimental data best for the S1, S4, S7, and S8 formulations was the zero-order model, with a determination coefficient greater than 0.9934, and the values of the release rate of

the insulin were between 0.342 min^{-1} and 0.538 min^{-1}. The power law model fit the other systems better, where R^2 was higher than 0.9958.

Table 4. Comparison of determination coefficients (R) for the Higuchi, zero-order, and power law kinetic models; kinetic parameters specific to the zero-order and power law models; and the cumulative drug-release percentage.

System	Determination Coefficient (R^2)			Kinetic Parameters			Drug Released (%)
	Higuchi Model	Zero-Order Model	Power Law Model	Zero-Order Model	Power Law Model		
				Kinetic Constant (1/min)	Kinetic Constant ($1/min^n$)	Release Exponent (n)	
1	0.9248	0.9959	0.9934	0.538	0.891	0.896	95.91
2	0.9710	0.9819	0.9962	0.445	1.885	0.703	74.35
3	0.9790	0.9771	0.9972	0.427	2.146	0.668	69.86
4	0.9128	0.9934	0.9852	0.342	0.522	0.913	62.53
5	0.9515	0.9913	0.9958	0.534	1.419	0.799	91.53
6	0.9585	0.9899	0.9980	0.517	1.554	0.774	88.06
7	0.9026	0.9962	0.9905	0.444	0.482	0.983	82.18
8	0.8857	0.9978	0.9968	0.412	0.282	1.076	76.65

All the samples had over 60% diffusion through the membrane. System S1 released the highest amount of insulin, 95.91%, which was followed by S5 at 91.53%.

Based on these results, we can conclude that for the same amount of insulin, the highest cumulative drug release was for the systems with CMC 1% w/v. We can also compare for the same amount of insulin and the same concentration of CMC; for this situation, the samples with the CMC/NaHA ratio 1/1 had a better release versus the 1/2 ratio.

In the first interval (Figure 3), all the samples had a good release, which is the most important, because the release should be quick in order to avoid a wash-out of the systems by mucociliary clearance.

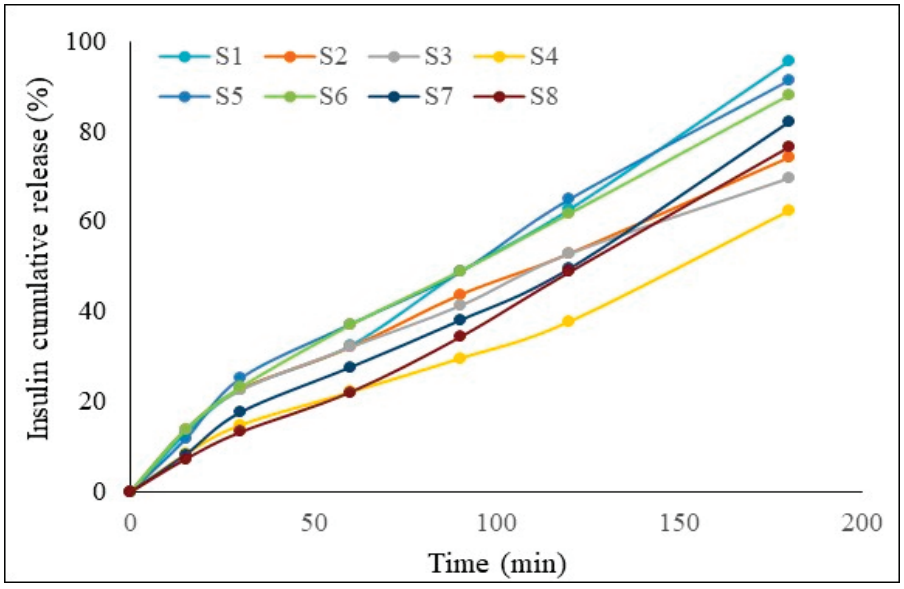

Figure 3. Cumulative release profiles of insulin from the hydrocolloidal systems.

2.4. Experimental Design Screening

The partial least squares (PLS) linear model was applied to evaluate the influence of the quantitative individual parameters (X1, X2, and X3) on the response parameters: work of adhesion (Y1), consistency index (Y2), and drug release (Y3). The statistical parameters that were used to evaluate the experiment were generated with Modde software, version 13; R2 was assessed as a statistical parameter to evaluate the goodness of fit for the experimental model and Q2 to estimate the goodness of prediction.

Taking into consideration that R2 was higher than 0.8 and Q2 > 0.5 for the response's consistency index and drug release, and the response work of adhesion was R2 > 0.6 and Q2 > 0.2, the values fulfilled the expectations (Figure 4); thus, the model fits well and has predictive power.

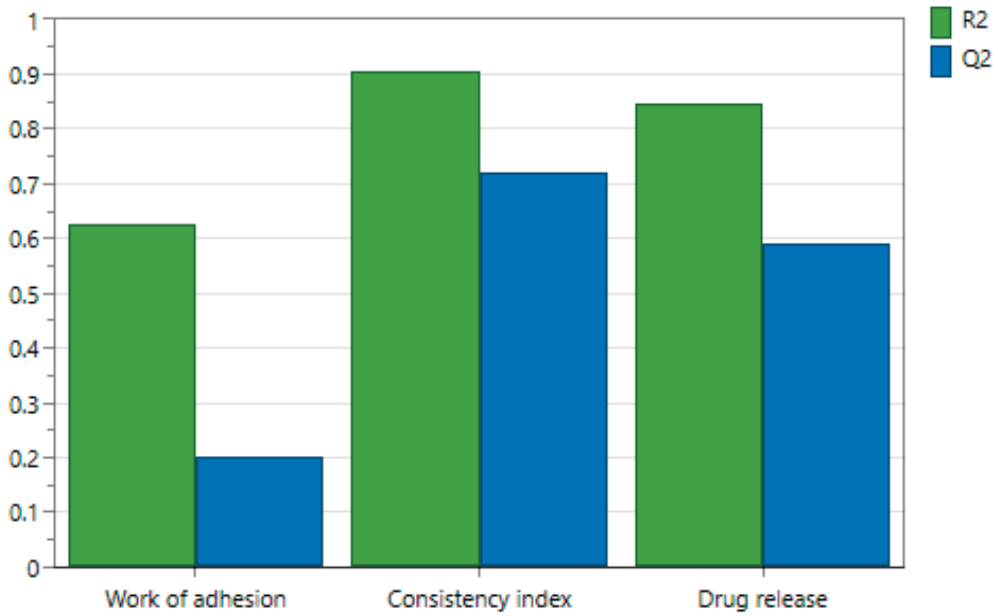

Figure 4. Graphical representation of statistical parameters R2 and Q2.

Modde software was used to design the experimental plan and provide the 3D response surface and contour plots, which were used to observe the tendency of the response variables based on the changes in the formulation parameter.

In Figure 5a–f, the tridimensional response surface plot is represented for each response parameter, varying X1—CMC concentration and X2—CMC/NaHA ratio, and maintaining the amount of insulin (X3) constant for the lower (−1) and upper (1) limits. At the lower amount of insulin, the work of adhesion varies proportionally with the concentration of CMC (Figure 5a), unlike the systems where the loading of insulin is at the upper level (Figure 5b). The consistency index is influenced proportionally by X1 and X2 in both situations (X3 = −1 and X3 = 1) (Figure 5c,d). On the other hand, the percentage of the drug release is influenced inversely proportionally by the concentration of CMC, and the ratio of the polymers impact negatively the release when the ratio is 1/2 for both amounts of insulin (Figure 5e,f).

The contour plot gives an overview of the experimental design, and based on Figure 6a–f, depicts the tendency of changing for each response parameter according to independent variables X1 and X2.

For all the responses analyzed, an ANOVA test was performed as a function of F and *p* values. The models were considered statistically significant when the *p* values were below 0.5.

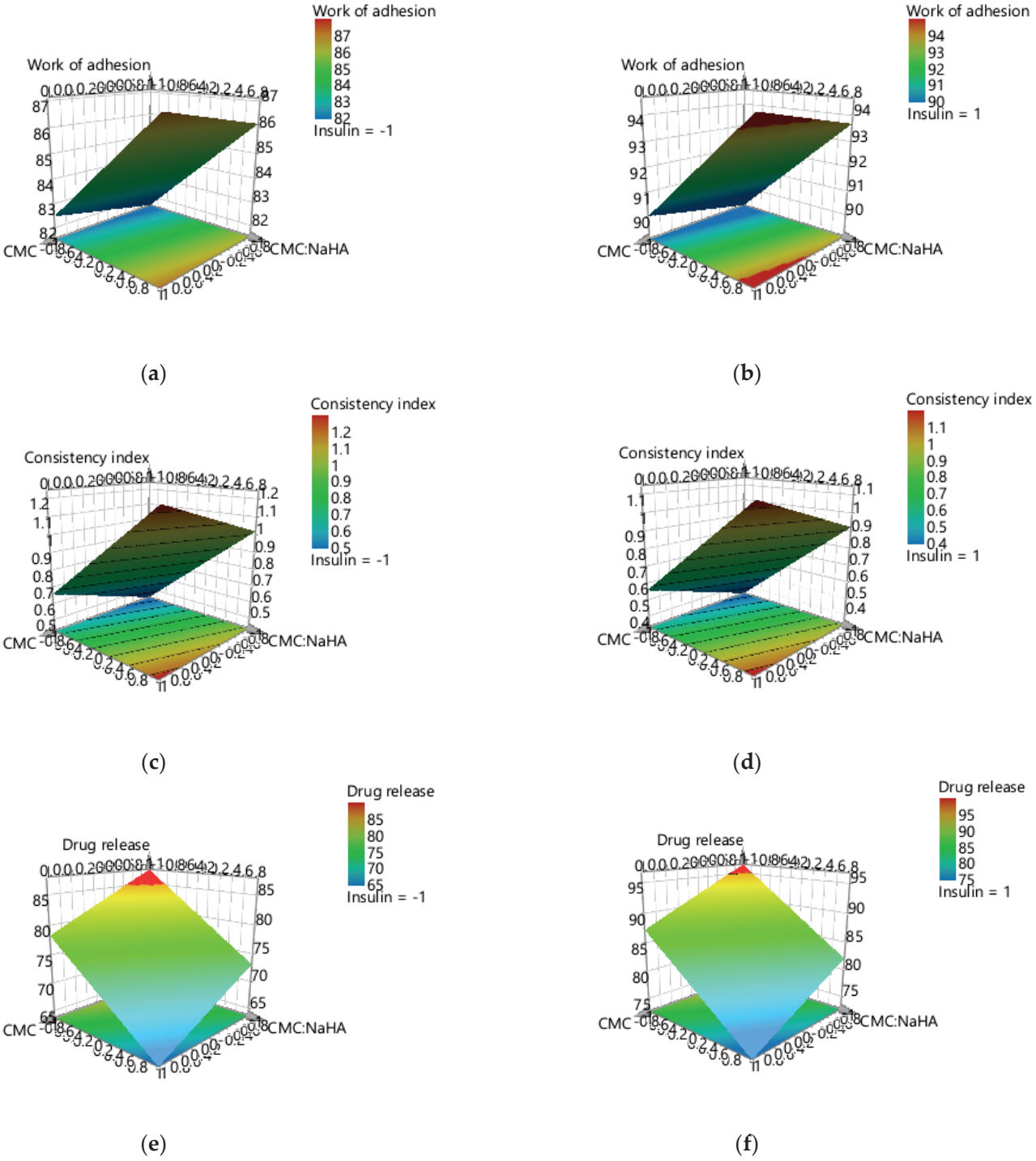

Figure 5. Three-dimensional surface plots representing the three responses when X3 is constant, (**a**) work of adhesion when X3 = −1, (**b**) work of adhesion when X3 = 1, (**c**) consistency index when X3 = −1, (**d**) consistency index when X3 = 1, (**e**) drug release when X3 = −1, (**f**) drug release when X3 = 1.

Minitab statistical software was used to analyze the data and to complete the screening provided by the Modde program, by generating the regression equations and the Pareto charts for each response factor.

The work of adhesion (Y1) was negatively influenced by X2—the ratio between CMC and NaHA based on the regression equation (Equation (1)), where the *p* value is higher

than 0.05 and the F value equals 2.25, although according to the statistical parameters, the model is not significant.

$$Y1 = 74.8 + 0.96X1 - 9.27X2 + 0.753X3 \quad (1)$$

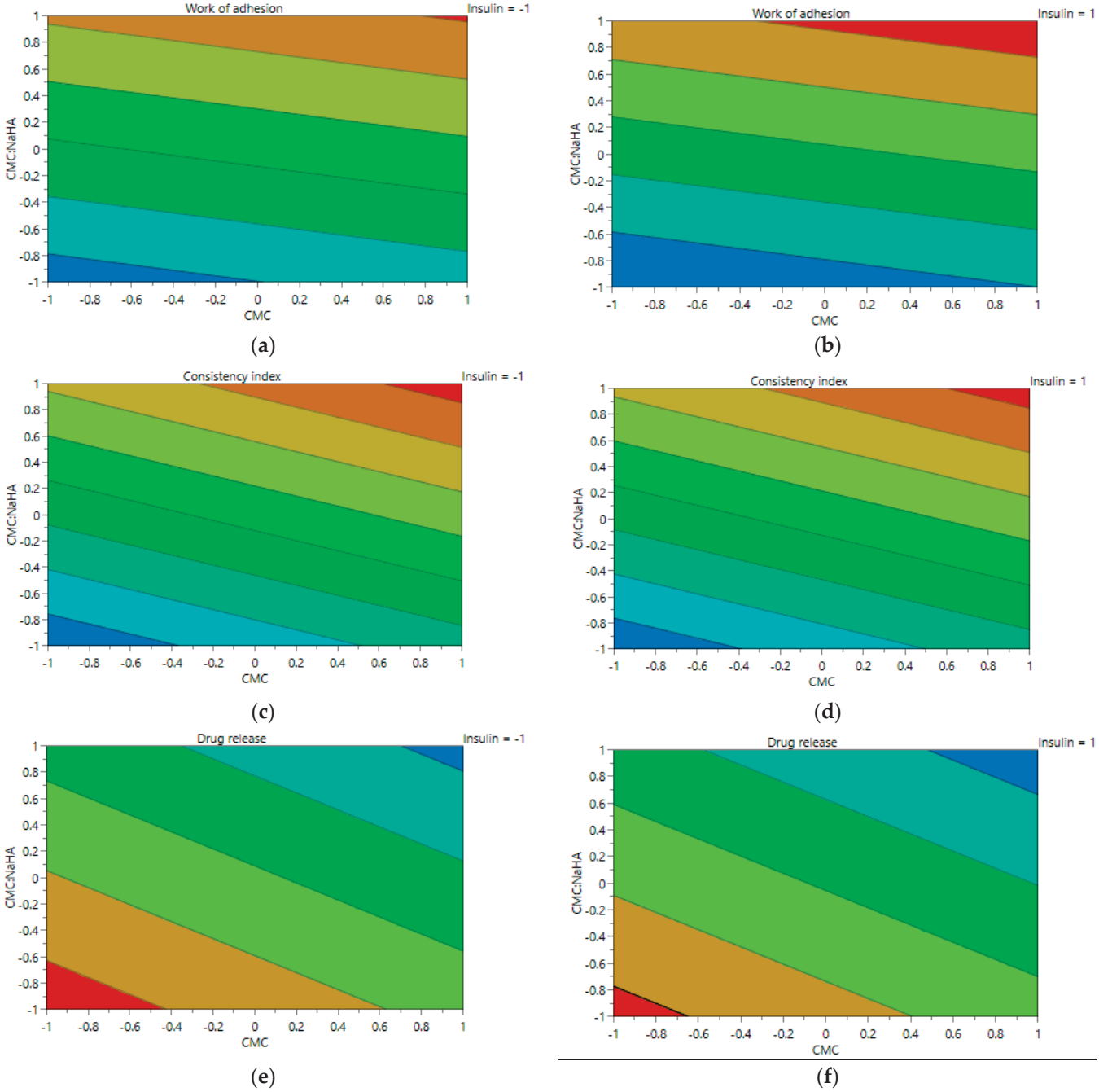

Figure 6. Contour plot for each response parameter, when X3 is constant, (**a**) work of adhesion when X3 = −1, (**b**) work of adhesion when X3 = 1, (**c**) consistency index when X3 = −1, (d) consistency index when X3 = 1, (**e**) drug release when X3 = −1, (**f**) drug release when X3 = 1.

Using a Pareto chart, the standardized effect for the response work of adhesion, explained previously by the linear regression equation, is presented in Figure 7. According to the graph, the main effect on the work of adhesion was given by the amount of insulin loaded in the systems.

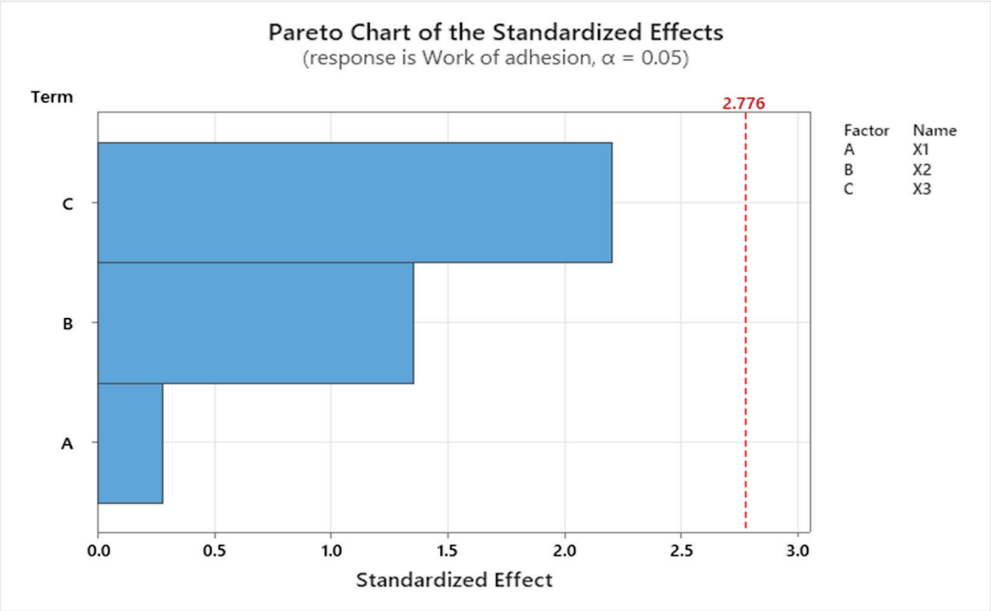

Figure 7. Pareto chart showing the standardized effect of the work of adhesion, where C (X3) is the amount of insulin, B (X2) is the CMC/NaHA ratio, and A (X1) is the CMC concentration.

Regarding the second response, the consistency index (Y2) regression model represented by Equation (2) was significant with a *p* value of 0.016 and F value of 12.76. As it was for Y1, the CMC/NaHA ratio had a negative impact on the consistency index response.

$$Y2 = 1.576 + 0.226X1 - 1.177X2 - 0.0098X3 \quad (2)$$

Figure 8 represents the standardized effect for the consistency index using the Pareto chart, which shows the impact of the formulation variables on the response parameter. It confirms that the ratio between the two polymers had the main impact on the consistency index.

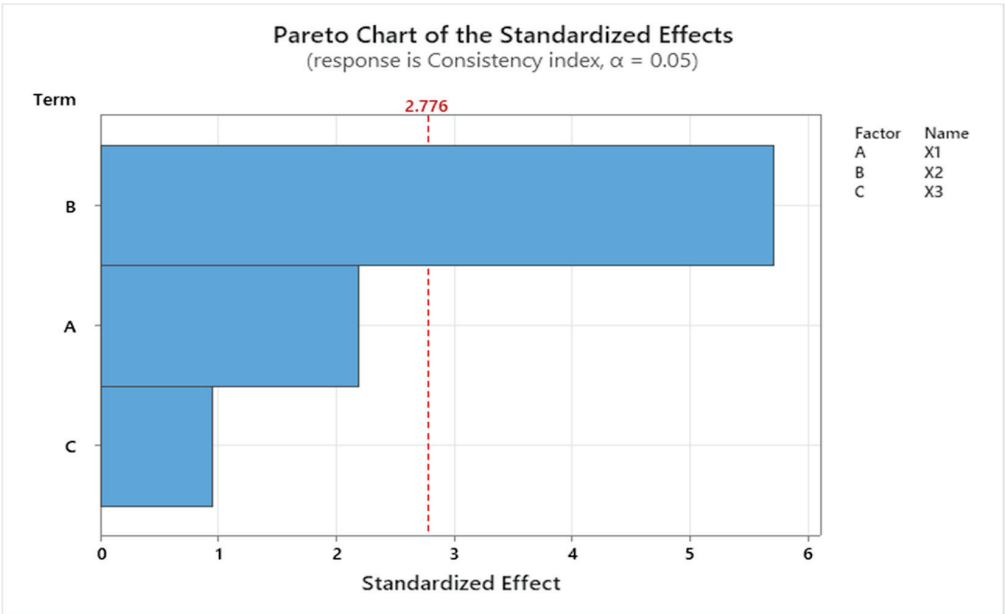

Figure 8. Pareto chart showing the standardized effect of the consistency index, where B (X2) is the CMC/NaHA ratio, A (X1) is the CMC concentration, and C (X3) is the amount of insulin.

Following the mathematical modeling (Equation (3)), the drug-release response (Y3) was significantly influenced by X2—the CMC/NaHA ratio, and negatively influenced by X1—the concentration of CMC. The model analyzed was considered significant, with the *p* value = 0.041 and F value = 7.45.

$$Y3 = 50.0 - 9.47X1 + 29.31X2 + 0.894X3 \quad (3)$$

The impact of the independent variable X2 (CMC/NaHA ratio) on the last response analyzed, Y3—drug release, is confirmed by the Pareto chart (Figure 9), where the standardized effect of the parameters is plotted.

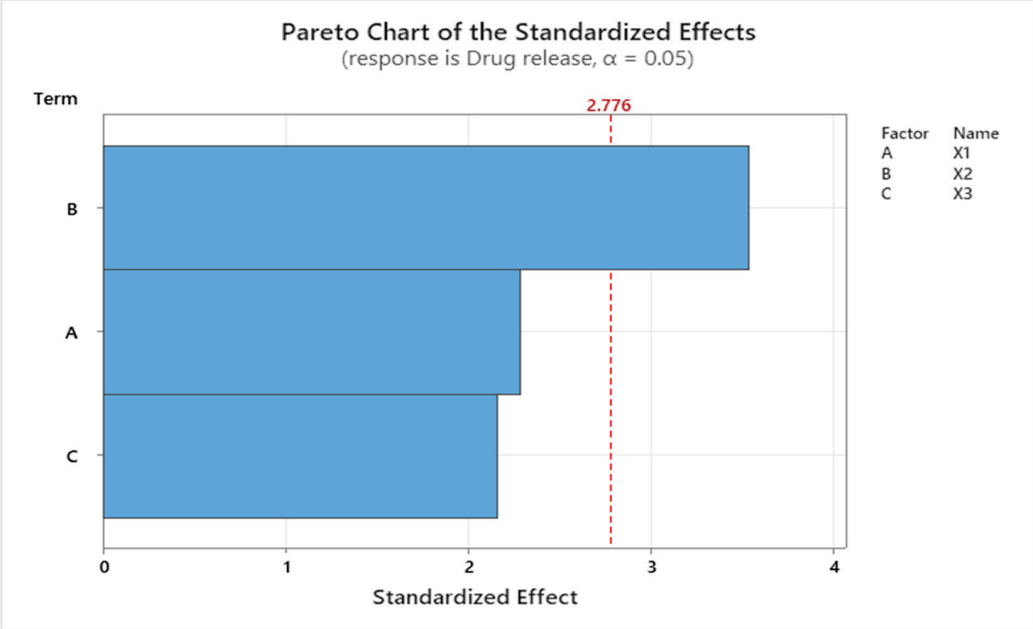

Figure 9. Pareto chart showing the standardized effect of drug release, where B (X2) is the CMC/NaHA ratio, A (X1) is the CMC concentration, and C (X3) is the amount of insulin.

Combining all the interpretations previously mentioned, the importance of each parameter on each response variable can be seen. Based on the variable importance in the projection (Figure 10), it can be concluded that the work of adhesion was influenced by the amount of insulin (X3) and by the CMC/NaHA ratio (X2). For the consistency index response, the ratio between the polymers had a high significance. The CMC/NaHA ratio also had a pronounced meaning regarding the insulin drug release and the other two formulation parameters had similar significance. As noted before, the higher amount of NaHA influenced negatively the release of the active ingredient from the systems.

The use of Design of Experiments (DoE), as part of Quality by Design (QbD) principles, provides an overview of the experiment and performs a screening of the importance of the formulation parameters on the response parameters [54].

The predictive analysis was made with Modde and the optimal setpoint is presented in Table 5, with a probability of failure of 0.23%. Corroborating with the experimental results, samples S5, S7, and S8 scored close to the predicted system regarding the work of adhesion. The value for S7 fit the predicted value best regarding the consistency index. Systems S1, S5, S6, and S7 exceeded the cumulative release percentage compared to the optimal setpoint predicted. In conclusion, S7 is the most eloquent system when compared with the predictive setpoint.

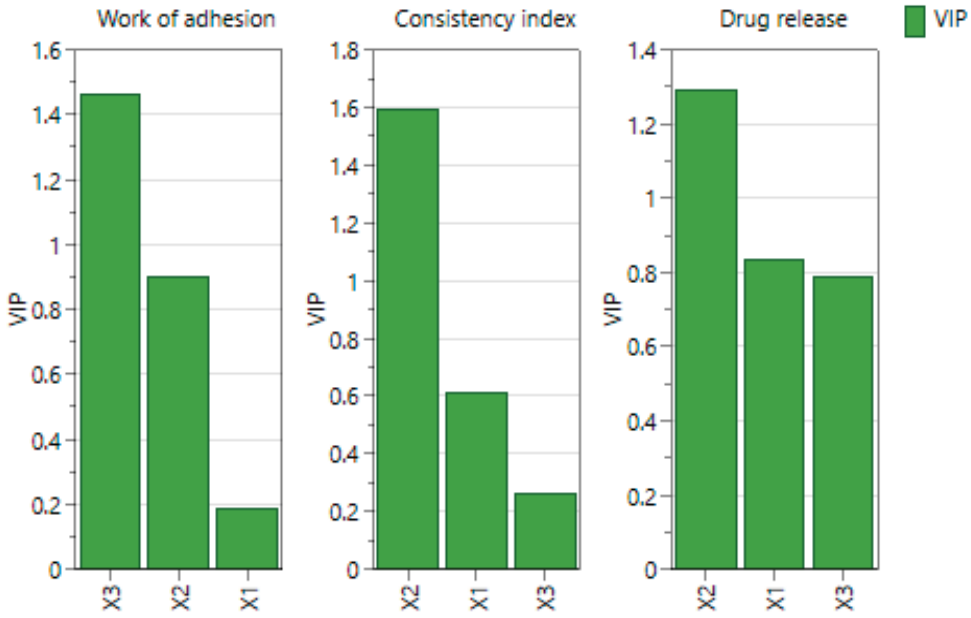

Figure 10. Variable importance in the projection (VIP) of the independent parameters, where X1 is the CMC concentration, X2 is the CMC/NaHA ratio, and X3 is the amount of insulin.

Table 5. Optimal setpoint generated by Modde software.

Response	Optimal Setpoint
Work of adhesion (mN/m)	92.55
Consistency index (Pa·s^n)	0.89
Drug release (%)	81.64

The experimental plan was designed using Modde software, while Minitab software was employed to evaluate the relationship between the formulation variables and the response factors, highlighting the complementary strengths of both tools in the research process.

3. Discussion

The aim of this research was the formulation and the initial evaluation of hydrocolloidal systems containing insulin for intranasal administration, based on the intrinsic properties of CMC and NaHA. The in vitro study was based on the analysis of the influence of the formulation factors and the relationships between them on the work of adhesion and spreading at the level of the nasal mucosa, the flow behavior profiles, and on the cumulative quantity of the released drug.

The samples obtained were homogeneous, with a clear appearance and without impurities. The pH values of the hydrocolloid systems were at the tolerance limit of nasal mucosa [55]; pH lower than 4 would lead to nasal discomfort and damage to the nasal epithelium [56]. Both polymers, CMC and NaHA, are biocompatible with the mucosa and are not toxic [57].

The evaluation of the contact angle provides information about the ability of a liquid to wet a solid surface and its tendency to adhere to the solid. A contact angle lower than 90° indicates a high wetting capacity (wetting fluid) [58,59]. All the studied samples had recorded values of the contact angle lower than 90°, and thus we can state that the formulations obtained have the ability to wet the nasal mucosa.

The surface tension of liquid systems is an important parameter in the development of pharmaceutical products and can provide information about the quality of formulations, the bioavailability, and the absorption of substances [60,61]. The average surface tension of pharmaceutical preparations with intranasal administration is 30.3 mN/m to

44.9 mN/m [61,62]. The determinations made in this experiment showed that S1 had the closest value to the physiological surface tension of nasal mucosa, followed by S3, S6, and S7. However, all the samples had a higher surface tension compared with the average ST of the products with nasal administration.

The formulation of intranasal systems requires the use of tight junction modulators [1] and modulators of viscosity that have mucoadhesive properties [56]. As previously mentioned, both polymers have mucoadhesive properties; they have the ability to enhance the absorption of the active pharmaceutical ingredient through the tight junction of the epithelial mucosa.

Thus, the values obtained for the contact angle and the surface tension were used to calculate the work of adhesion and the work of cohesion, thereby determining the spreading capacity of the liquid formulations, based on the difference between the work of adhesion and the work of cohesion. All of these determinations referred to above are interconnected and help to evaluate the mucoadhesive properties of the hydrocolloidal systems based on adhesion and cohesion forces [63]. Mucoadhesion is defined as the intermolecular interactions between the formulations and the mucosa, quantified in this case by the work of adhesion. The work of cohesion indicates the interactions formed inside the systems, between the components of the product. Regarding the current study, both parameters recorded high values, but analysis from the point of view of the spreading coefficient, in the case of the series with a lower loading of insulin, S1 had a value of the spreading coefficient closer to 0, and for the series with an upper amount of insulin, S7 and S8. According to the literature, a liquid can be classified as spreadable when the contact angle is equal to 0° [64].

The same method was used by Spindler et al. to determine the spreading capacity of 10–30 mg/mL hyaluronate solution for nasal administration. The results indicated that contact angle values were below 90° and the surface tension was 46.82 mN m^{-1}, with a high work of adhesion (over 80 mN m^{-1}), and the spreading capacity was close to zero (-3.5 mN m^{-1} for the lowest concentration and -12.5 mN m^{-1} for the highest) [65].

Additionally, adhesion and cohesion forces can influence the flow behavior and viscosity of the formulations. The flow behavior of the eight systems was pseudoplastic, in accordance with the individual behavior of the polymers involved in the formulation of the hydrocolloidal systems and with other nasal products [66–68], and also with other formulations based on Carbopol, methyl cellulose, and glycerin, which were studied for the intranasal administration of insulin, according to the research of Ostrozka-Cieslik and collaborators [69].

Khodaverdi et al. also reported pseudoplastic behavior in casein-based hydrogel loaded with insulin, in which the viscosity of the systems showed a reduction when the shear rate was increased [70].

Viscosity is an important parameter that influences both the quality of the products and the bioavailability of the active pharmaceutical ingredient [52,71–73]. That is why systems with medium viscosity are preferred, which have an optimal contact time with the nasal mucosa but do not interfere with the physiological mucociliary clearance [74–76]. A high viscosity of solutions can lead to local adverse effects, such as nasal congestion or edema [77].

From the point of view of drug release, the expectation is that it should release rapidly to avoid the wash-out effect from mucociliary movements. The zero-order release kinetics has the advantage that the concentration of the drug is constant during a period of time [78]. All systems had an optimal release during the initial time interval; subsequently, S1 and S5 recorded the highest percentage of cumulative-released insulin, over 90%.

Mohamad et al. recorded a fast insulin release of 15–25% after 10 min and 65–90% after 30 min from hydroxypropyl methyl cellulose and polyvinyl alcohol films that contained insulin for nasal administration [79].

The data reported by Nazar and collaborators describe the in vitro release of insulin from a thermo-responsive gel based on N-trimethyl chitosan chloride, where a burst release was recorded during the first 12 min, with circa 70% insulin release [80].

The study conducted by Muntu et al. showed rapid release of insulin from a nasal powder, using trehalose as a stabilizer, in the first 30 min (49–60%) and a cumulative release of 79–88% after 1 h [81].

According to de Von Zuben et al., who investigated the controlled release of insulin from the liposomes after intranasal administration, in the first 2 h there was immediate release of the insulin, and a rapid effect was obtained [82]. The same researchers reported that the same burst effect was obtained in the first 2 h, based on their study of the comparative release of insulin from insulin solution, hydroxyethylcellulose-based hydrogels with insulin, or HEC-based hydrogel containing insulin-loaded liposomes after nasal administration [68].

In another study, Sharma and collaborators reported that nanoparticles based on chitosan and loaded with insulin for intranasal administration had a cumulative drug release of 93.32%, with a significant burst effect of 22.25% during approximately the first 30 min [83].

Regarding the research performed by other authors, Li et al. described a rapid release of insulin in the first 1 h from deep eutectic solvents for nasal delivery, which combined malic acid and choline chloride, and a total release of 75% after 5 h of experiments [84].

Using the 3D-response surface-plot representation and the contour plot for each response parameter generated by Modde software, combined with the regression equations and Pareto charts generated by Minitab software, the results help show the impact of each parameter on the hydrocolloidal systems. The screening of the experimental design, especially in the initial assessment, provides valuable information regarding the significance of each formulation's factors, the reproducibility, and the validity of the model, and can predict the future experiments. Corroborating all the results obtained with the predicted analysis, the systems with 1% chitosan and CMC/NaHA 1/1 ratio were the most effective, regardless the loading of insulin. Even if the percentage of cumulative release of the active ingredient was high for S1 and S5, the system S7 fit better in the predictive analysis and can be included in future research.

Further studies can be carried out on the hydrocolloidal liquid formulations regarding the administration devices that have advanced from sprays, nebulizers, nasal pumps, or single-dose vials, to innovative systems with precise release at the level of the olfactory region in the nasal cavity (precision olfactory delivery devices) [1,5,55,77,85].

4. Materials and Methods

4.1. Materials

Carboxymethyl chitosan with viscosity 200–300 cPs (1% water) and Sodium Hyaluronate purchased from Sigma Aldrich (Saint Louis, MO, USA). Human insulin (Humulin R 100 UI/mL, Lilly France, Fegersheim, France) was bought from a local pharmacy. Ultrapure distilled water was provided by a Milli-Q water purification system (Merck Millipore, Bedford, MA, USA) and was used as solvent for the preparation of the formulations.

4.2. Preparation of the Hydrocolloidal Systems and Experimental Design

CMC was dissolved in ultrapure distilled water under continuous stirring at room temperature. Solutions of CMC 1% *w*/*v* and 2% *w*/*v* were obtained. The solution of NaHA 1% w/v was obtained by dissolving the NaHA in ultrapure water. After overnight storage of all the solutions in a refrigerator, the final samples were mixed according to the appropriate ratio, and then the insulin solution was added under continuous homogenization. A 2^3 fractional factorial plan was developed, in which there are three independent variables at two levels of variation: X1—concentration of the CMC, X2—the ratio between CMC and NaHA, and X3—the amount of insulin. The design of the experiment is presented in Table 6.

Table 6. Experimental design.

Factors	Independent Variables	Levels of Variation	
		Lower (−1)	Upper (+1)
X1	Carboxymethyl chitosan (% w/v)	1	2
X2	CMC/NaHA ratio	1/1	1/2
X3	Insulin (IU/mL)	20	30

The objective of this research was to develop and characterize the hydrocolloidal systems based on CMC and NaHA for nasal administration of insulin.

4.3. Physico-Chemical Characterization of Hydrocolloidal Systems

4.3.1. Visual Aspect and pH Determination

The formulations obtained were visually examined to observe the aspect, color, and instability (precipitation, separation or other changes), if any, that may have occurred during the preparation.

The pH was determined using a Mettler-Toledo pH meter (Mettler-Toledo GmbH, Im Langacher 44, 8606 Greifensee, Switzerland) at room temperature. Before the determinations, the pH meter was calibrated with buffer solutions at pH 4 and 7. The accuracy of the measurement was ±0.01 pH.

4.3.2. Contact Angle Determination

The contact angle measurements were performed with CAM 101 (KSV Instruments Ltd., Espoo, Finland) equipped with a Hamilton syringe, at room temperature. The sessile drop method was used. The drops at the contact with the solid surface were analyzed using a digital video camera. Based on the images, the CA was automatically calculated using the Young–Laplace method with the software supplied by the producer of the goniometer.

4.3.3. Surface Tension Determination

The surface tension measurement was made following the same technique as presented for CA, but the pedant drop method was used for this parameter. The ST was calculated based on the images of the drops that were captured just before detachment from the needle.

4.3.4. Work of Adhesion, Work of Cohesion, and Spreading Coefficient Determinations Based on Superficial Properties

The adhesion properties of the systems were evaluated using the work of adhesion, which was calculated based on the CA and ST values using the Young–Dupré Equation (4):

$$\mathrm{Wa} = \mathrm{ST}(1 + \mathrm{cosCA}) \quad (4)$$

where Wa is work of adhesion (mN/m), ST is surface tension (mN/m), and CA is contact angle (rad).

The work of cohesion represents the intermolecular bonding between the formulation parameters and can influence the spreading capacity and the viscosity of the systems. It is determined based on Equation (5):

$$\mathrm{Wc} = 2\mathrm{ST} \quad (5)$$

where Wc is work of cohesion (mN/m) and ST is surface tension (mN/m).

The system display of on the nasal mucosa was assessed using the spreading coefficient. Equation (6) was used to obtain the spreading coefficient.

$$\mathrm{S} = \mathrm{Wa–Wc} \quad (6)$$

where S is spreading coefficient (mN/m), Wa is work of adhesion (mN/m), and Wc is work of cohesion (mN/m).

4.3.5. Rheology Analysis

The rheological analysis was performed at 35 ± 0.5 °C with a Lamy RM100 rheometer (Lamy Rheology Instruments, Champagne au Mont d'Or, France) equipped with CP2000 Plus thermostat. A cone-plate CP6020 (2°, 60 mm diameter) was used, and the rotational speed applied was between 0.3 rpm and 60 rpm. The mathematical power law model was applied (Equation (7)), which shows the relation between the shear stress and shear rate, in order to analyze the flow behavior:

$$\tau = K \cdot \dot{\gamma}^{n} \quad (7)$$

where τ is shear stress (Pa), K is consistency index (Pa·s^n), $\dot{\gamma}$ is shear rate (s^{-1}), and n is flow index.

4.4. In Vitro Drug Release

In vitro release rates were evaluated using a Franz-diffusion cell system (Teledyne Hanson Research, Hanson, MA, USA). The experiment was performed at 35 ± 0.5 °C in phosphate-buffered saline (PBS) at pH 7.4. PBS was added in the receptor compartments (7 mL) and stirred with magnetic bars at 300 rpm. The receptor and donor compartments were separated by cellulose acetate membrane diffusion (area 1.77 cm^2). The donor phase contained 20 IU/mL or 30 IU/mL insulin. At predefined times during a period of 2 h, samples were taken from the receptor compartments and were replaced with fresh PBS. The amount of insulin diffused was determined spectrophotometrically at 271 nm. The insulin-release kinetics followed the Higuchi model (Equation (8)), zero-order model (Equation (9)) and power law model (Equation (10)) [72,86], and the cumulative percentage was plotted as a function of time.

Higuchi model:

$$\frac{m_t}{m_\infty} = k \cdot t^{0.5} \quad (8)$$

Zero-order model:

$$\frac{m_t}{m_\infty} = k \cdot t \quad (9)$$

Power law model:

$$\frac{m_t}{m_\infty} = k \cdot t^{n} \quad (10)$$

where $\frac{m_t}{m_\infty}$ is the fraction of drug released at time t, k is the kinetic constant, and n is the release exponent.

4.5. Experimental Design Screening

The influence of the experimental factors on the response parameters was evaluated using Modde statistical software (Version 13.1, Sartorius, Goettingen, Germany) [87]. The partial least squares (PLS) linear method was used to fit the experimental data. The responses were defined as work of adhesion (Y1), consistency index (Y2), and cumulative drug release (Y3). An ANOVA statistical evaluation was performed. A linear regression equation was generated for each response parameter with Minitab software [88] to analyze the influence of the independent factors (X1, X2, and X3) and to generate the Pareto charts, which show the impact of the independent variable on the responses [89].

5. Conclusions

The presented research offers preliminary information regarding the potential use of hydrocolloidal systems in the nasal administration targeting nose-to-brain delivery. The two polymers, CMC and NaHA, were chosen based on their mucoadhesive characteristics, which are sustained by their biocompatibility, biodegradability, and non-toxic properties.

The pH was in the physiological tolerability limit for all eight systems. The wetting capacity of the formulations was confirmed by the CA evaluation, where the values for all the systems were below 90°. The ST values were near the value of the nasal mucosa, especially for S1. The mucoadhesion properties were confirmed by the work of adhesion results for all the formulations. The pseudoplastic behavior obtained for the hydrocolloidal systems is adequate for the products with nasal administration.

The initial assessment also included the in vitro cumulative release of insulin, where S1 and S5 exhibited a high percentage of cumulative release and all the systems had a rapid release of the pharmaceutical active ingredient, which was according to our expectations, but further investigations should be conducted.

According to the results from the two programs used in this research, for the two responses, consistency index and drug release, where the model had statistical significance, the ratio between CMC and NaHA had the main impact on the response variables, and was followed by the concentration of CMC.

The topic addressed in this study, insulin administered intranasally for diseases associated with the central nervous system, is still very broad. Additional studies are still needed to investigate its effects and transport from the nose to the brain. The formulations in this research were preliminarily analyzed in vitro from the point of view of the influence of the formulation factors on their superficial, rheological, and release properties. In order to evaluate the permeation, bioavailability, and toxicology on the systems, these formulations are suitable for further animal and human research.

Author Contributions: Conceptualization, R.P., M.V.G. and L.P.; methodology, R.P., L.P. and M.V.G.; software R.P.; validation, R.P., L.P. and M.V.G.; resources, L.P., M.V.G., V.A. and C.-E.D.-P.; writing—original draft preparation, R.P.; writing—review and editing, L.P., R.P. and M.V.G.; supervision, L.P.; funding acquisition, C.-E.D.-P. and V.A. All authors have read and agreed to the published version of the manuscript.

Funding: This research was funded through the Institutional Program Publish Not Perish—2023.

Institutional Review Board Statement: Not applicable.

Informed Consent Statement: Not applicable.

Data Availability Statement: The data presented in this study are available in the article.

Acknowledgments: This scientific paper was financially supported by the "Carol Davila" University of Medicine and Pharmacy Bucharest through contract CNFIS-FDI-2024-F-0570.

Conflicts of Interest: The authors declare no conflicts of interest.

References

1. Wong, C.Y.J.; Baldelli, A.; Hoyos, C.M.; Tietz, O.; Ong, H.X.; Traini, D. Insulin Delivery to the Brain via the Nasal Route: Unraveling the Potential for Alzheimer's Disease Therapy. *Drug Deliv. Transl. Res.* **2024**, *14*, 1776–1793. [CrossRef] [PubMed]
2. Zakharova, I.O.; Bayunova, L.V.; Avrova, D.K.; Tretyakova, A.D.; Shpakov, A.O.; Avrova, N.F. The Autophagic and Apoptotic Death of Forebrain Neurons of Rats with Global Brain Ischemia Is Diminished by the Intranasal Administration of Insulin: Possible Mechanism of Its Action. *Curr. Issues Mol. Biol.* **2024**, *46*, 6580–6599. [CrossRef] [PubMed]
3. Luo, D.; Ni, X.; Yang, H.; Feng, L.; Chen, Z.; Bai, L. A comprehensive review of advanced nasal delivery: Specially insulin and calcitonin. *Eur. J. Pharm. Sci.* **2023**, *192*, 106630. [CrossRef]
4. Lofts, A.; Abu-Hijleh, F.; Rigg, N.; Mishra, R.K.; Hoare, T. Using the Intranasal Route to Administer Drugs to Treat Neurological and Psychiatric Illnesses: Rationale, Successes, and Future Needs. *CNS Drugs* **2022**, *36*, 739–770. [CrossRef]
5. Smith, K.; Fan, J.; Marriner, G.A.; Gerdes, J.; Kessler, R.; Zinn, K.R. Distribution of insulin in primate brain following nose-to-brain transport. *Alzheimers Dement.* **2024**, *10*, e12459. [CrossRef]
6. Xu, D.; Song, X.J.; Chen, X.; Wang, J.W.; Cui, Y.L. Advances and future perspectives of intranasal drug delivery: A scientometric review. *J. Control. Release* **2024**, *367*, 366–384. [CrossRef]
7. Vohra, M.; Amir, M.; Sharma, A.; Wadhwa, S. Formulation strategies for nose-to-brain drug delivery in Alzheimer's disease. *Health Sci. Rev.* **2023**, *6*, 100075. [CrossRef]
8. Shrewsbury, S.B. The Upper Nasal Space: Option for Systemic Drug Delivery, Mucosal Vaccines and "Nose-to-Brain". *Pharmaceutics* **2023**, *15*, 1720. [CrossRef]

9. Marcello, E.; Chiono, V. Biomaterials-Enhanced Intranasal Delivery of Drugs as a Direct Route for Brain Targeting. *Int. J. Mol. Sci.* **2023**, *24*, 3390. [CrossRef]
10. Ziegler, A.-G.; Danne, T.; Daniel, C.; Bonifacio, E. 100 Years of insulin: Lifesaver, immune target, and potential remedy for prevention. *Med* **2021**, *2*, 1120–1137. [CrossRef]
11. White, M.F.; Kahn, C.R. Insulin action at a molecular level—100 years of progress. *Mol. Metab.* **2021**, *52*, 101304. [CrossRef] [PubMed]
12. Raj, S.K.; Babu, M.R.; Vishwas, S.; Chaitanya, M.V.N.L.; Harish, V.; Gupta, G.; Chellappan, D.K.; Dua, K.; Singh, S.K. An overview of recent advances in insulin delivery and wearable technology for effective management of diabetes. *J. Drug Deliv. Sci. Technol.* **2022**, *75*, 103728. [CrossRef]
13. Gaddam, M.; Singh, A.; Jain, N.; Avanthika, C.; Jhaveri, S.; De la Hoz, I.; Sanka, S.; Goli, S.R. A Comprehensive Review of Intranasal Insulin and Its Effect on the Cognitive Function of Diabetics. *Cureus* **2021**, *13*, e17219. [CrossRef] [PubMed]
14. Gulley, L.D.; Shomaker, L.B.; Kelly, N.R.; Chen, K.Y.; Olsen, C.H.; Tanofsky-Kraff, M.; Yanovski, J.A. Examining cognitive-behavioral therapy change mechanisms for decreasing depression, weight, and insulin resistance in adolescent girls at risk for type 2 diabetes. *J. Psychosom. Res.* **2022**, *157*, 110781. [CrossRef]
15. Shpakov, A.O.; Zorina, I.I.; Derkach, K.V. Hot Spots for the Use of Intranasal Insulin: Cerebral Ischemia, Brain Injury, Diabetes Mellitus, Endocrine Disorders and Postoperative Delirium. *Int. J. Mol. Sci.* **2023**, *24*, 3278. [CrossRef]
16. Dove, A.; Shang, Y.; Xu, W.; Grande, G.; Laukka, E.J.; Fratiglioni, L.; Marseglia, A. The impact of diabetes on cognitive impairment and its progression to dementia. *Alzheimers Dement.* **2021**, *17*, 1769–1778. [CrossRef]
17. Ribaric, S. The Contribution of Type 2 Diabetes to Parkinson's Disease Aetiology. *Int. J. Mol. Sci.* **2024**, *25*, 4358. [CrossRef]
18. Muleiro Alvarez, M.; Cano-Herrera, G.; Martinez, M.F.O.; Gonzales-Portillo, J.V.; Monroy, G.R.; Perez, R.M.; Torres-Rios, J.A.; van Tienhoven, X.A.; Bernot, E.M.G.; Salazar, F.E.; et al. A Comprehensive Approach to Parkinson's Disease: Addressing Its Molecular, Clinical, and Therapeutic Aspects. *Int. J. Mol. Sci.* **2024**, *25*, 7183. [CrossRef]
19. ClinicalTrials.gov. Available online: https://www.clinicaltrials.gov (accessed on 10 July 2024).
20. Schatz, S.; Gutierrez, G.R. Enhancing socio-communicative functions in an MCI patient with intra-nasal insulin: A case report. *Front. Psychiatry* **2024**, *15*, 1326702. [CrossRef]
21. Lioutas, V.A.; Novak, V. Intranasal insulin neuroprotection in ischemic stroke. *Neural Regen. Res.* **2016**, *11*, 400–401. [CrossRef]
22. Benedict, C.; Frey, W.H., II; Schioth, H.B.; Schultes, B.; Born, J.; Hallschmid, M. Intranasal insulin as a therapeutic option in the treatment of cognitive impairments. *Exp. Gerontol.* **2011**, *46*, 112–115. [CrossRef] [PubMed]
23. Adem, M.A.; Decourt, B.; Sabbagh, M.N. Pharmacological Approaches Using Diabetic Drugs Repurposed for Alzheimer's Disease. *Biomedicines* **2024**, *12*, 99. [CrossRef] [PubMed]
24. Craft, S.; Baker, L.D.; Montine, T.J.; Minoshima, S.; Watson, G.S.; Claxton, A.; Arbuckle, M.; Callaghan, M.; Tsai, E.; Plymate, S.R.; et al. Intranasal insulin therapy for Alzheimer disease and amnestic mild cognitive impairment: A pilot clinical trial. *Arch. Neurol.* **2012**, *69*, 29–38. [CrossRef] [PubMed]
25. Kellar, D.; Register, T.; Lockhart, S.N.; Aisen, P.; Raman, R.; Rissman, R.A.; Brewer, J.; Craft, S. Intranasal insulin modulates cerebrospinal fluid markers of neuroinflammation in mild cognitive impairment and Alzheimer's disease: A randomized trial. *Sci. Rep.* **2022**, *12*, 1346. [CrossRef]
26. Saha, P.; Kathuria, H.; Pandey, M.M. Intranasal nanotherapeutics for brain targeting and clinical studies in Parkinson's disease. *J. Control. Release* **2023**, *358*, 293–318. [CrossRef]
27. Fine, J.M.; Stroebel, B.M.; Faltesek, K.A.; Terai, K.; Haase, L.; Knutzen, K.E.; Kosyakovsky, J.; Bowe, T.J.; Fuller, A.K.; Frey, W.H.; et al. Intranasal delivery of low-dose insulin ameliorates motor dysfunction and dopaminergic cell death in a 6-OHDA rat model of Parkinson's Disease. *Neurosci. Lett.* **2020**, *714*, 134567. [CrossRef]
28. Novak, P.; Maldonado, D.A.P.; Novak, V. Safety and preliminary efficacy of intranasal insulin for cognitive impairment in Parkinson disease and multiple system atrophy: A double-blinded placebo-controlled pilot study. *PLoS ONE* **2019**, *14*, e0214364. [CrossRef]
29. Schneider, E.; Spetter, M.S.; Martin, E.; Sapey, E.; Yip, K.P.; Manolopoulos, K.N.; Tahrani, A.A.; Thomas, J.M.; Lee, M.; Hallschmid, M.; et al. The effect of intranasal insulin on appetite and mood in women with and without obesity: An experimental medicine study. *Int. J. Obes.* **2022**, *46*, 1319–1327. [CrossRef]
30. Edwin Thanarajah, S.; Iglesias, S.; Kuzmanovic, B.; Rigoux, L.; Stephan, K.E.; Bruning, J.C.; Tittgemeyer, M. Modulation of midbrain neurocircuitry by intranasal insulin. *Neuroimage* **2019**, *194*, 120–127. [CrossRef]
31. Zhang, H.; Zhao, L.; Li, M.; Li, X.; Li, R.; Wu, D. Efficacy and safety of intranasal insulin on postoperative cognitive dysfunction in elderly patients after laparoscopic radical resection of colorectal cancer: A double-blind pilot study. *Front. Aging Neurosci.* **2024**, *16*, 1375841. [CrossRef]
32. Mantik, K.E.K.; Kim, S.; Gu, B.; Moon, S.; Kwak, H.B.; Park, D.H.; Kang, J.H. Repositioning of Anti-Diabetic Drugs against Dementia: Insight from Molecular Perspectives to Clinical Trials. *Int. J. Mol. Sci.* **2023**, *24*, 11450. [CrossRef] [PubMed]
33. Novak, V.; Mantzoros, C.S.; Novak, P.; McGlinchey, R.; Dai, W.; Lioutas, V.; Buss, S.; Fortier, C.B.; Khan, F.; Becerra, L.A.; et al. MemAID: Memory advancement with intranasal insulin vs. placebo in type 2 diabetes and control participants: A randomized clinical trial. *J. Neurol.* **2022**, *269*, 4817–4835. [CrossRef] [PubMed]
34. Schmid, V.; Kullmann, S.; Gfrorer, W.; Hund, V.; Hallschmid, M.; Lipp, H.P.; Haring, H.U.; Preissl, H.; Fritsche, A.; Heni, M. Safety of intranasal human insulin: A review. *Diabetes Obes. Metab.* **2018**, *20*, 1563–1577. [CrossRef] [PubMed]

35. Craft, S.; Raman, R.; Chow, T.W.; Rafii, M.S.; Sun, C.K.; Rissman, R.A.; Donohue, M.C.; Brewer, J.B.; Jenkins, C.; Harless, K.; et al. Safety, Efficacy, and Feasibility of Intranasal Insulin for the Treatment of Mild Cognitive Impairment and Alzheimer Disease Dementia: A Randomized Clinical Trial. *JAMA Neurol.* **2020**, *77*, 1099–1109. [CrossRef]
36. Kupila, A.; Sipila, J.; Keskinen, P.; Simell, T.; Knip, M.; Pulkki, K.; Simell, O. Intranasally administered insulin intended for prevention of type 1 diabetes—A safety study in healthy adults. *Diabetes Metab. Res. Rev.* **2003**, *19*, 415–420. [CrossRef]
37. Kashyap, B.; Hanson, L.R.; Frey, W.H., II. Intranasal Insulin: A Treatment Strategy for Addiction. *Neurotherapeutics* **2020**, *17*, 105–115. [CrossRef]
38. Hamidovic, A. Targeting Mediators of Smoking Persistence with Intranasal Insulin. *Front. Pharmacol.* **2017**, *8*, 706. [CrossRef]
39. Wang, X.; Chen, Y.; Dong, J.; Ge, J.; Liu, X.; Liu, J. Neurobiology of Stress-Induced Nicotine Relapse. *Int. J. Mol. Sci.* **2024**, *25*, 1482. [CrossRef]
40. Hamidovic, A.; Khafaja, M.; Brandon, V.; Anderson, J.; Ray, G.; Allan, A.M.; Burge, M.R. Reduction of smoking urges with intranasal insulin: A randomized, crossover, placebo-controlled clinical trial. *Mol. Psychiatry* **2017**, *22*, 1413–1421. [CrossRef]
41. Hallschmid, M. Intranasal insulin. *J. Neuroendocrinol.* **2021**, *33*, e12934. [CrossRef]
42. Pang, H.T.; Chen, X.G.; Park, H.J.; Cha, D.S.; Kennedy, J.F. Preparation and rheological properties of deoxycholate-chitosan and carboxymethyl-chitosan in aqueous systems. *Carbohydr. Polym.* **2007**, *69*, 419–425. [CrossRef]
43. Geng, Y.; Xue, H.; Zhang, Z.; Panayi, A.C.; Knoedler, S.; Zhou, W.; Mi, B.; Liu, G. Recent advances in carboxymethyl chitosan-based materials for biomedical applications. *Carbohydr. Polym.* **2023**, *305*, 120555. [CrossRef] [PubMed]
44. Upadhyaya, L.; Singh, J.; Agarwal, V.; Tewari, R.P. Biomedical applications of carboxymethyl chitosans. *Carbohydr. Polym.* **2013**, *91*, 452–466. [CrossRef]
45. Irimia, T. Contributions on Formulation and Preliminary Evaluation of Ocular Colloidal Systems of Chitosan and Poloxamer 407 with Bupivacaine Hydrochloride. *Farmacia* **2019**, *67*, 702–708. [CrossRef]
46. Popa, L.; Ghica, M.V.; Dinu-Pirvu, C.E. Periodontal Chitosan-Gels Designed for Improved Local Intra-Pocket Drug Delivery. *Farmacia* **2013**, *61*, 240–250.
47. Alhowyan, A.A.; Kalam, M.A.; Iqbal, M.; Raish, M.; El-Toni, A.M.; Alkholief, M.; Almomen, A.A.; Alshamsan, A. Mesoporous Silica Nanoparticles Coated with Carboxymethyl Chitosan for 5-Fluorouracil Ocular Delivery: Characterization, In Vitro and In Vivo Studies. *Molecules* **2023**, *28*, 1260. [CrossRef]
48. Mourya, V.K.; Inamdara, N.; Tiwari, N.A. Carboxymethyl Chitosan and Its Applications. *Adv. Mater. Lett.* **2010**, *1*, 11–33. [CrossRef]
49. Islam, M.M.; Islam, R.; Hassan, S.M.M.; Karim, M.R.; Rahman, M.M.; Rahman, S.; Hossain, M.N.; Islam, D.; Shaikh, M.A.A.; Georghiou, P.E. Carboxymethyl chitin and chitosan derivatives: Synthesis, characterization and antibacterial activity. *Carbohydr. Polym. Technol. Appl.* **2023**, *5*, 100283. [CrossRef]
50. Horvat, S.; Feher, A.; Wolburg, H.; Sipos, P.; Veszelka, S.; Toth, A.; Kis, L.; Kurunczi, A.; Balogh, G.; Kurti, L.; et al. Sodium hyaluronate as a mucoadhesive component in nasal formulation enhances delivery of molecules to brain tissue. *Eur. J. Pharm. Biopharm.* **2009**, *72*, 252–259. [CrossRef]
51. Cuomo, F.; de Nigris, A.; Zeppa, L.; Lopez, F.; Ambrosone, L. Viscosimetric properties of sodium hyaluronate and hypromellose solutions for medical devices. *J. Mol. Liq.* **2024**, *398*, 124182. [CrossRef]
52. Anicescu, M.C.; Dinu-Pirvu, C.E.; Talianu, M.T.; Ghica, M.V.; Anuta, V.; Prisada, R.M.; Nicoara, A.C.; Popa, L. Insights from a Box-Behnken Optimization Study of Microemulsions with Salicylic Acid for Acne Therapy. *Pharmaceutics* **2022**, *14*, 174. [CrossRef] [PubMed]
53. Tudoroiu, E.-E.; Kaya, M.G.A.; Titorencu, I.; Dinu-Pîrvu, C.E.; Marin, M.M.; Roșca, A.-M.; Popa, L.; Anuța, V.; Antoniac, A.; Chelaru, C.; et al. Design and evaluation of new wound dressings based on collagen-cellulose derivatives. *Mater. Des.* **2023**, *236*, 112469. [CrossRef]
54. Popa, L.; Ghica, M.V.; Popescu, R.; Irimia, T.; Dinu-Pîrvu, C.-E. Development and Optimization of Chitosan-Hydroxypropyl Methylcellulose In Situ Gelling Systems for Ophthalmic Delivery of Bupivacaine Hydrochloride. *Processes* **2021**, *9*, 1694. [CrossRef]
55. Marx, D.; Williams, G.; Birkhoff, M. Intranasal Drug Administration—An Attractive Delivery Route for Some Drugs. In *Drug Discovery and Development—From Molecules to Medicine*; IntechOpen Limited: London, UK, 2015. [CrossRef]
56. Pires, P.C.; Rodrigues, M.; Alves, G.; Santos, A.O. Strategies to Improve Drug Strength in Nasal Preparations for Brain Delivery of Low Aqueous Solubility Drugs. *Pharmaceutics* **2022**, *14*, 588. [CrossRef]
57. Popescu, R.; Ghica, M.V.; Dinu-Pirvu, C.E.; Anuta, V.; Lupuliasa, D.; Popa, L. New Opportunity to Formulate Intranasal Vaccines and Drug Delivery Systems Based on Chitosan. *Int. J. Mol. Sci.* **2020**, *21*, 5016. [CrossRef]
58. Behnoudfar, D.; Dragila, M.I.; Meisenheimer, D.; Wildenschild, D. Contact angle hysteresis: A new paradigm? *Adv. Water Resour.* **2022**, *161*, 104138. [CrossRef]
59. Yuan, Y.; Lee, T.R. Contact Angle and Wetting Properties. In *Surface Science Techniques*; Springer: Heidelberg, Germany, 2013; pp. 3–34. [CrossRef]
60. Chen, H.; Muros-Cobos, J.L.; Holgado-Terriza, J.A.; Amirfazli, A. Surface tension measurement with a smartphone using a pendant drop. *Colloids Surf. A Physicochem. Eng. Asp.* **2017**, *533*, 213–217. [CrossRef]
61. Li, Y.; Shi, J.; Zhang, X.; Ji, M.; Ni, Y.; Han, R.; Li, Z.; Xiong, Y.; Tu, J.; He, D.; et al. Exploration of surface tension measurement methods for pharmaceutical excipients. *Int. J. Pharm.* **2024**, *655*, 123848. [CrossRef]

62. Han, K.; Woghiren, O.E.; Priefer, R. Surface tension examination of various liquid oral, nasal, and ophthalmic dosage forms. *Chem. Cent. J.* **2016**, *10*, 31. [CrossRef]
63. Von Fraunhofer, J.A. Adhesion and cohesion. *Int. J. Dent.* **2012**, *2012*, 951324. [CrossRef]
64. Marshall, S.J.; Bayne, S.C.; Baier, R.; Tomsia, A.P.; Marshall, G.W. A review of adhesion science. *Dent. Mater.* **2010**, *26*, e11–e16. [CrossRef] [PubMed]
65. Spindler, L.M.; Serpetsi, S.; Flamm, J.; Feuerhake, A.; Böhler, L.; Pravda, M.; Borchers, K.; Tovar, G.E.M.; Schindowski, K.; Gruber-Traub, C. Hyaluronate spreading validates mucin-agarose analogs as test systems to replace porcine nasal mucosa explants: An experimental and theoretical investigation. *Colloids Surf. B Biointerfaces* **2022**, *217*, 112689. [CrossRef]
66. Sosnowski, T.R.; Rapiejko, P.; Sova, J.; Dobrowolska, K. Impact of physicochemical properties of nasal spray products on drug deposition and transport in the pediatric nasal cavity model. *Int. J. Pharm.* **2020**, *574*, 118911. [CrossRef] [PubMed]
67. Eccleston, G.M.; Bakhshaee, M.; Hudson, N.E.; Richards, D.H. Rheological behavior of nasal sprays in shear and extension. *Drug Dev. Ind. Pharm.* **2000**, *26*, 975–983. [CrossRef]
68. Von Zuben, E.S.; Eloy, J.O.; Inacio, M.D.; Araujo, V.H.S.; Baviera, A.M.; Gremiao, M.P.D.; Chorilli, M. Hydroxyethylcellulose-Based Hydrogels Containing Liposomes Functionalized with Cell-Penetrating Peptides for Nasal Delivery of Insulin in the Treatment of Diabetes. *Pharmaceutics* **2022**, *14*, 2492. [CrossRef]
69. Ostrozka-Cieslik, A.; Maciazek-Jurczyk, M.; Pozycka, J.; Dolinska, B. Pre-Formulation Studies: Physicochemical Characteristics and In Vitro Release Kinetics of Insulin from Selected Hydrogels. *Pharmaceutics* **2021**, *13*, 1215. [CrossRef]
70. Khodaverdi, E.; Maftouhian, S.; Aliabadi, A.; Hassanzadeh-Khayyat, M.; Mohammadpour, F.; Khameneh, B.; Hadizadeh, F. Casein-based hydrogel carrying insulin: Preparation, in vitro evaluation and in vivo assessment. *J. Pharm. Investig.* **2018**, *49*, 635–641. [CrossRef]
71. Alabdly, A.A.; Kassab, H.J. Rheological characterization, In vitro release, and Ex vivo permeation of Nefopam Thermosensitive and mucoadhesive intranasal in situ gel. *J. Pharm. Negat. Results* **2022**, *13*, 715–726.
72. Ghica, M.V.; Albu, M.G.; Dinu-Pîrvu, C.; Moisescu, Ş. In vitro kinetic release and flow behaviour of some collagen-minocycline topical hydrogels. *Rev. De Chim.* **2012**, *9*, 929–935.
73. Maaz, A.; Blagbrough, I.S.; De Bank, P.A. In Vitro Evaluation of Nasal Aerosol Depositions: An Insight for Direct Nose to Brain Drug Delivery. *Pharmaceutics* **2021**, *13*, 1079. [CrossRef]
74. Popescu, R.; Dinu-Pîrvu, C.E.; Ghica, M.V.; Anuța, V.; Popa, L. Development and preliminary evaluation of intranasal hydrocolloidal systems based on chitosan and PVA with insulin, for central nervous system-associated diseases. *Farmacia* **2024**, *72*, 963–974.
75. Singh, S.K.; Rajoria, K.; Kumar, A.; Sharma, S. A double-blind controlled clinical trial to evaluate the effects of nasal therapy with *Vrihatajivakadya* oil on different viscosities in patients with migraine. *J. Ayurveda Integr. Med.* **2023**, *14*, 100662. [CrossRef] [PubMed]
76. De Barros, C.; Portugal, I.; Batain, F.; Portella, D.; Severino, P.; Cardoso, J.; Arcuri, P.; Chaud, M.; Alves, T. Formulation, design and strategies for efficient nanotechnology-based nasal delivery systems. *RPS Pharm. Pharmacol. Rep.* **2022**, *1*, rqac003. [CrossRef]
77. Wong, C.Y.J.; Baldelli, A.; Tietz, O.; van der Hoven, J.; Suman, J.; Ong, H.X.; Traini, D. An overview of in vitro and in vivo techniques for characterization of intranasal protein and peptide formulations for brain targeting. *Int. J. Pharm.* **2024**, *654*, 123922. [CrossRef]
78. Zhao, Y.N.; Xu, X.; Wen, N.; Song, R.; Meng, Q.; Guan, Y.; Cheng, S.; Cao, D.; Dong, Y.; Qie, J.; et al. A Drug Carrier for Sustained Zero-Order Release of Peptide Therapeutics. *Sci. Rep.* **2017**, *7*, 5524. [CrossRef]
79. Mohamad, S.A.; Badawi, A.M.; Mansour, H.F. Insulin fast-dissolving film for intranasal delivery via olfactory region, a promising approach for the treatment of anosmia in COVID-19 patients: Design, in-vitro characterization and clinical evaluation. *Int. J. Pharm.* **2021**, *601*, 120600. [CrossRef]
80. Nazar, H.; Caliceti, P.; Carpenter, B.; El-Mallah, A.I.; Fatouros, D.G.; Roldo, M.; van der Merwe, S.M.; Tsibouklis, J. A once-a-day dosage form for the delivery of insulin through the nasal route: In vitro assessment and in vivo evaluation. *Biomater. Sci.* **2013**, *1*, 306–314. [CrossRef]
81. Muntu, C.M.; Avanti, C.; Hayun; Surini, S. Promising brain biodistribution of insulin via intranasal dry powder for nose-to-brain delivery. *Heliyon* **2024**, *10*, e33657. [CrossRef]
82. De Souza Von Zuben, E.; Eloy, J.O.; Araujo, V.H.S.; Gremião, M.P.D.; Chorilli, M. Insulin-loaded liposomes functionalized with cell-penetrating peptides: Influence on drug release and permeation through porcine nasal mucosa. *Colloids Surf. A Physicochem. Eng. Asp.* **2021**, *622*, 126624. [CrossRef]
83. Sharma, A.; Mishra, S.S. Preparation and Characterization of Chitosan Nanoparticles of Insulin for Nasal Delivery. *J. Drug Deliv. Ther.* **2018**, *8*, 400–406.
84. Li, Y.; Wu, X.; Zhu, Q.; Chen, Z.; Lu, Y.; Qi, J.; Wu, W. Improving the hypoglycemic effect of insulin via the nasal administration of deep eutectic solvents. *Int. J. Pharm.* **2019**, *569*, 118584. [CrossRef] [PubMed]
85. Wingrove, J.; Swedrowska, M.; Scherliess, R.; Parry, M.; Ramjeeawon, M.; Taylor, D.; Gauthier, G.; Brown, L.; Amiel, S.; Zelaya, F.; et al. Characterisation of nasal devices for delivery of insulin to the brain and evaluation in humans using functional magnetic resonance imaging. *J. Control. Release* **2019**, *302*, 140–147. [CrossRef] [PubMed]
86. Ioan, D.C.; Rau, I.; Kaya, M.G.A.; Radu, N.; Bostan, M.; Zgarian, R.G.; Tihan, G.T.; Dinu-Pirvu, C.E.; Lupuliasa, A.; Ghica, M.V. Ciprofloxacin-Collagen-Based Materials with Potential Oral Surgical Applications. *Polymers* **2020**, *12*, 1915. [CrossRef] [PubMed]

87. MODDE®. Available online: https://www.sartorius.com/en/products/process-analytical-technology/data-analytics-software/doe-software/modde (accessed on 1 May 2020).
88. Minitab. Available online: https://www.minitab.com/en-us/ (accessed on 16 June 2024).
89. Javed, M.N.; Alam, M.S.; Waziri, A.; Pottoo, F.H.; Yadav, A.K.; Hasnain, M.S.; Almalki, F.A. QbD Applications for the Development of Nanopharmaceutical Products. In *Pharmaceutical Quality by Design*; Academic Press: Cambridge, MA, USA, 2019; pp. 229–253. [CrossRef]

International Journal of
Molecular Sciences

MDPI

Article

Chitosan-Based Beads Incorporating Inorganic–Organic Composites for Copper Ion Retention in Aqueous Solutions

Andreea Miron [1,2,†], Tanta-Verona Iordache [1,†], Artur J. M. Valente [3], Luisa Maria Rocha Durães [4], Andrei Sarbu [1], Georgeta Ramona Ivan [1], Anamaria Zaharia [1], Teodor Sandu [1], Horia Iovu [2] and Anita-Laura Chiriac [1,*]

[1] Advanced Polymer Materials and Polymer Recycling Group, National Institute for Research & Development in Chemistry and Petrochemistry ICECHIM, Spl. Independentei 202, 6th District, 060021 Bucharest, Romania; andreea.miron@icechim.ro (A.M.); tanta-verona.iordache@icechim.ro (T.-V.I.); andrei.sarbu@icechim.ro (A.S.); georgeta.ivan@icechim.ro (G.R.I.); anamaria.zaharia@icechim.ro (A.Z.); teodor.sandu@icechim.ro (T.S.)
[2] Advanced Polymer Materials Group, National University of Science and Technology Politehnica Bucharest, 1–7 Gh. Polizu Street, 011061 Bucharest, Romania; horia.iovu@upb.ro
[3] CQC-IMS, Department of Chemistry, University of Coimbra, Rua Larga, 3004-535 Coimbra, Portugal; avalente@ci.uc.pt
[4] CIEPQPF, Department of Chemical Engineering, University of Coimbra, Rua Sílvio Lima, 3030-790 Coimbra, Portugal; luisa@eq.uc.pt
* Correspondence: anita-laura.radu@icechim.ro; Tel.: +40-723-599-783
† These authors contributed equally to this work.

Abstract: In recent years, there has been a challenging interest in developing low-cost biopolymeric materials for wastewater treatment. In the present work, new adsorbents, based on different types of chitosan (commercial, commercial chitin-derived chitosan and chitosan synthesized from shrimp shell waste) and inorganic–organic composites have been evaluated for copper ions removal. The efficacy of the synthesis of chitosan-based composite beads has been determined by studying various characteristics using several techniques, including FTIR spectroscopy, X-ray diffraction, porosimetry (N_2 adsorption), and scanning electron microscopy (SEM). Adsorption kinetics was performed using different adsorption models to determine the adsorption behavior of the materials in the aqueous media. For all composite beads, regardless of the type of chitosan used, good capacity to remove copper ions from simulated waters was observed (up to 17 mg/g), which proves that the new materials hold potential for heavy metal retention. However, the adsorption efficiency was influenced by the type of chitosan used. Thus, for the series where commercial chitosan (CC) was used, the removal efficiency was approximately 29%; for the series with chitosan obtained from commercial chitin (SC), the removal efficiency was approximately 34%; for the series with chitosan enriched with $CaCO_3$ (SH), the removal efficiency was approximately 52%.

Keywords: chitosan; inorganic–organic composites; polymeric beads adsorbents; water treatment; Cu^{2+} removal

1. Introduction

Pollution, in general terms, is a process of introducing toxic substances into the environment, causing devastating effects on ecosystems. In general, pollutants can be classified into several categories—chemical, biological, and natural chemical—and are derived from several sources such as anthropogenic activities, hazardous waste generation, or industrial emissions. Pollution is a factor that has a negative impact on the quality of water sources as well as air and soil. Water is an extremely important resource for sustaining life on Earth [1,2]. Due to increasing population density, industrial development and technology, water pollution has become a serious global problem. In this context, the rapid expansion of communities and industrial development near waterways has led

to increased environmental hazards, especially due to heavy metal pollution. Therefore, contamination of water sources, with concentrations above the maximum limits allowed under the legislation, is mainly due to agricultural activities but also industrial activities (mining, metallurgy, refineries, etc.). Among the most harmful heavy metals, Cd^{2+}, Zn^{2+}, Cr^{3+}, Ni^{2+}, Pb^{2+} and Mn^{2+} can be mentioned [2,3]. The legislation lays down maximum limits for the discharge of wastewater into the aquatic environment, but these limits are often exceeded due to inefficient treatment of water from industrial activities [4]. In addition to anthropogenic activities (industry, mining, agriculture, etc.), natural processes such as volcanic eruptions, grinding of rocks with metal content, and forest fires are also responsible for contaminating the aquatic and terrestrial ecosystem with heavy metals [5]. The major problem of heavy metal contamination is the multiple routes through which such pollutants enter the human body, i.e., direct ingestion, skin absorption, and inhalation through the mouth and nose [6]. From water, heavy metals most often enter the human body through ingestion or dermal absorption [7].

Among the main techniques used to remove heavy metal ions from wastewater, we can mention ion exchange [8], membrane filtration techniques [9], chemical precipitation [10], electrochemical treatment technology, biological treatment, and adsorption [11,12]. Nevertheless, all these techniques have advantages and disadvantages; the most notable disadvantages are high production costs, generation of potentially hazardous waste, and high energy costs [11]. Adsorption using adsorbent materials can overtake some of those drawbacks. Adsorption is one of the most common treatments widely applied in industry to remove heavy metals from water. Recent studies have shown a great interest of researchers in the production of inexpensive and environmentally friendly adsorbent materials. Several classes of adsorbents are presented in the literature that are effectively used to remove heavy metals from water [13,14]. Among them, commercially available adsorbents such as graphene and carbon nanotubes can be mentioned [15]. Yet, their high adsorption properties do not seem to balance their high price. Thus, farther research was directed towards the production of more cost-effective adsorbent materials ranging from natural adsorbents such as zeolites, titanium dioxide, or silica, to waste-derived adsorbents (using eggshells, fruit/vegetable peels, shellfish carcasses but also industrial waste such as red mud and ash [16]).

Inorganic structures such as silica, zeolites, titania, alumina, and carbon derivatives (carbon nanotubes, activated carbon, graphene oxide) have also been used as adsorbents due to their properties such as thermal and mechanical stability, porosity, the orderly structure that inorganic structures generally possess and the relatively easy to adjust size and shape [17]. In addition, their abundance in nature together with the recent industrial development has led to the wide use of these inorganic structures as adsorbents [18]. On the other hand, the major problem with the use of inorganic materials is the disposal of waste, generally requiring the use of chemicals and generating hazardous waste that is dangerous to the environment [19]. Yet, recent studies have shown that the use of composites instead of the inorganic material alone is more efficient and may reduce the amount of waste after treatment, especially because the waste materials can be collected and reconditioned for reuse [20–23]. Other notable advantages of using composites are given by the increased surface area, resulting in higher affinity or selectivity for a target ion, and improved textural characteristics and mechanical properties, such as elasticity [24].

In recent years, chitosan (CC), a chitin-derived polysaccharide, has been reported as a promising biopolymer for the development of adsorbents due to its properties such as biodegradability, low price and abundance in nature [25,26]. Chitosan is obtained most often by the chemical deacetylation of chitin, this being found in the exoskeleton of marine crustaceans such as shrimps, crayfish, lobsters, and crabs. Therefore, the cheapest way to obtain chitosan is by recovering waste carcasses from the food industry. This action can have a double environmental effect: (1) reuse of waste to obtain new materials; and (2) use of the materials to treat wastewater [27]. Furthermore, the literature has provided information about the ability of chitosan alone to remove a wide variety of heavy metals

such as cadmium, nickel, copper, and chromium [28]. This is mainly due to hydroxyl and amino groups occurring in the chitosan structure, available to form strong coordination bonds with metal ions. However, biopolymers such as chitosan have their limitations in terms of thermal and mechanical resistance. Therefore, it is mandatory to combine biopolymers with other materials that can improve the targeted properties of the final adsorbent [29,30]. In this respect, inorganic materials are some of the most used reinforcing components for improving the features of thus formed composites [24]. For instance, Hasan et al. [31] obtained polymer composite beads based on chitosan and perlite for the removal of Cu^{2+} from wastewater. Their study has demonstrated that the adsorption capacity for Cu^{2+} was approximately 104 mg/g, at pH 4.5.

The interest in developing new materials capable of absorbing copper has been driven by the fact that copper is a valuable and widely used metal [16,32], but, at the same time, when present in the environment in excessive amounts, it can have harmful effects on ecosystems and human health [33]. Long-term exposure of the human body to high concentrations of copper has been associated with adverse health effects including gastrointestinal disorders, tachycardia, respiratory problems, insomnia [34]. As a result, the European Union, through the World Health Organization (WHO), has enforced the maximum acceptable limit of copper in drinking water at 2 mg/L. Thus, industries should explore new and efficient methods of treating the effluents resulting from their activities in order to meet these legislative requirements [2,16]. In this context, the goal of the present paper was to develop polymeric beads based on chitosan and inorganic–organic composites for advanced treatment of waters containing heavy metal ions, with particular focus on Cu^{2+} removal. In an original attempt, the beads prepared in this study were obtained with a titanium oxide–polyacrylonitrile inorganic–organic composite, prepared by a host–guest method [35] for obtaining intermediates for titanium nitride. The use of this type of filler material for preparing chitosan-based beads as adsorbent materials for Cu^{2+} is described herein for the first time. The samples were first characterized to determine the influence of the chitosan type and the filler percentage on the structure, morphology, specific surface area, pore size and volume. However, the following adsorption assays helped clarify the mechanism for Cu^{2+} retention by fitting the data to several kinetic adsorption models.

2. Results and Discussion

2.1. Synthesis of Composite Beads

For a better understanding of the influence of chitosan type and filler percentage on bead properties, studies were performed using three types of chitosan (commercial chitosan—CC, chitosan obtained from commercial chitin—SC and chitosan obtained from shrimp carcasses waste containing native minerals—SH) with different inorganic–organic composite ratios (10% and 33%, respectively). The samples are designated as X-Ti_PAN Y% where X represents the type of chitosan used (CC, SC, or SH) and Y the percentage of the titanium oxide–polyacrylonitrile composite filler.

2.1.1. Structure Evaluation of Composite Beads

To emphasize the distinct groups in the chitosan-based beads, Figure 1a compares the FTIR spectra of the three series of beads with that of titanium oxide- polyacrylonitrile filler alone. Studies involving beads with different filler ratios were carried out and several similarities between the beads were observed.

According to the literature, the typical bands for the functional groups of chitosan are observed at 2924–2874 cm^{-1}, associated with the stretching vibration of the -CH bond, which is a characteristic bond in polysaccharides including other species such as xylan and glucan [20]. The bands at 1320 cm^{-1}, assigned to the C=O tensile vibration in amide III, and at 1652 cm^{-1}, for the C=O bond stretching vibration in amide I, are characteristic and distinct for residual N-acetyl groups [36]. The low intensity of the band at 1556 cm^{-1}, which is characteristic of the N-H group bending vibration in amide II, may be justified

by the higher deacetylation degrees of all chitosan samples used in this study [37]. In addition, chitosan exhibits bands at 1420 cm^{-1} and 1376 cm^{-1}, characteristic of symmetric deformations of the -CH_2 and -CH_3 groups, respectively, while the characteristic bands of -NH oscillations and C-O-C extension (indicates the saccharide structure of chitosan) are present in the spectra at 1153 cm^{-1} and 1028 cm^{-1}, respectively [38].

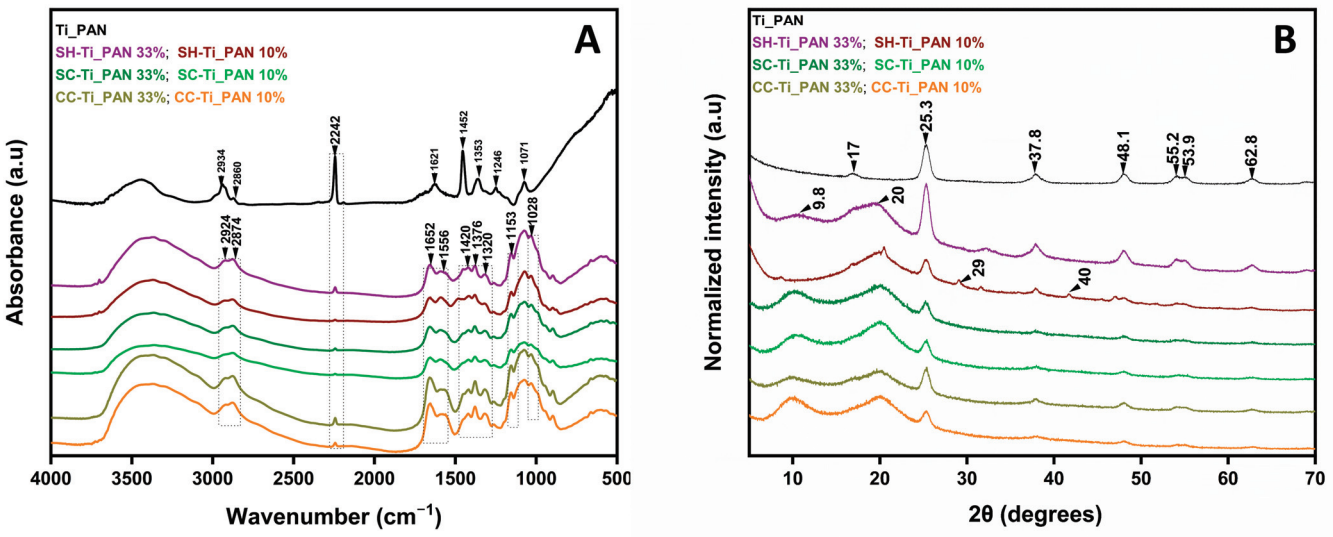

Figure 1. Structure evaluation by FTIR (**A**) and XRD (**B**), for the chitosan-based polymeric (CC-Ti_PAN 10%, CC-Ti_PAN 33%, SC-Ti_PAN 10%, SC-Ti_PAN 33%, SH-Ti_PAN 10% and SH-Ti_PAN 33%) beads compared to Ti_PAN composite reference.

C-H vibrations may be observed at 1246, 1353, and 1452 cm^{-1} in the Ti_PAN composite reference spectrum, as well as in all the spectra of beads. A band at 1455 cm^{-1} suggests CH2 deformation, while the methylene group's stretching vibrations are displayed at 2860 and 2934 cm^{-1}. At the same time, the stretching vibration of the C≡N group, characteristic of polyacrylonitrile, can be observed at 2242 cm^{-1}, which confirms the presence of the composite filler in the polymeric beads [35,39].

XRD patterns of the all-polymeric beads and the composite (Figure 1b) show strong diffraction peaks at 2θ values of 25.3°, 37.8° and 48.1°, indicating TiO_2 in the anatase phase corresponding to planes 101, 103 and 004 [31]. In addition, the composite shows a characteristic peak of acrylonitrile approximately 17.0° attributed to the (100) plane of pure polymer [40]. In the case of polymeric beads this peak most likely disappears due to the high peak intensity at 20°. At the same time, other peaks, with lower intensity, confirm the presence of the anatase phase at 2θ values of 53.9°, 55.2°, 62.8° corresponding to the planes 105, 211 and 118 [41]. Thus, the success of the composite filler incorporation into the chitosan-based beads is confirmed. In agreement with the previous work [42], chitosan shows two characteristic peaks at 2θ values of 9.8° and 20° corresponding to the 020 and 110 planes observed in all types of chitosan-based beads, which indicate the presence of ordered crystalline structure of chitosan. In the SH-Ti_PAN 10% sample, the characteristic peaks for $CaCO_3$ can be observed at 2θ values of 29° and 40° attesting its presence from the initial synthesis of chitosan [43]. Their absence in the SH-Ti_PAN 33% beads may be attributed to its lower ratio in the composite as a result to the increased amount of the inorganic–organic composite, particularly of TiO_2. Other differences may be observed, such as disappearance of the chitosan peak at 9.8° in SH-Ti_PAN 10% and similar peak intensities of TiO_2 regardless of Ti_PAN content for SC-based systems, which may be due to the heterogenous distribution of chitosan and TiO_2 in the material.

2.1.2. N_2 Adsorption/Desorption Measurements and Morphology of Composite Beads

The measurement of N_2 adsorption/desorption was carried out to reveal the specific surface area and porosity of the composite beads. Figure 2 shows the isotherms and pore size distribution for each type of composite beads. In agreement with the IUPAC nomenclature, which classifies BET isotherms into six types [44], the polymer beads presented herein reveal a type IV curve alignment, specific to mesoporous materials. The hysteresis loop presented in each case is H-4 type, with an almost horizontal and parallel aspect over a wide pressure (P/P0) range. This type of hysteresis loop is often associated with narrow pores [42].

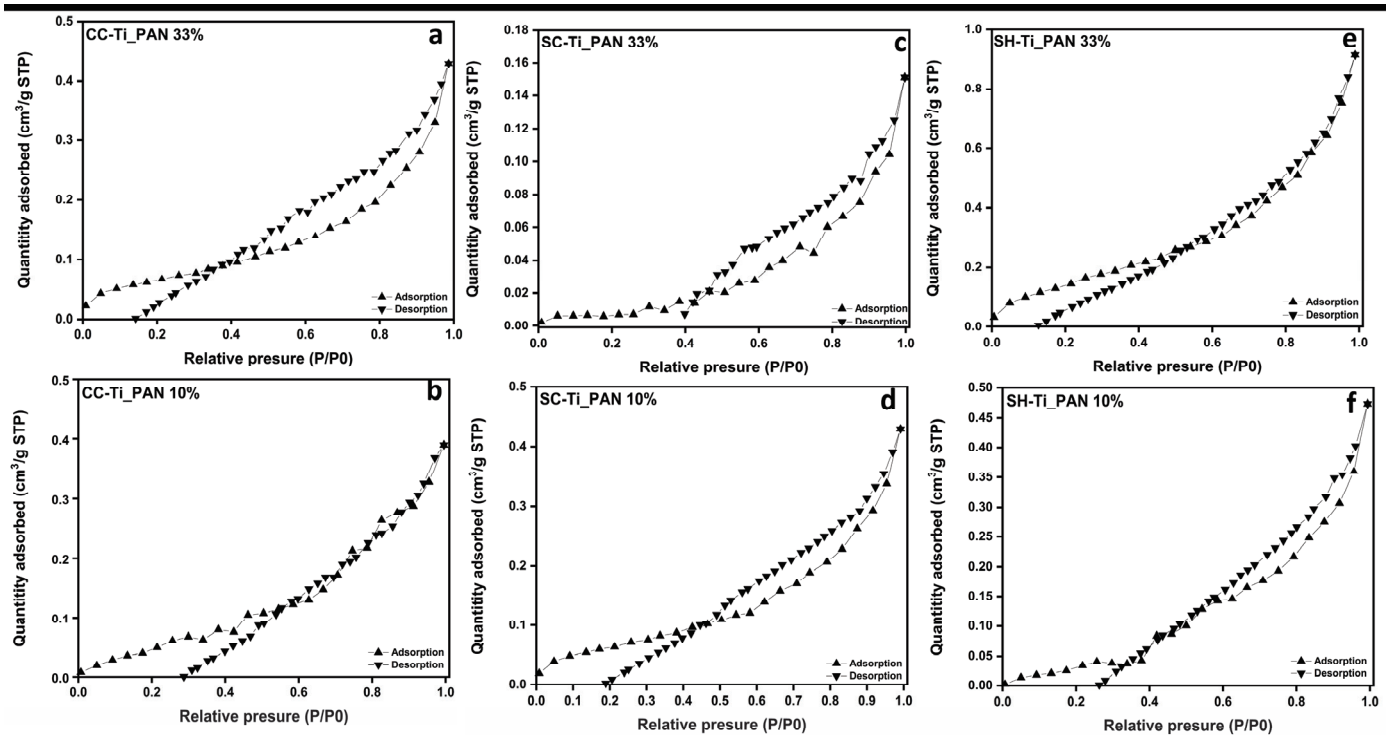

Figure 2. Adsorption/desorption isotherms and pore size distribution for series of chitosan-based polymer (CC-Ti_PAN 10% (**a**); CC-Ti_PAN 33% (**b**); SC-Ti_PAN 10% (**c**); SC-Ti_PAN 33% (**d**); SH-Ti_PAN 10% (**e**); SH-Ti_PAN 33% (**f**)) samples.

Furthermore, the BET surface area and pore surface area for each type of polymeric beads, as resumed in Table 1, present important variations with the change in chitosan type or with the increase in filler. Interestingly, all the beads have presented little variation in pore diameter and volume, which means that the filler has a very low influence on the porosity of the composite beads, regardless of the amount used. The largest BET surface area (3.334 m^2g^{-1}) was recorded for SH-Ti_PAN 10%, which also revealed the largest pore surface area (9.443 m^2g^{-1}) and micropore volume (0.011 cm^3g^{-1}). The obtained data from BET were also confirmed by the morphology analysis in Figure 3, which in the case of SH-based beads, meaning SH-Ti_PAN 10% and SH-Ti_PAN 33%, Figure 3e,f, respectively, displays the presence of large pores on the surface of the beads. Meanwhile, CC-Ti_PAN 33% and SC-Ti_PAN 33% beads (Figure 3b,d, respectively) present a homogeneous but rough surface with no visible pore structures. Yet, the presence of the titanium oxide–polyacrylonitrile filler is visible on the surface of all beads, as granular microstructures of different sizes dispersed relatively homogeneously.

Table 1. BET surface area and pore analysis of the polymeric beads.

Sample	BET Surface Area (m^2 g^{-1})	Pore Surface Area (m^2 g^{-1})	Maximum Pore Diameter [1] (nm)	Micropore Volume [2] (cm^3 g^{-1})
CC-Ti_PAN 33%	1.108	1.880	4.343	0.002
CC-Ti_PAN 10%	1.260	1.911	4.543	0.002
SC-Ti_PAN 33%	0.357	2.415	4.343	0.002
SC-Ti_PAN 10%	0.977	1.725	4.152	0.002
SH-Ti_PAN 33%	2.401	2.994	4.543	0.004
SH-Ti_PAN 10%	3.334	9.443	4.543	0.011

[1] Calculated by BJH method. [2] Measured at P/P0 = 0.99.

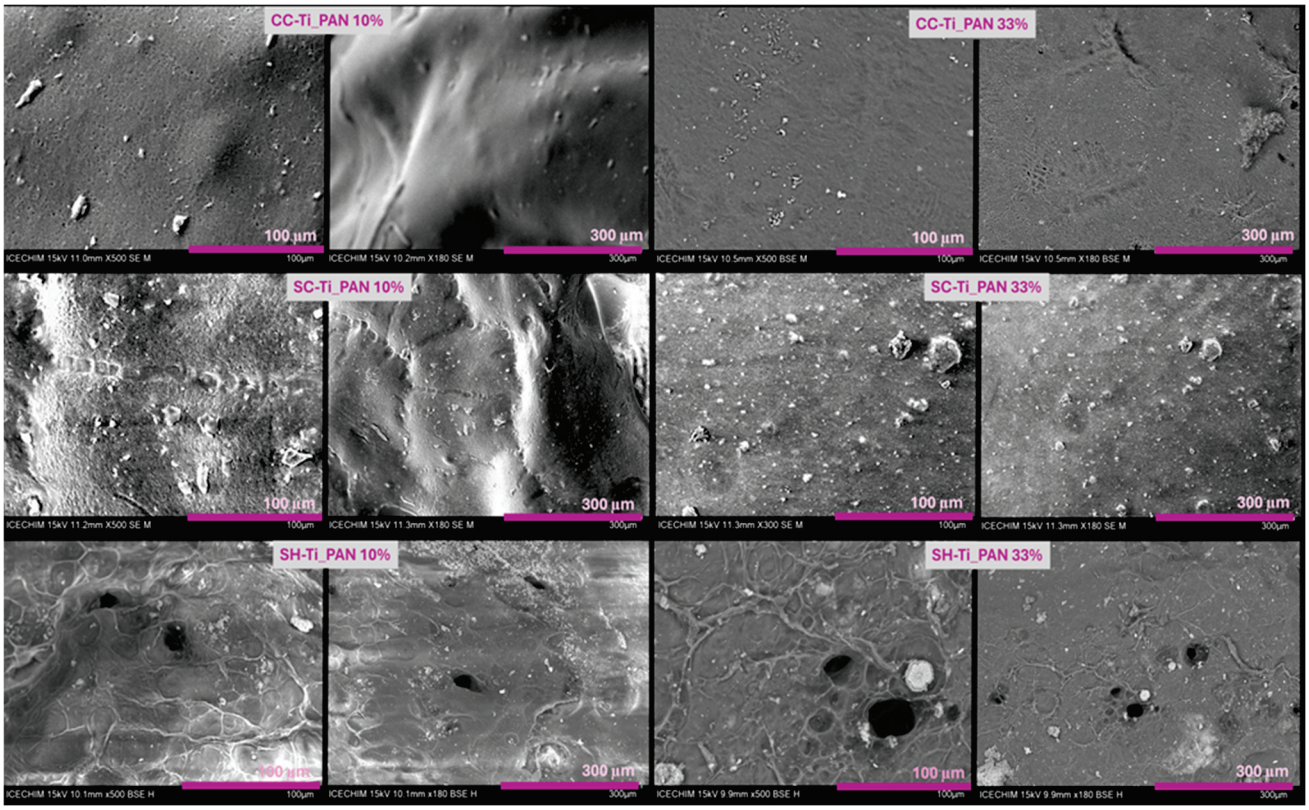

Figure 3. SEM micrographs for the composite beads series based on commercial chitosan (CC-Ti_PAN 10%; CC-Ti_PAN 33%, commercial chitin-derived chitosan (SC-Ti_PAN 10%; SC-Ti_PAN 33%) and chitosan obtained from shrimp wastes (SH-Ti_PAN 10%; SH-Ti_PAN 33%) at 100 µm and 300 µm.

2.2. Adsorption Kinetics of Cu^{2+} Ions

In this section, three important factors that characterize the adsorption processes (in terms of adsorption capacity, efficiency, and adsorption mechanism) were investigated and described.

In this respect, Cu^{2+} adsorption at pH = 5 and 25 °C was measured as a function of contact time starting from a solution of 100 mg/L, and $R_{S/L}$ = 1.5 mg mg/L, as shown in Figure 4. Adsorption studies using chitosan-based composite beads were performed over a time range from 90 min (1.5 h) to 1440 min (24 h). The adsorption rate was quite fast in the first 420 min, when attaining equilibrium and forming a plateau. It can be observed that both the percentage of titanium oxide–polyacrylonitrile filler and the type of chitosan influence the Cu^{2+} retention properties onto polymeric beads. A clear difference can be noticed for the series of beads with SH (Figure 4c and Table 2—adsorption capacities), in which case the polymeric beads with lower amount of composite, i.e., SH-Ti_PAN 10%,

retain higher amounts of Cu^{2+} than the counterpart with 33% composite (up to 17.03 mg/g vs. 15.52 mg/g, respectively). However, for the series with CC and SC, lower adsorption capacities were registered at 10% composite amount vs. 33%. It can also be noted that the highest adsorption capacity was attained by the SH-Ti_PAN 10% system. The removal efficiency (%) of the polymeric beads for Cu^{2+} was also calculated and summarized in Table 2, in which case it can be observed that the highest Cu^{2+} retention efficiency is again recorded for the system SH-Ti_PAN 10% (51.7%). It can also be observed that removal efficiency depends on the type of chitosan used and the percentage of inorganic–organic composite present in the structure of the polymer composite beads, and ranges from 29.5% and 51.6%. Thus, for commercial chitosan-based beads, the removal efficiency (Figure 4) is similar for both filler percentages (approximately 30%); for beads obtained from commercial chitin-derived chitosan, it is approximately 33% and for samples with chitosan obtained from shrimp shell waste, it is 49.6% for 33% filler and 51.6% for 10% filler, respectively.

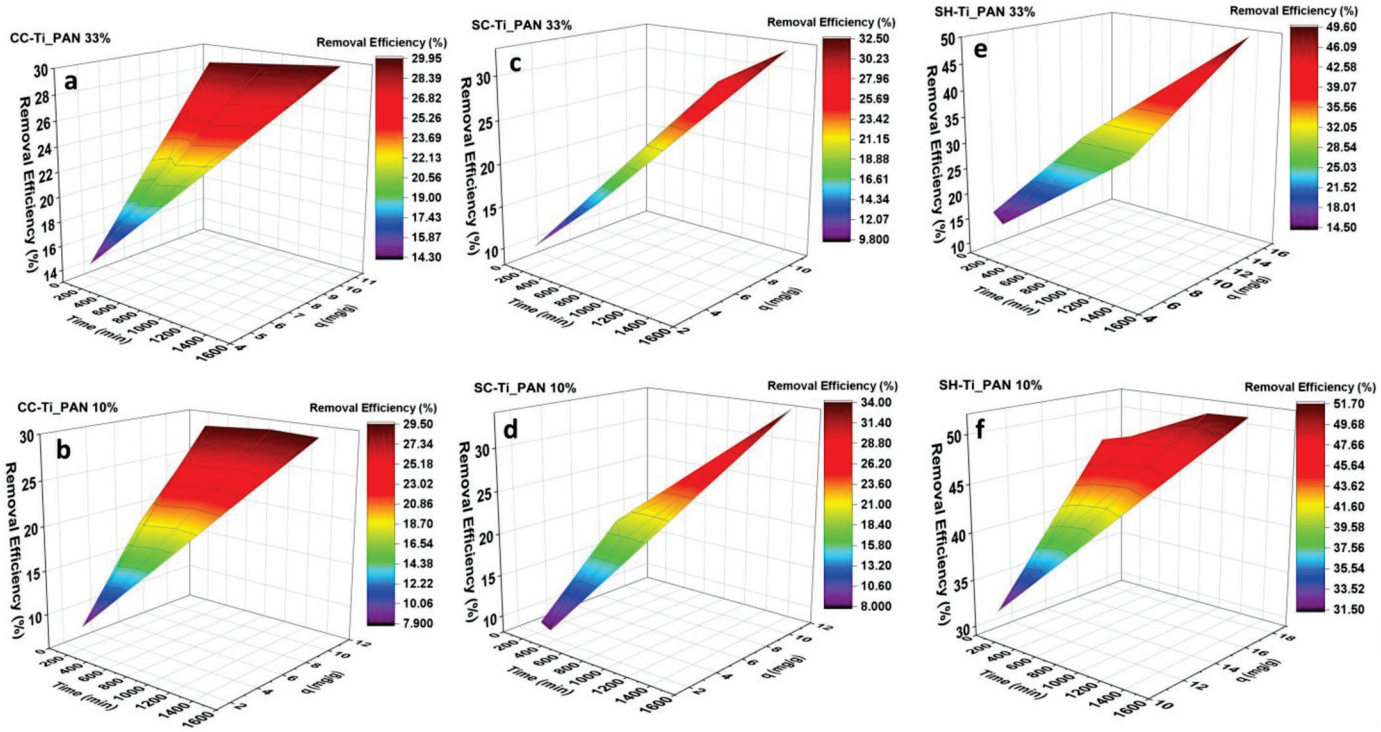

Figure 4. Effect of time on the removal efficiency and adsorption capacity on Cu^{2+} adsorption at 25 °C, for the CC series (**a**,**b**); SC series (**c**,**d**) and SH series (**e**,**f**) (in this experiment $R_{S/L}$ = 1.5 mg/mL; pH = 5 and initial concentration of 100 mg/L).

Table 2. Comparison of maximum adsorption capacities of various adsorbents for Cu^{2+}.

Sample	Adsorption Capacity, q (mg/g) after 24 h	Retention Efficiency after 24 h (%)	Cu^{2+} Initial Concentration	Ref.
CC-Ti_PAN 33%	10.7	29.9	100	This study
CC-Ti_PAN 10%	10.1	29.5	100	This study
SC-Ti_PAN 33%	10.7	32.5	100	This study
SC-Ti_PAN 10%	11.1	34.0	100	This study
SH-Ti_PAN 33%	15.5	49.6	100	This study
SH-Ti_PAN 10%	17.0	51.7	100	This study

Table 2. *Cont.*

Sample	Adsorption Capacity, q (mg/g) after 24 h	Retention Efficiency after 24 h (%)	Cu^{2+} Initial Concentration	Ref.
Chitosan-coated sand (CCS)	1.2	99.77	100	[44]
Modified chitosan transparent thin membrane (MCTTM)	8.5	-	25	[45]
Pine sawdust	1.7	-	300	[46]

To evaluate the improvement for Cu^{2+} adsorption properties recorded for the polymer beads; the data obtained herein were compared with other literature records for several types of adsorbents. Table 2 provides a comparison between the adsorption capacity of polymer beads and adsorbent materials obtained by other authors [45–47], where it can be observed that the adsorption capacity of the polymeric beads is significantly higher compared to references [46,47]. However, in the study of Wan et al. [44], the high removal efficiency of 99.77% is also due to a high $R_{S/L}$ value, of approximately 83.33 mg/mL (2.5 g of sample in 30 mL of solution) compared to the present study, in which case the $R_{S/L}$ was 1.5 mg/mL (meaning 15 mg of sample to 10 mL of Cu^{2+} ion solution). For the other two studies [46,47], the removal efficiency was not reported.

Further on, the assessment of adsorption kinetics has been used to ascertain the reaction rate and the adsorption mechanism. The mechanism of adsorption kinetics is an important parameter, as it describes the adsorption rate of the adsorbent and controls the residual time of the whole process. To better understand the adsorption process, the pseudo-second-order kinetic (PSO), Elovich and intraparticle diffusion (ID) (Figure 5) models were fitted to the existing experimental data and the parameters are summarized in Table 3. The determination coefficient (R^2) for PSO ranged from 0.898 to 0.989, for Elovich values ranging from 0.910 to 0.975 and for ID between 0.772 and 0.958.

Table 3. Kinetic parameters for Cu^{2+} adsorption for chitosan-based polymer beads, at $R_{S/L}$ = 1.5 mg/mL, pH = 5, initial Cu^{2+} concentration of 100 mg/L, and time range 0–1440 min.

Kinetic Model	Parameters	CC-Ti_PAN 33%	CC-Ti_PAN 10%	SC-Ti_PAN 33%	SC-Ti_PAN 10%	SH-Ti_PAN 33%	SH-Ti_PAN 10%
Experimental data	$q_{e,\,exp}$ (mg/g)	10.714	10.128	10.687	11.124	15.521	17.039
PSO	$q_{e2}{}^2$/(mg/g)	12.053	13.202	18.232	16.385	18.575	19.180
	k_2/(g/(mg·min)	3.889	2.788	5.545	8.053	1.068	5.284
	R^2	0.973	0.951	0.995	0.947	0.898	0.989
Elovich	α (mg/(g·min)	0.114	0.074	0.021	0.025	0.049	1.196
	β (g/mg)	0.385	0.307	0.167	0.190	0.192	0.345
	R^2	0.970	0.921	0.959	0.949	0.910	0.975
ID	k_d (mg/g·$min^{1/2}$)	0.275	0.298	0.275	0.282	0.373	0.437
	C (mg/g)	1.351	0.925	9.900	9.890	2.284	4.488
	R^2	0.902	0.847	0.958	0.931	0.922	0.772

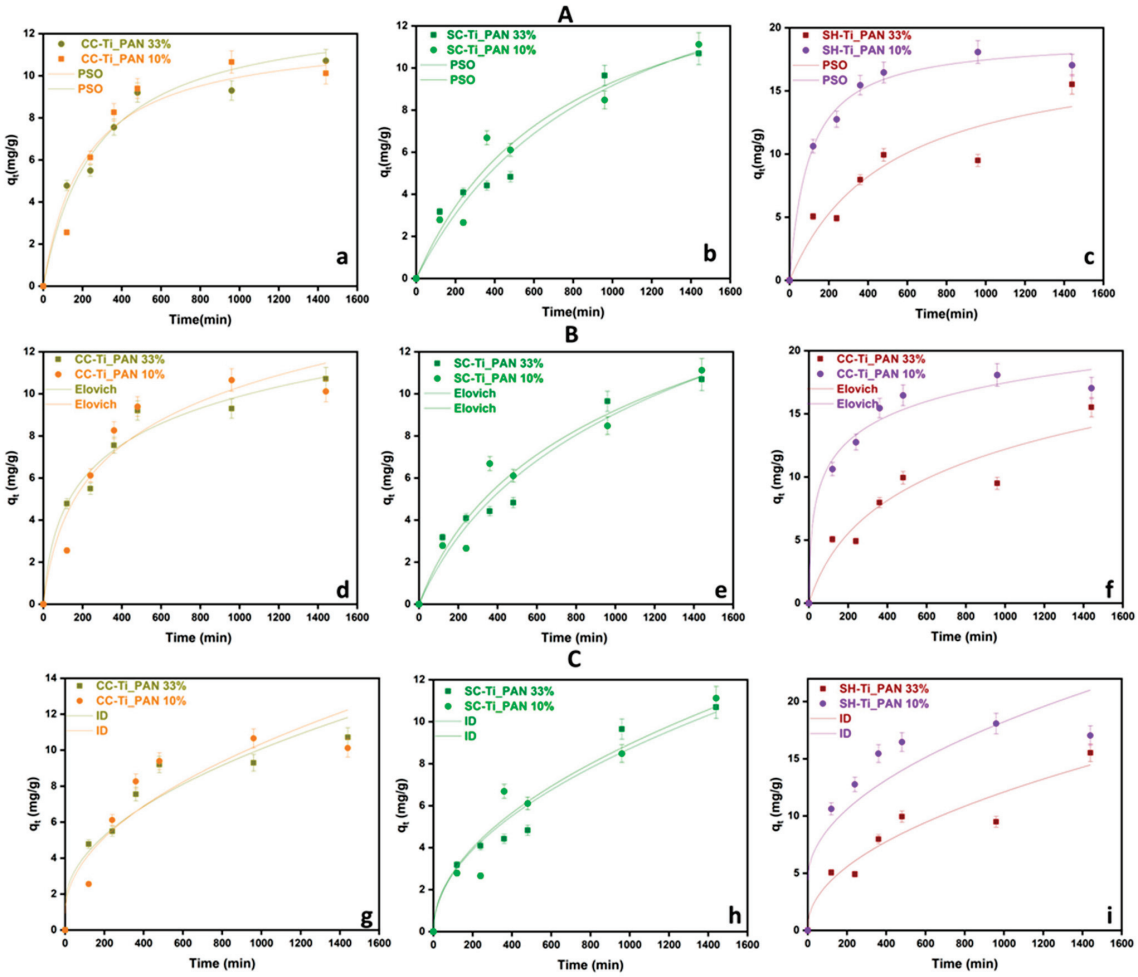

Figure 5. Kinetic models PSO (**A**), Elovich (**B**) and ID (**C**) for Cu^{2+} ion adsorption for chitosan-based polymer beads at $R_{S/L}$ = 1.5 mg/mL, pH = 5, initial Cu^{2+} concentration of 100 mg/L, time range 0–1440 min, and error bars of 5% relative to the measured raw data, for the CC series (**a**,**d**,**g**); SC series (**b**,**e**,**h**) and SH series (**c**,**f**,**i**).

The best representation of the results overall came from the PSO model, followed by Elovich and ID. The PSO model suggests surface-limited adsorption, which is explained by the formation of metal–ligand bonds [48,49]. It can also be mentioned that SC-Ti_PAN 10% and SH-Ti_PAN 33% samples were better fitted by the Elovich model, indicating that, for these two types of materials, the adsorbing surfaces are more heterogeneous and this influences the chemisorption mechanism in a higher extent [50]. Moreover, it seems that all beads' systems are limited by a chemisorption mechanism, since the ID model (that describes adsorption processes through diffusional mechanisms) was not very well adjusted on the experimental data.

Therefore, the PSO kinetic model revealed that CC-Ti_PAN 33% beads show a moderate equilibrium adsorption (q_e) and a moderate adsorption rate (k_2). However, for the CC-Ti_PAN 10%, the q_e value is slightly higher and the adsorption rate slightly slower. Polymeric beads SC-Ti_PAN 33% and SC-Ti_PAN 10% also show good q_e values while k_2 indicates a relatively fast adsorption rate compared to the other studied samples. For the shrimp waste-derived chitosan samples (SH-Ti_PAN) the behavior is relatively similar. In the case of the SH-Ti_PAN 10%, the q_e value is high and the velocity, represented by the k_2 value shows a slower adsorption rate. However, the R^2 value is the lowest, suggesting a lower accuracy of the PSO kinetic model compared to the other studied models. On the other hand, the SH-Ti_PAN 10% sample shows the highest equilibrium concentration value and a moderate to high k_2 rate, with a good fitting of the pseudo second-order kinetic model.

For the Elovich kinetic model, the R^2 values in the range of 0.910–975 suggest a fairly good fit of the model to all the experimental data. The desorption constant β values range from 0.167 to 0.385, suggesting that the interaction between the adsorbent molecules and the adsorbent surface is relatively similar regardless of the sample, while α (initial adsorption rate) has a significant variation between samples. The 1.196 maximum value of α was found for the SH-Ti_PAN 10% sample, indicating a higher adsorption rate and a higher affinity of the beads for Cu^{2+}. At the same time, the lowest α value was determined for the SC-Ti_PAN 33% sample, indicating a lower affinity of the beads for Cu^{2+} [51–53].

The intraparticle diffusion kinetic model reveals k_{dif} values in the range 0.275–0.437 mg/g $min^{1/2}$, indicating that the diffusion velocity has the same order of magnitude. However, the value of *C* has a significant variation between the samples, i.e., 0.925–9.900 mg/g, suggesting major differences in the variation in the boundary layer. The highest values of *C* recorded for the SC series, meaning 9.900 mg/g for SC-Ti_PAN 33% and 9.890 mg/g SC-Ti_PAN 10%, indicate a faster rate of intraparticle diffusion compared to the other chitosan types [54–56].

In conclusion, the kinetic study indicated that the adsorption properties are more linked to the porous structure of beads. Nevertheless, the higher deacetylation degree of SH (which means more -NH_2 groups that bind Cu^{2+}) may also be responsible for the higher adsorption capacities registered for the SH series of composite beads [54].

Furthermore, using SEM microscopy, elemental mapping and EDX spectra were collected for all series of chitosan-based composite beads after Cu^{2+} ion adsorption. As shown in Figure 6, EDX spectra confirm the presence of the major constituents of chitosan, carbon and oxygen. In addition, significant amounts of copper were found on the surface of polymeric beads, with percentages ranging between 3.5 and 16%. The percentage of Cu^{2+} on the surface of the polymeric beads varies according to both the type of chitosan used and the percentage of composite in the sample. The lowest percentage on the surface of 3.5% is found in the case of SH-Ti_PAN 33%. The percentages for commercial chitosan samples are similar (5.9%); for samples based on commercial chitin-derived chitosan, the ratios are 4.1% for SC-Ti_PAN 33% and 7% for SC-Ti_PAN 10%. Interestingly, the highest percentage of 16% was recorded for the system SH-Ti_PAN 10% beads, which seems to confirm the results obtained previously by the adsorption kinetics study.

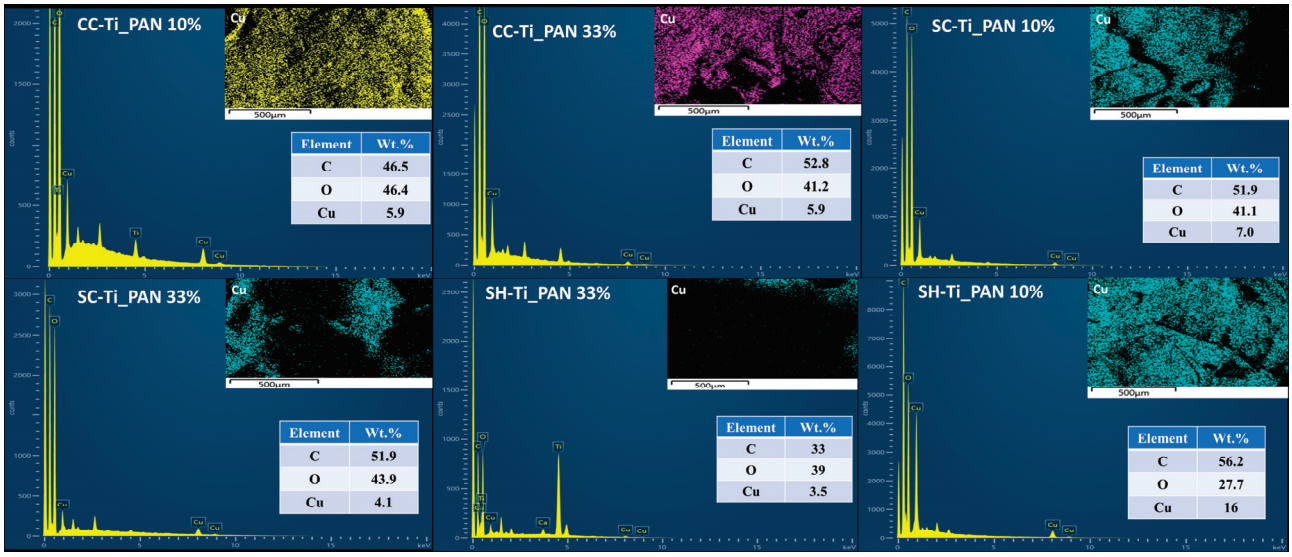

Figure 6. EDX micrographs and distribution map of adsorbed Cu^{2+} ions on the surface of the series of commercial chitosan (CC-Ti_PAN 10%, CC-Ti_PAN 33%), commercial chitin-derived chitosan (SC-Ti_PAN 10%, SC-Ti_PAN 33%) and chitosan obtained from shrimp wastes (SH-Ti_PAN 10%, SH-Ti_PAN 33%) beads.

3. Materials and Methods

3.1. Materials

Commercial chitosan with a degree of deacetylation ≥75% (CC, Sigma Aldrich-St Louis, MO, USA) was used without further purification. Commercial chitin-derived chitosan with a degree of deacetylation ≥78 (SC), and chitosan obtained from shrimp shell (SH) with a degree of deacetylation ≥75 were synthesized in the laboratory by a previously reported method [42]. Glacial acetic acid (CHIMREACTIV SRL-Bucharest, Romania) was used to prepare 1%, 3% and 10% solutions in distilled water. A coagulation bath of 5% NaOH solution was prepared by dissolving NaOH (CHIMREACTIV SRL-Bucharest, Romania) in distilled water).

Inorganic–organic polymer composites were synthesized by the host–guest method, starting from mesoporous titania (TiO_2) and acrylonitrile (AN), by a previously reported process [22]. The two steps of the process included the ultrasound-assisted impregnation/adsorption of AN into TiO_2 pores in the first phase and the ultrasound-assisted polymerization of AN in the second phase [22].

Copper (II) acetate monohydrate (≥98%), purchased from J.T. Baker (Center Vally, PA, USA), was used for adsorption tests. All reagents, described further, used for the quantitative determination of copper were of analytical purity. Standard solutions of Certipur, 1000 mg/L and 100 mg/L, respectively, from Merk (Darmstadt, Germany) were used to draw a calibration curve 65% solution (*w*/*w*) of nitric acid from Scharlau and ultrapure water produced by Milli-Q, Integral System (Merk) with a resistivity of 18.2 MΩ/cm to prepare the standard solutions and samples. The purge gas for the ICP-OES was Argon 5.0 of 99.999% purity (Messer Romania Gaz SRL).

3.2. Synthesis of Composite Beads

To prepare chitosan-based polymer composite beads with inorganic–organic content, several steps were necessary. Firstly, 2% chitosan was dissolved in acetic acid solution under magnetic stirring (800 rpm) at a temperature of 60 °C for 5 h. Depending on the type of chitosan used, the concentration of acetic acid solution was 1% in the case of commercial chitosan (CC), 3% in the case of commercial chitin-derived chitosan (SC) and 10% in the case of chitosan obtained from shrimp shell wastes (SH). In the second step, after complete dissolution of the biopolymer and the formation of the gel, a 33% (wt. relative to the chitosan mass) or 10% (wt. relative to the chitosan mass) ratio of inorganic–organic composite based on mesoporous titanium dioxide and acrylonitrile was added. After complete homogenization, the warm solution was added into a syringe and dripped from 80 cm into a coagulation bath containing the 5% NaOH solution, under gentle magnetic stirring (50 rpm). The composite beads were left in the coagulation bath for 12 h for complete bead formation. After coagulation, the beads were washed several times with distilled water to neutral pH. The diameter of the beads was in the range of 4–5 mm. The last step of the process was freezing the samples at −20 °C followed by freeze-drying (at −70 °C). The notation of samples based on the three types of chitosan, and the percentage of inorganic–organic composite used in bead synthesis is summarized in Table 4.

Table 4. Sample preparation.

Sample Code	Chitosan Type (Abbreviation)	Inorganic–Organic Composite, Ti_PAN (wt. %)
CC-Ti_PAN 33%	Commercial chitosan (CC)	33
CC-Ti_PAN 10%	Commercial chitosan (CC)	10
SC-Ti_PAN 33%	Chitosan from commercial chitin (SC)	33
SC-Ti_PAN 10%	Chitosan from commercial chitin (SC)	10
SH-Ti_PAN 33%	Chitosan from shrimp shell (SH)	33
SH-Ti_PAN 10%	Chitosan from shrimp shell (SH)	10

3.3. Characterization Techniques

Fourier-Transform Infrared (FTIR) spectra of the samples were recorded on a Nicolet™ Summit PRO FTIR Spectrometer (Thermo Fisher Scientific, Waltham, MA, USA) by acquiring 16 scans with a 4 cm^{-1} resolution in the 4000–500 cm^{-1} region.

X-ray diffraction (XRD) patterns were collected with a SmartLab (Rigaku Wilmington, MA, USA) equipment, operated at 45 kV and 200 mA, with Cu Kα radiation (wavelength λ = 0.1541 nm) in a parallel-beam configuration ($2\theta/\theta$ scan mode). The scanned range was 2θ = 2–70°, with a scan rate of 8°/min.

The Brunauer–Emmett–Teller (BET) and Barrett–Joyner–Halenda (BJH) Methods. BET surface area and pore measurements for raw and obtained materials were carried out by nitrogen adsorption using a NOVA 2200 analyzer (Quantachrome Instruments, Odelzhausen, Germany). Nitrogen sorption isotherms at −196 °C were recorded after all the samples were outgassed at 40 °C for 4 h under vacuum prior to N_2 adsorption.

Scanning electron microscopy (SEM) images of the polymeric composite beads were obtained using a TM4000 plus II product by (Hitachi, Krefeld, Germany) scanning electron microscope equipped with a secondary electron (SE) detector at an acceleration voltage of 15 kV. Energy-dispersive X-ray spectroscopy (EDS) was used for spectrum recording and elemental mapping of samples with an Oxford Instruments (High Wycombe, UK) equipment. SEM images were recorded on wet beads after rigorous washing while mapping and EDX analysis were recorded on freeze-dried beads after the adsorption process.

3.4. Adsorption Study

In order to determine the heavy metal ion (Cu^{2+}) concentrations, the Optima 2100 DV ICP-OES System (Perkin Elmer, Waltham, MA, USA) was used, a dual-view optical system with axial and radial views of the plasma in a single working sequence, operating with an independent transistorized radio frequency generator (40 MHz), used to determine Cu^{2+} ion traces. The nebulizer system is equipped with a PEEK Mira Mist® (Perkin Elmer, Waltham, MA, USA) nebulizer coupled with a spray chamber—Baffled Cyclonic. The spectrometer consists of an optical module comprising an Echelle monochromator with a two-dimensional charged coupled device (CCD) detector, and a spectral range 165–800 nm. For the determination of copper in liquid samples (aqueous solutions) on the calibration slide with a concentration range of 1–10 mg/L, the dilution factor used was 1:25. Samples thus diluted were acidified with 0.5 mL of 65% nitric acid solution.

To evaluate the adsorption kinetics of the polymer composite beads, the following process was considered. The Cu^{2+} solution was prepared in distilled water (100 mg/L) and the solution was brought to pH 5. The experiments were carried out in 15 mL tubes, in which solutions were prepared with a liquid solid ratio, $R_{S/L}$ = 1.5 mg/mL. The term $R_{S/L}$ refers to the amount of material used in relation to the amount of solution, expressed in mg sample/mL solution. The tubes were closed to minimize evaporation of the solution and placed in a shaker (BENCHMARK SCIENTIFIC H5000-HC Multitherm Shake) at a stirring speed of 200 rpm. The beads were left in contact with the Cu^{2+} solution for a very specific period (2 h, 4 h, 6 h, 8 h, 16 h, and 24 h). After the time had elapsed, the solution was filtered and placed in a bottle with a silicon cap for and the following analysis.

Quantification of the equilibrium adsorption process was performed by calculating the removal efficiency (%) (Equation (1)) and the adsorption capacity for metal ions (q, mg/g) (Equation (2)), knowing the initial (C_0, mg/L) and the final (C_f, mg/L) concentrations of metal ions, the solution volume (V, L) and the adsorbent mass (m, g).

$$Removal\ Efficiency\ (\%) = \frac{(C_0 - C_f)}{C_0} \times 100 \quad (1)$$

$$q = \frac{\left(C_0 - C_f\right) \times V}{\mathrm{m}} \quad (2)$$

The obtained adsorption data were evaluated based on three distinct kinetic models, pseudo-second-order (PSO) kinetic model, the Elovich kinetic model and the intraparticle diffusion model. To fit the kinetic models, the adsorption capacity after 1440 min was used as the equilibrium adsorption capacity, $q_{e.}$ The equations of the kinetic models used are shown below:

The pseudo-second-order (PSO) kinetic model:

$$q_t = \frac{k_2 q_e^2 t}{1 + k_2 q_e^2 t} \tag{3}$$

where q_e (mg/g) is the adsorbate amount adsorbed at equilibrium, t (min) is time and k_2 (g/mg·min) is the rate constant.

The Elovich kinetic model:

$$q_t = \beta ln(\alpha \beta t) \tag{4}$$

where β (g/mg) is the desorption constant of Elovich and α (mg/g min) is the rate constant.

The intraparticle diffusion (ID) model:

$$q_t = k_{diff} \times t^{\frac{1}{2}} + C \tag{5}$$

where k_{diff} (mg/g $min^{1/2}$) is the rate constant and C is the parameter related to the layer thickness of the boundary.

4. Conclusions

The present study was carried out to evaluate the efficacy of new types of composite adsorbents, based on different chitosan and inorganic–organic composite fillers for the efficient removal of Cu^{2+} ions from simulated waters. Comprehensive research on the adsorption capacity of the materials was undertaken, and composite polymer beads based on three types of chitosan were developed: commercial chitosan, commercial chitin-derived chitosan and chitosan obtained from shrimp wastes enhanced with $CaCO_{3,}$ and a titanium oxide–polyacrylonitrile composite at different percentages. Polymer composite beads were evaluated in terms of morphology, physicochemical characteristics, and adsorption capacity.

FTIR spectroscopy confirmed that the TiO_2–polyacrilonitrile composite was incorporated into the biopolymer matrix; the presence of the composite in the structure of the materials being attested by the band at 2242 cm^{-1}, characteristic of the C-N group in the polyacrylonitrile structure. XRD patterns showed an anatase-type crystal structure of TiO_2 and an ordered crystal structure of chitosan. BET analysis revealed a higher porosity, with a larger surface area and pore volume for the SH-Ti_PAN 10% beads compared to the other studied samples, which was confirmed by SEM analysis, indicating a roughness due to the presence of the composite in granular form on the entire surface of the beads.

The adsorption capacity of the beads was tested at pH 5 in a simulated solution with Cu^{2+} ions at a concentration of 100 mg/L, and the adsorption kinetic parameters (90–1440 min) were studied over time using three kinetic models (PSO, Elovich and ID). The results showed that the kinetic model that best fitted the obtained experimental data was the PSO model, suggesting limited surface adsorption and metal–ligand bond formation. Furthermore, the adsorption study showed that the type of chitosan used and the filler percentage significantly influence the adsorption capacity of the beads, the maximum capacity of 19.2 mg/g being registered for the SHC-Ti_PAN 10% sample. The adsorption properties of composite beads were mostly influenced by the type of chitosan used, judging from the small variations in the adsorption capacity and the retention efficiency between samples with the same type of chitosan. For instance, the removal efficiency for commercial chitosan-based composites varied between 29.5 and 29.9%; for commercial chitin derived-chitosan, the variation was between 32.5 and 34.0%; for chitosan obtained from shrimp shell waste, the variation fluctuated was between 49.6 and 51.7%. In support of these

adsorption results, EDX mapping highlighted the presence of increased Cu^{2+} ions on the surface of the beads, particularly for SHC-Ti_PAN 10%.

As a concluding remark, the composite beads obtained in this study can serve as potential adsorbents of Cu^{2+} in wastewater treatment. Unlike powder adsorbents, the composite beads can be easily recovered after treatment by simple filtration procedures.

Author Contributions: Conceptualization, A.-L.C., T.-V.I. and A.J.M.V.; methodology, A.M., T.-V.I., H.I. and A.S.; validation, A.-L.C., L.M.R.D. and A.S.; formal analysis, A.M., A.Z., T.S. and G.R.I.; investigation, A.M., A.Z., T.S. and G.R.I.; data curation, A.M., L.M.R.D. and T.-V.I.; writing—original draft preparation, A.M.; writing—review and editing, A.-L.C., T.-V.I. and A.J.M.V.; supervision, T.-V.I., A.J.M.V. and H.I.; project administration, A.-L.C., T.-V.I. and A.S.; funding acquisition, A.-L.C. and A.M. All authors have read and agreed to the published version of the manuscript.

Funding: The authors would like to thank the Ministry of Research, Innovation and Digitalization for funding in the frame of 15PFE/2021" Susținerea competitivității și excelenței cercetării și inovării din INCDCP-ICECHIM". The funding from ICECHIM was also partially supported by the PN-III-Human Resources Programme-YOUNG RESEARCH TEAMS-PN-III-P1-1.1-TE-2021-0915, grant no. 135/2022 project—I-ON-MEM.

Institutional Review Board Statement: Not applicable.

Informed Consent Statement: Not applicable.

Data Availability Statement: All the data are available from the corresponding author, Anita-Laura Chiriac, email: anita-laura.radu@icechim.ro.

Acknowledgments: The authors thank "BIOSHELL" (Ref. BLUEBIO/0003/2019, financed by FCT, and ctr. 157/2020 as financed by UEFISCDI) within the program ERA-NET Cofund on Blue Bioeconomy (BlueBio). Funding was received from the Coimbra Chemistry Centre and CIEPQPF, which is supported by the Fundação para a Ciência e a Tecnologia (FCT) through the programs UID/QUI/00313/2020 and UIDP/EQU/00102/2020.

Conflicts of Interest: The authors declare no conflicts of interest. The funders had no role in the design of the study; in the collection, analyses, or interpretation of data; in the writing of the manuscript; or in the decision to publish the results.

References

1. Azizullah, A.; Khattak, M.N.K.; Richter, P.; Häder, D.-P. Water Pollution in Pakistan and Its Impact on Public Health—A Review. *Environ. Int.* **2011**, *37*, 479–497. [CrossRef]
2. Vardhan, K.H.; Kumar, P.S.; Panda, R.C. A Review on Heavy Metal Pollution, Toxicity and Remedial Measures: Current Trends and Future Perspectives. *J. Mol. Liq.* **2019**, *290*, 111197. [CrossRef]
3. Vareda, J.P.; Valente, A.J.M.; Durães, L. Assessment of Heavy Metal Pollution from Anthropogenic Activities and Remediation Strategies: A Review. *J. Environ. Manag.* **2019**, *246*, 101–118. [CrossRef] [PubMed]
4. Mitra, S.; Chakraborty, A.J.; Tareq, A.M.; Emran, T.B.; Nainu, F.; Khusro, A.; Idris, A.M.; Khandaker, M.U.; Osman, H.; Alhumaydhi, F.A.; et al. Impact of Heavy Metals on the Environment and Human Health: Novel Therapeutic Insights to Counter the Toxicity. *J. King Saud Univ. Sci.* **2022**, *34*, 101865. [CrossRef]
5. Singh, A.; Sharma, A.; Verma, R.K.; Chopade, R.L.; Pandit, P.P.; Nagar, V.; Aseri, V.; Choudhary, S.K.; Awasthi, G.; Awasthi, K.K.; et al. Heavy Metal Contamination of Water and Their Toxic Effect on Living Organisms. In *The Toxicity of Environmental Pollutants*; IntechOpen: London, UK, 2022; ISBN 978-1-80355-580-5.
6. Wu, B.; Zhao, D.Y.; Jia, H.Y.; Zhang, Y.; Zhang, X.X.; Cheng, S.P. Preliminary Risk Assessment of Trace Metal Pollution in Surface Water from Yangtze River in Nanjing Section, China. *Bull. Environ. Contam. Toxicol.* **2009**, *82*, 405–409. [CrossRef] [PubMed]
7. Teixeira, R.N.P.; Sousa Neto, V.O.; Oliveira, J.T.; Oliveira, T.C.; Melo, D.Q.; Silva, M.A.A.; Nascimento, R.F. Study on the Use of Roasted Barley Powder for Adsorption of Cu2+ Ions in Batch Experiments and in Fixed-Bed Columns. *BioResources* **2013**, *8*, 3556–3573. [CrossRef]
8. Zhang, M.; Zhang, Z.; Peng, Y.; Feng, L.; Li, X.; Zhao, C.; Sarfaraz, K. Novel Cationic Polymer Modified Magnetic Chitosan Beads for Efficient Adsorption of Heavy Metals and Dyes over a Wide pH Range. *Int. J. Biol. Macromol.* **2020**, *156*, 289–301. [CrossRef] [PubMed]
9. Sudha Rani, K.; Srinivas, B.; GouruNaidu, K.; Ramesh, K.V. Removal of Copper by Adsorption on Treated Laterite. *Mater. Today Proc.* **2018**, *5*, 463–469. [CrossRef]
10. Ramos, V.C.; Utrilla, J.R.; Sánchez, A.R.; Ramón, M.V.L.; Polo, M.S. Marble Waste Sludges as Effective Nanomaterials for Cu (II) Adsorption in Aqueous Media. *Nanomaterials* **2021**, *11*, 2305. [CrossRef]

11. Shehzad, H.; Ahmed, E.; Sharif, A.; Farooqi, Z.H.; Din, M.I.; Begum, R.; Liu, Z.; Zhou, L.; Ouyang, J.; Irfan, A.; et al. Modified Alginate-Chitosan-TiO_2 Composites for Adsorptive Removal of Ni(II) Ions from Aqueous Medium. *Int. J. Biol. Macromol.* **2022**, *194*, 117–127. [CrossRef]
12. Ariffin, N.; Abdullah, M.M.A.B.; Zainol, M.R.R.M.A.; Murshed, M.F.; Faris, M.A.; Bayuaji, R. Review on Adsorption of Heavy Metal in Wastewater by Using Geopolymer. *MATEC Web Conf.* **2017**, *97*, 01023. [CrossRef]
13. Zaimee, M.Z.A.; Sarjadi, M.S.; Rahman, M.L. Heavy Metals Removal from Water by Efficient Adsorbents. *Water* **2021**, *13*, 2659. [CrossRef]
14. Qasem, N.A.A.; Mohammed, R.H.; Lawal, D.U. Removal of Heavy Metal Ions from Wastewater: A Comprehensive and Critical Review. *Npj Clean Water* **2021**, *4*, 36. [CrossRef]
15. Renu; Agarwal, M.; Singh, K. Heavy Metal Removal from Wastewater Using Various Adsorbents: A Review. *J. Water Reuse Desalination* **2017**, *7*, 387–419. [CrossRef]
16. Chakraborty, R.; Asthana, A.; Singh, A.K.; Jain, B.; Susan, A.B.H. Adsorption of Heavy Metal Ions by Various Low-Cost Adsorbents: A Review. *Int. J. Environ. Anal. Chem.* **2022**, *102*, 342–379. [CrossRef]
17. Zito, P.; Shipley, H.J. Inorganic Nano-Adsorbents for the Removal of Heavy Metals and Arsenic: A Review. *RSC Adv.* **2015**, *5*, 29885–29907. [CrossRef]
18. Sabzehmeidani, M.M.; Mahnaee, S.; Ghaedi, M.; Heidari, H.; Roy, V.A.L. Carbon Based Materials: A Review of Adsorbents for Inorganic and Organic Compounds. *Mater. Adv.* **2021**, *2*, 598–627. [CrossRef]
19. Upadhyay, U.; Sreedhar, I.; Singh, S.A.; Patel, C.M.; Anitha, K.L. Recent Advances in Heavy Metal Removal by Chitosan Based Adsorbents. *Carbohydr. Polym.* **2021**, *251*, 117000. [CrossRef]
20. Awual, M.R. Novel Ligand Functionalized Composite Material for Efficient Copper(II) Capturing from Wastewater Sample. *Compos. B Eng.* **2019**, *172*, 387–396. [CrossRef]
21. Wan Ngah, W.S.; Teong, L.C.; Hanafiah, M.A.K.M. Adsorption of Dyes and Heavy Metal Ions by Chitosan Composites: A Review. *Carbohydr. Polym.* **2011**, *83*, 1446–1456. [CrossRef]
22. Zhao, G.; Wu, X.; Tan, X.; Wang, X. Sorption of Heavy Metal Ions from Aqueous Solutions: A Review. *J. Colloid Sci.* **2010**, *4*, 19–31. [CrossRef]
23. Jamshaid, A.; Iqbal, J.; Hamid, A.; Ghauri, M.; Muhammad, N.; Nasrullah, A.; Rafiq, S.; Shah, N.S. Fabrication and Evaluation of Cellulose-Alginate-Hydroxyapatite Beads for the Removal of Heavy Metal Ions from Aqueous Solutions. *ZPC* **2019**, *233*, 1351–1375. [CrossRef]
24. Elwakeel, K.Z.; El-Bindary, A.A.; Kouta, E.Y.; Guibal, E. Functionalization of Polyacrylonitrile/Na-Y-Zeolite Composite with Amidoxime Groups for the Sorption of Cu(II), Cd(II) and Pb(II) Metal Ions. *Chem. Eng. J.* **2018**, *332*, 727–736. [CrossRef]
25. . Aranaz, I.; Alcántara, A.R.; Civera, M.C.; Arias, C.; Elorza, B.; Heras Caballero, A.; Acosta, N. Chitosan: An Overview of Its Properties and Applications. *Polymers* **2021**, *13*, 3256. [CrossRef]
26. Su, C.; Berekute, A.K.; Yu, K.-P. Chitosan@TiO_2 Composites for the Adsorption of Copper(II) and Antibacterial Applications. *Sustain. Environ. Res.* **2022**, *32*, 27. [CrossRef]
27. Ablouh, E.; Hanani, Z.; Eladlani, N.; Rhazi, M.; Taourirte, M. Chitosan Microspheres/Sodium Alginate Hybrid Beads: An Efficient Green Adsorbent for Heavy Metals Removal from Aqueous Solutions. *Sustain. Environ. Res.* **2019**, *29*, 5. [CrossRef]
28. Mohanasrinivasan, V.; Mishra, M.; Paliwal, J.S.; Singh, S.K.; Selvarajan, E.; Suganthi, V.; Subathra Devi, C. Studies on Heavy Metal Removal Efficiency and Antibacterial Activity of Chitosan Prepared from Shrimp Shell Waste. *3 Biotech* **2014**, *4*, 167–175. [CrossRef]
29. Zhang, L.; Zeng, Y.; Cheng, Z. Removal of Heavy Metal Ions Using Chitosan and Modified Chitosan: A Review. *J. Mol. Liq.* **2016**, *214*, 175–191. [CrossRef]
30. Begum, S.; Yuhana, N.Y.; Md Saleh, N.; Kamarudin, N.H.N.; Sulong, A.B. Review of Chitosan Composite as a Heavy Metal Adsorbent: Material Preparation and Properties. *Carbohydr. Polym.* **2021**, *259*, 117613. [CrossRef] [PubMed]
31. Hasan, S.; Ghosh, T.K.; Viswanath, D.S.; Boddu, V.M. Dispersion of Chitosan on Perlite for Enhancement of Copper(II) Adsorption Capacity. *J. Hazard. Mater.* **2008**, *152*, 826–837. [CrossRef]
32. Latorre, M.; Troncoso, R.; Uauy, R. Chapter 4—Biological Aspects of Copper. In *Clinical and Translational Perspectives on WILSON DISEASE*; Kerkar, N., Roberts, E.A., Eds.; Academic Press: Cambridge, MA, USA, 2019; pp. 25–31. ISBN 978-0-12-810532-0.
33. Rehman, M.; Liu, L.; Wang, Q.; Saleem, M.H.; Bashir, S.; Ullah, S.; Peng, D. Copper Environmental Toxicology, Recent Advances, and Future Outlook: A Review. *Environ. Sci. Pollut. Res.* **2019**, *26*, 18003–18016. [CrossRef]
34. Bost, M.; Houdart, S.; Oberli, M.; Kalonji, E.; Huneau, J.-F.; Margaritis, I. Dietary Copper and Human Health: Current Evidence and Unresolved Issues. *J. Trace Elem. Med. Biol.* **2016**, *35*, 107–115. [CrossRef] [PubMed]
35. Locovei, C.; Chiriac, A.-L.; Miron, A.; Iftimie, S.; Antohe, V.-A.; Sârbu, A.; Dumitru, A. Synthesis of Titanium Nitride via Hybrid Nanocomposites Based on Mesoporous TiO_2/Acrylonitrile. *Sci. Rep.* **2021**, *11*, 5055. [CrossRef]
36. Al Shaqsi, N.H.K.; Al Hoqani, H.A.S.; Hossain, M.A.; Al Sibani, M.A. Isolation, Characterization and Standardization of Demineralization Process for Chitin Polymer and Minerals from the Crabs Waste of Portunidae Segnis. *Adv. Biomark. Sci. Technol.* **2020**, *2*, 45–58. [CrossRef]
37. Al-Sagheer, F.; Al-Sughayer, M.A.; Muslim, S.; Elsabee, M. Extraction and Characterization of Chitin and Chitosan from Marine Sources in Arabian Gulf. *Carbohydr. Polym.* **2009**, *77*, 410–419. [CrossRef]

38. Kuczajowska-Zadrożna, M.; Filipkowska, U.; Jóźwiak, T. Adsorption of Cu (II) and Cd (II) from Aqueous Solutions by Chitosan Immobilized in Alginate Beads. *J. Environ. Chem. Eng.* **2020**, *8*, 103878. [CrossRef]
39. Kudłacik-Kramarczyk, S.; Głąb, M.; Drabczyk, A.; Kordyka, A.; Godzierz, M.; Wróbel, P.S.; Krzan, M.; Uthayakumar, M.; Kędzierska, M.; Tyliszczak, B. Physicochemical Characteristics of Chitosan-Based Hydrogels Containing Albumin Particles and Aloe Vera Juice as Transdermal Systems Functionalized in the Viewpoint of Potential Biomedical Applications. *Materials* **2021**, *14*, 5832. [CrossRef]
40. Zhang, H.; Xu, L.; Yang, F.; Geng, L. The Synthesis of Polyacrylonitrile/Carbon Nanotube Microspheres by Aqueous Deposition Polymerization under Ultrasonication. *Carbon* **2010**, *48*, 688–695. [CrossRef]
41. Thamaphat, K.; Limsuwan, P.; Ngotawornchai, B. Phase Characterization of TiO_2 Powder by XRD and TEM. *Agric. Nat. Resour.* **2008**, *42*, 357–361.
42. Miron, A.; Sarbu, A.; Zaharia, A.; Sandu, T.; Iovu, H.; Fierascu, R.C.; Neagu, A.-L.; Chiriac, A.-L.; Iordache, T.-V. A Top-Down Procedure for Synthesizing Calcium Carbonate-Enriched Chitosan from Shrimp Shell Wastes. *Gels* **2022**, *8*, 742. [CrossRef]
43. Swain, S.K.; Dash, S.; Kisku, S.K.; Singh, R.K. Thermal and Oxygen Barrier Properties of Chitosan Bionanocomposites by Reinforcement of Calcium Carbonate Nanopowder. *J. Mater. Sci. Technol.* **2014**, *30*, 791–795. [CrossRef]
44. Abebe, B.; Murthy, H.C.A.; Amare, E. Summary on Adsorption and Photocatalysis for Pollutant Remediation: Mini Review. *J. Encapsulation Adsorpt. Sci.* **2018**, *08*, 225–255. [CrossRef]
45. Wan, M.-W.; Kan, C.-C.; Rogel, B.D.; Dalida, M.L.P. Adsorption of Copper (II) and Lead (II) Ions from Aqueous Solution on Chitosan-Coated Sand. *Carbohydr. Polym.* **2010**, *80*, 891–899. [CrossRef]
46. Cheng, Z.; Liu, X.; Han, M.; Ma, W. Adsorption Kinetic Character of Copper Ions onto a Modified Chitosan Transparent Thin Membrane from Aqueous Solution. *J. Hazard. Mater.* **2010**, *182*, 408–415. [CrossRef]
47. Orozco, C.I.; Freire, M.S.; Gómez-Díaz, D.; González-Álvarez, J. Removal of Copper from Aqueous Solutions by Biosorption onto Pine Sawdust. *Sustain. Chem. Pharm.* **2023**, *32*, 101016. [CrossRef]
48. Emara, A.A.A.; Tawab, M.A.; El-ghamry, M.A.; Elsabee, M.Z. Metal Uptake by Chitosan Derivatives and Structure Studies of the Polymer Metal Complexes. *Carbohydr. Polym.* **2011**, *83*, 192–202. [CrossRef]
49. Matias, P.M.C.; Sousa, J.F.M.; Bernardino, E.F.; Vareda, J.P.; Durães, L.; Abreu, P.E.; Marques, J.M.C.; Murtinho, D.; Valente, A.J.M. Reduced Chitosan as a Strategy for Removing Copper Ions from Water. *Molecules* **2023**, *28*, 4110. [CrossRef] [PubMed]
50. Nikiforova, T.E.; Kozlov, V.A.; Telegin, F.Y. Chemisorption of Copper Ions in Aqueous Acidic Solutions by Modified Chitosan. *Mater. Sci. Eng. B* **2021**, *263*, 114778. [CrossRef]
51. Wu, F.-C.; Tseng, R.-L.; Juang, R.-S. Characteristics of Elovich Equation Used for the Analysis of Adsorption Kinetics in Dye-Chitosan Systems. *Chem. Eng. J.* **2009**, *150*, 366–373. [CrossRef]
52. Dos Santos, L.N.; Santos, A.S.; Das Graças Fernandes Dantas, K.; Ferreira, N.R. Adsorption of Cu (II) Ions Present in the Distilled Beverage (Sugar Cane Spirit) Using Chitosan Derived from the Shrimp Shell. *Polymers* **2022**, *14*, 573. [CrossRef]
53. Chang, M.-Y.; Juang, R.-S. Equilibrium and Kinetic Studies on the Adsorption of Surfactant, Organic Acids and Dyes from Water onto Natural Biopolymers. *Colloids Surf. A Physicochem. Eng. Asp.* **2005**, *269*, 35–46. [CrossRef]
54. An, B. Cu(II) and As(V) Adsorption Kinetic Characteristic of the Multifunctional Amino Groups in Chitosan. *Processes* **2020**, *8*, 1194. [CrossRef]
55. Hameed, B.H.; El-Khaiary, M.I. Malachite Green Adsorption by Rattan Sawdust: Isotherm, Kinetic and Mechanism Modeling. *J. Hazard. Mater.* **2008**, *159*, 574–579. [CrossRef]
56. Moussout, H.; Ahlafi, H.; Aazza, M.; Maghat, H. Critical of Linear and Nonlinear Equations of Pseudo-First Order and Pseudo-Second Order Kinetic Models. *Karbala Int. J. Mod. Sci.* **2018**, *4*, 244–254. [CrossRef]

International Journal of
Molecular Sciences

MDPI

Article

α-Chitosan and β-Oligochitosan Mixtures-Based Formula for In Vitro Assessment of Melanocyte Cells Response

Verginica Schröder [1], Daniela Gherghel [2,*], Manuela Rossemary Apetroaei [3], Cristiana Luminița Gîjiu [4], Raluca Isopescu [4], Daniel Dinculescu [4,*], Miruna-Maria Apetroaei [5], Laura Elena Enache [4], Cosmin-Teodor Mihai [6,†], Ileana Rău [4] and Gabriela Vochița [2,†]

1 Departament of Cellular and Molecular Biology, Faculty of Pharmacy, Ovidius University of Constanta, 6 Capt. Aviator Al. Șerbănescu Street, Campus C, 900470 Constanta, Romania; verginica.schroder@univ-ovidius.ro
2 Institute of Biological Research Iasi, Branch of NIRDBS—National Institute of Research and Development of Biological Sciences Bucharest, 47 Lascar Catargi, 700107 Iasi, Romania; gabrielacapraru@yahoo.com
3 Department of Marine Electric and Electronic Engineering, Faculty of Marine Engineering, Mircea cel Batran Naval Academy, 1 Fulgerului Street, 900218 Constanta, Romania; manuela.apetroaei@anmb.ro
4 Faculty of Chemical Engineering and Biotechnologies, National University of Science and Technology POLITEHNICA Bucharest, 011061 Bucharest, Romania; luminita.gijiu@upb.ro (C.L.G.); raluca.isopescu@upb.ro (R.I.); laura.ena21@gmail.com (L.E.E.); ileana.rau@upb.ro (I.R.)
5 Faculty of Pharmacy, Carol Davila University of Medicine and Pharmacy, 6 Traian Vuia Street, 020956 Bucharest, Romania; miruna-maria.apetroaei@rez.umfcd.ro
6 Praxis Medical Investigations, Moara de Vant St. 35, 700376 Iasi, Romania; mihai.cosmin.teo@gmail.com
* Correspondence: daniela.gherghel@icbiasi.ro (D.G.); daniel.dinculescu@upb.ro (D.D.)
† These authors contributed equally to this work.

Abstract: Chitosan is a natural polymer with numerous biomedical applications. The cellular activity of chitosan has been studied in various types of cancer, including melanoma, and indicates that these molecules can open new perspectives on antiproliferative action and anticancer therapy. This study analyzes how different chitosan conformations, such as α-chitosan (CH) or β-oligochitosan (CO), with various degrees of deacetylation (DDA) and molar mass (MM), both in different concentrations and in CH–CO mixtures, influence the cellular processes of SK-MEL-28 melanocytes, to estimate the reactivity of these cells to the applied treatments. The in vitro evaluation was carried out, aiming at the cellular metabolism (MTT assay), cellular morphology, and chitinase-like glycoprotein YKL-40 expression. The in vitro effect of the CH–CO mixture application on melanocytes is obvious at low concentrations of α-chitosan/β-oligochitosan (1:2 ratio), with the cell's response supporting the hypothesis that β-oligo-chitosan amplifies the effect. This oligochitosan mixture, favored by the β conformation and its small size, penetrates faster into the cells, being more reactive when interacting with some cellular components. Morphological effects expressed by the loss of cell adhesion and the depletion of YKL-40 synthesis are significant responses of melanocytes. β-oligochitosan (1.5 kDa) induces an extension of cytophysiological effects and limits the cell viability compared to α-chitosan (400–900 kDa). Statistical analysis using multivariate techniques showed differences between the CH samples and CH–CO mixtures.

Keywords: α-chitosan; β-oligochitosan; SK-MEL-28 melanocytes; YKL-40

1. Introduction

Melanoma is one of the cancers with increasing incidence worldwide [1]. The mechanisms that induce phenotypic plasticity of tumor cells [2,3], as well as the methods of therapy [1,4,5], are topics of great interest. Chemotherapy is less effective in this type of cancer [6], and resistance to therapy is a frequent issue. Therefore, alternative options are being sought to improve therapeutic outcomes and patient survival rates [5,7,8]. Using

molecules of polymeric nature [1,4] or nanoparticles [1,5,9] targeting cancer cells or different intracellular components is a promising alternative.

Chitosan, obtained by deacetylation of chitin, is a potential drug delivery molecule used in targeted melanoma therapy [4,5,9]. Chitin (CT) and chitosan (CH) are among the most important biopolymers obtained from natural sources, including recycled waste, and are considered prospective molecules due to the diversity of applications [10,11]. Chitin is a homopolymer of N-acetyl-β-glucosamine (GlcNAc) and is the second most abundant polymer in nature. In vivo structural characteristics indicate that chitin is among the most resistant organic materials; this property is based on the molecular arrangement and the ability to combine with proteins or other components to form hybrid materials. In the evolved forms of eukaryotes and human cells, chitin structural units (chitobioses) are present at the level of glycoproteins or chitotriosidases, with a role in immune mechanisms in macrophages [12].

Chitosan is one of the biopolymers with applications in different fields, such as medicine, biotechnology, drug delivery, etc. [13–16]. Chitosan derives from various natural sources such as shellfish waste, molluscs, insect sloughs (exuviae), etc. The emerging modern research trends are identifying new sources, such as mollusc egg capsules [17,18], or developing methods to increase the efficiency of obtaining these materials [19,20]. Depending on the natural source and the processing methods of both the source and the chitin, chitosan acquires molecular versatility [21–23]. Thus, in acidic solutions, the amino groups of chitosan can be protonated, giving a polycationic behavior (at pH less than 6). At an increasing pH of around 6.6, the amino groups are unprotonated and form interpolymeric bonds that could induce polymer remodeling and interaction with proteins [24].

This behavior gives chitosan capabilities related to solubility in slightly acidic aqueous media and active bioadhesivity to build bonds with negatively charged substances, which are important features for understanding biological action. These particularities are related to the possibility of making forms of chitosan carriers with applications in the medical field, like drug delivery [25,26]. With breaking or swelling capabilities, the chitosan molecular network can be optimized for the coordinated release of active substances in the aqueous environment [27]. This biomaterial's positive surface charge and biocompatibility allow it to effectively support cell growth, while its hydrophilic surface facilitates cell adhesion, proliferation, and differentiation [24,26,28].

Although these abilities make chitosan one of the polymers with the most studied applications, from a biological point of view, some phenomena limit the use of chitosan or low-deacetylating chitin-type polymers. The limitations of biological actions for these molecules relate to physicochemical characteristics such as solubility, viscosity, or molar mass of chitosan (CH) and chitin (CT).

The biological actions of chitosan (polymer or oligomer) can also be influenced by polymorphic forms. The conformation of the chains is modulated by temperature, ions, and pH so that cellular components (membranes, endosomes, lysosomes) can be targeted. Chitin polysaccharides can be of several types, α, β, and γ, differing in the arrangement of chains in the crystalline region [29].

Specific forms of chitosan or chitin from marine organisms are contingent upon the level of evolution [29]. Therefore, less-developed forms that have not yet been calcified could be significant sources of β-oligochitosan. On the other hand, evolutionary forms contain α-chitin, which, in its complex crystalline state, provides sea creatures with support and strength, found as mineralized shells [30]. Thus, based on the evolved forms of organisms, the different sources of chitin are represented by α-chitin, found mainly in the exoskeleton of crustaceans or insects; β-chitin, which has been identified in molluscs (squid) and algae (diatoms); while γ-chitin is found in fungi and yeasts [31–33]. After deacetylation, α- and β-chitosan can be used for developing biological applications. However, few studies can be found on the uses of β-chitosan due to its relatively limited availability, especially from squid species. Still, this compound is notable for its structural changes influencing solubility, swelling capacity, and biocompatibility [33].

Chitooligosaccharides (COS) have recently gained attention due to their synthesis through the degradation of chitin and chitosan. These include 2–20 units (β-(1-4)-N-acetyl-D-glucosamine and predominantly D-glucosamine residues) characterized by a low molar mass (less than 3900 Da). These compounds have been gaining much interest due to their increased solubility in water compared to chitin and chitosan [34,35].

The biological activity of these chitooligosaccharides is yet insufficiently established, as it depends on several parameters, such as polymerization degree, molar mass, deacetylation degree, acetylation fractions, and the origin of acetylation [19].

The β-(1-4)-glycosidic bonds between the N-acetylglucosamine and glucosamine units of chitin and chitooligosaccharides [23] are degraded by chitinase hydrolysis enzymes, which exist in different organisms, from viral forms, archaebacteria, bacteria, fungi, protists, and arthropods to plants and mammals. They are involved in many physiological processes, such as nutrition, parasitism, morphogenesis, and immunity.

Additionally, several inactive chitinases (chitinase-like lectins) are present in organisms. However, these lectins have no catalytic activity but a functional regulatory role. The best-known lectins belong to the 18 and 19 glycosyl hydrolase families of chitinases, and few belong to the 23 and 48 families, as identified in the last few years [36,37].

Hollak et al. detected the first human chitinase, which was found to have high chitinolytic activity in the serum of patients with Gaucher disease. Due to its ability to hydrolyze chitotriobase, it has been named chitotriosidase. Activated macrophages specifically express this protein and have a pH optimum of 6 [38].

Boot et al. discovered another chitinase with a catalytic capacity at pH 2, hence its name—acidic mammalian chitinase (AMCase). Genes for these enzymes have activity in the gastric epithelium, in lung macrophages, and in the lung epithelium on asthmatic inflammation [37,39].

These aspects suggest the existence of both chitooligosaccharide and chitin components in the extracellular and intracellular space, AMCase being active in lysosomes. The substrate probably reaches the cellular system in the form of chitooligosaccharides. Human chitinase-like proteins (CLPs) include YKL-40, YKL-39, and SI-CLP, molecules that are secreted by cancer cells, macrophages, neutrophils, synovial cells, and chondrocytes; of these, YKL-40 is the most investigated in cancer. This YKL-40 molecule is correlated with an inferior prognosis in breast, lung, prostate, liver, colon, and other cancers and is used as a predictive biomarker for tumorigenesis [40–43].

YKL-40 is also associated with an inflammatory effect in the intestine, for which a series of inhibitors, such as caffeine, theophylline, and pentoxifylline, may reduce the inflammatory process, thus showing promise in therapy. No selective small drug-like molecules that bind to the YKL-40 have been identified [37].

This study aims to evaluate how the polymorphic chitosan could modify the cell proliferation of a melanoma tumor culture (SK-MEL-28) by using α-and β-chitosan forms (polymer and oligomer) with different characteristics (deacetylation degree, DDA, molar mass, MM) and from different natural sources. For antiproliferative assay effects, in our study, α-chitosan from shrimp exoskeletons and β-oligochitosan from *R. venosa* egg capsule [17] mixtures were used. Our study hypothesized that the polymer mixture (α-chitosan–β-oligochitosan) induces various or synergistic interactions of biological activities. The intermolecular forces of β-chitosan are weaker than in α-chitosan, with these particularities making β-chitosan more soluble, reactive, and permeable [44]. Chitosan blending is a commonly employed technique for modifying polymers in terms of their functionality [29].

The present study also aims to identify the correlations between the chitosan forms and their influence on the expression of the chitinase-like protein YKL-40 on a melanoma cell line SK-MEL-28 (ATCC HTB-72). Studies have identified the affinity of YKL-40 for chitooligosaccharides [45], and experimental induction of these intracellular interactions could increase protein blockage. Taking into account the involvement of YKL-40 as a proinflammatory factor [46,47], its role in tumorigenesis [46,48,49], or in amplifying cancer progression (metastasis) [49–51], the alternative of inhibiting these proteins is a prospective direction.

2. Results

2.1. Physicochemical Characteristics of α-Chitosan and β-Chitosan

2.1.1. Scanning Electron Microscopy of the Powders

Chitosan powders analyzed by scanning electron microscopy (FEI Company, Hillsboro, OR, USA) reveal particles with different appearances. Thus, β-oligochitosan is granular (Figure 1a,b), with rounded shapes and delicate overlapping layers. It has a semicrystalline appearance and rounded edges that can be distinguished in Figure 1b. The α-polymer particles (Figure 1c,d) have a compact, semicrystalline disposition but with very sharp edges. The data can be correlated with the results of our previous study, which indicated that X-ray diffraction (XRD) measurements of chitosan samples showed a reduction in the crystallinity index with DD increasing [52]. These details suggest the size and, respectively, the morphology of the particles generated by the bonds between the oligomeric β-chitosan matrix and the polymeric α-chitosan. Particle size and morphology are characteristics of particular interest in drug delivery and pharmacokinetics polymer applications [53,54].

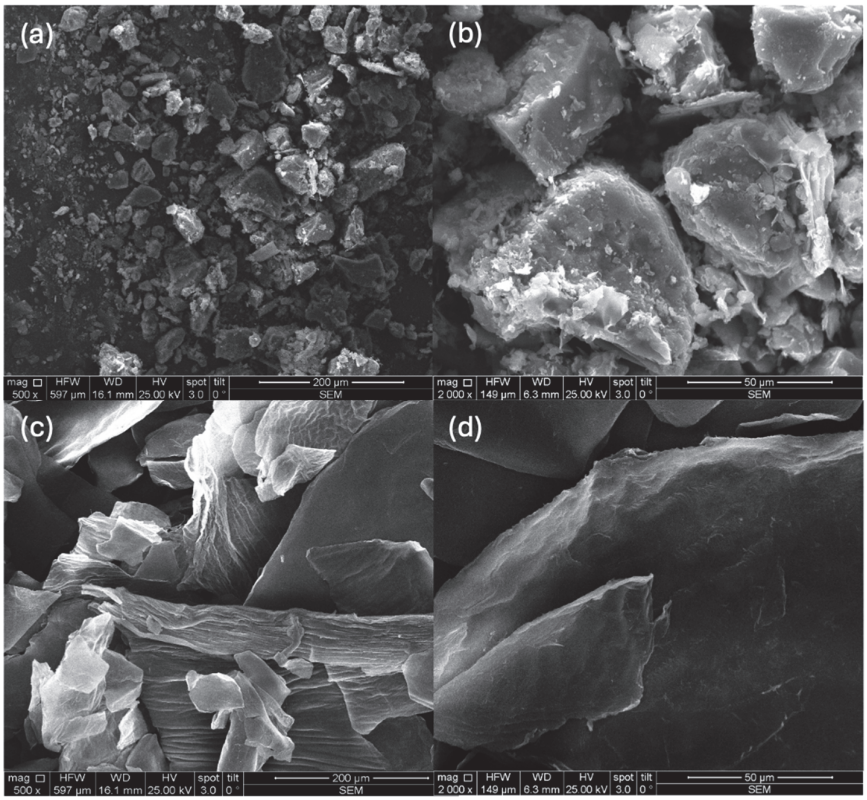

Figure 1. Details of powders analyzed by scanning electron microscopy (SEM); (**a**) β-oligochitosan magnification 500×; (**b**) β-oligochitosan magnification 2000×; (**c**) α-chitosan magnification 500×; (**d**) α-chitosan magnification 2000×.

Previous studies have shown that this chitosan has a β-type structure, semicrystalline with parallel polymer chains, characterized by a crystallinity index (33.53%) much lower than an α-type chitosan (40–80%) [55].

2.1.2. Biopolymer Solutions

To identify the optimal formula for in vitro cell assays, the chitosan and oligochitosan powders extracted from marine wastes were characterized by DDA and MM. The data obtained are presented in Table 1.

Table 1. Physicochemical characteristics of tested samples.

Sample Code	DDA (%)	MM (kDa)	Chitosan Conformation
CHP1	96.27	819.99	α-chitosan
CHP2	86.65	804.33	α-chitosan
CHP3	88.50	475.43	α-chitosan
COP4	70.00	1.50	β-oligochitosan
MIX1(mixture CHP1 + COP4) *	78.76	2.25	α-chitosan and β-oligochitosan (1:2)
MIX2 (mixture CHP2 + COP4) *	75.55	2.25	
MIX3 (mixture CHP3 + COP4) *	76.17	2.25	

* Calculated with Equations (1) and (2), respectively.

For the first time, this study uses mixtures of α-chitosan and β-oligochitosan solubilized in 1% acetic acid solutions to obtain the optimal formula for cell growth with broad applications. Given their versatility and their chemical structure and different characteristics (DDA and MM), these blended biopolymers were developed to confer various applications, especially in the medical and pharmaceutical fields [56].

The chitosan mixtures used in this study were formed using the blending technique. This process of blending α-chitosan with β-oligochitosan involves the mix of two biopolymers that, despite their chemical similarity, exhibit different physical and chemical characteristics because of variations in their molar mass and degree of deacetylation. Regarding the chemical characteristics of the blending process, several interactions and modifications that could enhance or modify the characteristics of the new formulation have been considered.

The novel combination of α-and β-chitosan used in this study is based on the interactions between their molecular chains, favored by the following key parameters: molar mass, deacetylation degree, and structural arrangement. It is well known that the molar mass value influences the solubility of each type of chitosan. Thus, the combination based on mixing α-chitosan with β-chitosan provides an equilibrium between the strength and flexibility of the new formulations.

2.1.3. Antioxidant Activity Assay

The antioxidant activity is reduced in the mixture compared to the nonblended samples, except for CHP1, where the mixture (MIX1) induces a minor change (from 13.28 ± 1.59% to 14.27 ± 1.81%) (Table 2). The polymer–oligomer interaction can explain the modification of the antioxidant activity; thus, a molecular remodeling occurs via the -OH or -NH_2 groups, initially unavailable for the anti-free radical's effect. The results indicate lower antioxidant activity of the tested samples.

Table 2. Evaluation of antioxidant activity (%) for samples used in SK-MEL-28 cell culture assay (CHP1, CHP2, CHP3, COP4, MIX1, MIX2, MIX3); DPPH assays were evaluated at 37 °C.

Samples	Antioxidant Activity (%), ± SD
CHP1	13.28 ± 1.59
CHP2	18.79 ± 1.04
CHP3	15.15 ± 0.05
COP4	11.57 ± 0.11
MIX1	14.27 ± 1.81
MIX2	10.52 ± 0.16
MIX3	11.63 ± 1.37

2.2. Biological Effects

2.2.1. Evaluation of the Effects on Cell Viability by the MTT Method

The MTT viability assay revealed a decrease in the viability of SK-MEL-28 melanoma cells with the increase in the tested doses and in the treatment duration. Thus, at the minimum tested concentration (4.375 µg/mL), cell viability after 24 h of treatment varied from 99.08% in the presence of the oligomer (MIX1) to 92.57% when the CHP2 polymer was added. The viability of SK-MEL-28 cells at 48 h, under the action of the minimum tested dose, ranged between 96.60% (MIX2) and 75.04% (MIX3), proving an increase in the cytotoxic effect. A more pronounced interference with cell viability was observed as the dose increased at the maximum concentration (35 µg/mL) with values ranging from 85.62% (CHP1) to 74.58% (CHP2) after 24 h of treatment. Significant decreases in cell viability were observed after 48 h of contact of SK-MEL-28 cells with the studied solutions, with values of 72.03% (CHP3) and 61.85% (CHP2). All these aspects are illustrated in Figure 2a,b.

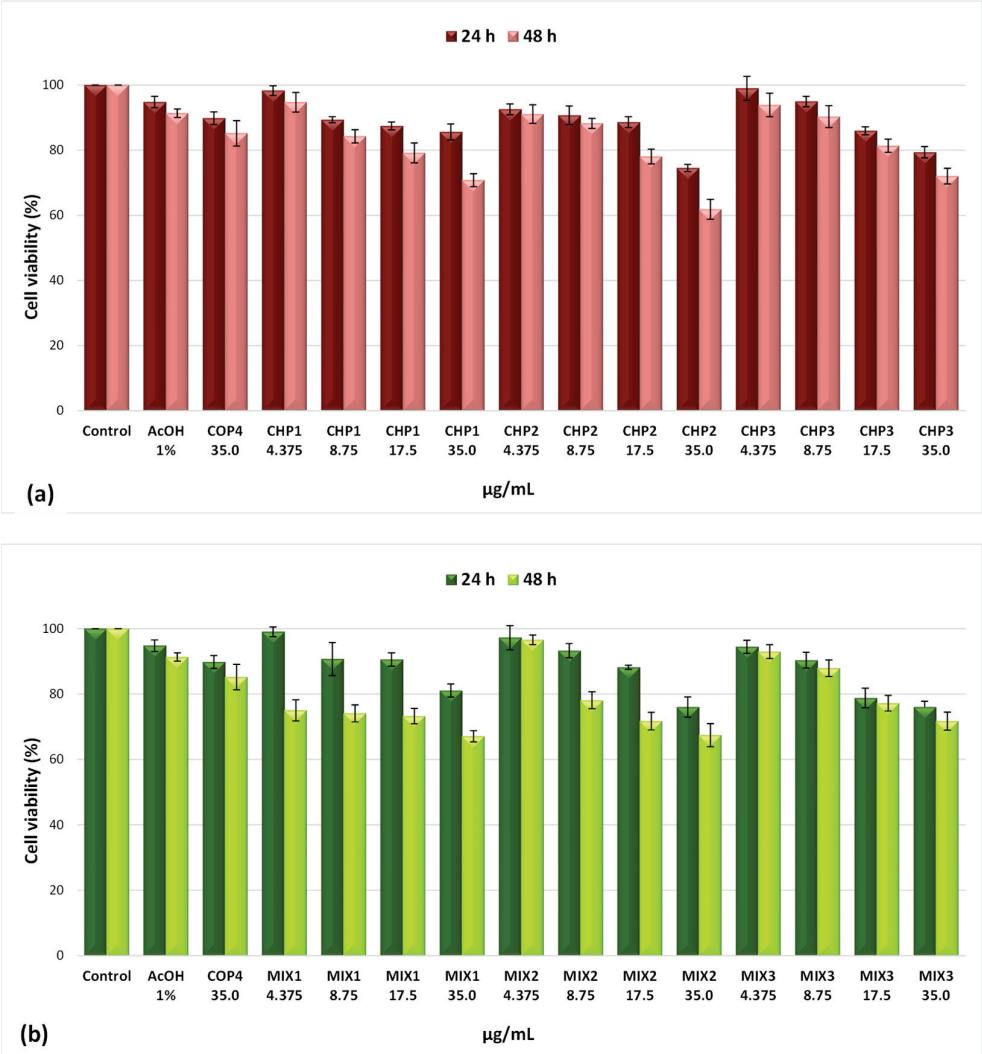

Figure 2. SK-MEL-28 cell viability after 24 h and 48 h treatment with different chitosan polymers—CHP1, CHP2, CHP3—(**a**) and mixtures—MIX1, MIX2, MIX3—(**b**); as well as acetic acid (AcOH) and oligomer (COP4) (mean values and SD).

Pursuant to the cell viability test, it was found that the formulations with oligochitosan showed a significant cytotoxic effect after 48 h of treatment and at the maximum dose. In the case of the MIX2 combination, a slightly higher viability value was recorded (67.46%), compared to 61.85% determined in the case of the CHP2 polymer. The most bioactive

sample was MIX1, with cell viability of 67.11%, compared to the 70.83% value found in the case of polymer CHP1. The solvent used, 1% acetic acid, did not have a negative effect on cell viability (91.36%), thus proving its nontoxic nature. The degree of cytotoxicity of the oligomer (COP4) was insignificant, registering a cell viability value of 85.20% compared to the untreated control (100%).

The IC_{50} values indicate slight changes in the effect at 24 h of exposure to the CHP1 compound (88.74 μg/mL) compared to CHP2 (78.45 μg/mL) and CHP3 (73.98 μg/mL). Similar values were obtained in the case of mixtures, varying between 73.40 μg/mL (MIX2) and 75.01 μg/mL (MIX1 and MIX3). After 48 h of exposure, differences between the samples are noticeable without showing a clear relationship with sample type (Table 3).

Table 3. Inhibition concentrations (IC_{50}) values after treatment application with various formulas of chitosan evaluated.

Samples	IC_{50} 24 h (μg/mL)	IC_{50} 48 h (μg/mL)
CHP1	88.74	62.91
CHP2	78.45	47.01
CHP3	73.98	64.58
MIX1	75.01	59.21
MIX2	73.40	53.06
MIX3	75.01	64.22

2.2.2. The Cell Morphology Test

Evaluation of the interaction of different chitosan formulas with the morphology of SK-MEL-28 cells revealed that the main changes at the cytomorphological level consisted of the reduction in the ability to adhere and to form a cell monolayer.

The loss of the intercellular connections that ensured the unity of the monolayer leading to the reduction in the number of confluent cells and the appearance of isolated cells, more or less spherical floating in the culture medium, was much more intense at the maximum tested concentration (35 μg/mL) and after 48 h of treatment (Figures 3–8).

2.2.3. Determination of YKL-40 Protein Expression

YKL-40 is a glycoprotein synthesized by cells in response to microenvironmental factors, which induces the modeling of cellular activity [16]. In the present study, the evaluation of YKL-40 activity led to the recording of some quantitative variations in the level of this protein. After lipopolysaccharide (LPS) stimulation, SK-MEL-28 cells increased glycoprotein synthesis by 9.27 pg/mL, representing an increase of 3.17%, compared to the unstimulated cells. According to the results after the application of the mixtures (Figure 9), the level of YKL-40 decreases in the case of the tested solutions by 7% for MIX2, 18% for MIX1, and 28% when administering the MIX3 mixture compared to the control sample. The inhibition effects of YKL-40 synthesis are related to the presence of chitosan oligomers. In the samples without oligochitosan, increases in the level of YKL-40 by 9% (CHP2, LPS stimulated) and 12% (CHP3, LPS stimulated), respectively, were found. No changes were noted that correlate with the particularities of the polymer, which denotes similar mechanisms of molecular stimulation in the cell.

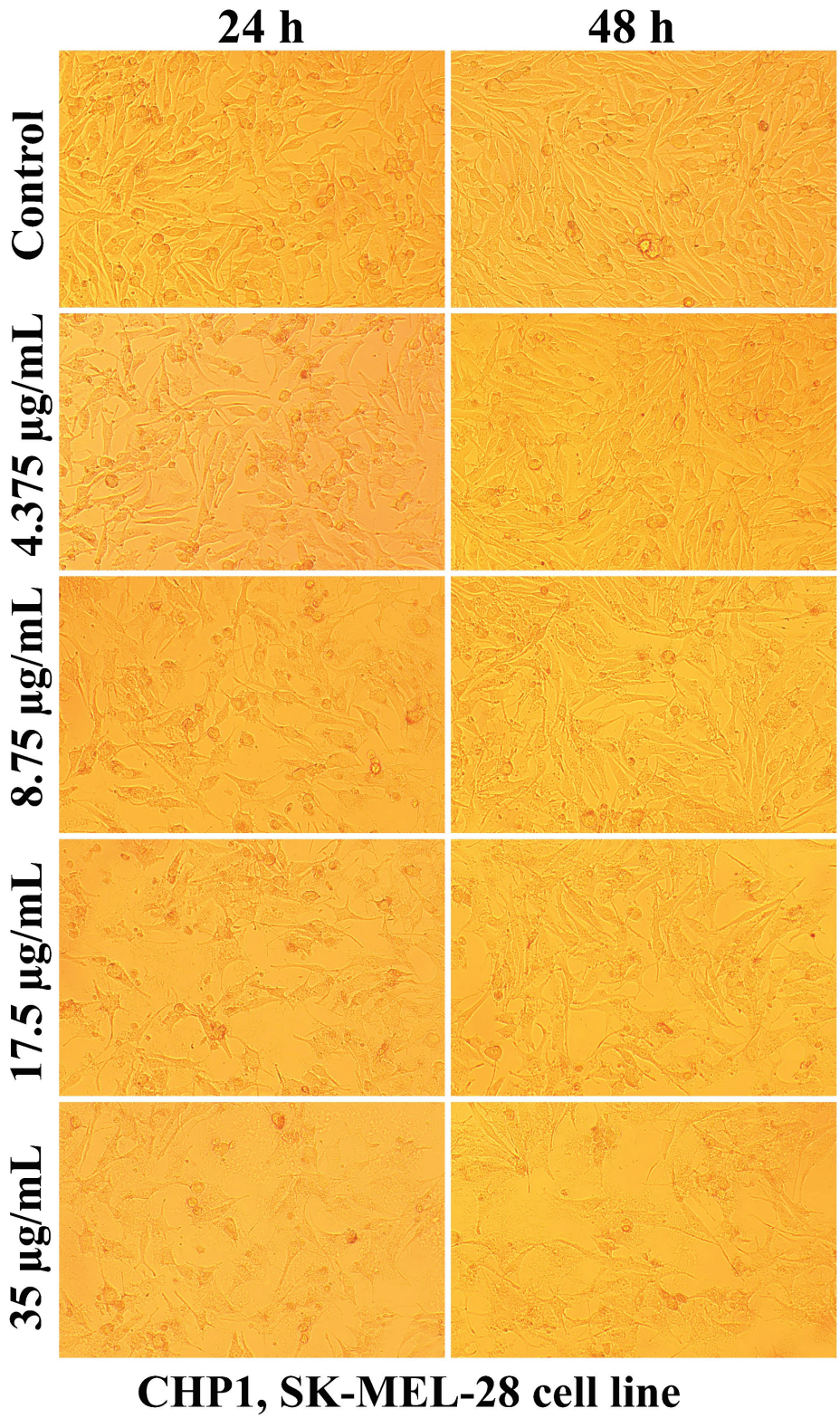

Figure 3. Morphological aspects of SK-MEL-28 human melanoma cells after CHP1 treatment for 24 and 48 h.

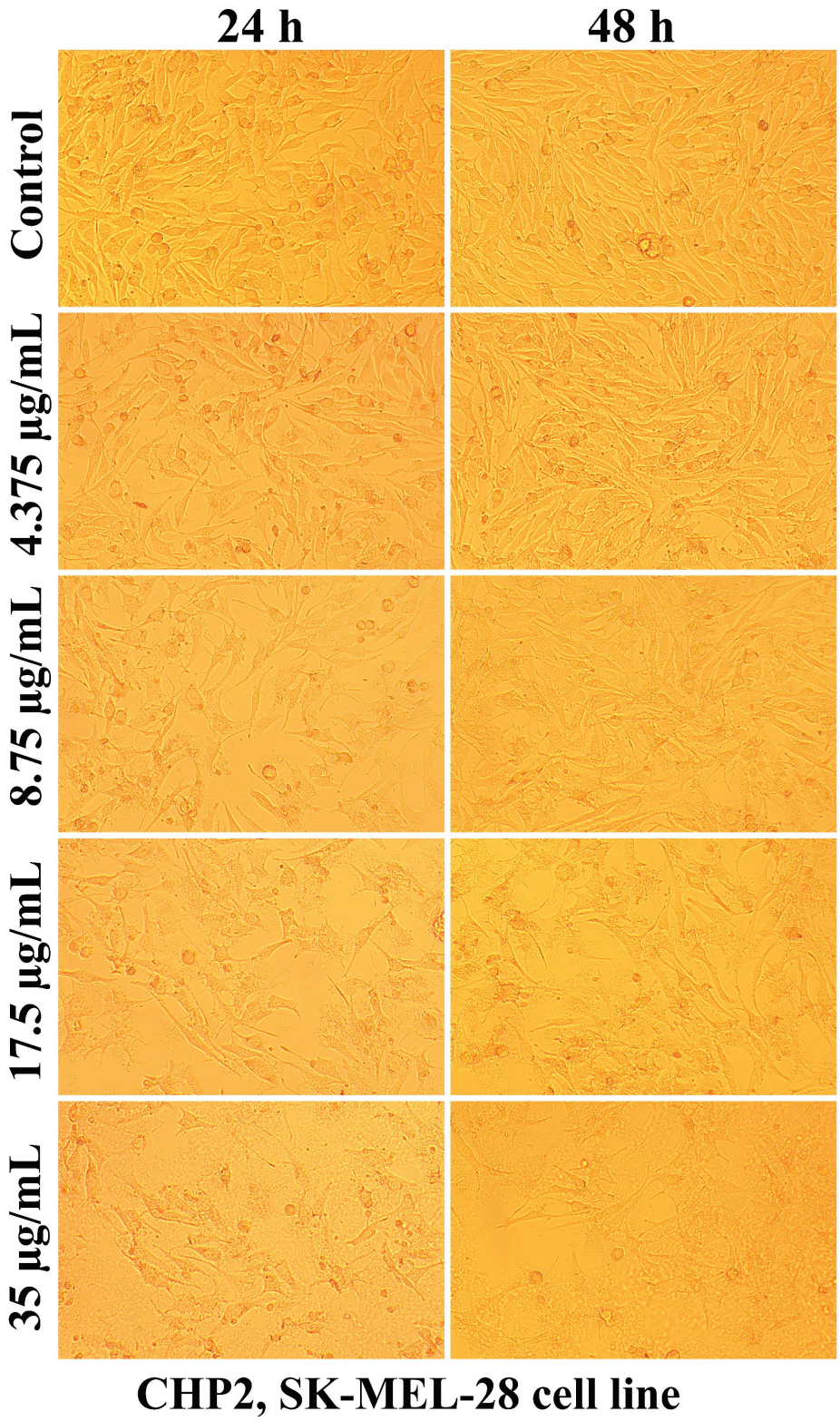

Figure 4. Morphological aspects of SK-MEL-28 human melanoma cells after CHP2 treatment for 24 and 48 h.

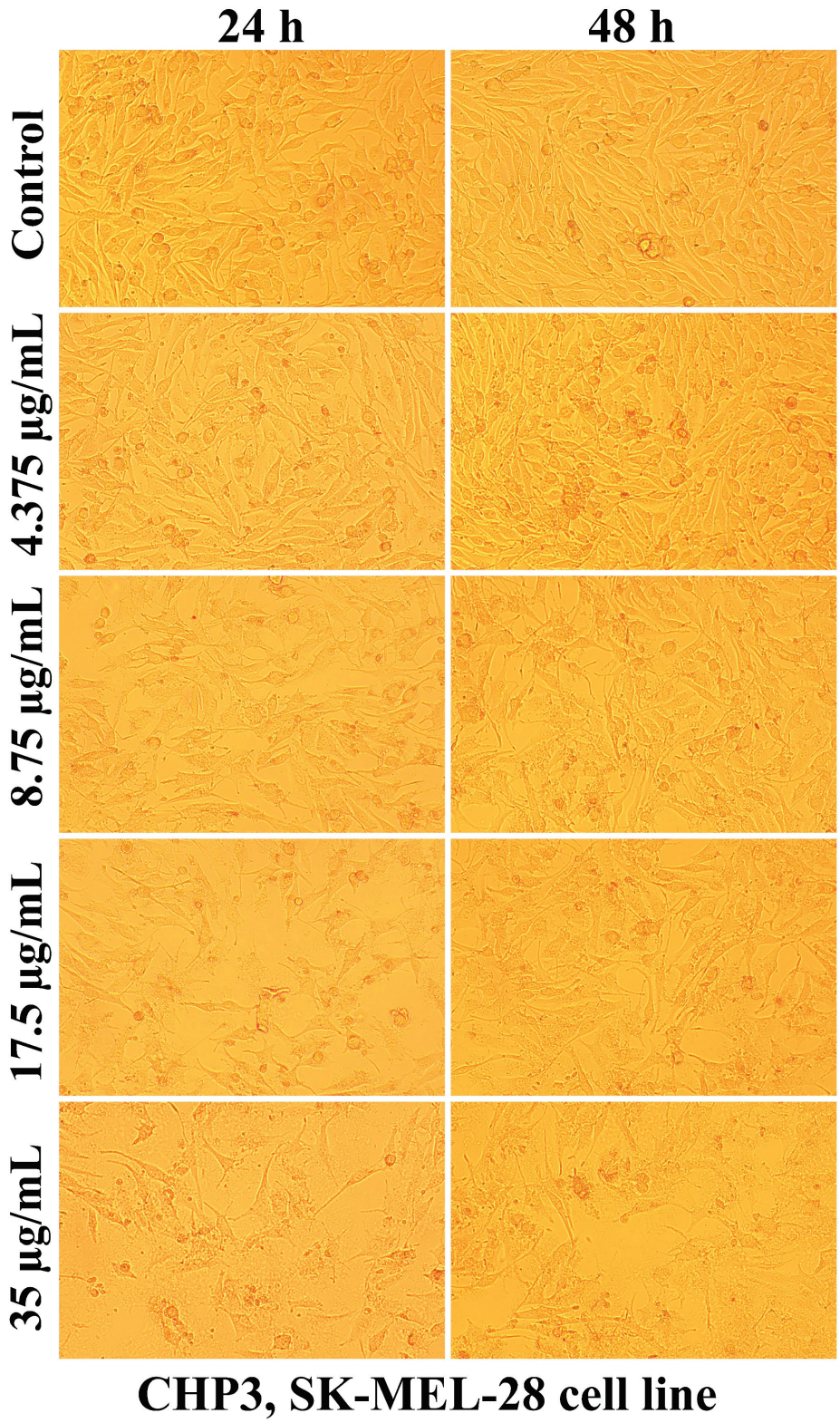

Figure 5. Morphological aspects of SK-MEL-28 human melanoma cells after CHP3 treatment for 24 and 48 h.

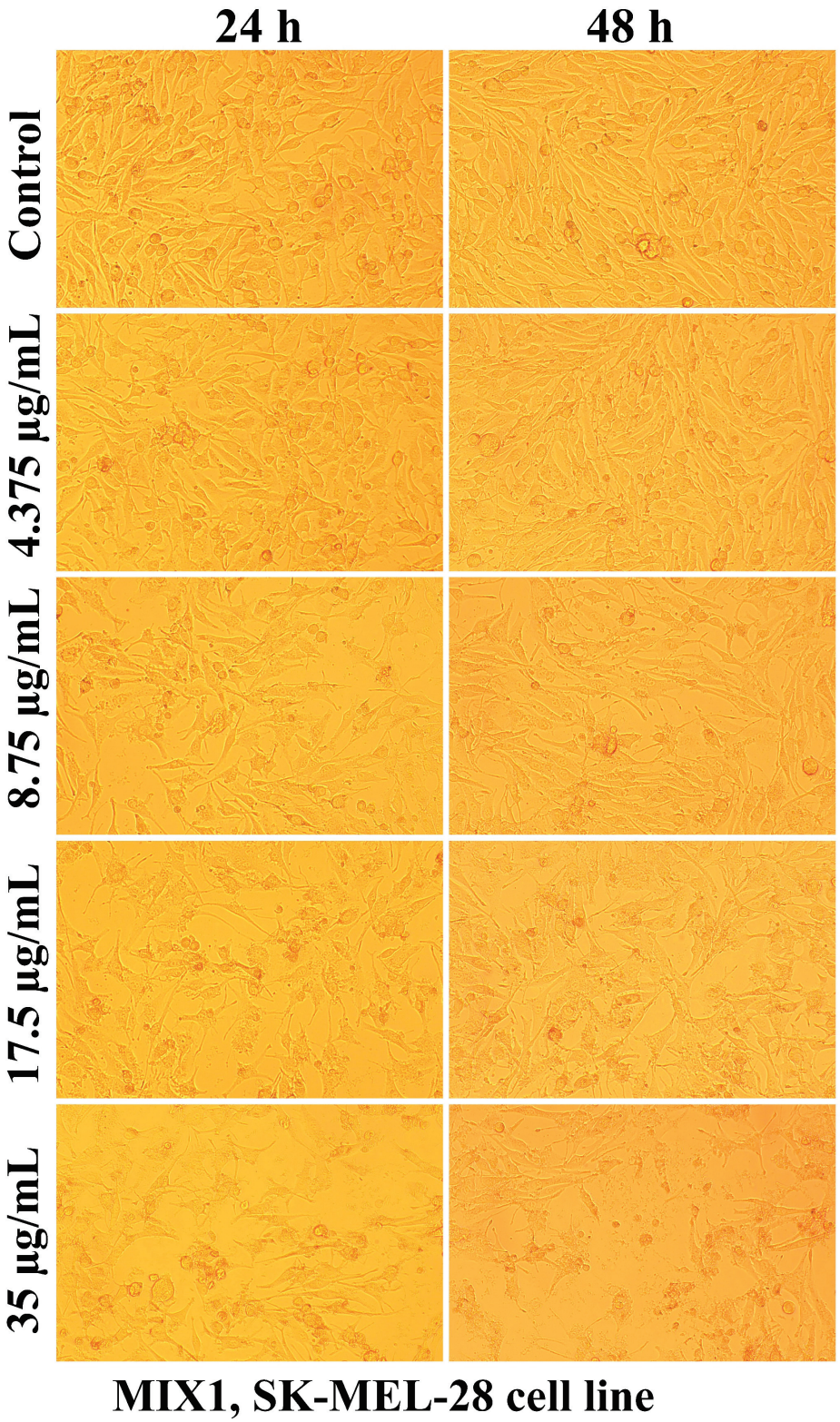

Figure 6. Morphological aspects of SK-MEL-28 human melanoma cells after treatment with MIX1 for 24 and 48 h.

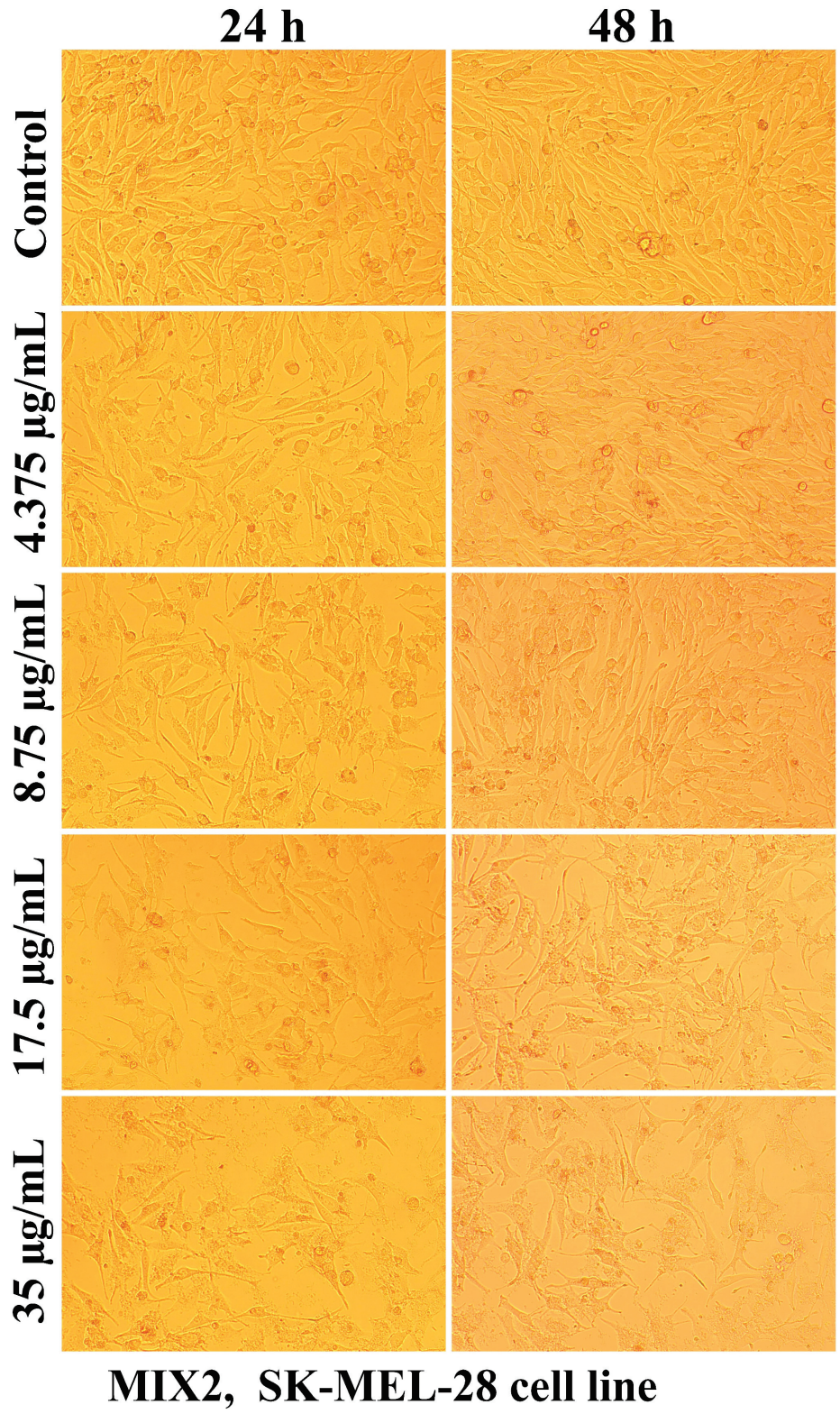

Figure 7. Morphological aspects of SK-MEL-28 human melanoma cells after treatment with MIX2 for 24 and 48 h.

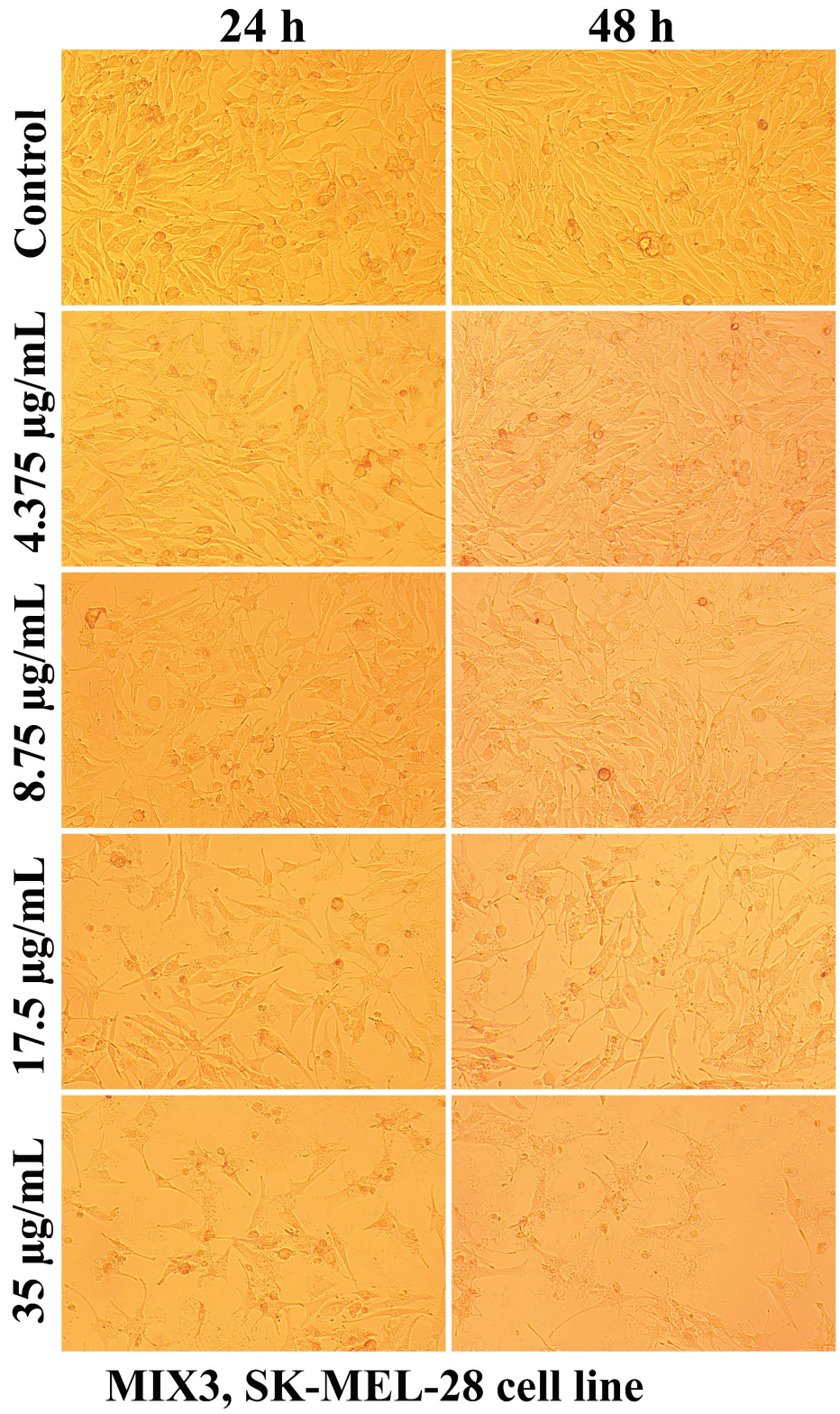

Figure 8. Morphological aspects of SK-MEL-28 human melanoma cells after treatment with MIX3 for 24 and 48 h.

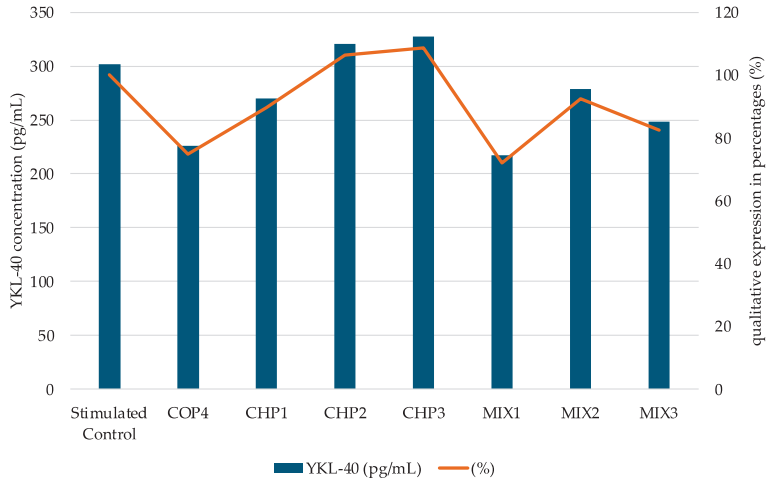

Figure 9. YKL-40 levels (pg/mL) samples interpolated from the standard curve and percentage expression of samples compared with control; SK-MEL-28 human melanoma cells LPS stimulated and α-chitosan (CHP1, CHP2, CHP3) and α-chitosan–β-oligochitosan (1:2) (MIX1, MIX2, MIX3) samples treatment (mean values); qualitative expression percentages among the samples and the control (LPS stimulated).

YKL-40 expression is identified at the cytoplasmic level, or, in the case of tumors, in the extracellular matrix, which denotes its exocytosis while maintaining the negative cell membrane [17]. The study on several types of tumor cells highlighted the in vitro low expression of this protein, which is also pointed out in our studies, the evaluations being of the order of pg/mL.

2.3. Statistical Analysis of Experimental Data

The results obtained using chitosan and oligochitosan mixtures were statistically analyzed using principal component analysis (PCA) and ANOVA.

A global view aiming to emphasize the differences between the six different experimental conditions according to the use of three chitosan samples (CHP1, CHP2, and CHP3) and their mixtures with oligochitosan, denoted by MIX1, MIX2, and MIX3, respectively, was carried out using PCA. These pure chitosans and blended biopolymers were characterized by six variables linked to their main characteristics (DDA and MM) and by the effects in biological tests: the enhancement of glycoprotein YKL-40 and the IC_{50} indexes for a contact time of 24 h (IC_{50}-24) and 48 h (IC_{50}-48) during the treatment of SK-MEL-28 cells as well as the antioxidant capacity (DPPH). The DDA value of the mixtures was calculated (Equation (1)) considering the mass ratios chitosan/oligochitosan (1/2) used and the DDAs of chitosan and oligochitosan, taking into consideration that the basic chitin–chitosan dimer is the same in all structures.

$$DDA_{mix} = \left(DDA_{chitosan} + 2 \cdot DDA_{oligochitosan}\right)/3 \quad (1)$$

The mean molar mass of the mixtures was calculated using mol base, considering the molar mass of chitosan and oligo-chitosan and the mass ratio in the mix, which is 1/2 (Equation (2)).

$$MM_{mix} = 3/\left(1/MM_{chitosan} + 2/MM_{oligochitosan}\right) \quad (2)$$

According to PCA, the six variables implied were grouped in principal components (PCs), which encompasses the variability in the dataset in decreasing order and also shows a possible grouping of the samples. The first three PCs reflect about 90% of the variability (PC1—49%, PC2—22%, PC3—21%), and the representation of the samples in PC1–PC2 coordinates (Figure 10) shows that the chitosan samples are clearly separated from the mixture samples.

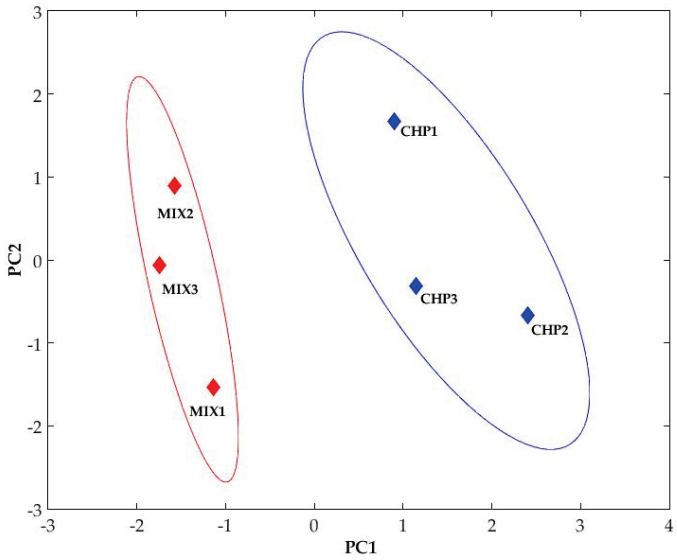

Figure 10. Samples representation in the first two PCA components.

Analyzing the variable loadings on PC1 and PC2 as expected, the highest loading in PC1 corresponds to the MM, which drastically varied between the samples, followed by the loading of DPPH (91% from the loading of MM) and DDA and YKL40, about 80% from the loading of MM. IC_{50}-24 h and IC_{50}-48 h have high loadings in PC2 and PC3, respectively. This analysis demonstrates that the sample differentiation is made by modifying MM and DDA due to mixing and, to a considerable extent, due to the different effects in the biological system (YKL-40 synthesis and antioxidant capacity).

Figure 11 depicts the relative importance of variable loadings and proves the positive correlation between MM and YKL-40, MM and DPPH, with DDA and DPPH standing for the decrease in protein YKL-40 when the molar mass is lower and increase in antioxidant capacity at higher deacetylation degrees. Therefore, the mixture chitosan–oligochitosan can improve both the antioxidant capacity and the DDA of the mixture, which is enhanced by the presence of chitosan. At the same time, the molar mass is mainly influenced by the oligomer, which leads to an important decrease in the YKL-40 generation.

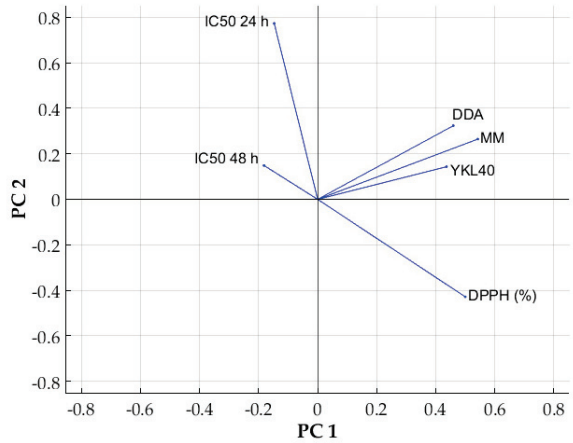

Figure 11. Variable loadings on the first two components.

The experimental viability of SK-MEL-28 cells treated with various solutions containing chitosan and chitosan–oligochitosan mixture was further analyzed using the factor analysis technique. The factors examined are the biopolymer type, the solution concentration (4.375, 8.75, 17.5, and 35 μg/mL), and contact duration (24 and 48 h). The three-way

ANOVA performed in the frame of Matlab2023 (Table 4) shows *p*-values for all three factors lower than 0.05, which stands for their significance in the variation of the cells' viability.

Table 4. Analysis of variance in three-way ANOVA.

Source of Variation	SS	df	MS	F	*p*-Value
Time	685.58	1	685.58	51.58	0
Concentration	2927.71	3	975.90	73.43	0
Polymer	238.21	5	47.64	3.58	0.0248
Time × Concentration	28.18	3	9.39	0.71	0.5628
Time × Polymer	305.56	5	61.11	4.60	0.0096
Concentration × Polymer	299.70	15	19.98	1.50	0.2195
Within	199.37	15	13.29		
Total	4684.31	47			

The interaction between time and polymer type is also important ($p = 0.0096$), which means that not all polymers have the same influence when the duration of the treatment varies (also reflected in Figure 2). Consequently, a two-way ANOVA was performed considering the influence of polymer type and concentration separately for the two process durations (24 and 48 h). For the samples analyzed after 24 h, the two-way ANOVA test (Table 5) shows the significance of both concentration and polymer type, and there is no interaction between the two factors.

Table 5. Analysis of variance for samples at 24 h contact time.

Source of Variation	SS	df	MS	F	*p*-Value
Polymers	284.46	5	56.89	3.69	0.0066
Concentration	3065.01	3	1021.67	66.31	0.0000
Interaction	389.28	15	25.95	1.68	0.0867
Within	739.55	48	15.41		
Total	4478.30	71			

The post hoc Tukey test allows us to highlight more critical differences between the means of all possible pairs using a studentized range distribution. Figure 12 shows a graphical representation of the differentiations between groups and shows that the lowest SK-MEL-28 cell viability is registered for high concentration (35 μg/mL) using polymer CHP2, the thicker blue line. The blue lines represent groups with similar results and correspond to other chitosan polymers at a high concentration (35 μg/mL) and the chitosan–oligochitosan mixtures at lower concentrations (17.5 and 8.75 μg/mL). The red lines represent all other samples that are significantly different. This may support the assumption that for a contact time of 24 h, the mixtures of chitosan and oligochitosan may have better results.

For the experimental data obtained at 48 h contact time, two-way ANOVA proved significant effects for both main factors and interaction, imposing a further analysis focused on evaluating the polymer type effect at each concentration.

This study proved that at low concentrations (4.75 and 8.45 μg/mL), the biopolymer type has an important influence on the measured viability. In contrast, at higher concentrations (17.5 and 35 μg/mL), the changes in the biopolymer used made no significant differences in the viability of melanoma cells (Table 6).

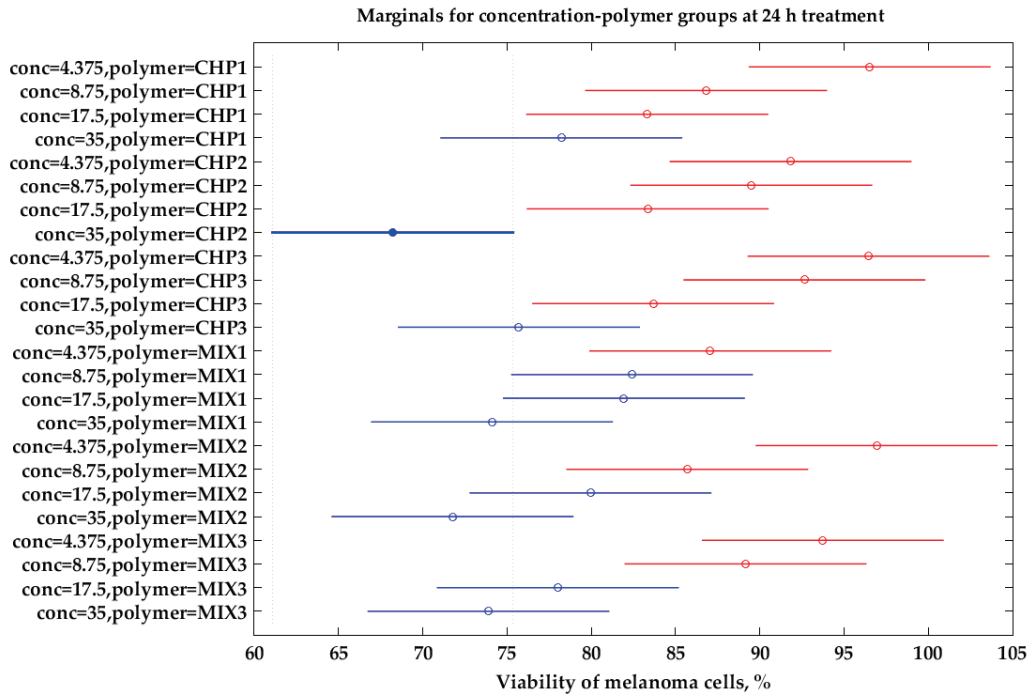

Figure 12. Marginals for sample reflecting melanoma cells' viability for different oligopolymers and solution concentrations.

Table 6. ANOVA results for melanoma cells' viability using the investigated biopolymers for a contact time of 48 h and solution concentration 4.375 μg/mL (a), solution concentration 8.75 μg/mL (b), solution concentration 17.5 μg/mL (c), and solution concentration 35 μg/mL (d).

	Source of Variation	SS	df	MS	F	*p*-Value
(a)	Between Groups	936.24	5	187.2	7.91	0.00167
	Within Groups	284.03	12	23.67		
	Total	1220.26	17			
	Source of Variation	**SS**	**df**	**MS**	**F**	***p*-Value**
(b)	Between Groups	616.52	5	123.3	6.52	0.00375
	Within Groups	226.89	12	18.91		
	Total	843.41	17			
	Source of Variation	**SS**	**df**	**MS**	**F**	***p*-Value**
(c)	Between Groups	198.82	5	39.76	2.15	0.12908
	Within Groups	222.20	12	18.52		
	Total	421.03	17			
	Source of Variation	**SS**	**df**	**MS**	**F**	***p*-Value**
(d)	Between Groups	226.83	5	45.37	2.17	0.12598
	Within Groups	250.80	12	20.9		
	Total	477.63	17			

This result may lead to the conclusion that all biopolymers can have comparable effects at high solution concentrations and prolonged contact time. In contrast, at shorter contact time and/or low solution concentrations, the nature of the biopolymer has a significant effect, with the chitosan–oligochitosan mixture being more effective in treating melanoma cells.

Analyzing the mean viability of SK-MEL-28 cells using a concentrated solution of 35 μg/mL of chitosan, a chitosan–oligochitosan mixture, and oligochitosan, it can be easily noticed that the mixture gives better results than both chitosan and oligochitosan, which

stands for the synergetic effect of the oligomer–biopolymer compounds in defining the biological properties (Figure 13).

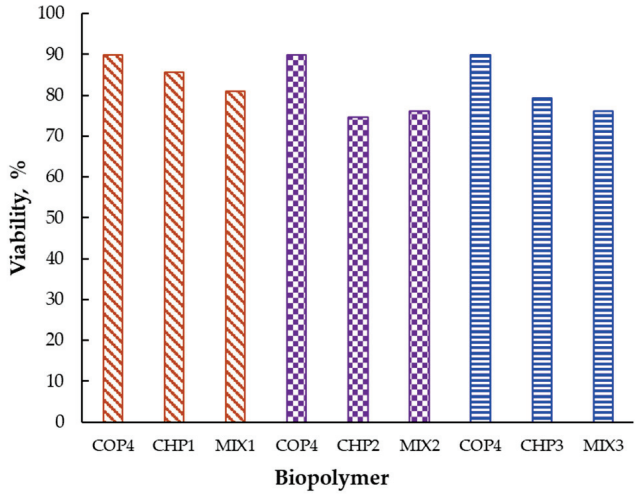

Figure 13. Mean viability of SK-MEL-28 cells after 24 h of treatment with 35 μg/mL solutions of oligochitosan (COP4), chitosan (CHP1, CHP2, CHP3), and the corresponding composite (MIX1, MIX2, MIX3).

As Figure 13 shows, oligochitosan alone is the least efficient, but combining it with chitosan can enhance its potency.

3. Discussion

Using chitosan with different characteristics modeled by the obtaining methods (DDA and MM) emphasizes that the molecules behave differently due to the presence of amino and acetyl groups. The degree of deacetylation influences the density of amino groups available for ion-bonding interactions, either with other chitosan molecules or within chitosan chains. Using chitosan with different deacetylation degrees (DDA) could improve the newly formed material's solubility, charge density, and bioactivity. The structural arrangement of the new formulation, through changes brought about by the presence of β-chitosan, such as differences in chain flexibility or the presence of branching, could explain how these polymer molecules interact with chitosan matrices or gels. In this way, the different interactions and biological effects purchased with pure chitosan can be explained.

This is due to reactive functional groups in the glycosidic ring structure: the primary hydroxyl group at C^3, the secondary hydroxyl group at C^6, and the reactive amino group at C^2, which are involved in inter- and intramolecular bonding. Data in the literature show that these reactive functional groups provide the basis for enhancing chitosan functionalization by modifying the chemical structure of chitosan through alkylation, acylation, esterification, oxidation reactions, etc. The resulting functionalized chitosan-type products exhibit higher selectivity than their nonfunctionalized counterparts and, thus, can be used in a broader range of applications [29,57].

Chitosan is studied for its various biological properties: antitumor, antimicrobial, antioxidant, and anti-inflammatory. The polymer's physicochemical characteristics, such as molar mass, DDA, concentration, or solubility, are the main intrinsic factors influencing effects in biological systems. Intracellular oxidative stress causes necrosis and cell degradation, but the cell is equally adapted to maintain a redox balance. Understanding how these intracellular relationships can be manipulated may provide an advantage in preventing and treating diseases [58].

The antioxidant activity of chitosan is related to its ability to bind free radicals, an activity that depends on active hydroxyl and amino groups in their polymer [59,60]. Various methods used to analyze scavenger capacity show that the level of antioxidant activity

depends on the concentration level of chitosan or oligochitosan as well as molecular weight [10,59,60].

The maximum concentration tested of chitosan (35 μg/mL) showed that scavenging activity is below 20%. Other studies looking at chitosan, chitosan oligomers, or its derivatives at concentrations below 1 mg/mL have demonstrated similar results [59,61,62]. Chitosan oligomers can have a scavenging effect of only 7% at MM of about 15 kDa [59].

Although the level of antioxidant activity is low, for our study, it represents an advantageous response in the sense that at the tested concentrations and in the combinations used in this experiment, the antioxidant activity indicated in vitro preserves the conditions of cell availability, favoring the desired cytotoxic and antitumor effects.

Chitosan of different origins and characteristics, with MM ranging from 1.5 KDa (COP4) to 2.25 KDa in mixtures (MIX 1, MIX2, MIX3) to 819.99 KDa (CHP1), 804.33 KDa (CHP2), and 475.43 KDa (CHP3), induces similar mechanisms at the same concentration, which changes the perspective of understanding the level of versatility of chitosan. Numerous studies are searching for solutions to limit melanoma cell proliferation by targeting some matrix components or intracellular structures. Also, combined therapies such as chemotherapy, radiotherapy, or immunotherapy are explored [7]. Our studies have proven a decrease in cell viability after 24 and 48 h for all the experimental variants compared to the untreated control. Mixtures with oligochitosan favor changes that attract attention through significant differences regarding cell viability. There are several possibilities by which these changes are accomplished: either the oligochitosan interacts with other membrane or intracytoplasmic components, or there are molecular changes of the oligomer by organizing into micelles, along with the change in intracellular pH [12,63].

The mechanisms of action of chitosan and oligochitosan or mixtures occur in successive stages. In the first stage, we appreciate that interaction with cancer cell membranes occurs. These interactions induce changes in the morphology and adhesion of cells (Figures 3–8), observed in our experimental conditions.

Chitosan is a polymer with amino groups, which are positively charged and will react with the negative charges of membrane surfaces. These interactions may explain the differences in the response of different cell lines in contact with chitosan molecules or oligochitosan [64].

The mentioned electrostatic interactions can be correlated with the higher negative charges on the membranes of cancer cells compared to normal cells, hence the variability of chitosan cytotoxicity on different cell lines [65]. A study on the influence of chitosan on melanoma revealed a decrease in the proliferation of primary melanoma cells, the SK-MEL-28 line, as well as cells derived from metastatic lymph nodes, the RPMI-7951 line, by activating the proapoptotic pathways. In the same study, another cell line, A-375, also a primary melanoma, skin-derived cells, does not show the same proliferative changes as SK-MEL-28, without the exposure time being correlated with the change in the proliferation of these cells [66].

The effects of these chitosan molecules are correlated with the regulation of proliferative processes, more precisely intervening in cell signaling through the phosphatidylinositol 3-kinase (PI3K)-AKT pathway, one of the most important signaling pathways associated with tumorigenesis and cancer treatment. According to other studies in this direction, there are controversial opinions. Amirani et al. highlighted the anticancer role of chitosan and oligochitosan by affecting PI3K-AKT [67].

Another study points out the intracellular manifestation of chitosan with the role of stimulating the PI3K/AKT1/mTOR pathway. The amplified expression of proteins that increase cell proliferation in the presence of chitosan nanoparticles (DDA = 75–80%) in liver cancer cells, CCL 13 and HepG2, can conclude that the use of the polymer with 75–85% deacetylation and low molar mass presents a risk regarding the use of chitosan in antitumor applications on these cells [14]. Another study reveals the anticancer activity of oligochitosan by inducing some electrical changes [68].

The observations from our study denote the correlation between the particularities of chitosan molecules and the amplification of cytotoxic effects. Thus, chitosan with high DDA (CHP1) has an impact of inhibiting cell viability. Still, the decrease in MM leads to the acceleration and maintenance of the effect (CHP3), a phenomenon explained by the increase in the rate of penetration and possible accumulation at the endosomal level. Cancer cells use different adaptations in the malignancy process, including inhibiting some antiapoptotic or antioxidant pathways induced by various chemical substances used in therapy. Activation of these cellular signaling pathways leads to drug resistance and stimulation of proliferation. Chitosan acts as a scavenger through the hydrogen ion of NH_3 from the C^2 position. The mechanism of the antioxidant activity induced by chitosan is influenced by the physical–chemical characteristics (DDA or MM). Still, these effects are also related to the concentration of the polymer molecules [69,70].

Many studies have tried to elucidate the mechanisms of chitosan's action. However, it has been concluded that this polymer and its derivatives produce different responses in different cell types [65]. The quantified effects (IC_{50}) and concentrations used are also very varied. Thus, Zou et al. [64] report, in their studies, that the IC_{50} value of oligochitosan was observed for different cell lines: IC_{50} = 1329.9 ± 93.4 μg/mL for HCT-116, IC_{50} = 48.6 ± 7.0 μg/mL MCF-7, respectively [65], IC_{50} = 800 ± 131.45 μg/mL on Ca9-22, but not HaCaT cells [71]. Srinivasan et al. reported the lowest concentration of chitosan (10 μg/mL) used in vitro ovarian cell testing (ovarian cancer cell line—PA-1) with an antitumor effect of 100% [72]. Another study showed that the highest concentration of oligochitosan tested was 40 mg/mL [73] on HeLA cells, with morphological effects. As a result, chitosan concentration is another variable parameter that is not very well understood.

The decrease in SK-MEL-28 cell viability after applying different chitosan-based polymers was correlated with cytomorphological changes, such as reduced cell adhesion, the appearance of floating cells in the culture medium, thinning of pseudopods, and widening intercellular spaces.

Cultivation of some colon cancer cell lines and hepatocellular carcinoma cells on chitosan and hyaluronan grafted chitosan membranes determined alterations of the normal morphology (monolayer formation) materialized by the formation of spheroids or colonies as a result of 72 h treatment with chitosan-based membranes [74].

The YKL-40 (Chitinase-3-like protein 1) molecule, under experimental conditions, initiates cell proliferation through the ERK1/2-MAPK pathway and supports angiogenesis through the interaction of syndecan-1 (SDc-1/αVβ3) and with receptors (IL-13Rα2) at the level of endothelial cells. It also stimulates metastasis by activating proinflammatory cytokine-type factors (TNF-alpha, interleukin-1beta, interleukin-6, interferon-gamma) and proinvasive factors (MMP9, CCL2, CXCL2) [75,76]. YKL-40 is a lectin that binds carbohydrates with a preference for chitin, heparin, and hyaluronic acid. YKL-40 is synthesized and secreted by many cells (macrophages, neutrophils, synoviocytes, chondrocytes, fibroblast-like cells, smooth muscle cells, and tumor cells). It plays an important role in the cellular response to environmental changes (tissue damage, inflammation, tissue repair). YKL-40 has been shown to be overexpressed in a variety of human and animal cancer models with roles in cancer cell growth, proliferation, invasion and metastasis, angiogenesis, activation of tumor-associated macrophages, and Th2 polarization of CD4+ T cells [77]. That is why YKL-40-based targeted therapy is increasingly being approached in cancer pathologies [50,51].

The in vitro stimulation of YKL-40 synthesis in samples with LPS and samples with α-chitosan and LPS indicates that SK-MEL-28 melanocytes react to the introduction of β-oligochitosan in the mixture. According to other studies, these molecules may show an affinity for YKL-40, which blocks the release into the extracellular space. It should also be mentioned that chitosan–oligochitosan concentrations that induced a significant decrease in cell viability (IC_{50}) were used for this test, which means that cytotoxic effects can be considered. The SK-MEL-28 melanoma line is characterized by a low expression level of YKL-40 [44]. Regarding skin cancers, the SK-MEL-28 line is among those with a low value

of nTPM values (representing the number of RNA transcripts per million) of 0.6 for the gene responsible for transcribing the YKL-40 protein [78].

Through these observations and statistical analysis of the results, the action of chitosan can be anticipated and correlated with doses and combinations that favor the desired processes. Statistical analysis showed significant changes in melanoma cells at low concentrations of chitosan in the first 24 h (Table 6), while high concentrations did not correlate with chitosan types.

It is possible that chitosan might have a sensibilization activity on the cells and could, thus, through controlled molecular characteristics, become a therapeutic agent in combination therapies [79] targeting cellular components.

A number of experiments highlight the versatility of chitosan and its use in various anticancer applications, either as codelivery of oxaliplatin and rapamycin for synergistic chemotherapy [80] or by triggering other mechanisms, such as inhibition of the permeation-glycoprotein (P-gp), a protein with an important role in the management of cancer [81].

Our study showed that mixing (alpha and beta forms) of chitosan can induce changes in cellular responses (metabolic, morphologic, and protein synthesis). Further to cytotoxicity, the presence of oligomer leads to the synthesis of YKL-40 (Figure 9), a protein involved in various cellular processes and angiogenesis. Inhibition of angiogenesis is the focus of modern antitumor studies [82]. Our study, thus, allows the observation of a correlated process between chitosan and melanoma cell response, while the mathematical modeling (Figures 10–13, Table 6) is useful to classify quantified processes and differentiate them based on statistical significance and the dynamics of their appearance in the cells.

4. Materials and Methods

4.1. Materials

According to Dinculescu et al. [83], chitosan powders (CHP1, CHP2, CHP3) were obtained by optimizing shrimp waste through a recovery process. The oligochitosan powder (COP4) was chemically extracted from *Rapana venosa* capsule waste, aligning with the previous study's methodology [30].

The other chemical reagents employed were as follows: HCl (Chemical Company S.A., Iasi, Romania), NaOH pellets (ChimReactiv SRL, Bucharest, Romania), ethyl alcohol (Sigma Aldrich, Taufkirchen, Germany), acetone (p.a.) (Sigma Aldrich, Taufkirchen, Germany), acetic acid solution (Sigma Aldrich, Taufkirchen, Germany), methanol (Merck KGaA, Darmstadt, Germany), dimethyl sulfoxide (DMSO) (Merck KGaA, Darmstadt, Germany), trypsin/EDTA (Biowest, Nuaillé, France), 3-(4,5-dimethylthiazol-2-yl)-2,5-diphenyltetrazolium bromide (MTT) (Merck KGaA, Darmstadt, Germany), 2,2-diphenyl-1-picryl-hydrazyl-hydrate (DPPH) (Aldrich Chemistry, MM:394.32, Steinheim, Germany), melanoma cell line SK-MEL-28 (ATCC HTB-72), Eagle's Minimum Essential Medium (PAN-Biotech GmbH, Aidenbach, Germany), fetal bovine serum (SFB, Euroclone S.p.A., Milan, Italy), antibiotic solution (mixture of penicillin 100 µg/mL and streptomycin 100 IU/mL—Capricorn Scientific GmbH, Ebsdorfergrund, Germany), lipopolysaccharide from *Escherichia coli* O55:B5 (MedChemExpress, Monmouth Junction, NJ, USA), CHI3L1 ELISA Kit (antibodies-online GmbH, Aachen, Germany).

4.2. Synthesis and Characterization of Chitosan Samples

The extraction procedure of chitosan powders [84,85] involved a demineralization step, using 4% HCl solution in the ratio of shrimp waste powder to HCl solution of 1:13 (m/v) at room temperature for 50 min. The deproteinization step involved a 5% NaOH solution in the mixture ratio of demineralized powder to NaOH solution of 1:16 (m/v), at 65 °C, under continuous stirring for two hours. Prior to the deacetylation stage, the obtained chitin powder was subjected to a decolorization process using a mixture of ethyl alcohol and acetone in a volumetric ratio of 1:1 (v/v) at room temperature. The deacetylation procedure of the obtained chitin samples was carried out with 45% NaOH solution for 120 min under continuous medium agitation and in a solid-to-liquid ratio of 1:18 for CHP1

and CHP2 and in a solid-to-liquid ratio of 1:9.5 for CHP3. Following each stage of the above-specified procedure, the material was rinsed with distilled water until achieving a neutral pH. Subsequently, the material was dried to a constant weight. By using different solid–liquid ratios (m_{chitin}:$vol_{NaOH\ sol}$) under the same temperature conditions (95 °C), contact time (120 min), and the same NaOH concentration, it was desired to obtain chitosan samples with high values for DD, but with different values for molar mass. Thus, at ratios of m_{chitin}:$vol_{NaOH\ sol}$ =1:9.5, in the case of the CHP3 sample, the measured molar mass was almost half that of CHP1 and CHP2, which were obtained at ratios of 1:18 (solid–liquid).

According to our previous study [30], the oligochitosan powder (COP4) was obtained by chemical extraction of *R. venosa* capsule waste using a 6.5% NaOH solution in a capsule mass: NaOH solution ratio of 1:40 (*m*/*v*) at 90 °C, under medium agitation, for 120 min. The obtained alkaline suspension underwent centrifugation at 3500 rpm. After supernatant removal, the chitosan pellets were washed repeatedly with distilled water until a neutral pH was reached. To eliminate potential traces of lipids, proteins, or pigments, the chitosan pellets were washed with a 1:1 mixture of ethyl alcohol and acetone, using a ratio of 1:10 (*m*/*v*) between the wet chitosan pellets mass and the solvent mixture volume. The organic solvents were then removed through centrifugation and multiple washings with distilled water. Finally, the resulting wet chitosan pellets were dried in an oven at 105 °C. All the chitosan powders obtained were stored in a desiccator at room temperature, readying them for physicochemical characterization and the preparation of test solutions.

MM and DDA of polymer molecules are the essential features that influence most structure–function relationships. Therefore, the DDA characterization was carried out using potentiometric pH measurements [30,74], in triplicate. Equations (3) and (4) were used for the determination of DDA values:

$$\text{DDA}\ (\%) = \frac{203 \cdot \text{Q}}{1 + 42 \cdot \text{Q}} \tag{3}$$

$$\text{Q} = \frac{\text{C}_\text{M} \cdot \Delta\text{V}}{\text{m}} \tag{4}$$

where C_M is the molar concentration of the NaOH solution used for titration (mol/L); ΔV represents the difference volume between the two inflexion points (L); m is the mass of chitosan analyzed (g); 203 is a coefficient that represents the molar mass of chitin (g/mol); and 42 is a coefficient that represents the molar mass of acetyl group (g/mol).

The molar mass (MM) was determined by measuring the intrinsic viscosity of diluted acid solutions of chitosan prepared in 2% acetic acid with 0.1 M KCl [86] using an Ostwald-type capillary viscometer (model 518 10, SI Analytics GmbHTM, Mainz, Germany, capillary tube inner diameter Øi = 0.43 mm) [30,83]. The measurements were carried out at 25 ± 1 °C, in triplicate. The approach employed in this study relies on the correlation between the viscosimetric-average molar mass, MM (g/mol), and the intrinsic viscosity, [η] (mL/g), as described by Mark–Houwink–Sakurada [30,83] and illustrated by Equation (5).

$$[\eta] = \text{K} \cdot \text{M}_\text{v}^{\alpha} \tag{5}$$

In this equation, the constants K and α are influenced by factors such as the solvent's characteristics, temperature, and the chemical arrangement of the polymer ($K = 13.8 \times 10^{-3}$ mL/g, $\alpha = 0.85$) [52,86].

For testing, chitosan powder samples (CHP1, CHP2, CHP3) were mixed with oligochitosan powder in mass ratios of 1:2 (m/m) and then solubilized in dilute 1% acetic acid solutions. The powders of α-chitosan, β-oligochitosan, and their mixtures were solubilized on a hotplate under continuous medium stirring (500 rpm) at 40 °C for 24 h.

The characterization was performed using a scanning electronic microscope (SEM) (FEI QUANTA 250) with an energy-dispersive spectrometer. Images with a magnitude of 500× and 2000× and details of the microparticle disposition were photomicrographed.

4.3. Antioxidant Activity

The antioxidant activity of the samples was determined by the DPPH (2,2-diphenyl-1-picryl-hydrazyl-hydrate) method. DPPH (Sigma Aldrich) in methanol solutions (100 mL) were prepared before performing the test (fresh solution). Fresh chitosan solutions in 1% acetic acid were prepared. The samples were stirred for two hours before assay and after that, they were kept warm at 37 °C. A volume of 100 µL of the sample (35 µg/mL concentration), including chitosan solutions (CHP1, CHP2, CHP3) and mixtures (MIX1, MIX2, MIX3), were mixed with 1 mL of DPPH. The solutions were stirred for 10 s and kept at the thermostat (37 °C) in the dark for 30 min. The evaluation was carried out with a UV/VIS Nanospectrophotometer, NABI (MicroDigital Co., Ltd., Seongnam-si, Republic of Korea), and the reading was carried out at 517 nm. The DPPH solution was used as control, and methanol was used as a blank. The free radical's scavenger activity of chitosan solutions was calculated as follows (Equation (6)):

$$\text{DPPH } (\%) = \frac{A_{control} - A_{sample}}{A_{control}} \cdot 100 \quad (6)$$

where $A_{control}$ and A_{sample} represent the absorbance values at 517 nm [61].

All variants were completed in triplicate. The results are presented as an average value with standard deviation (±SD).

4.4. Cell Culturing Conditions

Eagle's Minimum Essential Medium (Eagle's Minimum Essential Medium, PAN-Biotech GmbH, Aidenbach, Germany) was used for the SK-MEL-28 cell line, with both types of nutrient media supplemented with 10% fetal bovine serum (Euroclone S.p.A., Milan, Italy) and 1% antibiotic solution (mixture of penicillin 100 µg/mL and streptomycin 100 IU/mL—Capricorn Scientific GmbH, Ebsdorfer-grund, Germany). Cells were grown in culture plates in an incubator (Binder GmbH, Tuttlingen, Germany) at 37 °C in a humid atmosphere with 5% CO_2 [87].

SK-MEL-28 cells were cultured in the presence of chitosan solutions (CHP1, CHP2, CHP3) of different concentrations (4.375, 8.75, 17.5, and 35 µg/mL) and mixtures of chitosan–oligochitosan MIX1 (CHP1 + COP4), MIX2 (CHP2 + COP4), and MIX3 (CHP3 + COP4).

4.5. MTT Assay

The MTT assay, which allows the evaluation of the percentage of cell viability, was used in order to determine optimal doses to express the biological effect of the tested compounds, based on which the IC_{50} value was calculated. The 3-(4,5-dimethylthiazol-2-yl)-2,5-diphenyl tetrazolium bromide (MTT) colorimetric method was used, adapted from Mosmann [88], Laville et al. [89], and van Meerloo et al. [90]. This is based on the ability of living cells to convert the yellow water-soluble substrate of MTT, with the help of mitochondrial dehydrogenases, into dark, blue-colored formazan. Briefly, 10 µL of DMSO in each well was added in order to solubilize formazan crystals and to stop the reaction. The amount of formazan produced is hypothesized to be directly proportional to the number of living cells [91].

Initially, SK-MEL-28 cells were grown in 75 cm^2 culture flasks and, after monolayer formation, were detached with trypsin/EDTA, counted, and resuspended in 96-well microplates at a density of 1×10^4 cells/well. After forming the monolayer (approximately 24 h), the cells were treated with the formulas of α-chitosan and β-oligochitosan in the following doses: 4.375, 8.75, 17.5, and 35 µg/mL, with the duration of treatment being 24 and 48 h. A 1% acetic acid solution was used to solubilize the powdered chitosan.

At the end of the treatment, the cells were processed following the protocol of the MTT test, and the extinctions were measured at 570 nm using the automatic microplate reader

Biochrom EZ Read 400 (Biochrom Ltd., Cambridge, UK). Cell viability was calculated according to Equation (7).

$$\text{Cell viability } (\%) = \left(E_{sample}/E_{control}\right) \cdot 100 \quad (7)$$

where E_{sample} is the extinction of the sample and $E_{control}$ is the extinction of the untreated control.

The IC_{50} values of the tested chitosan formulations were calculated using polynomial dose–response curve plots for each concentration used in the MTT assay.

4.6. Cell Morphology Test

The interaction of different chitosan formulas with cellular structures was also evaluated regarding the morphological changes they induced after 24 and 48 h of treatment. Cell morphology was visualized using a Nikon Eclipse TS100 inverted microscope equipped with a MshOt MS60 (Nikon, Tokyo, Japan) digital camera, with photographs taken with a 10× objective.

4.7. Determination of YKL-40 Protein Expression

The melanoma cell line SK-MEL-28 was used to evaluate the expression of the chitinase-like YKL-40 protein. Eagle growth medium (Eagle's Minimum Essential Medium) was supplemented with 10% fetal bovine serum and 1% antibiotic solution. Cells were grown in culture flasks in an incubator (Binder GmbH, Tuttlingen, Germany) at 37 °C in a humid atmosphere with 5% CO_2 [87].

The evaluation of the expression levels of chitinase-like proteins, especially YKL-40, was performed by the ELISA test. The test was initiated by culturing SK-MEL-28 cells in 150 cm^2 plates to obtain cellular mass, after which the cells were trypsinized with trypsin/EDTA, counted, and distributed in 12-well plates at a density of 3.6×10^4 cells/well. After the formation of the monolayer (24 h), the growth medium was removed and replaced with fresh medium; the cells were stimulated with 50 ng/mL of lipopolysaccharide (LPS, MedChemExpress, Monmouth Junction, NJ, USA) for one hour, after which they were treated for 24 h with chitosan and chitosan–oligochitosan mixtures. The concentrations used are for each compound tested, concentrations that induce similar effects (IC_{50}). After the treatment ended, the supernatant was collected and processed according to the specific instructions of the ELISA kit. To calculate the results expressed in pg/mL, a standard curve consisting of 8 samples with known protein concentration was drawn up. The results were expressed in percentages (%), and the alterations in the chitosan-exposed samples (mean values) were compared with the control sample (LPS stimulated control).

4.8. Statistical Analysis

Results of in vitro tests were expressed as mean ± standard error (SE). The difference between mean values for each index was expressed using Student's *t*-test [92]. Statistical significance was established at $p < 0.05$; each test was performed in triplicate. All the registered data were analyzed using multi-ANOVA implemented in Matlab 2023, checking the influence of the three factors implied: duration of the treatment; concentration; and polymer type.

5. Conclusions

The results obtained provide promising information on modeling the efficiency of antitumor action. Thus, α-chitosan, with different degrees of deacetylation (DDA) and molar mass (MM), in combination with β-oligochitosan, can form mixtures with favorable effects on the cell processes, activating antitumor mechanisms by disrupting cellular activity and maintaining the nonproliferative status. Our study showed decreased tumor cell viability and YKL-40 expression in the association conditions of α-chitosan–β-oligochitosan mixtures after cell stimulation. These results highlight the importance of obtaining carefully controlled solutions from a molecular point of view that correlate with the targeted cellular

processes. We appreciate that DDA is a critical factor in relation to the extent of the effects, while MM influences the conditions of the chitosan penetration and, implicitly, the rate of the induced reactions.

The results support the conclusion that the chitosan mixtures determined a dose- and duration-dependent cellular reactivity. The intensity of the response was correlated with the degree of damage to cell viability. The morphological changes highlighted the decrease in the ability to adhere and, implicitly, to form the cell monolayer.

Our future studies aim to investigate the mechanisms by which these mixtures of another α-chitosan–β-oligochitosan combination ratio can better amplify the antiproliferative effect in melanocytes and other tumoral cell lines.

Author Contributions: Conceptualization, V.S., M.R.A., D.G., G.V., C.L.G. and R.I.; methodology, V.S., D.G., G.V., M.R.A. and D.D.; software, R.I., C.L.G. and D.D.; validation, G.V., R.I. and I.R.; formal analysis, D.D. and M.-M.A.; investigation, V.S., D.G., G.V. and M.R.A.; resources, V.S., M.R.A., D.G. and G.V.; data curation, D.D., C.L.G. and R.I.; writing—original draft preparation, V.S., D.G., G.V., M.R.A., L.E.E., C.L.G., D.D. and C.-T.M.; writing—review and editing, V.S., D.G., G.V., C.L.G., M.R.A., R.I. and C.-T.M.; visualization, G.V., M.R.A., M.-M.A. and I.R.; supervision, I.R.; project administration, I.R.; funding acquisition, I.R. All authors have read and agreed to the published version of the manuscript.

Funding: This work was supported by a grant from the Romanian Ministry of Education and Research, CNCS—UEFISCDI: project number PN-III-P4-ID-PCE-2020-2243 and partially: Romanian Ministry of Research, Innovation and Digitization Core-Program: project 7N/23020402/2023.

Institutional Review Board Statement: Not applicable.

Informed Consent Statement: Not applicable.

Data Availability Statement: Data is contained within the article.

Acknowledgments: We would like to thank Ciprian Valentin Mihali for SEM images technical support.

Conflicts of Interest: The authors declare no conflicts of interest.

References

1. Kim, H.J.; Kim, Y.H. Molecular Frontiers in Melanoma: Pathogenesis, Diagnosis, and Therapeutic Advances. *Int. J. Mol. Sci.* **2024**, *25*, 2984. [CrossRef] [PubMed]
2. Rambow, F.; Marine, J.-C.; Goding, C.R. Melanoma Plasticity and Phenotypic Diversity: Therapeutic Barriers and Opportunities. *Genes Dev.* **2019**, *33*, 1295–1318. [CrossRef] [PubMed]
3. Hossain, S.M.; Eccles, M.R. Phenotype Switching and the Melanoma Microenvironment; Impact on Immunotherapy and Drug Resistance. *Int. J. Mol. Sci.* **2023**, *24*, 1601. [CrossRef]
4. Xu, K.; Wang, Y.; Xie, Y.; Zhang, X.; Chen, W.; Li, Z.; Wang, T.; Yang, X.; Guo, B.; Wang, L.; et al. Anti-Melanoma Effect and Action Mechanism of a Novel Chitosan-Based Composite Hydrogel Containing Hydroxyapatite Nanoparticles. *Regen. Biomater.* **2022**, *9*, rbac050. [CrossRef] [PubMed]
5. Adamus-Grabicka, A.A.; Hikisz, P.; Sikora, J. Nanotechnology as a Promising Method in the Treatment of Skin Cancer. *Int. J. Mol. Sci.* **2024**, *25*, 2165. [CrossRef] [PubMed]
6. Lie, K.C.M.; Bonturi, C.R.; Salu, B.R.; de Oliveira, J.R.; Bonini Galo, M.; Paiva, P.M.G.; Correia, M.T.d.S.; Oliva, M.L.V. Impairment of SK-MEL-28 Development—A Human Melanoma Cell Line—By the Crataeva Tapia Bark Lectin and Its Sequence-Derived Peptides. *Int. J. Mol. Sci.* **2023**, *24*, 10617. [CrossRef] [PubMed]
7. Czarnecka, A.M.; Bartnik, E.; Fiedorowicz, M.; Rutkowski, P. Targeted Therapy in Melanoma and Mechanisms of Resistance. *Int. J. Mol. Sci.* **2020**, *21*, 4576. [CrossRef] [PubMed]
8. Jia, Y.; Wu, C.; Zhang, B.; Zhang, Y.; Li, J. Ferruginol Induced Apoptosis on SK-Mel-28 Human Malignant Melanoma Cells Mediated through P-P38 and NF-KB. *Hum. Exp. Toxicol.* **2019**, *38*, 227–238. [CrossRef] [PubMed]
9. Chen, H.; Hou, K.; Yu, J.; Wang, L.; Chen, X. Nanoparticle-Based Combination Therapy for Melanoma. *Front. Oncol.* **2022**, *12*, 928797. [CrossRef] [PubMed]
10. Piekarska, K.; Sikora, M.; Owczarek, M.; Jóźwik-Pruska, J.; Wiśniewska-Wrona, M. Chitin and Chitosan as Polymers of the Future—Obtaining, Modification, Life Cycle Assessment and Main Directions of Application. *Polymers* **2023**, *15*, 793. [CrossRef] [PubMed]
11. Riccardo, A.A.; Gupta, N.S. (Eds.) Chitin. In *Topics in Geobiology*; Springer: Dordrecht, The Netherlands, 2011; Volume 34, ISBN 978-90-481-9683-8.

12. Stie, M.B.; Thoke, H.S.; Issinger, O.-G.; Hochscherf, J.; Guerra, B.; Olsen, L.F. Delivery of Proteins Encapsulated in Chitosan-Tripolyphosphate Nanoparticles to Human Skin Melanoma Cells. *Colloids Surf. B Biointerfaces* **2019**, *174*, 216–223. [CrossRef] [PubMed]
13. Petroni, G.; Buqué, A.; Zitvogel, L.; Kroemer, G.; Galluzzi, L. Immunomodulation by Targeted Anticancer Agents. *Cancer Cell* **2021**, *39*, 310–345. [CrossRef] [PubMed]
14. Yang, M.-H.; Yuan, S.-S.; Huang, Y.-F.; Lin, P.-C.; Lu, C.-Y.; Chung, T.-W.; Tyan, Y.-C. A Proteomic View to Characterize the Effect of Chitosan Nanoparticle to Hepatic Cells: Is Chitosan Nanoparticle an Enhancer of PI3K/AKT1/MTOR Pathway? *BioMed Res. Int.* **2014**, *2014*, 789591. [CrossRef] [PubMed]
15. Frank, L.A.; Onzi, G.R.; Morawski, A.S.; Pohlmann, A.R.; Guterres, S.S.; Contri, R.V. Chitosan as a Coating Material for Nanoparticles Intended for Biomedical Applications. *React. Funct. Polym.* **2020**, *147*, 104459. [CrossRef]
16. Wu, J.; Liu, G.; Qin, Y.-X.; Meng, Y. Effect of Low-Intensity Pulsed Ultrasound on Biocompatibility and Cellular Uptake of Chitosan-Tripolyphosphate Nanoparticles. *Biointerphases* **2014**, *9*, 031016. [CrossRef] [PubMed]
17. Apetroaei, M.R.; Zgârian, R.G.; Manea, A.-M.; Rau, I.; Tihan, G.T.; Schroder, V. New Source of Chitosan from Black Sea Marine Organisms Identification. *Mol. Cryst. Liq. Cryst.* **2016**, *628*, 102–109. [CrossRef]
18. Schröder, V.; Rău, I.; Dobrin, N.; Stefanov, C.; Mihali, C.-V.; Pădureţu, C.-C.; Apetroaei, M.R. Micromorphological Details and Identification of Chitinous Wall Structures in Rapana Venosa (Gastropoda, Mollusca) Egg Capsules. *Sci. Rep.* **2020**, *10*, 14550. [CrossRef] [PubMed]
19. Kaczmarek, M.B.; Struszczyk-Swita, K.; Li, X.; Szczęsna-Antczak, M.; Daroch, M. Enzymatic Modifications of Chitin, Chitosan, and Chitooligosaccharides. *Front. Bioeng. Biotechnol.* **2019**, *7*, 243. [CrossRef] [PubMed]
20. Morin-Crini, N.; Lichtfouse, E.; Torri, G.; Crini, G. Applications of Chitosan in Food, Pharmaceuticals, Medicine, Cosmetics, Agriculture, Textiles, Pulp and Paper, Biotechnology, and Environmental Chemistry. *Environ. Chem. Lett.* **2019**, *17*, 1667–1692. [CrossRef]
21. Minh, N.C.; Nguyen, V.H.; Schwarz, S.; Stevens, W.F.; Trung, T.S. Preparation of Water Soluble Hydrochloric Chitosan from Low Molecular Weight Chitosan in the Solid State. *Int. J. Biol. Macromol.* **2019**, *121*, 718–726. [CrossRef] [PubMed]
22. Hosseinnejad, M.; Jafari, S.M. Evaluation of Different Factors Affecting Antimicrobial Properties of Chitosan. *Int. J. Biol. Macromol.* **2016**, *85*, 467–475. [CrossRef] [PubMed]
23. Ahmed, K.F.; Aschi, A.; Nicolai, T. Formation and Characterization of Chitosan-Protein Particles with Fractal Whey Protein Aggregates. *Colloids Surf. B Biointerfaces* **2018**, *169*, 257–264. [CrossRef] [PubMed]
24. Sarabandi, K.; Jafari, S.M. Effect of Chitosan Coating on the Properties of Nanoliposomes Loaded with Flaxseed-Peptide Fractions: Stability during Spray-Drying. *Food Chem.* **2020**, *310*, 125951. [CrossRef] [PubMed]
25. Huang, J.; Qin, J.; Zhang, P.; Chen, X.; You, X.; Zhang, F.; Zuo, B.; Yao, M. Facile Preparation of a Strong Chitosan-Silk Biocomposite Film. *Carbohydr. Polym.* **2020**, *229*, 115515. [CrossRef] [PubMed]
26. Tao, F.; Cheng, Y.; Shi, X.; Zheng, H.; Du, Y.; Xiang, W.; Deng, H. Applications of Chitin and Chitosan Nanofibers in Bone Regenerative Engineering. *Carbohydr. Polym.* **2020**, *230*, 115658. [CrossRef] [PubMed]
27. Wei, Y.; Huang, Y.-H.; Cheng, K.-C.; Song, Y.-L. Investigations of the Influences of Processing Conditions on the Properties of Spray Dried Chitosan-Tripolyphosphate Particles Loaded with Theophylline. *Sci. Rep.* **2020**, *10*, 1155. [CrossRef] [PubMed]
28. Mota, J.; Yu, N.; Caridade, S.G.; Luz, G.M.; Gomes, M.E.; Reis, R.L.; Jansen, J.A.; Walboomers, X.F.; Mano, J.F. Chitosan/Bioactive Glass Nanoparticle Composite Membranes for Periodontal Regeneration. *Acta Biomater.* **2012**, *8*, 4173–4180. [CrossRef] [PubMed]
29. Li, B.; Elango, J.; Wu, W. Recent Advancement of Molecular Structure and Biomaterial Function of Chitosan from Marine Organisms for Pharmaceutical and Nutraceutical Application. *Appl. Sci.* **2020**, *10*, 4719. [CrossRef]
30. Dinculescu, D.; Gîjiu, C.L.; Apetroaei, M.R.; Isopescu, R.; Rău, I.; Schröder, V. Optimization of Chitosan Extraction Process from Rapana Venosa Egg Capsules Waste Using Experimental Design. *Materials* **2023**, *16*, 525. [CrossRef] [PubMed]
31. Alvarez-Lorenzo, C.; Blanco-Fernandez, B.; Puga, A.M.; Concheiro, A. Crosslinked Ionic Polysaccharides for Stimuli-Sensitive Drug Delivery. *Adv. Drug Deliv. Rev.* **2013**, *65*, 1148–1171. [CrossRef] [PubMed]
32. Merz, C.R. Physicochemical and Colligative Investigation of α (Shrimp Shell)- and β (Squid Pen)-Chitosan Membranes: Concentration-Gradient-Driven Water Flux and Ion Transport for Salinity Gradient Power and Separation Process Operations. *ACS Omega* **2019**, *4*, 21027–21040. [CrossRef] [PubMed]
33. Jampafuang, Y.; Tongta, A.; Waiprib, Y. Impact of Crystalline Structural Differences Between α- and β-Chitosan on Their Nanoparticle Formation Via Ionic Gelation and Superoxide Radical Scavenging Activities. *Polymers* **2019**, *11*, 2010. [CrossRef] [PubMed]
34. Masselin, A.; Rousseau, A.; Pradeau, S.; Fort, L.; Gueret, R.; Buon, L.; Armand, S.; Cottaz, S.; Choisnard, L.; Fort, S. Optimizing Chitin Depolymerization by Lysozyme to Long-Chain Oligosaccharides. *Mar. Drugs* **2021**, *19*, 320. [CrossRef] [PubMed]
35. Muzzarelli, R.A.A.; Boudrant, J.; Meyer, D.; Manno, N.; De Marchis, M.; Paoletti, M.G. Current Views on Fungal Chitin/Chitosan, Human Chitinases, Food Preservation, Glucans, Pectins and Inulin: A Tribute to Henri Braconnot, Precursor of the Carbohydrate Polymers Science, on the Chitin Bicentennial. *Carbohydr. Polym.* **2012**, *87*, 995–1012. [CrossRef]
36. Chen, W.; Jiang, X.; Yang, Q. Glycoside Hydrolase Family 18 Chitinases: The Known and the Unknown. *Biotechnol. Adv.* **2020**, *43*, 107553. [CrossRef] [PubMed]
37. Adrangi, S.; Faramarzi, M.A. From Bacteria to Human: A Journey into the World of Chitinases. *Biotechnol. Adv.* **2013**, *31*, 1786–1795. [CrossRef] [PubMed]

38. Young, E.; Chatterton, C.; Vellodi, A.; Winchester, B. Plasma Chitotriosidase Activity in Gaucher Disease Patients Who Have Been Treated Either by Bone Marrow Transplantation or by Enzyme Replacement Therapy with Alglucerase. *J. Inherit. Metab. Dis.* **1997**, *20*, 595–602. [CrossRef] [PubMed]
39. Boot, R.G.; Blommaart, E.F.C.; Swart, E.; Ghauharali-van der Vlugt, K.; Bijl, N.; Moe, C.; Place, A.; Aerts, J.M.F.G. Identification of a Novel Acidic Mammalian Chitinase Distinct from Chitotriosidase. *J. Biol. Chem.* **2001**, *276*, 6770–6778. [CrossRef] [PubMed]
40. Mazur, M.; Zielińska, A.; Grzybowski, M.M.; Olczak, J.; Fichna, J. Chitinases and Chitinase-Like Proteins as Therapeutic Targets in Inflammatory Diseases, with a Special Focus on Inflammatory Bowel Diseases. *Int. J. Mol. Sci.* **2021**, *22*, 6966. [CrossRef] [PubMed]
41. Ziatabar, S.; Zepf, J.; Rich, S.; Danielson, B.T.; Bollyky, P.I.; Stern, R. Chitin, Chitinases, and Chitin Lectins: Emerging Roles in Human Pathophysiology. *Pathophysiology* **2018**, *25*, 253–262. [CrossRef] [PubMed]
42. Ismail, H.; Helby, J.; Hölmich, L.R.; Chakera, A.H.; Bastholt, L.; Klyver, H.; Sjøgren, P.; Schmidt, H.; Schöllhammer, L.; Johansen, J.S.; et al. Measured and Genetically Predicted Plasma YKL-40 Levels and Melanoma Mortality. *Eur. J. Cancer* **2019**, *121*, 74–84. [CrossRef] [PubMed]
43. Xiao, X.-Q.; Hassanein, T.; Qun-Fang, L.; Liu, W.; Zheng, Y.-H.; Chen, J. YKL-40 Expression in Human Hepatocellular Carcinoma: A Potential Biomarker? *Hepatobiliary Pancreat. Dis. Int.* **2011**, *10*, 605–610. [CrossRef] [PubMed]
44. Richard, B.; Price, P. YKL-40 MONOCLONAL AUTHORITY 2011. U.S. Patent US8053563B2, 8 November 2011. Available online: https://patents.google.com/patent/US8053563B2/en (accessed on 16 June 2024).
45. Kognole, A.A.; Payne, C.M. Inhibition of Mammalian Glycoprotein YKL-40. *J. Biol. Chem.* **2017**, *292*, 2624–2636. [CrossRef] [PubMed]
46. Özdemir, E.; Çiçek, T. S71 THE ASSOCIATION OF SERUM YKL-40 LEVEL WITH TUMOR BURDEN AND METASTATIC STAGE OF PROSTATE CANCER. *Eur. Urol. Suppl.* **2011**, *10*, 593. [CrossRef]
47. Saleh, A.A.; Alhanafy, A.M.; Elbahr, O.; El-Hefnawy, S.M. Chitinase 3-like 1 Gene (T/C) Polymorphism and Serum YKL-40 Levels in Patients with Hepatocellular Carcinoma. *Meta Gene* **2020**, *24*, 100686. [CrossRef]
48. Bi, J.; Lau, S.-H.; Lv, Z.-L.; Xie, D.; Li, W.; Lai, Y.-R.; Zhong, J.-M.; Wu, H.; Su, Q.; He, Y.; et al. Overexpression of YKL-40 Is an Independent Prognostic Marker in Gastric Cancer. *Hum. Pathol.* **2009**, *40*, 1790–1797. [CrossRef] [PubMed]
49. Pouyafar, A.; Heydarabad, M.Z.; Mahboob, S.; Mokhtarzadeh, A.; Rahbarghazi, R. Angiogenic Potential of YKL-40 in the Dynamics of Tumor Niche. *Biomed. Pharmacother.* **2018**, *100*, 478–485. [CrossRef] [PubMed]
50. Chang, M.-C.; Chen, C.-T.; Chiang, P.-F.; Chiang, Y.-C. The Role of Chitinase-3-like Protein-1 (YKL40) in the Therapy of Cancer and Other Chronic-Inflammation-Related Diseases. *Pharmaceuticals* **2024**, *17*, 307. [CrossRef] [PubMed]
51. Böckelmann, L.C.; Felix, T.; Calabrò, S.; Schumacher, U. YKL-40 Protein Expression in Human Tumor Samples and Human Tumor Cell Line Xenografts: Implications for Its Use in Tumor Models. *Cell. Oncol.* **2021**, *44*, 1183–1195. [CrossRef] [PubMed]
52. Pădureţu, C.-C.; Isopescu, R.; Rău, I.; Apetroaei, M.R.; Schröder, V. Influence of the Parameters of Chitin Deacetylation Process on the Chitosan Obtained from Crab Shell Waste. *Korean J. Chem. Eng.* **2019**, *36*, 1890–1899. [CrossRef]
53. Khanmohammadi, M.; Elmizadeh, H.; Ghasemi, K. Investigation of Size and Morphology of Chitosan Nanoparticles Used in Drug Delivery System Employing Chemometric Technique. *Iran. J. Pharm. Res. IJPR* **2015**, *14*, 665–675. [PubMed]
54. Duarte, A.R.C.; Gordillo, M.D.; Cardoso, M.M.; Simplício, A.L.; Duarte, C.M.M. Preparation of Ethyl Cellulose/Methyl Cellulose Blends by Supercritical Antisolvent Precipitation. *Int. J. Pharm.* **2006**, *311*, 50–54. [CrossRef] [PubMed]
55. Apetroaei, M.R.; Rau, I.; Schroder, V. *Chitosan: Biopolymer Identified in Rapana Venosa (Gastropoda, Mollusca) [Available in Romanian]*; Editura Pim: Iasi, Romania, 2020; ISBN 978-606-13-5543-3.
56. Joseph, S.M.; Krishnamoorthy, S.; Paranthaman, R.; Moses, J.A.; Anandharamakrishnan, C. A Review on Source-Specific Chemistry, Functionality, and Applications of Chitin and Chitosan. *Carbohydr. Polym. Technol. Appl.* **2021**, *2*, 100036. [CrossRef]
57. Negm, N.A.; Hefni, H.H.H.; Abd-Elaal, A.A.A.; Badr, E.A.; Abou Kana, M.T.H. Advancement on Modification of Chitosan Biopolymer and Its Potential Applications. *Int. J. Biol. Macromol.* **2020**, *152*, 681–702. [CrossRef]
58. Gutteridge, J.M.C.; Halliwell, B. Free Radicals and Antioxidants in the Year 2000: A Historical Look to the Future. *Ann. N. Y. Acad. Sci.* **2000**, *899*, 136–147. [CrossRef] [PubMed]
59. Sun, T.; Zhou, D.; Xie, J.; Mao, F. Preparation of Chitosan Oligomers and Their Antioxidant Activity. *Eur. Food Res. Technol.* **2007**, *225*, 451–456. [CrossRef]
60. Aranaz, I.; Alcántara, A.R.; Civera, M.C.; Arias, C.; Elorza, B.; Heras Caballero, A.; Acosta, N. Chitosan: An Overview of Its Properties and Applications. *Polymers* **2021**, *13*, 3256. [CrossRef]
61. Si Trung, T.; Bao, H.N.D. Physicochemical Properties and Antioxidant Activity of Chitin and Chitosan Prepared from Pacific White Shrimp Waste. *Int. J. Carbohydr. Chem.* **2015**, *2015*, 706259. [CrossRef]
62. Xing, R.; Liu, S.; Guo, Z.; Yu, H.; Wang, P.; Li, C.; Li, Z.; Li, P. Relevance of Molecular Weight of Chitosan and Its Derivatives and Their Antioxidant Activities in Vitro. *Bioorg. Med. Chem.* **2005**, *13*, 1573–1577. [CrossRef] [PubMed]
63. Boudier, A.; Aubert-Pouëssel, A.; Gérardin, C.; Devoisselle, J.-M.; Bégu, S. PH-Sensitive Double-Hydrophilic Block Copolymer Micelles for Biological Applications. *Int. J. Pharm.* **2009**, *379*, 212–217. [CrossRef] [PubMed]
64. Zou, P.; Yang, X.; Zhang, Y.; Du, P.; Yuan, S.; Yang, D.; Wang, J. Antitumor Effects of Orally and Intraperitoneally Administered Chitosan Oligosaccharides (COSs) on S180-Bearing/Residual Mouse. *J. Food Sci.* **2016**, *81*, H3035–H3042. [CrossRef]
65. Farhadihosseinabadi, B.; Zarebkohan, A.; Eftekhary, M.; Heiat, M.; Moosazadeh Moghaddam, M.; Gholipourmalekabadi, M. Crosstalk between Chitosan and Cell Signaling Pathways. *Cell. Mol. Life Sci.* **2019**, *76*, 2697–2718. [CrossRef] [PubMed]

66. Gibot, L.; Chabaud, S.; Bouhout, S.; Bolduc, S.; Auger, F.A.; Moulin, V.J. Anticancer Properties of Chitosan on Human Melanoma Are Cell Line Dependent. *Int. J. Biol. Macromol.* **2015**, *72*, 370–379. [CrossRef] [PubMed]
67. Amirani, E.; Hallajzadeh, J.; Asemi, Z.; Mansournia, M.A.; Yousefi, B. Effects of Chitosan and Oligochitosans on the Phosphatidylinositol 3-Kinase-AKT Pathway in Cancer Therapy. *Int. J. Biol. Macromol.* **2020**, *164*, 456–467. [CrossRef] [PubMed]
68. Huang, R.; Mendis, E.; Rajapakse, N.; Kim, S.-K. Strong Electronic Charge as an Important Factor for Anticancer Activity of Chitooligosaccharides (COS). *Life Sci.* **2006**, *78*, 2399–2408. [CrossRef] [PubMed]
69. Kim, K.W.; Thomas, R.L. Antioxidative Activity of Chitosans with Varying Molecular Weights. *Food Chem.* **2007**, *101*, 308–313. [CrossRef]
70. Kong, C.-S.; Kim, J.-A.; Ahn, B.; Byun, H.-G.; Kim, S.-K. Carboxymethylations of Chitosan and Chitin Inhibit MMP Expression and ROS Scavenging in Human Fibrosarcoma Cells. *Process Biochem.* **2010**, *45*, 179–186. [CrossRef]
71. Wimardhani, Y.S.; Suniarti, D.F.; Freisleben, H.J.; Wanandi, S.I.; Siregar, N.C.; Ikeda, M.-A. Chitosan Exerts Anticancer Activity through Induction of Apoptosis and Cell Cycle Arrest in Oral Cancer Cells. *J. Oral Sci.* **2014**, *56*, 119–126. [CrossRef] [PubMed]
72. Srinivasan, H.; Kanayairam, V.; Ravichandran, R. Chitin and Chitosan Preparation from Shrimp Shells Penaeus Monodon and Its Human Ovarian Cancer Cell Line, PA-1. *Int. J. Biol. Macromol.* **2018**, *107*, 662–667. [CrossRef] [PubMed]
73. Chokradjaroen, C.; Rujiravanit, R.; Watthanaphanit, A.; Theeramunkong, S.; Saito, N.; Yamashita, K.; Arakawa, R. Enhanced Degradation of Chitosan by Applying Plasma Treatment in Combination with Oxidizing Agents for Potential Use as an Anticancer Agent. *Carbohydr. Polym.* **2017**, *167*, 1–11. [CrossRef] [PubMed]
74. Chang, P.-H.; Sekine, K.; Chao, H.-M.; Hsu, S.; Chern, E. Chitosan Promotes Cancer Progression and Stem Cell Properties in Association with Wnt Signaling in Colon and Hepatocellular Carcinoma Cells. *Sci. Rep.* **2017**, *7*, 45751. [CrossRef] [PubMed]
75. Yeo, I.J.; Lee, C.-K.; Han, S.-B.; Yun, J.; Hong, J.T. Roles of Chitinase 3-like 1 in the Development of Cancer, Neurodegenerative Diseases, and Inflammatory Diseases. *Pharmacol. Ther.* **2019**, *203*, 107394. [CrossRef] [PubMed]
76. He, C.H.; Lee, C.G.; Dela Cruz, C.S.; Lee, C.-M.; Zhou, Y.; Ahangari, F.; Ma, B.; Herzog, E.L.; Rosenberg, S.A.; Li, Y.; et al. Chitinase 3-like 1 Regulates Cellular and Tissue Responses via IL-13 Receptor A2. *Cell Rep.* **2013**, *5*, 1156. [CrossRef]
77. Zhao, T.; Su, Z.; Li, Y.; Zhang, X.; You, Q. Chitinase-3 like-Protein-1 Function and Its Role in Diseases. *Signal Transduct. Target. Ther.* **2020**, *5*, 201. [CrossRef] [PubMed]
78. Uhlén, M.; Fagerberg, L.; Hallström, B.M.; Lindskog, C.; Oksvold, P.; Mardinoglu, A.; Sivertsson, Å.; Kampf, C.; Sjöstedt, E.; Asplund, A.; et al. Tissue-Based Map of the Human Proteome. *Science* **2015**, *347*, 1260419. [CrossRef] [PubMed]
79. Mokhtari, R.B.; Homayouni, T.S.; Baluch, N.; Morgatskaya, E.; Kumar, S.; Das, B.; Yeger, H. Combination Therapy in Combating Cancer. *Oncotarget* **2017**, *8*, 38022–38043. [CrossRef] [PubMed]
80. Wande, D.P.; Qiu, Y.; Chen, S.; Yao, L.; Xu, Y.; Yao, J.; Xiong, H. Modified Chitosan Nanogel-Polymersomes for Oral Co-Delivery of Oxaliplatin and Rapamycin for Synergistic Chemotherapy. *J. Drug Deliv. Sci. Technol.* **2022**, *77*, 103852. [CrossRef]
81. Sangnim, T.; Dheer, D.; Jangra, N.; Huanbutta, K.; Puri, V.; Sharma, A. Chitosan in Oral Drug Delivery Formulations: A Review. *Pharmaceutics* **2023**, *15*, 2361. [CrossRef] [PubMed]
82. Liu, Z.-L.; Chen, H.-H.; Zheng, L.-L.; Sun, L.-P.; Shi, L. Angiogenic Signaling Pathways and Anti-Angiogenic Therapy for Cancer. *Signal Transduct. Target. Ther.* **2023**, *8*, 198. [CrossRef]
83. Dinculescu, D.D.; Apetroaei, M.R.; Gîjiu, C.L.; Anton, M.; Enache, L.; Schröder, V.; Isopescu, R.; Rău, I. Simultaneous Optimization of Deacetylation Degree and Molar Mass of Chitosan from Shrimp Waste. *Polymers* **2024**, *16*, 170. [CrossRef] [PubMed]
84. Pădureț u, C.-C.; Apetroaei, M.R.; Rau, I.; Schröder, V. Characterization of Chitosan Extracted from Different Romanian Black Sea Crustaceans. *UPB Sci. Bull. B Chem. Mater. Sci.* **2018**, *80*, 13–24.
85. Apetroaei, M.R.; Manea, A.M.; Tihan, G.; Zgârian, R.; Schröder, V.; Rău, I. Improved Method of Chitosan Extraction from Different Crustacean Species of Romanian Black Sea Coast. *UPB Sci. Bull. B Chem. Mater. Sci.* **2017**, *79*, 13–24.
86. Al Sagheer, F.A.; Al-Sughayer, M.A.; Muslim, S.; Elsabee, M.Z. Extraction and Characterization of Chitin and Chitosan from Marine Sources in Arabian Gulf. *Carbohydr. Polym.* **2009**, *77*, 410–419. [CrossRef]
87. Vunjak-Novakovic, G.; Freshney, R.I. *Culture of Cells for Tissue Engineering*; Wiley: New York, NY, USA, 2006; ISBN 9780471741800.
88. Mosmann, T. Rapid Colorimetric Assay for Cellular Growth and Survival: Application to Proliferation and Cytotoxicity Assays. *J. Immunol. Methods* **1983**, *65*, 55–63. [CrossRef] [PubMed]
89. Laville, N.; Aït-Aïssa, S.; Gomez, E.; Casellas, C.; Porcher, J. Effects of Human Pharmaceuticals on Cytotoxicity, EROD Activity and ROS Production in Fish Hepatocytes. *Toxicology* **2004**, *196*, 41–55. [CrossRef] [PubMed]
90. van Meerloo, J.; Kaspers, G.J.L.; Cloos, J. Cell Sensitivity Assays: The MTT Assay. *Methods Mol. Biol.* **2011**, *731*, 237–245. [PubMed]
91. Stockert, J.C.; Blázquez-Castro, A.; Cañete, M.; Horobin, R.W.; Villanueva, Á. MTT Assay for Cell Viability: Intracellular Localization of the Formazan Product Is in Lipid Droplets. *Acta Histochem.* **2012**, *114*, 785–796. [CrossRef] [PubMed]
92. Cann, A.J. *Maths from Scratch for Biologists*; Wiley: New York, NY, USA, 2002; ISBN 978-0-471-49835-3.

International Journal of
Molecular Sciences

MDPI

Article

Salicylic Acid Mediates Chitosan-Induced Immune Responses and Growth Enhancement in Barley

Pawel Poznanski [1], Abdullah Shalmani [1], Marcin Bryla [2] and Waclaw Orczyk [1,*]

[1] Plant Breeding and Acclimatization Institute—National Research Institute, Radzików, 05-870 Blonie, Poland; p.poznanski@ihar.edu.pl (P.P.)
[2] Institute of Agricultural and Food Biotechnology—State Research Institute, Rakowiecka 36, 02-532 Warsaw, Poland; marcin.bryla@ibprs.pl
* Correspondence: w.orczyk@ihar.edu.pl

Abstract: Chitosan (CS), derived from the partial deacetylation and hydrolysis of chitin, varies in the degree of deacetylation, molecular weight, and origin, influencing its biological effects, including antifungal properties. In plants, CS triggers immune responses and stimulates biomass growth. Previously, we found that the antifungal activity of CS was strongly dependent on its physicochemical properties. This study revealed that the chitosan batch CS_10 with the strongest antifungal activity also effectively activated plant immune responses and promoted biomass growth. Barley treated with CS_10 exhibited systemic acquired resistance (SAR), characterized by micronecrotic reactions upon *Puccinia hordei* (*Ph*) inoculation and reduced symptoms following *Fusarium graminearum* (*Fg*) infection, representing biotrophic and necrotrophic pathogens, respectively. CS_10 treatment (concentration 200 ppm) also enhanced plant biomass growth (by 11% to 15%) and promoted the accumulation of salicylic acid (SA), a hormone that regulates both plant immune responses and growth. Low levels of exogenous SA applied to plants mirrored the stimulation observed with CS_10 treatment, suggesting SA as a key regulator of CS_10-induced responses. Transcriptomic analysis identified SA-regulated genes as drivers of enhanced immunity and biomass stimulation. Thus, CS_10 not only fortifies plant defenses against pathogens like *Ph* and *Fg* but also boosts growth through SA-dependent pathways.

Keywords: barley transcriptome; cereal crops; deacetylation degree; *Fusarium graminearum*; *Hordeum vulgare*; necrotic reactions; pathogenesis related (PR) proteins; *Puccinia hordei*; reactive oxygen species (ROS); systemic acquired resistance (SAR)

1. Introduction

Chitin, the second most abundant natural polysaccharide after cellulose, is a key component of crustacean and insect exoskeletons, fungal cell walls, and cephalopod beaks. It is a linear polymer composed of β-1,4-linked N-acetyl-D-glucosamine (GlcNAc) [1]. As the main component of fungal cell walls, chitin oligomers released during pathogenesis act as plant immune elicitors. Chitosan (CS), derived from the partial deacetylation and hydrolysis of chitin, is a copolymer of N-acetyl-D-glucosamine (GlcNAc) and deacetylated D-glucosamine (GlcN). Each CS batch varies in its degree of deacetylation (DD), average molecular weight (MW), and biological origin [2]. CS is soluble in water at acidic pH (at pH < 6), when most amino groups are protonated. Depending on their molecular characteristics, the CS molecules can influence biological processes in diverse organisms with strong antifungal properties that restricts the growth of pathogenic fungi [3] and significantly reduce mycotoxin levels in plant material [4,5]. Chitosan serves as an effective elicitor of plant immunity, enhancing plants' defenses against a wide range of pathogens, including bacteria, fungi, and viruses. In addition to its protective role, chitosan application promotes plant growth, boosts yield, and stimulates the production of diverse secondary metabolites [6]. These beneficial characteristics, along with biocompatibility and biodegradation, make

CS a suitable candidate for various applications, including sustainable agriculture [7–10]. Its strong antifungal effects against *Fusarium* species, inhibition of mycotoxin accumulation [4], and enhancement of plant immunity position makes CS a promising compound for mitigating *Fusarium*-related diseases. However, the precise biological mechanisms by which CS affects both fungal and plant processes are only partially understood and warrant further investigation.

Barley (*Hordeum vulgare* L.) is a major cereal crop globally, but it is highly susceptible to Fusarium head blight (FHB), a severe disease affecting various cereals. FHB is primarily caused by the *Fusarium oxysporum* species complex (FOSC), a soil-borne pathogen that includes *Fusarium graminearum* (*Fg*). FOSC ranks fifth among the top economically damaging pathogens, impacting over 100 crop species. FHB not only reduces crop yields but also degrades grain quality due to the accumulation of harmful mycotoxins, which can render the harvest unsuitable for food and feed use [11–13]. *Fg* exhibits a biotrophic growth phase early in infection, followed by a necrotrophic phase during active pathogenesis, during which it produces mycotoxins, including deoxynivalenol (DON). The Golden Promise cultivar was selected for this study due to its widespread use as a model in cereal genetics and breeding research. It is particularly valuable because its entire genome has been sequenced and fully annotated, providing a comprehensive resource for genetic and functional studies.

Plant immunity activated by pathogen-associated molecular patterns (PAMPs) involves the reprogramming of host cellular processes to resist pathogen attacks. Chitin- and chitosan-derived elicitors serve as fungal PAMPs, triggering defense responses in plants [14]. These responses include the rapid accumulation of reactive oxygen species (ROS) at the infection site, which act as signaling molecules that activate the plant immune response and local necrotic reactions. ROS-dependent necroses directly impact pathogens, with varying effects based on their life strategies and pathogenesis types. For instance, biotrophic pathogens, like *Ph*, are quickly and strongly countered by ROS and local micronecrotic reactions [15–17]. In contrast, necrotrophic pathogens such as *Fg* can exploit host necrosis to enhance their pathogenesis. However, low to moderate ROS levels serve as signaling molecules that activate additional defense mechanisms in both pathogenesis systems. The plant immune system is highly sophisticated, with pathogen recognition being the critical initial step in preventing disease progression [18].

Salicylic acid (SA) is a plant hormone that regulates immune responses by controlling numerous crucial genes involved in defense [19,20]. Beyond its role in immunity, SA is also involved in stress response [21] and growth regulation [22,23]. Plants synthesize SA through two main pathways: the ICS (isochorismate synthase)-dependent and the PAL (phenylalanine ammonia-lyase)-dependent pathways [20,24]. The predominance of one pathway over the other varies by species and is influenced by environmental or biotrophic factors; in some cases, both pathways can operate simultaneously. For instance, rice primarily relies on the PAL-dependent pathway [25], while in Arabidopsis, the ICS-dependent pathway is dominant [26]. In soybeans, both PAL- and ICS-dependent pathways are equally important [27]. The involvement of each pathway can vary depending on the type of immune response or environmental condition. In barley, there are seven PAL paralogs and a single ICS gene [28], but their roles in SA biosynthesis are still under debate. Hao et al. [29] reported that the single ICS gene plays a major role in SA biosynthesis and the development of SA-dependent basal resistance to *Fg*. In their system, none of the known PAL paralogs influenced SA levels or resistance to *Fg*. Conversely, Qin et al. [30] found that knocking out the ICS gene did not affect basal SA levels, suggesting that the PAL-dependent pathway is responsible for maintaining them. These findings suggest that SA biosynthesis in barley is complex, likely involving both pathways. The PAL-dependent pathway may maintain basal SA levels, while ICS-dependent synthesis is triggered by external signals. In a previous article [4], we explored the antifungal effect of CS application, focusing on its ability to mitigate pathogenesis and inhibit mycotoxin synthesis. We found that only a specific batch of chitosan_10 (CS_10), characterized by a low molecular weight (MW) of

30 kDa and a high degree of deacetylation (DD) of ≥90, exhibited the desired antifungal properties in a concentration of 200 ppm [4]. CS oligomers showed no significant antifungal activity, while high MW CS batches were relatively ineffective.

In the current experiments, we discovered that the CS_10 sample with the strongest antifungal properties was among those which most effectively stimulated barley growth and immune responses. Therefore, the objective of this article was to investigate *Hordeum vulgare* cv Golden Promise response to CS_10 application, aiming to identify the factors responsible for: (i) enhanced immune response and resistance and (ii) increased plant biomass growth.

2. Results

2.1. CS_10 Treatment Activates Plant Immune Response in Barley Leaves Detectable as Smaller Necrotic Symptoms and Stronger Micronecroses After Fg and Ph Inoculations

Addressing the first hypothesis that CS_10 treatment activates the immune response, the two plant pathogens, which represented two different lifestyles, i.e., necrotrophic *Fg* and biotrophic *Ph*, were used. The *Fg* infection symptoms on the third leaves of mock-treated control plants showed medium to large dark-colored necrotic areas. The large chlorotic sections indicated widespread infection. The infection symptoms on the third leaves of CS_10-treated plants were smaller compared to the control. The dark necrotic spots were restricted to the inoculation sites, and they were surrounded by relatively small chlorotic areas. In mock-treated plants, necrotic sites and chlorotic areas were visibly larger compared to the control (Figure 1A). The rate of *Fg* infection in both variants was further quantified by qPCR using primers designed for *Fg (Fg_TRI5*) and barley (*Hv_EFG1*) genes (Table S1) and gDNA from the infected leaves as a template. In mock-treated plants, the ratio of *Fg*-specific *TRI5* gene per one copy of barley-specific *EFG1* varied from 0.11 to 0.21, with the average value of 0.15 (SD ± 0.04). In CS_10-treated plants, the ratio of *Fg_TRI5*/*Hv_EFG1* varied from 0.03 to 0.09, with an average of 0.06 (SD ± 0.02) (Figure 1B).

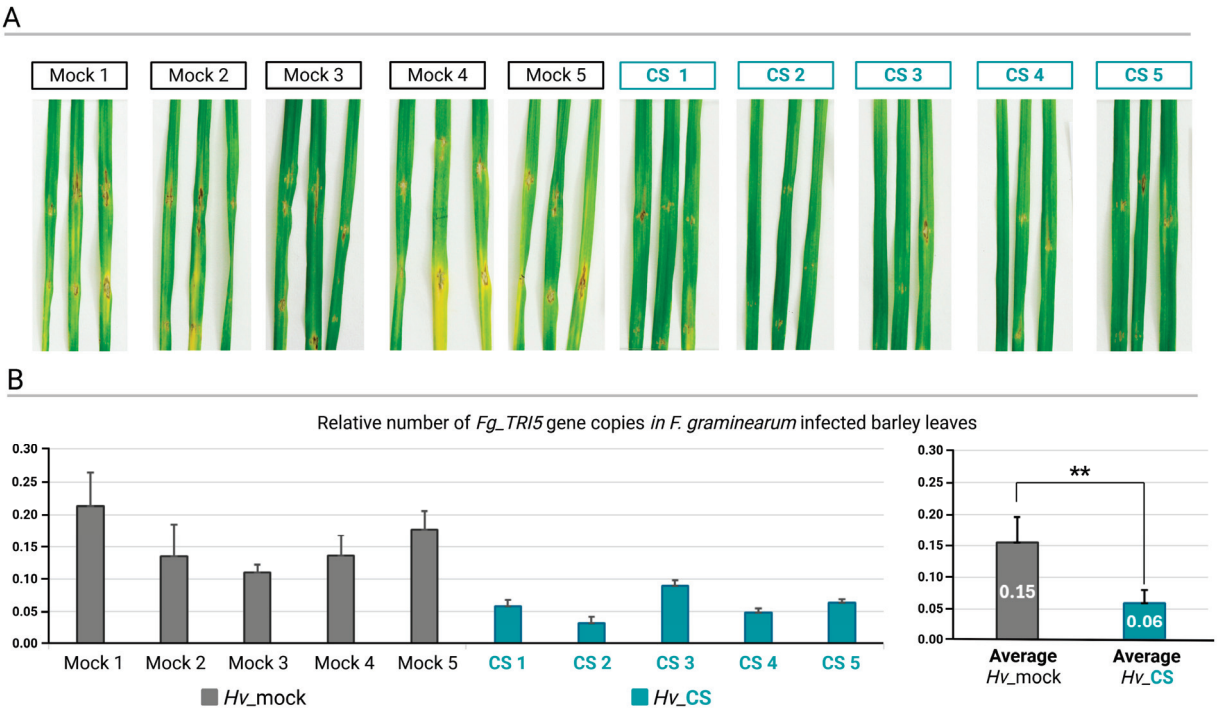

Figure 1. Representative picture of infection symptoms on the third barley leaves inoculated with *Fusarium graminearum* (*Fg*) in plants where the second leaves were mock (*Hv*-mock)- or chitosan_10 (CS)-treated (*Hv*_CS) (**A**). Relative number of *Fg TRI4* gene copies (*Fg_TRI5*) per one copy of barley *EFG1* gene (*Hv_EFG1*) is shown. The results are from five independent biological repetitions and the average values of genes' quantification are shown (**B**). Asterisks indicate significance level (based on one-way ANOVA and Tukey's post hoc test) ** $p \leq 0.01$.

Six days post-inoculation with *Ph*, the third leaves of the CS_10-sprayed plants exhibited fewer necrotic spots and weaker infection symptoms compared to the mock-treated plants (Figure 2A). Calcofluor white (CW) staining followed by the microscopic visualization of the infection sites showed the development of *Ph* infection structures and the presence of micronecrotic reactions of plant cells on different time days (Figure 2B).

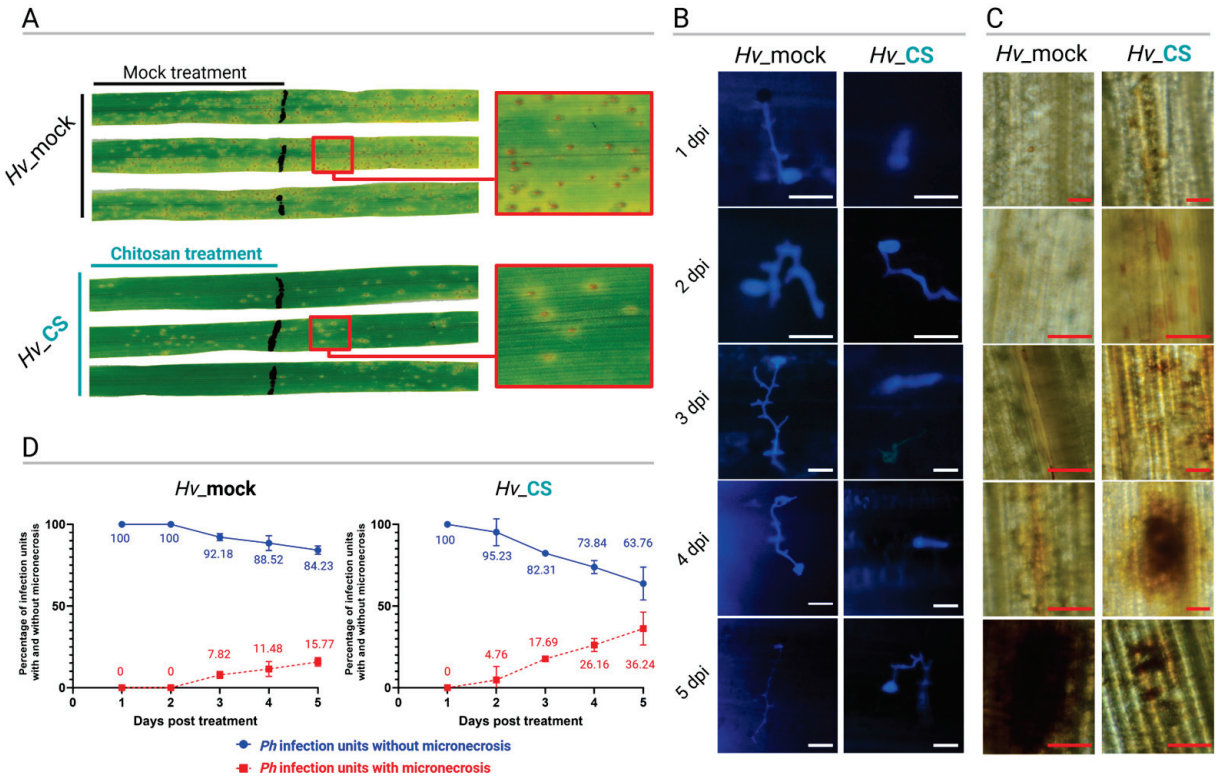

Figure 2. Plant–pathogen interaction of barley plants treated with mock (*Hv*-mock) or with chitosan_10 solution (*Hv*-CS) followed by inoculation with *Puccinia hordei* (*Ph*) urediniospores. The CS_10 or mock treatments were applied to the second leaves of the plants, and the third leaves of the same plants were inoculated with *Ph* urediniospores. This approach allowed us to detect the results of plant immune response induced by the CS-10 and not a direct inhibitory effect of the CS-10 on the pathogen. Representative pictures of infection symptoms on the third leaves of mock- and CS_10-treated plants scored six days post-inoculation (**A**). Representative pictures of microscopic observation of infection sites of calcofluor white stained leaf samples scored from 1 to 5 days post-inoculation. Scale bars = 100 µm (**B**). Representative pictures of leaf samples stained with DAB. Scale bars = 100 µm (**C**). The rates of micronecrotic reactions in *Ph* infection units on barley leaves. The mean values and standard deviation were calculated based on scoring one entire leaf from each time point and three biological replicates (**D**).

The germination of *Ph* urediniospores was observed already at 1-day post-inoculation (dpi) in mock-treated control, while in the CS_10-treated plants, a similar stage was observed a day later at 2 dpi. The subsequent stages of *Ph* development were delayed by about one day in CS_10-treated plants compared to the control (Figure 2B). The first micronecrotic reactions representing plant response, which further restricted *Ph* pathogenesis, were observed 2 dpi in CS_10-treated plants and 3 dpi in the control plants (Figure 2B). The CW-stained samples allowed for the quantitative scoring of infection sites with micronecroses. In mock-treated control plants, micronecroses were not detectable at 1 and 2 dpi. The infection rate of micronecroses at 3 dpi was 7.8%, and it increased to 11.5% and 15.8% at 4 and 5 dpi, respectively. In CS_10-treated plants, the micronecrotic responses were observed one day earlier compared to mock at 2 dpi, and the rate was 4.8%. On subsequent days, the rates were 17.7, 26.2, and 36.2% at 3, 4, and 5 dpi, respectively (Figure 2C).

Moreover, the samples of *Ph*-inoculated leaves collected from mock- and CS_10-treated plants were stained with DAB followed by microscopic observations. Brown precipitate, the result of DAB oxidization by hydrogen peroxide, indicated sites of hydrogen peroxide accumulation in plant tissues. The intensity of the DAB staining also allowed for the semi-quantitative analysis of H_2O_2 accumulation. A higher accumulation of H_2O_2 was observed in the CS_10-treated plants during the early days of infection, particularly at 3 and 4 dpi. In contrast, H_2O_2 accumulation was higher in the mock-treated plants after 5 dpi. Additionally, we noted that the number of infections was higher on the third leaf of the mock-treated plants compared to the CS_10-treated plants, which may be due to the early accumulation of H_2O_2 in the CS_10-treated plants (Figure 2D).

2.2. CS_10 Treatment of Barley Plants Leads to Elevated Levels of Salicylic Acid in the Leaves

SA concentration was quantified in the pooled second and third leaves of 14-day-old plants. The leaves were mock treated (*Hv*_mock), sprayed with CS_10 200 ppm solution (*Hv*_CS), and inoculated with *Fg* macrospores (*Hv_Fg*). The SA concentration were measured for all treatments in two timepoints: one day after treatment and three days after treatment. One day after mock treatment, the level of SA in mock-treated, CS_10-treated, and *Fg*-inoculated plants were 975 µg/kg, 967 µg/kg, and 1471 µg/kg, respectively. Three days after treatment, SA concentrations in mock-treated, CS_10-treated, and *Fg*-inoculated plants were 785 µg/kg, 1298 µg/kg, and 1646 µg/kg, respectively (Figure 3).

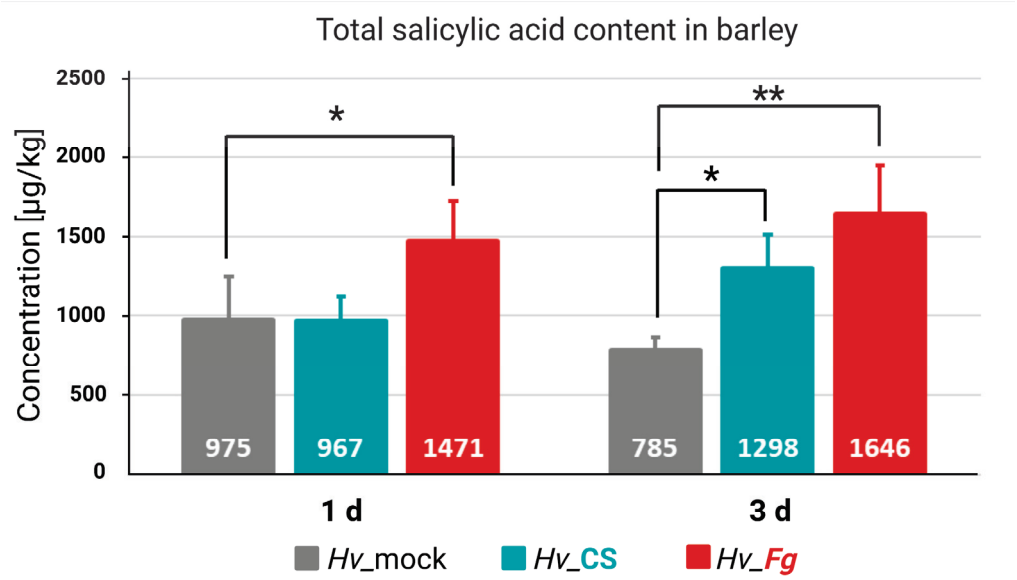

Figure 3. Concentration of total salicylic acid (SA) in barley leaves collected one day (1 d) and three days (3 d) after mock (*Hv*-mock) or chitosan_10 treatment (*Hv*-CS), or inoculation with *F. graminearum* (*Fg*) (*Hv_Fg*). Asterisks indicate significance level (based on one-way ANOVA and LSD post hoc test) * $p \leq 0.05$ and ** $p \leq 0.01$.

2.3. Treatments with CS_10 and SA Stimulates the Biomass Growth of Barley Seedlings

To investigate the stimulation of plant growth by different samples of CS (Table 1), barley seedlings were grown in a semi-hydroponic system in Hoagland medium. First, we investigated how different CS samples (Table 1), characterized by different deacetylation degrees (DDs), molecular weights (MWs), and biological origins, affected the growth of barley seedlings (Figure 4A). The relative biomass gains of the barley seedlings treated with different CS samples ranged from 0.93 to 1.16. Treatment with CS_5 and CS_100-300 showed a slight inhibition of growth by factors 0.93 and 0.96, respectively. Treatment with CS_8-15, CS_10, CS_10-120, CS_30-100, and CS_300-1k enhanced biomass growth by factors of 1.16, 1.11, 1.07, 1.06, and 1.13, respectively (Figure 4A). Although biomass enhancement was relatively modest, it was statistically significant for CS samples CS_8-15,

CS-10, CS_10-20, and CS_300-1k. For subsequent experiments, CS_10 was chosen due to its superior antifungal activity against *Fg*.

Table 1. Characteristics of the selected chitosan (CS) samples used in the experiments.

No.	Name of the Sample	Viscosity [cps]	Molecular Weight [kDa]	Deacetylation Degree [%]	Origin
1	CS_5	5	20	≥90	Shrimp
2	CS_10	10	30	≥90	Shrimp
3	CS_8-15	8–15	20–100	87.6–92.5	Shrimp
4	CS_10-120	10–120	NP *	≥85	*Aspergillus niger*
5	CS_30-100	30–100	250	≥90	Shrimp
6	CS_100-300	100–300	890	≥90	Shrimp
7	CS_300-1k	300–1000	1250	≥90	Shrimp

* NP—characteristic not provided by the distributor.

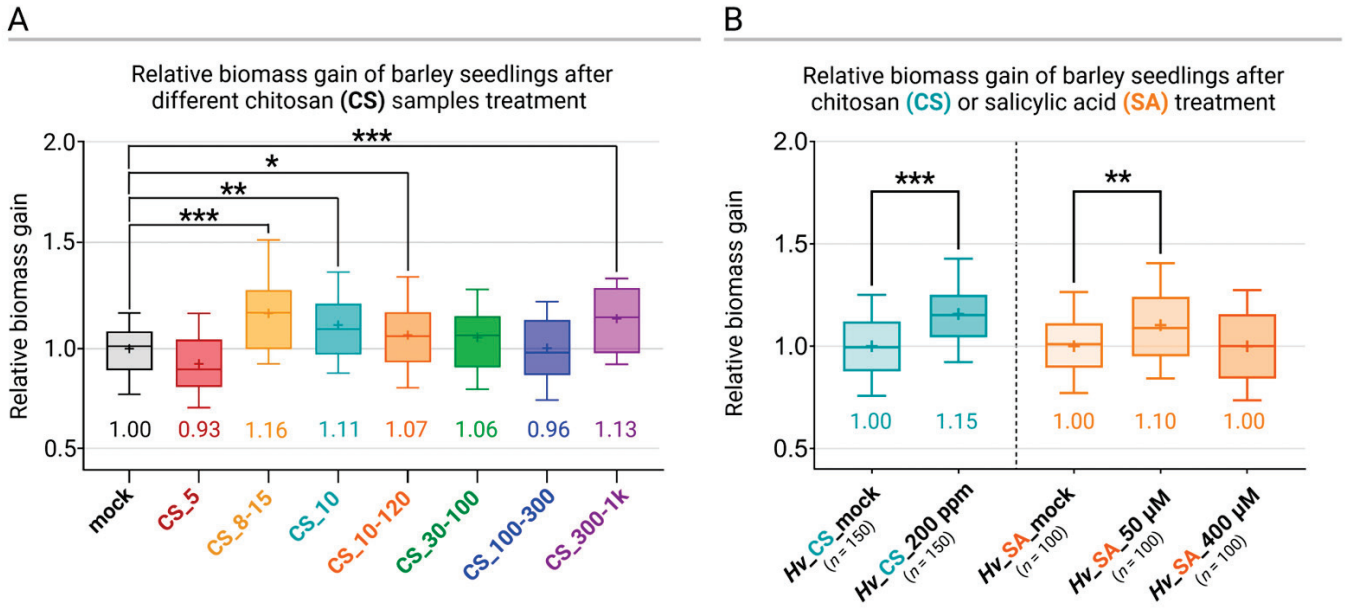

Figure 4. Relative biomass gain of barley seedlings after 19 days of cultivation in Hoagland medium after treatment with seven chitosan batches (200 ppm): CS_5, CS_8-15, CS_10, CS_10-120, CS_30-100, CS_100-300, and CS_300-1000. For each sample, 40 separate plants have been tested (**A**). Relative biomass gain of barley seedlings after 19 days of cultivation in Hoagland medium after chitosan (CS_10, 200 ppm) and after salicylic acid (SA, 50 µM and 400 µM) treatment (**B**). Each box represents the percentile in range 25–75; the whiskers represent the 10 and 90 percentiles. Asterisks indicate significance level (based on one-way ANOVA and Tukey's post hoc test) * $p \leq 0.05$, ** $p \leq 0.01$, and *** $p \leq 0.001$.

In another set of experiments, the relative biomass gain after treatment with CS_10 200 ppm was 1.15 (SD ± 0.17) (Figure 4B). The relative biomass gain after treatment with SA 50 µM was 1.10 (SD ± 0.21) and SA 400 µM was 1.00 ± 0.20) (Figure 4B).

2.4. Transcriptomic Analysis of Barley Response to CS_10 Treatment and Fg Inoculation

Barley transcriptome was analyzed in the following variants: barley inoculated with *Fg* (*Hv_Fg*), treated with CS_10 and inoculated with *Fg* (*Hv_Fg*_CS), barley treated with CS_10 (*Hv*_CS) and the control, mock-treated (*Hv*_mock) plants used as reference (Figure 5).

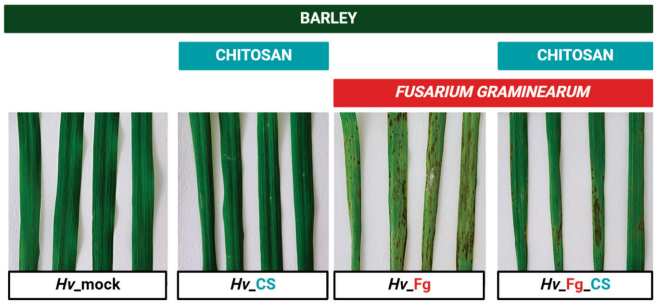

Figure 5. Representative picture of leaf samples used for RNA-seq analysis. *Hv*_mock—leaves treated with mock solution containing 0.05% acetic acid; *Hv*_CS—leaves treated with CS_10 (solutions of CS_10 also contained 0.05% acetic acid); *Hv_Fg*—leaves inoculated with *F. graminearum* (*Fg*); *Hv_Fg*_CS—leaves inoculated with *Fg* and treated with CS.

Initial variations between different variants were analyzed using hierarchical clustering distance (Pearson average distance on top 3000 genes) (Figure 6A). The correlation matrix represents the global relation between all variants. The average correlation coefficients (R^2) of gene expression between biological replicates of each treatment were high, ranging between 0.94 and 1. Treatment wise, *Hv*_mock and *Hv*_CS were closest, followed by *Hv_Fg*_CS and *Hv_Fg* (Figure 6B). All 12 samples (3 for each of the 4 variants) were analyzed with the use of principal component analysis (PCA). The treatments were separated by the first principal component (PC1), which accounted for 82.5% of the variation. The biological replicates grouped closest were based on their respective treatment (Figure 6C). Globally, the biggest difference was observed between *Fg*-inoculated (*Hv_Fg* and *Hv_Fg*_CS) and *Fg*-non-inoculated samples (*Hv*_mock and *Hv*_CS), indicating that inoculation with *Fg* had a significantly stronger effect than treatment with CS_10 (Figure 6).

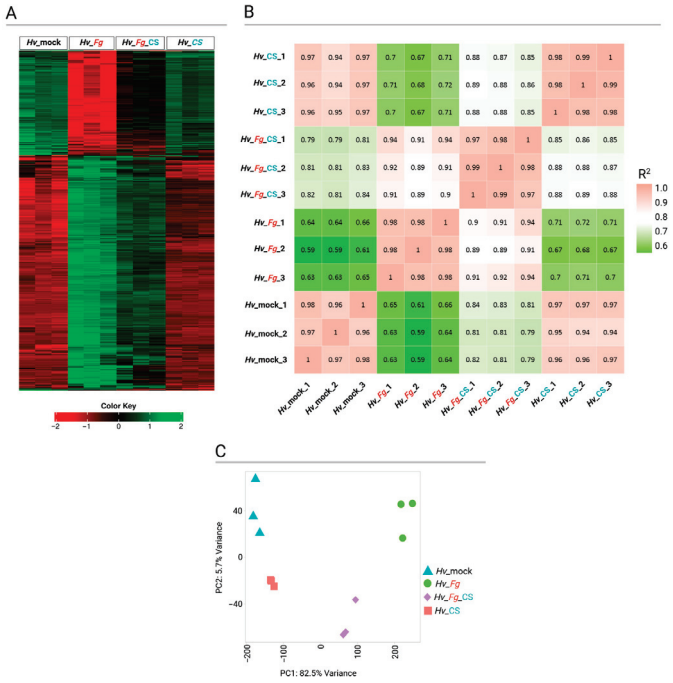

Figure 6. Hierarchical clustering heatmap of tested variants: leaf control samples (*Hv*_mock), leaves treated with CS_10 (*Hv*_CS), inoculated with *F.* graminearum (*Fg*) (*Hv_Fg*), and treated with CS_10 and inoculated with *Fg* (*Hv_Fg*_CS). The three columns in each variant represent the three biological replicates (**A**). Correlation matrix of all three biological replicates of each tested variant (**B**). Principal component analysis of all tested variants (**C**).

Genes with a false discovery rate (FDR) < 0.05 and genes with log2fold change > 2 were considered as differentially expressed genes (DEGs) between the variants (*Hv*_CS, *Hv_Fg*, and *Hv_Fg*_CS) in relation to the control (*Hv*_mock). The highest number of DEGs, 6652 downregulated and 6736 upregulated genes, was found in plants inoculated with *Fg* (*Hv_Fg*). *Fg* inoculation and CS_10 treatment (*Hv_Fg*_CS) led to 4715 upregulated and 3796 downregulated genes. CS_10 treatment (*Hv*_CS) led to downregulated 514 genes and upregulated 1198 genes (Figure 7A). The CS_10-treated sample (*Hv*_CS) showed 122 unique upregulated and 182 downregulated genes. An additional 91 upregulated and 39 downregulated genes were commonly found in the CS_10 treatment (*Hv*_CS) and CS_10 treatment and *Fg* inoculation (*Hv_Fg*_CS) variants. In the group of total 1198 genes upregulated after CS_10 treatment (*Hv*_CS), 985 (972 + 13) genes were also upregulated after *Fg* inoculation (*Hv_Fg*), and out of 514 downregulated genes, 293 (279 + 14) of these genes also overlapped with *Hv_Fg* downregulated genes (Figure 7B).

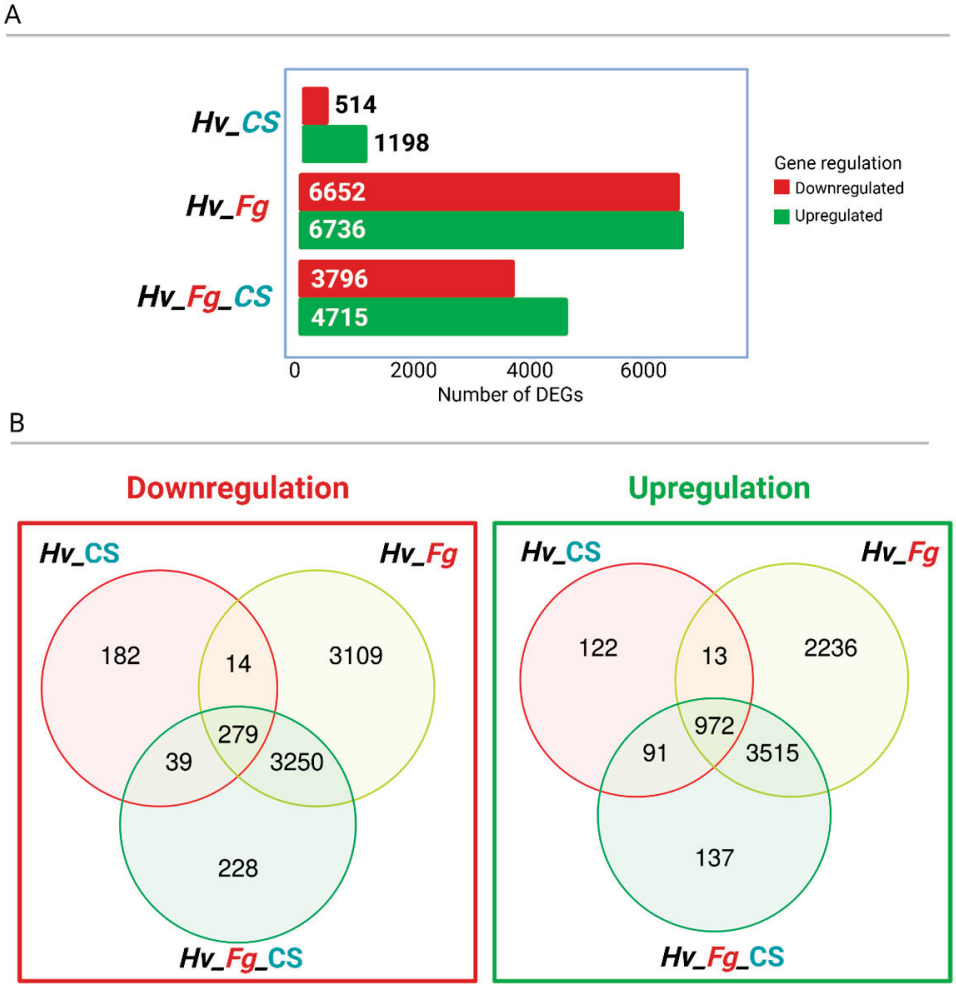

Figure 7. Numbers of differentially expressed genes (DEGs) in analyzed samples in relation to the control (*Hv*_mock). The tested variants include leaves treated with CS_10 (*Hv*-CS), leaves inoculated with *F. graminearum* (*Fg*) (*Hv-Fg*), and leaves treated with CS_10 and inoculated with *Fg* (*Hv_Fg*_CS) (**A**). Venn diagrams showing number of differentially expressed genes (DEGs) in each the three tested variants in relation to mock-treated control samples. Variants: leaves treated with CS_10 (*Hv*-CS), leaves inoculated with *Fg* (*Hv-Fg*), and leaves treated with CS_10 and inoculated with *Fg* (*Hv_Fg*_CS) (**B**). Presented genes are based on a cutoff value of FDR < 0.05 and log2fold change > 2.

2.5. The Top Five Terms of Biological Processes (BPs), Molecular Functions (MFs), and Cellular Components (CCs) Are More Strongly Affected by CS_10 Treatment than Fg Inoculation

Gene set enrichment analysis (GSEA) provides information on pathway enrichment across analyzed samples. It allows researchers to identify enriched or depleted sets of genes and describe them by respective Gene Ontology terms. This approach gives an overview of the main barley transcriptome responses differing in CS_10 treatment and *Fg* inoculation (Figure 8). In the two tested variants (*Hv*_CS and *Hv_Fg*), the biggest fold enrichment of biological processes (BPs) was in the "L-phenylalanine catabolic process". Similarly, "Aromatic amino acid family catabolic process" and "L-phenylalanine metabolic process" were among the most upregulated.

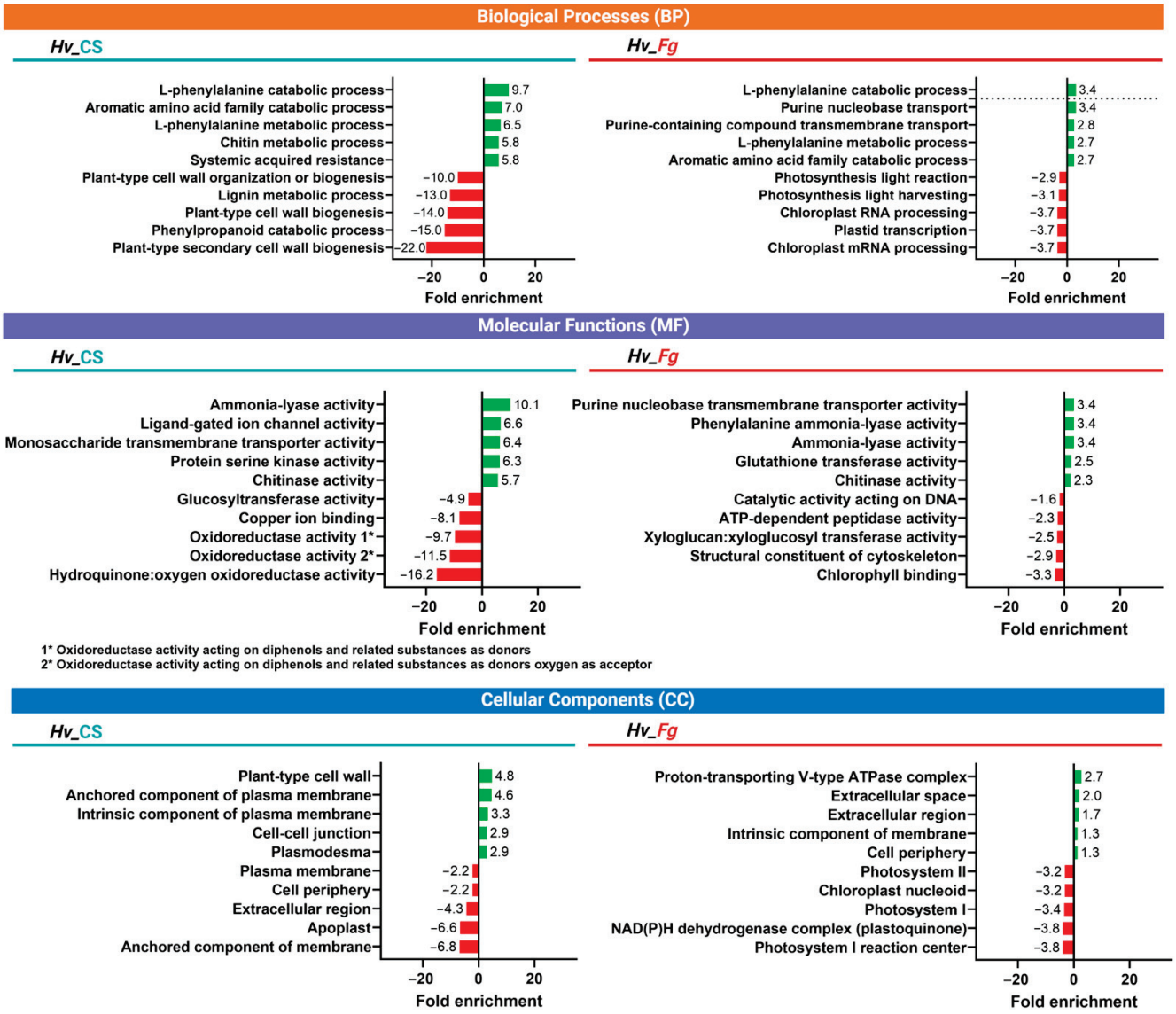

Figure 8. Top five Gene Ontology terms sorted by fold enrichment across chitosan_10 treated barley (*Hv*_CS) and *F. graminearum* inoculated barley (*Hv_Fg*) categorized into BPs (biological processes), MF (molecular function) and CC (cellular component) gene sets.

In *Hv*_CS, the top five downregulated GO terms were associated with the cell wall, lignin metabolic process, and plant cell wall organization. Differently, in *Hv_Fg*, the terms related to chloroplasts and photosynthesis were downregulated. In molecular functions (MFs), "Ammonia-lyase activity" and "Chitinase activity" were upregulated in both variants, *Hv*_CS and *Hv_Fg*. Large, downregulated differences between the variants were

related to oxidoreductase activities. In cellular components (CCs), the upregulated terms in *Hv*_CS were related to cell wall, plasma membrane, plasmodesma, and cell–cell junction. In *Hv_Fg*, the terms related to proton transport, and extracellular space were upregulated, while the terms related to photosynthesis were downregulated (Figure 8).

2.6. CS_10 Treatment and Inoculation with Fg Activates PAL-Dependent SA Synthesis and Strong Upregulation of PR-Encoding Immunity-Related Genes

SA functions as an important regulator of immune responses. Here, the genes related to SA synthesis and the SA-dependent signaling pathway were manually selected from the pool of genes with FDR > 0.05 and marked green if upregulated and red downregulated. This approach indicates a set of genes up- or downregulated in association with a particular variant. It is worth noting that out of the two PAL- and ICS-dependent SA biosynthesis pathways, the genes participating in the PAL-dependent pathway (*PAL1*, *PAL2*, *PAL3*) were upregulated in all variants, while the *ICS* gene was downregulated in all variants (Figure 9). The NPR1 protein functions as the main regulator of SA-dependent signaling pathways. In CS_10-treated variants, the NPR1-encoding gene was upregulated, while in the variant of only *Fg* inoculation, the expression of *NPR1* was on the same level as the control (Figure 9).

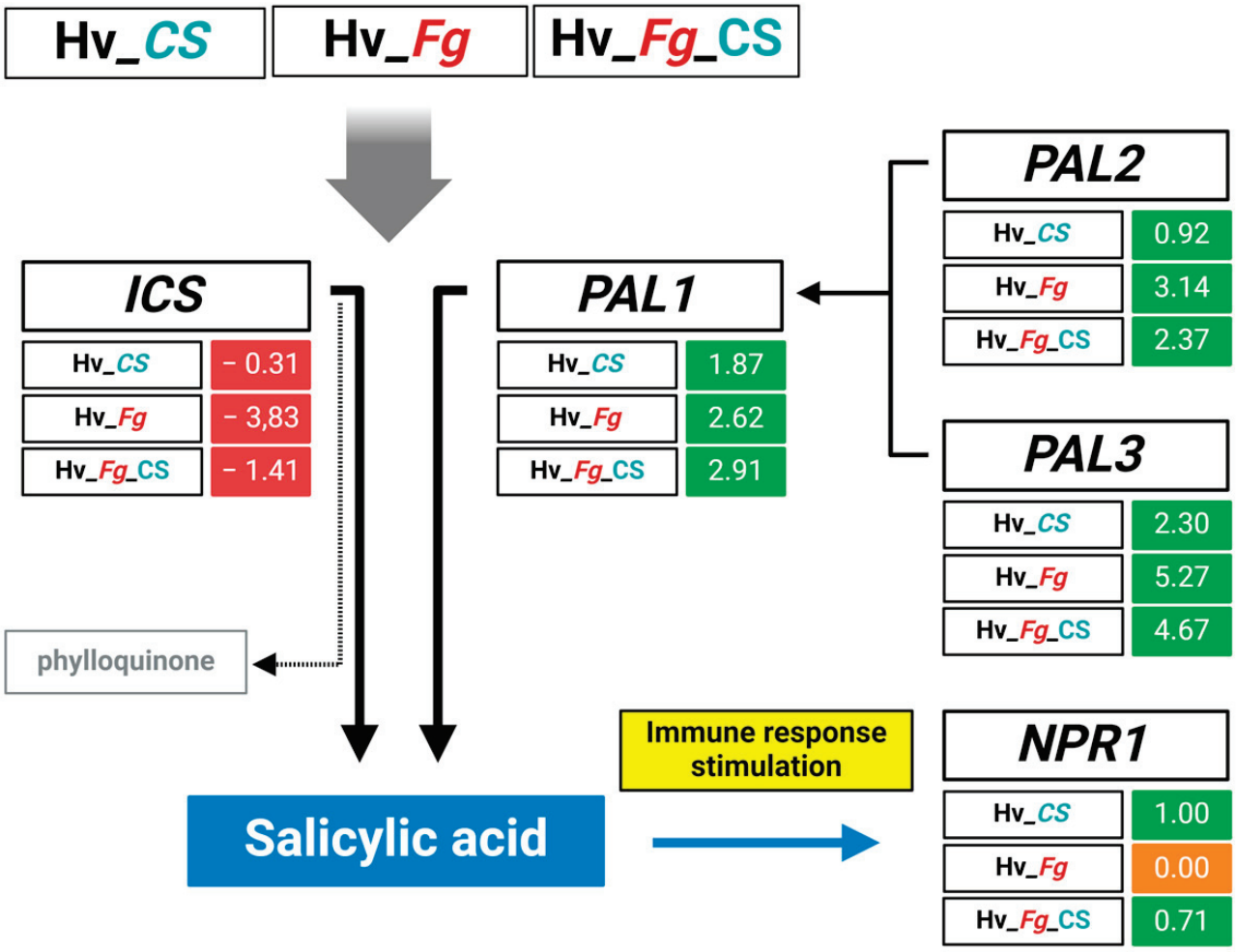

Figure 9. Regulation pattern of PAL- and ICS-encoding genes in variants of chitosan_10-treated (*Hv*_CS), *F. graminearum* (*Fg*)-inoculated (*Hv_Fg*), and CS_10-treated and *Fg*-inoculated barley.

NPR1 was upregulated in CS_10-treated barley (*Hv*_CS and *Hv_Fg*_CS), while no change in expression was observed in barley inoculated only with *Fg* (*Hv_Fg*). Among other genes considered as receptors and regulators of the SA-mediated immune response, *NPR3* was upregulated across all treatments. In contrast, *NPR4* showed increased expression

in *Fg*-inoculated barley (*Hv_Fg*) and CS_10-treated barley (*Hv*_CS) but not in barley simultaneously treated with both *Fg* and CS_10 (*Hv_Fg*_CS) (Figure 10). The expression of *NPR1*-activated genes encoding pathogenesis-related (PR) proteins displayed similar patterns of up- and downregulation across treatments. *PR1* to *PR5* genes had higher expression in *Hv_Fg* and *Hv_Fg*_CS than in *Hv*_CS. For example, *PR1* was highly expressed in *Hv_Fg* (7.9) and *Hv_Fg*_CS (6.5) compared to *Hv*_CS (2.1). Conversely, *PR6*, *PR7*, and *PR14* showed negative or low expression in *Hv_Fg* and *Hv_Fg*_CS, while they had moderate to low expression in *Hv*_CS. Genes such as *PR9*, *PR10*, *PR15*, and *PR16* were more highly expressed in *Hv_Fg* and *Hv_Fg*_CS than in *Hv*_CS (Figure 10).

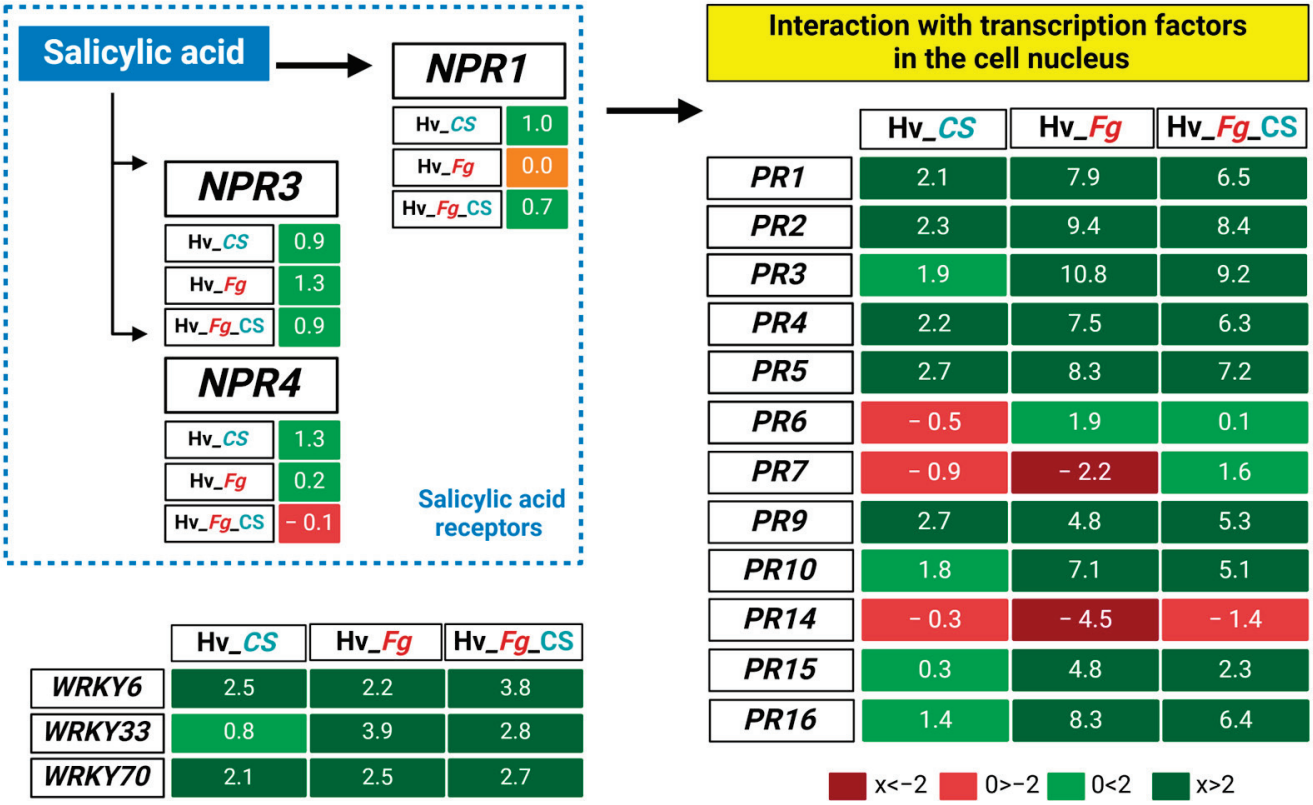

Figure 10. Regulation pattern of genes encoding NPR1, NPR3, and NPR4 regulators, selected WRKY transcription factors and pathogenesis-related (PR) proteins in variants of chitosan_10-treated (*Hv*_CS), *F. graminearum* (*Fg*)-inoculated (*Hv_Fg*), and chitosan_10-treated and *Fg*-inoculated barley plants. The blue color indicates the SA-related genes and pathways.

Selected WRKY transcription factors (*WRKY6*, *WRKY33*, *WRKY70*) were consistently upregulated across all variants (Figure 10). *WRKY6* showed the highest expression in the *Fg*-inoculated and CS_10-treated variant *(Hv_Fg*_CS) (3.8) compared to only CS_10-treated (*Hv*_CS) (2.5) and only *Fg*-inoculated barley (*Hv_Fg*) (2.2). In contrast, *WRKY33* had the highest expression in the *Fg*-inoculated variant (*Hv_Fg*) (3.9), compared to the CS_10-treated (*Hv*_CS) and *Fg*-inoculated barley (*Hv_Fg*). *WRKY70* showed consistent, moderate upregulation across all treatments (Figure 10). Genes' names and IDs are shown in Table S2.

2.7. RT-qPCR Analysis of Selected Barley Genes Confirms the Reliability of RNA-Seq Data

The four genes, *NPR1*, *PR9*, *PR4*, and *PR14*, each with a known role in plant immune response, were selected and used for the RT-qPCR verification of RNA-seq analysis. The results of RT-qPCR transcript quantification of the four genes were highly correlated (R^2 = 0.9329) with RNA-seq quantification (Figure 11). The results confirm the reliability of the RNA-seq results.

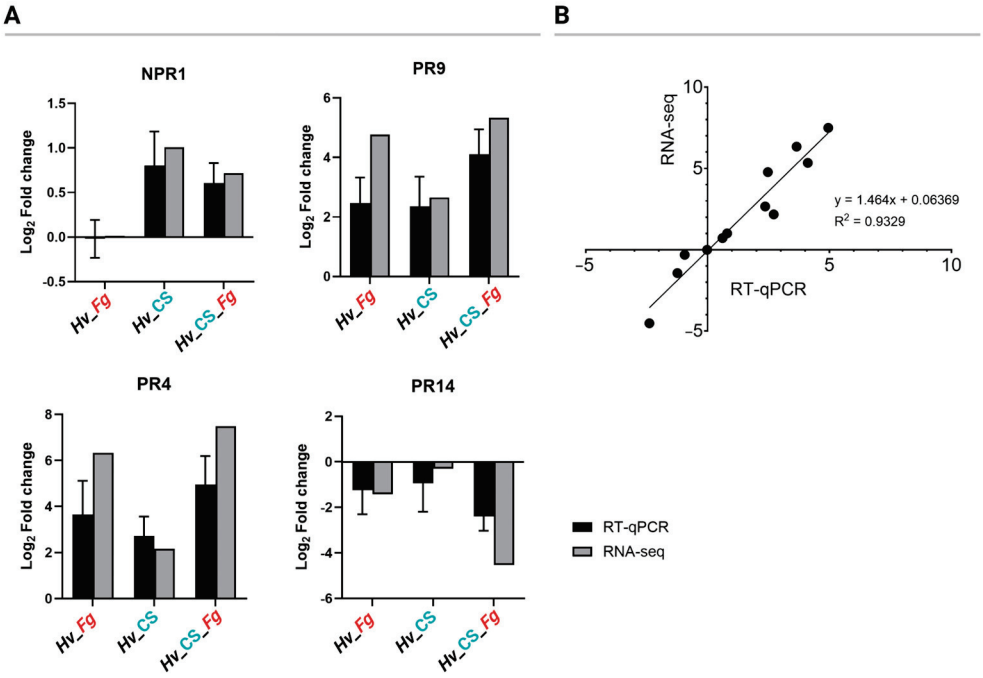

Figure 11. Validation of RNA-seq differentially expressed genes (DEGs) using RT-qPCR of four genes *NPR1*, *PR9*, *PR4*, and *PR14*. The log2-fold change values (**A**) and the linear regression between the log2-fold change of RNA-seq and RT-qPCR quantification are shown. The points represent individual results for each gene and the three variants (**B**).

3. Discussion

Pathogens remain the main threat to global food security despite advancement in resistance breeding and the widespread use of agrochemicals. One reason for this persistent threat is the rapid evolution of new virulent strains of pathogens, which overcomes both genetic resistance and the active ingredients of plant protection chemicals. Natural antifungal agents, like CS, tend to target multiple and complex pathways, as opposed to agrochemicals, which typically focus on single well-defined targets. This broader targeting reduces the likelihood of pathogens developing resistance to natural compounds. Although CS's antifungal activity is relatively modest, it can, when combined with partial genetic resistance, limit the progress of pathogenesis and potentially prevent field epidemics. In our previous research, we identified CS_10 as a batch of CS with significant antifungal activity, particularly in restricting *Fg* growth [4]. Using the same batch of CS_10, we treated barley plants to examine its effect on plant immune response, specifically looking for its ability to enhance resistance against pathogens with different modes of pathogenesis: the necrotrophic *Fg* and the biotrophic *Ph*. In our experimental setup, CS_10 was applied to the second leaves, while pathogen inoculation was conducted on the third leaves. This spatial separation allowed us to focus on the systemic immune response induced by CS_10 in plants rather than the direct antifungal action of CS_10.

The results showed that the CS_10 treatment reduced symptoms of *Fg* infection in the third leaves of plants treated with CS_10 compared to the mock-treated control (Figure 1B). This was confirmed by quantifying *Fg* gDNA in infected leaves. Plants treated with CS_10 exhibited a significant lower ration of *Fg* gDNA to barley gDNA—less than half of the level observed in mock-treated plants (Figure 1B). In barley (cv. Golden Promise), which is susceptible to the *Ph* strain used in the experiments, we measured micronecrotic reactions in response to *Ph* infection. This type of response is a hallmark of partial resistance to biotrophic *Puccinia* sp. first described by Niks [31]. It slows the rate of disease and restricts the field of epidemics [32]. In mock-treated plants, micronecrotic reactions were first detected at 3 days post-inoculation (dpi) in 7.8% of infection sites, increasing to 17.8% by 5 dpi. In CS_10-treated plants, this reaction occurred one day earlier, at 2 dpi, and reached

a ratio of 36.2% by 5 dpi (Figure 2). The results confirmed that CS_10 treatment triggered a systemic immune response in the leaves adjacent to those directly treated with CS_10, resulting in a faster and more widespread immune activation. The necroses induced in response to *Ph* infection in CS_10-treated plants resembled cell death patterns typically seen in prehaustorial non-host resistance or adult plant resistance against *Puccinia* sp. pathogens in barley and other *Triticeae* crops [33–35]. Both sets of experiments, i.e., with *Fg* and *Ph*, provided results that are consistent with those previously reported on CS_10-triggered immunity (CTI) against *Fg* in chickpea [36]. The authors observed coordinated metabolic and physiological changes after the application of CS_10, including the fortification of the extra-cellular matrix (ECM), elevated ROS, and ROS-dependent signaling. Li, et al. [37] reported a similar range of systemic acquired resistance (SAR)-like responses after CS_10 priming, followed by *Fusarium zanthoxyli* inoculation of prickly ash. It included the upregulation of twelve key genes related to SAR, increased levels of H_2O_2, elevated activities of peroxidase and catalase enzymes, and enhanced accumulation of lignin and flavonoids. In all plants, a significant reduction of the lesions from 46.8% to 75.1% was observed [38]. Elsharkawy, et al. [39] found the same set of physiological changes in wheat plants treated with CS_10 and inoculated with *Puccinia* urediniospores. This mode of response in which the CS_10-primed plant shows an oxidative burst and elevated activities of redox enzymes is the prerequisite of micronecroses and remains in line with the results presented in this manuscript.

We can conclude that CS_10 treatment activates a systemic-like immune response, which, in turn, delays pathogenesis and lowers the infection symptoms of *Fg* or, in another *Ph* pathosystem, initiates a faster and more widespread micronecrotic response.

Further analysis revealed elevated levels of salicylic acid (SA) in *Fg*-inoculated and CS_10-treated plants. SA accumulation occurred as early as 1-day post-inoculation with *Fg*, while CS_10 treatment induced a similar rise 3 days after treatment (Figure 3). The results confirmed that SA synthesis and accumulation were part of the plant response to both factors in the pathogen inoculation and the application of CS_10 with the former perceived by host cells as a fungal elicitor. *Fg* infection, as a stronger biotic stressor, activated SA accumulation on the first day of pathogenesis compared to the CS_10 treatment, which activated a very similar response two days later. The results are consistent with current knowledge on SA-dependent regulation in response to molecular elicitors of biotic stressors. In plant cells, SA can be synthesized through either the ICS- or PAL-dependent pathways, depending on the plant species. For example, the ICS-dependent SA synthesis was reported in Arabidopsis [40] and in barley [29], while PAL-dependent SA synthesis was found in rice [25,41]. In soybean, the cooperative PAL- and ICS-dependent SA synthesis was reported [27]. The authors highlighted the importance of PAL in the pathogen-induced synthesis of SA. Furthermore, they found that pathogen infection suppressed the expression of the ICS-encoding gene. In our system, only PAL-encoding genes were upregulated in CS_10-treated and *Fg*-inoculated plants. The levels of upregulation differed in the tested variants, indicating that all three paralogs shared their roles and participated in the SA biosynthesis pathway. Conversely, the ICS-encoding gene was repressed in all variants tested (Figure 9), mirroring similar findings in soybean inoculated with pathogens [27]. In tomatoes treated with CS_10, as reported by van Aubel, et al. [42], the genes regulated by SA-dependent pathways were activated and enhanced immunity against powdery mildew. The authors found a significant upregulation of pathogenesis-related (PR) proteins and SA-related genes.

The results gathered in our system showed that SA was involved in response to CS_10 treatment and *Fg* inoculation, and the PAL-dependent pathway is the predominant route for SA synthesis in response to CS_10 and *Fg*.

Although numerous studies have reported growth stimulation following CS_10 treatment, systemic investigations under controlled conditions are rare. In our study, we expected that CS_10-induced biomass gains would be relatively small and that the gains would be masked by biomass variation between individual plants. Considering this, we

adopted a semi-hydroponic system, which allowed us to track the biomass gains of individual plants and compared it with a mock-treated control. This approach confirmed that under controlled conditions, CS_10 treatment stimulated growth, and the relative biomass gain was 1.15 vs. 1.0 of the control. It should be noted that, despite a relatively small gain value, the significance of the results is high because of the large number of plants tested in five independent biological replications. Parallel experiments were performed to test whether SA treatment would affect plant growth. The results indicated that the SA application (50 μM) stimulated plant growth, and the relative gain in biomass was 1.10 vs. 1.00 of the control. The higher SA concentration (400 μM) had no effect. SA is a key regulator of immune reactions and plant growth, and the final outcome, i.e., growth stimulation or suppression, depends on SA concentrations and differs in different plant species. Shakirova, et al. [43] reported that 50 μM SA stimulated the growth of wheat seedlings by increasing the mitotic index in the root meristem and cell enlargement in the root extension zone. A similar effect was reported in Arabidopsis and *Matricaria chamomilla*. In Arabidopsis, Pasternak, et al. [44] showed that 50 μM SA treatment stimulated adventitious root formation and affected the apical meristem while concentrations greater than 50 μM inhibited the processes. The authors, in elucidating the mechanism, found that exogenous SA treatment led to changes in auxin synthesis and transport. In *Matricaria chamomilla*, 50 μM SA promoted growth, while 250 μM delayed it [45]. Generally, for a particular plant species, lower SA doses showed a stimulating effect, while larger doses restricted growth [46]. In our system, CS_10 treatment led to SA increase and simultaneously stimulated plant growth. We propose that plant growth stimulation observed after CS_10 treatment is dependent on SA.

The RNA sequencing of leaves treated with CS_10, inoculated with *Fg*, or treated with both revealed that *Fg* inoculation had the most significant impact on gene expression (Figure 7). Gene Ontology (GO) terms sorted by fold enrichment revealed that the top biological processes (BPs) were 'L-phenylalanine catabolic process', 'L-phenylalanine metabolic process', and 'Systemic acquired resistance (SAR)' (Figure 8). The first two categories are mutually related due to the PAL-dependent synthesis of SA, and this hormone is the main regulator of immune reactions, including SAR, which represents the third category. The most enriched categories of molecular functions (MFs) included 'Ammonia-lyase activity', 'Chitinase activity', and 'phenylalanine lyase activity' (Figure 8). They also represented functions directly related to PAL-dependent metabolic pathways, SA biosynthesis, and SA-regulated immune response. The cumulative analysis of the variants tested (Figure 9) indicated that the PAL-dependent pathway is the active pathway in our experimental system and each of the three PAL paralogs had its share in SA biosynthesis. Notably, *NPR1* (*NON-EXPRESSOR OF PR GENES1*), a key regulator of SA-mediated SAR, showed diverse expression patterns, confirming its active role in barley's immune response to both CS_10 and *Fg* inoculation (Figure 9).

The transduction of SA-dependent signaling is coordinated by *NPR1* and leads to the activation of genes encoding pathogenesis-related (PR) proteins. The transcriptomic results showed the upregulation of ten PR-encoding genes, the downregulation of one, and a mixed regulation pattern of two other genes (Figure 10). *PR3*, *PR8*, and *PR11* represent diverse classes of chitinases, which hydrolyze chitin, the structural component of the fungal cell wall, and restrict fungal pathogenesis [47]. In our system, *PR3* showed the strongest upregulation in all variants tested (Figure 10), and this may account for restricted symptoms of *Fg* pathogenesis. Along with *PR3* and *PR2*, the (1-3)-β-glucanase encoding gene showed very strong upregulation. Both proteins have antifungal activities that effectively restrict *Fusarium* pathogenesis in wheat, as reported by [48]. In another article, Simkovicova, et al. [49] tested the genetic resistance of tomato against *Fusarium* and found that the accumulation of *PR2* (1-3)-β-glucanase and glucan endo-1,3-β-D-glucosidases limited *Fusarium* colonization.

WRKY transcription factors (TFs) are key regulators in signaling pathways in plant defense [50]. They participate in SA biosynthesis and the SA signaling network that in-

cludes the activation of *NPR1/3* and *PR1* [51]. In our system, at least three genes, *WRKY6*, *WRKY33*, and *WRKY70*, were upregulated in tested variants (Figure 10), which was consistent with the elevated levels of SA and the upregulation of *PR*- and *NPR1*-encoding genes. The results are in line with the findings that the ectopic expression of *WRKY6* in wheat improved broad-spectrum resistance to *Puccinia triticina* and *Fusarium* crown rot [52], and the overexpression of *WRKY33* resulted in improved immunity against two necrotrophic fungal pathogens in an SA-dependent pattern [53]. The third protein, WRKY70, functioned as a coordinator of the SA and JA signaling pathways. Its expression, regulated by *NPR1*, improved plant resistance through the SA-induced pathogenesis-related (PR) proteins [37]. As discussed above, the results of the transcriptome analysis revealed a complex pattern of changes and coordinated regulation in selected groups of barley genes responding to CS_10 treatment and *Fg* inoculation.

4. Materials and Methods

Materials. CS samples are specified in Table 1. All CS samples were supplied by Pol-Aura (Warsaw, Poland).

Acetic acid (99.5–99.9%) and sodium hydroxide (NaOH) were from POCH (Warsaw, Poland). Potato Dextrose Broth (PDB) was supplied by ROTH (Karlsruhe, Germany). Hoagland medium (Hoagland Modified Basal Salt Mixture) was provided by PhytoTech LABS (Lenexa, KS, USA). Salicylic acid (SA) was provided by Sigma-Aldrich (Saint Louis, MO, USA). Salicylic acid-d4 (SA-d4) was from Toronto Research Chemicals Inc. (North York, ON, Canada). 3,3-diaminobenzidine tetrahydrochloride (DAB) supplied from Pol-Aura (Warsaw, Poland).

Barley cultivation. Barley seeds, *Hordeum vulgare* cv Golden Promise, were imbibed for 24 h (4 °C in the dark) on Petri plates with glass beads and tap water followed by germination (48 h, 21 °C, in the dark) and planted in pots with substrate soil (Aura-Hollas®, Paslek, Poland) for all inoculation experiments. For biomass measurements, plants were grown in a semi-hydroponic system. Briefly, germinated seeds were placed on sterilized filter paper (20 cm × 50 cm) soaked in Hoagland medium, covered with another filter paper, and, after rolling up, placed in the glass jars with a 2 cm layer of Hoagland medium [54]. Plants in soil or semi-hydroponics were grown at 21 °C, 70–95% relative humidity, and a 16 h photoperiod with an illumination intensity of 250–300 μmol m^{-2} s^{-1}.

The CS mock solution 4000 ppm was prepared by stirring 0.4 g of CS in 100 mL of 1% acetic acid (pH 3.0) overnight. The final solution, pH 5.6 (NaOH), was sterilized with a 0.22 μm pore diameter filter and stored at room temperature. The working CS 200 ppm solution was used for all plant treatments. The CS mock solution contained 0.05% acetic acid in water, pH 5.6 (NaOH). The second leaves of 14-day-old plants grown in soil were treated with CS solution or CS mock solution using a soft brush in experiments where CS-treated plants were used for further inoculation of third leaves with *Fg* and *Ph*. In experiments for biomass measurements, the upper part of the plants grown in semi-hydroponics were sprayed with either a CS solution (200 ppm) or CS mock solution.

Fg and *Ph* inoculation. *Fg* macroconidia were prepared as described [4]. Briefly, the V8-adapted liquid medium was inoculated with *Fg* mycelium, isolate BW5 (collection of Plant Breeding and Acclimatization Institute, Radzikow, Poland). After 2 weeks of culture (25 °C, continuous UV light (λmax = 365 nm), shaker 20 rpm), macroconidia were filtered through a sterile Miracloth. Suspension at a density of 10^6 conidia mL^{-1} was aliquoted and stored at −80 °C until further use. For plant inoculation, 1 mL of *Fg* macroconidia suspension in ddH_2O at a final density of 10^5 conidia·mL^{-1} was infiltrated into barley third leaf with a syringe. The plants were kept in the dark for 24 h and further cultivated before infiltration. The control plants were treated with ddH_2O. After inoculation, the plants were covered with a cellophane dome to ensure high humidity and kept in the dark for 24 h at 20 °C. After the cellophane dome was removed, the plants were treated with CS_10 200 ppm solution or mock solution (0.05% acetic acid). The inoculated plants were further cultured before additional inoculation. Inoculation with *Ph* urediniospores is based on the procedure outlined in [17]. Briefly, *Ph* urediniospores were suspended in

mineral oil (Novec™ 7100 fluid) at a density of 0.5^{-1} mg spores·mL^{-1}. The third leaves were inoculated by spraying suspended spores to obtain 40–150 spores cm^{-2} of the leaf surface. The inoculated plants were grown under 100% humidity for 24 h at 20 °C in the dark followed by cultivation under the same growth conditions as before inoculation.

To analyze barley immune response, the second barley leaves were sprayed with the mock or CS_10 solution, and the third leaves of the same plants were inoculated with macrospores of *Fg* or with *Ph* spores. The spatially separated CS_10 treatment (second leaf of the plant) and pathogen inoculation (the third leaf) allowed for the detection of plant immune response of the plant, not the direct antifungal effect of CS_10. The symptoms of pathogenesis were evaluated 5 days after inoculation with *Fg* and six days after inoculation with *Ph*.

DAB (3,3-diaminobenzidine tetrahydrochloride) staining. To evaluate the *Ph*–barley interaction, the third leaves, harvested 1, 2, 3, 4, 5, and 6 days post-inoculation (dpi) were stained with DAB. The leaf samples were placed in the DAB water solution (1 mg·mL^{-1}, pH 3.8 in the dark) for 4 h and destained overnight in the mixture of ethanol–chloroform (3:1 v/v) with 0.15% trichloroacetic acid (TCA). The brown precipitate formed by the reaction of DAB with H_2O_2 was examined under a light microscope.

Calcofluor white (CW) staining. The third leaves inoculated with *Ph* spores were harvested and placed overnight in the mixture of ethanol–chloroform (3:1) with 0.15% TCA. After this, the samples were washed twice with 50% ethanol, 15 min each, twice with 0.05 M NaOH, 15 min each, and three times with water. Then, the samples were stained with CW 35 μg·mL^{-1} in 0.1 M Tris-HCl (pH 9.0, in the dark), washed once with 0.1 M Tris-HCl (pH 8.5), once with water, and stored in 25% glycerol with 0.1% lactophenol. The samples, observed under a fluorescence microscope (Nikon Diaphot, Aizu, Japan, epifluorescence optics with excitation at 340–380 nm, barrier filter at 420 nm, and dichroic mirror at 400 nm), were scored for the number of infection sites, appressoria, haustoria mother cells (HMCs), and micronecrotic reactions. For each time point, three biological replicates containing one entire leaf were used, and the percentage was calculated by dividing the total infection sites per leaf by the number of different kinds of infection symptoms and multiplying by 100. For DAB staining, the oxidative burst on the infected leaf was observed under the fluorescence microscope.

Salicylic acid quantification. To determine SA in the analyzed leaf tissues, a modified extraction procedure described by Verberne, et al. [55] was used. The tissues, collected from the second and third leaves of 14-day-old soil grown plants were ground in liquid N2, weighed, transferred to a 2 mL Eppendorf tube, mixed with 1 mL of MetOH:H2O (9:1 v/v), and extracted using a Retsch MM400 mill (2 × 5 min, 50 Hz) (Retsch, Haan, Germany). The whole homogenate, transferred to a 15 mL Falcon tube, was supplemented with MetOH–H2O (9:1 v/v) to a final ratio of 100 μL per 100 mg of fresh weight and the SA internal standard, SA-d4 at a final concentration of 100 μg per 100 mg of fresh weight. After extraction, the homogenate was filtered with a nylon membrane (pore diameter 0.45 μm) into Eppendorf tubes. The 2 mL of the filtrate was vacuum-dried under the stream of nitrogen in a water bath (60 °C). The dried samples, resuspended in 300 μL of 8M hydrochloric acid, were heated in closed tubes in a heating block at 80 °C for 1 h. As a result of hydrolysis, bound forms of SA were released, and they were extracted from the solution with a 1.5 mL mixture of ethyl acetate–cyclohexane (1:1 v/v). The extraction was repeated two more times in a similar manner. After each extraction, the upper layer was collected and combined in a 5 mL reaction vial. The solvent was evaporated under a stream of nitrogen in a heating block. The dried samples were dissolved in 0.5 mL of a mixture of methanol–water (9:1 v/v), sonicated, and filtered through a nylon syringe filter with a pore size of 0.22 μm and an outer diameter of 13 mm. These prepared filtered samples were analyzed using the LC-HRMS technique.

An ACQUITY H-Class high-performance liquid chromatography coupled to an LCT Premier XE high-resolution mass spectrometer (Waters, Milford, MA, USA) was used to analyze SA in the samples. Analytes were separated on a UPLC C18 Cortecs chromatography

column (2.1 × 100 mm, 1.6 µm; Waters, Milford, MA, USA). The mobile phases consisted of methanol and water, i.e., 10:90 v/v (phase A) and 90:10 v/v (phase B). Both phases contained 0.1% formic acid and 5 mM ammonium formate. The flow rate was 0.3 mL/min. The following gradients were used: 100% phase A from 0 to 2 min; 50% phase A from 3 to 6 min; 10% phase A from 10 to 13 min; 100% phase A from 14 to 16 min. Five microliters of the sample were injected onto the column. The mass spectrometer was operated in negative polarization with electrospray ionization (ESI). The ion source and desolvation temperatures were 125 and 370 °C, respectively. The flow rate of the spray gas (nitrogen) was 650 L/min, and the flow rate of the drying gas was 20 L/min. The voltage on the capillary was 2200 V. Mode V of ion optics was used. The mass spectrometer was calibrated using a standard leucine-enkephalin solution. Test compounds (SA and SA-d4) in barley leaves were identified by comparing their molecular weights and retention times with standards of these substances. The following molecular ions (m/z) were used for quantitative analysis: SA–137.110 (M-H)-; SA-d4–141.113 (M-H)-.

To determine the reliability of the method, a validation experiment was performed to determine the recovery (R) and repeatability of the method (expressed as the mean standard deviation RSD). The limit of quantification (LOQ) and the limit of detection (LOD) were determined, as well as the linearity range. The recovery of the method was determined by adding the SA standard to the leaf tissue sample at three levels of addition, that is, 1, 2, and 3 mg/kg, and the addition of SA-d4 at the level described above. SA concentrations were determined using internal calibration. The calibration method was based on isotopic dilutions using SA-containing stable isotopes. The extraction procedure was used as described in the previous section. Recovery was determined from the difference in SA content in the fortified and blank samples used in the experiment. The average recovery was determined from at least three independent determinations. To determine the LOQ value, the SA concentration was assumed, at which the signal-to-noise ratio was at least 10 and, in the case of LOD, at least 3. Calibration solutions were prepared at seven different concentrations ranging from 0.025 to 1.6 mg/kg. SA-d4 was added to each solution in an amount corresponding to SA-d4 in the tested samples. The conducted validation experiment allowed us to determine the effectiveness of the analytical method. The recovery obtained for SA was 97% at the 1 mg/kg level: 93% for 2 mg/kg and 101% for 3 mg/kg. The repeatability of the method (RSD) was 7, 11, and 6%, respectively, while LOQ and LOD were 0.100 and 0.03 mg/kg. The value of the determination coefficient (R^2) for the determined calibration curve is at least 0.99.

RNA extraction and mRNA sequencing. Total RNA was extracted from 100 mg of barley leaves representing four tested variants, *Fv*_mock, *Hv*_CS, *Hv_Fg*_CS, and *Hv_Fg* (Figure 12), using an RNA isolation kit (Zymo-R2072, Irvine, CA, USA), RNA extraction buffer (Tris-HCl 50 mM pH = 8.0, LiCl 150 mM, EDTA 5 mM pH = 8.0, SDS 1%), Trizol reagent, phenol–chloroform (1:1 v/v) mixture, and 80% ethanol, according to the manufacturer's protocol. The isolated RNA was quantified using a NanoDrop spectrophotometer (NanoDrop Technologies®, Wilmington, DE, USA). The quality of RNA preparations was assessed on BioAnalyzer 2100 using 1% agarose gel (Agilent Technologies®, Santa Clara, CA, USA). Samples with a ration A260/A280 over 2.0, RIN number over 8, and concentration over 50 ng μL^{-1} were selected for downstream applications. Approximately 2 µg of high-quality RNA was sent to a biotech company (GENEWIZ®, Leipzig, Germany) to prepare the Illumina standard RNA library with polyA selection. The company performed Illumina NovaSeq sequencing with an estimated data output of ~20 M paired-end reads with a quality score of Q30. The company provided FASTQ format data that were used for further analysis.

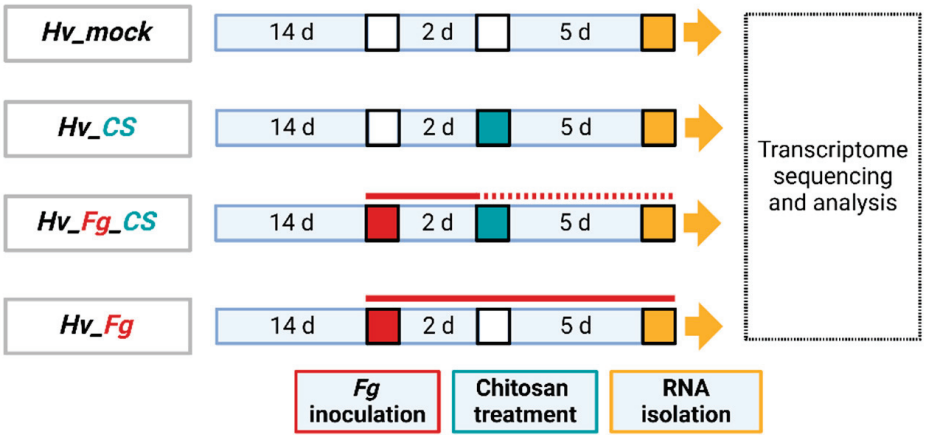

Figure 12. Schematic representation of experimental variants for transcriptome sequencing. Briefly, 14-day-old plants were inoculated with *F. graminearum* (*Fg*), followed by chitosan_10 (CS) treatment two days later and a collection of samples 5 days later. Description of tested variants: *Hv*_mock—barley treated with mock solution; *Hv*_CS—barley treated with chitosan 200 ppm; *Hv_Fg*_CS—barley inoculated with *Fg* and treated with chitosan 200 ppm; and *Hv_Fg*—barley inoculated with *Fg*.

The quality control and mapping sequence reads. FastQC toolkit version 0.12.0 (https://www.bioinformatics.babraham.ac.uk/projects/fastqc, accessed on 15 June 2024) was used to perform a quality check on the FastQ raw data, and default commands were used [56]. For alignment, the reference genome of Hordeum vulgare L. Golden Promise (Assembly: GCA_902500625.1, obtained from https://www.ebi.ac.uk/ena/browser/home, accessed on 15 June 2024) was used in Bowtie version 2.5.0 for the alignment of previously trimmed reads [57]. SAM tools were used to convert output alignment files into .bam files. Converted files were used for transcript reads analysis with the use of FeatureCounts and further analyzed with DESeq2 for differentially expressed genes. The cut-off values for DEG (differentially expressed genes) were false discovery rate (FDR) < 0.05 and log2-fold change > 2.

Analyzing RNA-Seq outputs. To determine variation between samples, principal component analysis (PCA) Bioconductor R PGSEA package (https://www.bioconductor.org/packages//2.10/bioc/html/PGSEA.html, accessed on 21 June 2024) with default settings was used. Hierarchical clustering heatmap and correlation matrix of biological replicates of each treatment were prepared using iDEP web application (http://bioinformatics.sdstate.edu/idep/, accessed on 21 June 2024). For functional enrichment analysis, the iDEP web application was used to interpret previously processed data with a false discovery rate (FDR) cutoff of <0.05 and a log2-fold change > 2.0. Gene Ontology (GO) terms were used to analyze pathways that underwent significant changes in their regulation based on biological processes (BPs), molecular functions (MFs), and cellular components (CCs) [58].

RT-qPCR of selected *H. vulgare* genes. Total RNA was extracted as stated in RNA extraction iboLock RNase inhibitor and 2 U of DNase1 (Roche Diagnostics®, Munich, Germany). Complete DNA degradation was confirmed by using 100 ng DNase-treated RNA as a template in a PCR reaction with *ARF* (*ADP-Ribosylation factor*, AJ508228) gene primers. Extracted RNA was used as the template for cDNA synthesis using the Revert Aid First Strand cDNA Synthesis Kit (ThermoFisher Scientific®, Waltham, MA, USA) along the manufacturers protocol (with use of oligo-dt primers). Obtained cDNA, 5-fold diluted, was used as a template for quantitative PCR. The qPCR reaction mix contained 2 µL of 5× HOT FIREPol EvaGreen qPCR Mix Plus (ROX) (Solis Biodyne®, Tartu, Estonia), 0.3 µL of primer F (10 µM), 0.3 µL of primer R (10 µM), 15 ng of template cDNA, and 10 µL of water. BioRad CFX384 Real-Time PCR System (BioRad, Hercules, CA, USA) was used for qPCR reaction The relative expression of selected barley genes was based on the $2^{-\Delta\Delta Ct}$ method, as previously described [59]. Values for the relative number of transcripts represent a

medium with a minimum of three biological replicates and three technical replicates. The geometric mean of two housekeeping genes AJ508228 [56] and AK362208.1 [57] was used as reference for RT-qPCR of selected barley genes. All the primers used for qPCR are listed in Table S1.

Fg genomic DNA quantification by qPCR. The inoculated third leaves of the CS_10- and mock-treated plants were harvested and ground in liquid N2. Genomic DNA (gDNA) was extracted from the leaves using the CTAB method. Briefly, 0.5 g of the N_2 ground sample was extracted with 800 µL of CTAB solution containing β-ME (2 µL mL^{-1} CTAB). The samples were incubated at 60 °C for 30–40 min, followed by extraction with 800 µL of chloroform–isoamyl alcohol (24:1 *v*/*v*) and centrifugation (10,000 rpm, 20 min) at room temperature. Subsequently, 600 µL of the supernatant was transferred into a new Eppendorf tube supplemented with 5 µL of RNase and incubated for 10–15 min at 37 °C. gDNA was precipitated by adding isopropanol (3/4 of the supernatant volume), freezing for 30 min, and centrifuging for 10,000 rpm, 10 min at room temperature. The precipitate was washed with 70% ethanol, and the pellet was dissolved in 200 µL of the TE buffer. The quality and quantity of DNA were checked using a Nanodrop, followed by 1% agarose gel electrophoresis. *Fusarium* DNA was quantified in total DNA isolated from infected leaves using qPCR, total DNA as a template and primers to barley *Hv_EFG1* (*translation elongation factor G1*, AY836205.1 [56]), and *Fg* gene *Fg_TRI5* (*trichodiene synthase5*, [60]). The qPCR reaction mix consisted of 2 µL of HOT FIREPol EvaGreen qPCR Mix Plus (ROX) (Solis Biodyne®, Tartu, Estonia), 50 ng of gDNA extracted from the respective sample, 0.3 µL of forward primer (10 µM), and 0.3 µL of reverse primer (10 µM) for each target gene. The quantification was based on three biological replicates and four technical replicates for each sample. The results were shown as the relative number of *Fg_TRI5* gene copies per *Hv_EFG1* gene copy. The primers used for qPCR are listed in Table S1.

Measurement of barley biomass. The leaves of semi-hydroponically grown barley seedlings were subjected to two separate applications of CS at a concentration of 200 ppm, the first one 3 days after imbibition and the second one 10 days after imbibition. The biomass was weighed twice for each plant after careful removal from the paper filter (Figure 13).

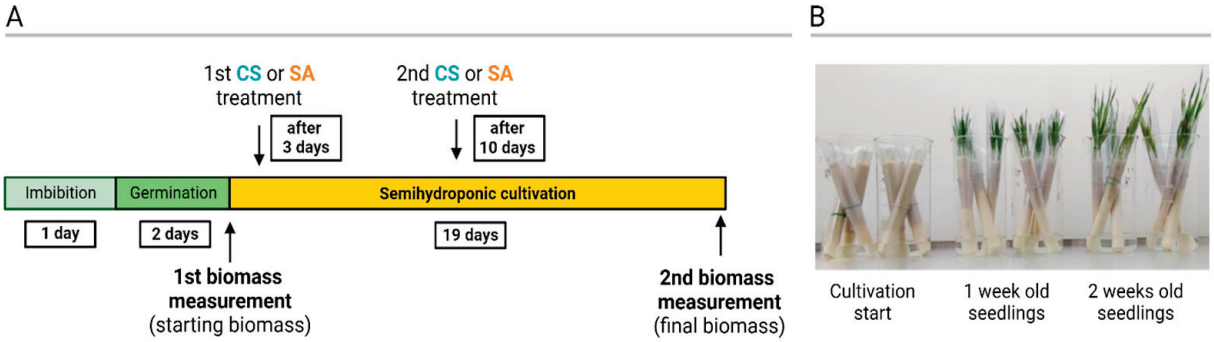

Figure 13. Schematic timeline of biomass measurements and chitosan (CS) or salicylic acid (SA) treatments (**A**). Representative picture of barley plants grown in semi-hydroponics (**B**).

The effects of CS and SA on plant growth were evaluated in two independent experiments. To account for biological variation among individual plants, biomass gain data were collected for individual plants from five independent experiments involving over 300 plants treated with CS and five experiments with over 300 plants treated with SA. Biomass measurements were recorded for 5-day-old (M5) and 24-day-old (M24) seedlings. These measurements were used to calculate the individual biomass gain (BG) for each seedling across the tested variants using Equation (1).

$$BG = M24 - M9 \quad (1)$$

To compare the biomass gains (BGs) of seedlings treated with CS and SA, the relative biomass gain (RBG) was calculated. For mock-treated plants, the RBG was set as 1.0. The RBG values for both treatments (CS and SA) were determined using Equation (2).

$$RBG = BG_{treatment}/BG_{mock} \quad (2)$$

The resulting data were then analyzed using one-way ANOVA, followed by Tukey's post hoc test for statistical comparisons.

Statistical analysis. All quantitative data are presented as the mean value and standard error. The data were processed by one-way analysis of variance (ANOVA) and post hoc least significant difference (LSD) or Tukey's test using Statistica 13 (StatSoft Polska, Kraków, Poland). Statistically significant results were marked with the following values: * $p < 0.05$, ** $p < 0.01$, and *** $p < 0.001$.

5. Conclusions

1. The batch of CS_10 with the strongest antifungal activity against *Fg* was also effective in activating plant immune responses and enhancing the growth of plant biomass.
2. The immune response induced by the application of CS_10 led to increased resistance against two pathogenic fungi, *Ph* and *Fg*, representing biotrophic and necrotrophic types of pathogenesis, respectively.
3. The two observed effects of CS_10 treatment in plants, i.e., enhanced immunity and biomass growth enhancement, were mediated by SA-dependent regulation, highlighting the dual role of CS in plant immunity and growth regulation. Barley transcriptome analysis confirmed that the activation of the immune response involved SA-regulated genes.

Supplementary Materials: The following supporting information can be downloaded at: https://www.mdpi.com/article/10.3390/ijms252413244/s1.

Author Contributions: Conceptualization, W.O.; methodology, W.O., P.P. and M.B.; validation, W.O., P.P. and M.B.; formal analysis, P.P., A.S. and M.B.; investigation, P.P., A.S. and M.B.; data curation, P.P., A.S. and M.B.; resources, P.P. and M.B.; writing—original draft preparation, W.O., P.P., A.S. and M.B.; writing—review and editing, W.O.; visualization, P.P.; supervision, W.O.; project administration W.O.; funding acquisition, W.O. All authors have read and agreed to the published version of the manuscript.

Funding: This research was funded by the National Science Centre, Poland, Grant no 2019/35/B/NZ9/00323 (W.O.).

Institutional Review Board Statement: Not applicable.

Informed Consent Statement: Not applicable.

Data Availability Statement: All data and materials are included in the article and the supplemental files. Raw data sets supporting the results of this article are available in the NCBI Sequence Read Archive repository: Accession: PRJNA1170567 ID: 1170567 'Effect of Chitosan on the Transcriptome of the *Fusarium graminearum* and *Hordeum vulgare* L. Pathosystem'.

Acknowledgments: Isolate BW5 of *Fg* was kindly provided by Barbara Wiewióra (Plant Breeding and Acclimatization Institute, Radzikow, Poland).

Conflicts of Interest: The authors declare no conflicts of interest.

References

1. Iber, B.T.; Kasan, N.A.; Torsabo, D.; Omuwa, J.W. A review of various sources of chitin and chitosan in nature. *J. Renew. Mater.* **2022**, *10*, 1097. [CrossRef]
2. Poznanski, P.; Hameed, A.; Orczyk, W. Chitosan and chitosan nanoparticles: Parameters enhancing antifungal activity. *Molecules* **2023**, *28*, 2996. [CrossRef] [PubMed]
3. El-Gazzar, N.; El-Hai, K.M.A.; Teama, S.A.M.; Rabie, G.H. Enhancing *Vicia faba*'s immunity against *Rhizoctonia solani* root rot diseases by arbuscular mycorrhizal fungi and nano chitosan. *BMC Plant Biol.* **2023**, *23*, 403. [CrossRef]

4. Poznanski, P.; Hameed, A.; Dmochowska-Boguta, M.; Bryla, M.; Orczyk, W. Low Molecular Weight and High Deacetylation Degree Chitosan Batch Alleviates Pathogenesis, Toxin Accumulation, and Fusarium Gene Regulation in Barley Leaf Pathosystem. *Int. J. Mol. Sci.* **2023**, *24*, 12894. [CrossRef]
5. Yu, H.; Su, L.; Jia, W.; Jia, M.; Pan, H.; Zhang, X. Molecular Mechanism Underlying Pathogenicity Inhibition by Chitosan in Cochliobolus heterostrophus. *J. Agric. Food Chem.* **2024**, *72*, 3926–3936. [CrossRef]
6. Chakraborty, M.; Hasanuzzaman, M.; Rahman, M.; Khan, M.A.R.; Bhowmik, P.; Mahmud, N.U.; Tanveer, M.; Islam, T. Mechanism of plant growth promotion and disease suppression by chitosan biopolymer. *Agriculture* **2020**, *10*, 624. [CrossRef]
7. El Hadrami, A.; Adam, L.R.; El Hadrami, I.; Daayf, F. Chitosan in plant protection. *Mar. Drugs* **2010**, *8*, 968–987. [CrossRef]
8. Kheiri, A.; Jorf, S.M.; Malihipour, A.; Saremi, H.; Nikkhah, M. Application of chitosan and chitosan nanoparticles for the control of Fusarium head blight of wheat (Fusarium graminearum) in vitro and greenhouse. *Int. J. Biol. Macromol.* **2016**, *93*, 1261–1272. [CrossRef]
9. Long, L.T.; Tan, L.V.; Boi, V.N.; Trung, T.S. Antifungal activity of water-soluble chitosan against Colletotrichum capsici in postharvest chili pepper. *J. Food Process. Preserv.* **2018**, *42*, e13339. [CrossRef]
10. Priyadarshi, R.; Rhim, J.-W. Chitosan-based biodegradable functional films for food packaging applications. *Innov. Food Sci. Emerg. Technol.* **2020**, *62*, 102346. [CrossRef]
11. Moonjely, S.; Ebert, M.; Paton-Glassbrook, D.; Noel, Z.A.; Roze, L.; Shay, R.; Watkins, T.; Trail, F. Update on the state of research to manage Fusarium head blight. *Fungal Genet. Biol.* **2023**, *169*, 103829. [CrossRef] [PubMed]
12. Fernando, W.D.; Oghenekaro, A.O.; Tucker, J.R.; Badea, A. Building on a foundation: Advances in epidemiology, resistance breeding, and forecasting research for reducing the impact of fusarium head blight in wheat and barley. *Can. J. Plant Pathol.* **2021**, *43*, 495–526. [CrossRef]
13. Hameed, A.; Poznanski, P.; Noman, M.; Ahmed, T.; Iqbal, A.; Nadolska-Orczyk, A.; Orczyk, W. Barley resistance to Fusarium graminearum infections: From transcriptomics to field with food safety concerns. *J. Agric. Food Chem.* **2022**, *70*, 14571–14587. [CrossRef]
14. Zanni, R.; Martinez-Cruz, J.; Galvez-Llompart, M.; Fernandez-Ortuno, D.; Romero, D.; Garcia-Domenech, R.; Perez-Garcia, A.; Galvez, J. Rational Design of Chitin Deacetylase Inhibitors for Sustainable Agricultural Use Based on Molecular Topology. *J. Agric. Food Chem.* **2022**, *70*, 13118–13131. [CrossRef] [PubMed]
15. Dmochowska-Boguta, M.; Kloc, Y.; Orczyk, W. Polyamine oxidation is indispensable for wheat (*Triticum aestivum* L.) oxidative response and necrotic reactions during leaf rust (*Puccinia triticina* Eriks.) infection. *Plants* **2021**, *10*, 2787. [CrossRef] [PubMed]
16. Dmochowska-Boguta, M.; Nadolska-Orczyk, A.; Orczyk, W. Roles of peroxidases and NADPH oxidases in the oxidative response of wheat (*Triticum aestivum*) to brown rust (*Puccinia triticina*) infection. *Plant Pathol.* **2013**, *62*, 993–1002. [CrossRef]
17. Orczyk, W.; Dmochowska-Boguta, M.; Czembor, H.; Nadolska-Orczyk, A. Spatiotemporal patterns of oxidative burst and micronecrosis in resistance of wheat to brown rust infection. *Plant Pathol.* **2010**, *59*, 567–575. [CrossRef]
18. Jones, J.D.; Dangl, J.L. The plant immune system. *Nature* **2006**, *444*, 323–329. [CrossRef]
19. Ding, Y.; Sun, T.; Ao, K.; Peng, Y.; Zhang, Y.; Li, X.; Zhang, Y. Opposite roles of salicylic acid receptors NPR1 and NPR3/NPR4 in transcriptional regulation of plant immunity. *Cell* **2018**, *173*, 1454–1467.e15. [CrossRef]
20. Zhang, Y.; Li, X. Salicylic acid: Biosynthesis, perception, and contributions to plant immunity. *Curr. Opin. Plant Biol.* **2019**, *50*, 29–36. [CrossRef]
21. Farooq, T.; Akram, M.N.; Hameed, A.; Ahmed, T.; Hameed, A. Nanopriming-mediated memory imprints reduce salt toxicity in wheat seedlings by modulating physiobiochemical attributes. *BMC Plant Biol.* **2022**, *22*, 540. [CrossRef] [PubMed]
22. Li, A.; Sun, X.; Liu, L. Action of salicylic acid on plant growth. *Front. Plant Sci.* **2022**, *13*, 878076. [CrossRef]
23. Abdelaal, K.A.; Attia, K.A.; Alamery, S.F.; El-Afry, M.M.; Ghazy, A.I.; Tantawy, D.S.; Al-Doss, A.A.; El-Shawy, E.-S.E.; M. Abu-Elsaoud, A.; Hafez, Y.M. Exogenous application of proline and salicylic acid can mitigate the injurious impacts of drought stress on barley plants associated with physiological and histological characters. *Sustainability* **2020**, *12*, 1736. [CrossRef]
24. Lefevere, H.; Bauters, L.; Gheysen, G. Salicylic acid biosynthesis in plants. *Front. Plant Sci.* **2020**, *11*, 338. [CrossRef]
25. Duan, L.; Liu, H.; Li, X.; Xiao, J.; Wang, S. Multiple phytohormones and phytoalexins are involved in disease resistance to Magnaporthe oryzae invaded from roots in rice. *Physiol. Plant.* **2014**, *152*, 486–500. [CrossRef]
26. Abreu, M.E.; Munne-Bosch, S. Salicylic acid deficiency in *NahG* transgenic lines and *s* mutants increases seed yield in the annual plant *Arabidopsis thaliana*. *J. Exp. Bot.* **2009**, *60*, 1261–1271. [CrossRef] [PubMed]
27. Shine, M.B.; Yang, J.W.; El-Habbak, M.; Nagyabhyru, P.; Fu, D.Q.; Navarre, D.; Ghabrial, S.; Kachroo, P.; Kachroo, A. Cooperative functioning between phenylalanine ammonia lyase and isochorismate synthase activities contributes to salicylic acid biosynthesis in soybean. *New Phytol.* **2016**, *212*, 627–636. [CrossRef] [PubMed]
28. Hückelhoven, R.; Fodor, J.; Preis, C.; Kogel, K.-H. Hypersensitive cell death and papilla formation in barley attacked by the powdery mildew fungus are associated with hydrogen peroxide but not with salicylic acid accumulation. *Plant Physiol.* **1999**, *119*, 1251–1260. [CrossRef]
29. Hao, Q.; Wang, W.; Han, X.; Wu, J.; Lyu, B.; Chen, F.; Caplan, A.; Li, C.; Wu, J.; Wang, W. Isochorismate-based salicylic acid biosynthesis confers basal resistance to Fusarium graminearum in barley. *Mol. Plant Pathol.* **2018**, *19*, 1995–2010. [CrossRef]
30. Qin, Y.; Torp, A.M.; Glauser, G.; Pedersen, C.; Rasmussen, S.K.; Thordal-Christensen, H. Barley isochorismate synthase mutant is phylloquinone-deficient, but has normal basal salicylic acid level. *Plant Signal. Behav.* **2019**, *14*, 1671122. [CrossRef]

31. Niks, R. Comparative histology of partial resistance and the nonhost reaction to leaf rust pathogens in barley and wheat seedlings. *Phytopathol. Res.* **1983**, *73*, 60–64. [CrossRef]
32. Rubiales, D.; Nicks, R.E. Combination of mechanisms of resistance to rust fungi as a strategy to increase durability. *CIHEAM Options Mediterr.* **1997**, *40*, 333–339.
33. Neu, C.; Keller, B.; Feuillet, C. Cytological and Molecular Analysis of the Hordeum vulgare–Puccinia triticina Nonhost Interaction. *Mol. Plant-Microbe Interact.* **2003**, *16*, 626–633. [CrossRef]
34. Dmochowska-Boguta, M.; Kloc, Y.; Zielezinski, A.; Werecki, P.; Nadolska-Orczyk, A.; Karlowski, W.M.; Orczyk, W. *TaWAK6* encoding wall-associated kinase is involved in wheat resistance to leaf rust similar to adult plant resistance. *PLoS ONE* **2020**, *15*, e0227713. [CrossRef]
35. Zhang, H.C.; Wang, C.F.; Cheng, Y.L.; Chen, X.M.; Han, Q.M.; Huang, L.L.; Wei, G.R.; Kang, Z.S. Histological and cytological characterization of adult plant resistance to wheat stripe rust. *Plant Cell Rep.* **2012**, *31*, 2121–2137. [CrossRef] [PubMed]
36. Narula, K.; Elagamey, E.; Abdellatef, M.A.E.; Sinha, A.; Ghosh, S.; Chakraborty, N.; Chakraborty, S. Chitosan-triggered immunity to Fusarium in chickpea is associated with changes in the plant extracellular matrix architecture, stomatal closure and remodeling of the plant metabolome and proteome. *Plant J.* **2020**, *103*, 561–583. [CrossRef]
37. Li, J.; Brader, G.; Palva, E.T. The WRKY70 transcription factor: A node of convergence for jasmonate-mediated and salicylate-mediated signals in plant defense. *Plant Cell* **2004**, *16*, 319–331. [CrossRef]
38. Li, P.; Liang, C.; Jiao, J.; Ruan, Z.; Sun, M.; Fu, X.; Zhao, J.; Wang, T.; Zhong, S. Exogenous priming of chitosan induces resistance in Chinese prickly ash against stem canker caused by *Fusarium zanthoxyli*. *Int. J. Biol. Macromol.* **2024**, *259*, 129119. [CrossRef]
39. Elsharkawy, M.M.; Omara, R.I.; Mostafa, Y.S.; Alamri, S.A.; Hashem, M.; Alrumman, S.A.; Ahmad, A.A. Mechanism of Wheat Leaf Rust Control Using Chitosan Nanoparticles and Salicylic Acid. *J. Fungi* **2022**, *8*, 304. [CrossRef]
40. Garcion, C.; Lohmann, A.; Lamodiere, E.; Catinot, J.; Buchala, A.; Doermann, P.; Metraux, J.P. Characterization and biological function of the ISOCHORISMATE SYNTHASE2 gene of Arabidopsis. *Plant Physiol.* **2008**, *147*, 1279–1287. [CrossRef]
41. Tonnessen, B.W.; Manosalva, P.; Lang, J.M.; Baraoidan, M.; Bordeos, A.; Mauleon, R.; Oard, J.; Hulbert, S.; Leung, H.; Leach, J.E. Rice phenylalanine ammonia-lyase gene OsPAL4 is associated with broad spectrum disease resistance. *Plant Mol. Biol.* **2015**, *87*, 273–286. [CrossRef] [PubMed]
42. van Aubel, G.; Cambier, P.; Dieu, M.; Van Cutsem, P. Plant immunity induced by COS-OGA elicitor is a cumulative process that involves salicylic acid. *Plant Sci.* **2016**, *247*, 60–70. [CrossRef] [PubMed]
43. Shakirova, F.M.; Sakhabutdinova, A.R.; Bezrukova, M.V.; Fatkhutdinova, R.A.; Fatkhutdinova, D.R. Changes in the hormonal status of wheat seedlings induced by salicylic acid and salinity. *Plant Sci.* **2003**, *164*, 317–322. [CrossRef]
44. Pasternak, T.; Groot, E.P.; Kazantsev, F.V.; Teale, W.; Omelyanchuk, N.; Kovrizhnykh, V.; Palme, K.; Mironova, V.V. Salicylic Acid Affects Root Meristem Patterning via Auxin Distribution in a Concentration-Dependent Manner. *Plant Physiol.* **2019**, *180*, 1725–1739. [CrossRef]
45. Kovacik, J.; Gruz, J.; Backor, M.; Strnad, M.; Repcak, M. Salicylic acid-induced changes to growth and phenolic metabolism in *Matricaria chamomilla* plants. *Plant Cell Rep.* **2009**, *28*, 135–143. [CrossRef]
46. Li, K.; Xing, R.; Liu, S.; Li, P. Chitin and Chitosan Fragments Responsible for Plant Elicitor and Growth Stimulator. *J. Agric. Food Chem.* **2020**, *68*, 12203–12211. [CrossRef]
47. Vaghela, B.; Vashi, R.; Rajput, K.; Joshi, R. Plant chitinases and their role in plant defense: A comprehensive review. *Enzym. Microb. Technol.* **2022**, *159*, 110055. [CrossRef]
48. Mohammadizadeh-Heydari, N.; Tohidfar, M.; Maleki Zanjani, B.; Mohsenpour, M.; Ghanbari Moheb Seraj, R.; Esmaeilzadeh-Salestani, K. Co-overexpression of chitinase and beta-1,3-glucanase significantly enhanced the resistance of Iranian wheat cultivars to Fusarium. *BMC Biotechnol.* **2024**, *24*, 35. [CrossRef]
49. Simkovicova, M.; Kramer, G.; Rep, M.; Takken, F.L.W. Tomato R-gene-mediated resistance against Fusarium wilt originates in roots and extends to shoots via xylem to limit pathogen colonization. *Front. Plant Sci.* **2024**, *15*, 1384431. [CrossRef]
50. Javed, T.; Gao, S.J. WRKY transcription factors in plant defense. *Trends Genet.* **2023**, *39*, 787–801. [CrossRef]
51. Sharma, A.; Kohli, S.K.; Khanna, K.; Ramakrishnan, M.; Kumar, V.; Bhardwaj, R.; Brestic, M.; Skalicky, M.; Landi, M.; Zheng, B. Salicylic Acid: A Phenolic Molecule with Multiple Roles in Salt-Stressed Plants. *J. Plant Growth Regul.* **2023**, *42*, 4581–4605. [CrossRef]
52. Li, M.; Zhao, S.; Yang, J.; Ren, Y.; Su, J.; Zhao, J.; Ren, X.; Wang, C.; Chen, S.; Yu, X.; et al. Exogenous expression of barley *HvWRKY6* in wheat improves broad-spectrum resistance to leaf rust, Fusarium crown rot, and sharp eyespot. *Int. J. Biol. Macromol.* **2022**, *218*, 1002–1012. [CrossRef] [PubMed]
53. Zheng, Z.; Qamar, S.A.; Chen, Z.; Mengiste, T. Arabidopsis WRKY33 transcription factor is required for resistance to necrotrophic fungal pathogens. *Plant J.* **2006**, *48*, 592–605. [CrossRef] [PubMed]
54. Hoagland, D.R.; Arnon, D.I. The water-culture method for growing plants without soil. *Circ. Calif. Agric.* **1938**, *347*, 1–32.
55. Verberne, M.C.; Brouwer, N.; Delbianco, F.; Linthorst, H.J.; Bol, J.F.; Verpoorte, R. Method for the extraction of the volatile compound salicylic acid from tobacco leaf material. *Phytochem. Anal.* **2002**, *13*, 45–50. [CrossRef]
56. Kloc, Y.; Dmochowska-Boguta, M.; Zielezinski, A.; Nadolska-Orczyk, A.; Karlowski, W.M.; Orczyk, W. Silencing of *HvGSK1.1* A GSK3/SHAGGY-Like Kinase Enhances Barley (*Hordeum vulgare* L.) Growth in Normal and in Salt Stress Conditions. *Int. J. Mol. Sci.* **2020**, *21*, 6616. [CrossRef]

57. Gao, J.; Bi, W.; Li, H.; Wu, J.; Yu, X.; Liu, D.; Wang, X. WRKY Transcription Factors Associated With NPR1-Mediated Acquired Resistance in Barley Are Potential Resources to Improve Wheat Resistance to *Puccinia triticina*. *Front. Plant Sci.* **2018**, *9*, 1486. [CrossRef]
58. Ge, S.X.; Son, E.W.; Yao, R. iDEP: An integrated web application for differential expression and pathway analysis of RNA-Seq data. *BMC Bioinform.* **2018**, *19*, 534. [CrossRef]
59. Song, X.-S.; Li, H.-P.; Zhang, J.-B.; Song, B.; Huang, T.; Du, X.-M.; Gong, A.-D.; Liu, Y.-K.; Feng, Y.-N.; Agboola, R.S. Trehalose 6-phosphate phosphatase is required for development, virulence and mycotoxin biosynthesis apart from trehalose biosynthesis in *Fusarium graminearum*. *Fungal Genet. Biol.* **2014**, *63*, 24–41. [CrossRef]
60. Brunner, K.; Kovalsky, P.M.P.; Paolino, G.; Bürstmayr, H.; Lemmens, M.; Berthiller, F.; Schuhmacher, R.; Krska, R.; Mach, R.L. A reference-gene-based quantitative PCR method as a tool to determine Fusarium resistance in wheat. *Anal. Bioanal. Chem.* **2009**, *395*, 1385–1394. [CrossRef]

International Journal of
Molecular Sciences

MDPI

Article

Chitosan-Electrospun Fibers Encapsulating Norfloxacin: The Impact on the Biochemical, Oxidative and Immunological Profile in a Rats Burn Model

Corneliu-George Coman [1,2], Alexandru Anisiei [3], Sandu Cibotaru [3], Daniela Ailincai [3], Sorin Aurelian Pasca [4], Caroline Chabot [5], Ioannis Gardikiotis [1,6,*] and Liliana Mititelu-Tartau [1]

[1] Pharmacology, Clinical Pharmacology and Algesiology Department, Faculty of Medicine, University of Medicine and Pharmacy "Grigore T. Popa" of Iasi, 700115 Iasi, Romania; dr.cgcoman@gmail.com (C.-G.C.); lylytartau@yahoo.com (L.M.-T.)
[2] Faculté de Médecine, Pharmacie et Sciences Biomédicales, Université de Mons, 7000 Mons, Belgium
[3] "Polycondensation and Thermostable Polymers" Department, "Petru Poni" Institute of Macromolecular Chemistry of Romanian Academy, 700487 Iasi, Romania
[4] Pathology Department, University of Agricultural Sciences and Veterinary Medicine 'Ion Ionescu de la Brad', 700490 Iasi, Romania
[5] Department de Radiologie, Cliniques Universitaires Saint-Luc, Université Catholique de Louvain, 1200 Bruxelles, Belgium
[6] Surgery Department, Advanced Research and Development Center for Experimental Medicine "Prof. Ostin C. Mungiu", University of Medicine and Pharmacy "Grigore T. Popa" of Iasi, 700115 Iasi, Romania
* Correspondence: dr.gardikiotis@yahoo.com

Abstract: This study investigates the impact of chitosan-based nanofibers on burn wound healing in a rat model. Two formulations of chitosan nanofibers were prepared through electrospinning. The formulations were then incorporated with different amounts of norfloxacin and underwent surface modifications with 2-formylphenylboronic acid. The burn model was applied to *Wistar* male rats by the contact method, using a heated steel rod attached to a thermocouple. The effectiveness of the nanofibers was tested against a negative control group and a standard commercial dressing (Atrauman Ag) on the described model and evaluated by wound diameter, histological analysis and biochemical profiling of systemic inflammatory markers. The results showed that chitosan-based dressings significantly accelerated burn healing compared to the control treatments. The high-concentration norfloxacin-infused chitosan coated with 2-formylphenylboronic acid' groups exhibited significant improvements in wound closure and reduced inflammation compared to the other groups; antioxidant enzymes SOD and GPx expression was significantly higher, $p < 0.05$, whereas pro-oxidative markers such as cortisol were lower ($p < 0.05$). Macroscopically, the wound area itself was significantly diminished in the chitosan-treated groups ($p < 0.05$). Furthermore, a histological evaluation indicated enhanced epithelialization and granulation tissue formation within the experiment time frame, while the biochemical panel revealed lower levels of inflammatory cytokines and lower leukocyte counts in the treated groups. These findings highlight the potential of the studied chitosan nanofibers as novel nanosystems for next-generation wound therapies, as well as the clinical utility of the novel chitosan fibers obtained by electrospinning technique.

Keywords: chitosan; electrospinning; nanofibers; burn model; norfloxacin; inflammation; wistar rats

1. Introduction

Chitosan is a biopolymer of natural origin which has long proved its excellent capacity for wound healing [1–5]. This is due to its intrinsic properties, such as its hemostatic effect, antimicrobial activity preventing wound infection, and its ability to promote the growth of granulation tissue, thereby accelerating skin regeneration, along with its biocompatibility, low toxicity, biodegradability and mucoadhesion. The chemical structure of chitosan is rich in

amine and hydroxyl functional units that allow groups functionalized with other components to enhance certain biological functions. Furthermore, chitosan can be processed into a large realm of biomaterials suitable for application on wounds, such as thin films, membranes, sponges, hydrogels, foams, nanobeads or nanofibers [6]. Vast research on chitosan-based dressings has shown promising results but also disadvantages, leaving room for future development for clinical applications [1,4,5,7–21]. Recent review papers have brought to researchers' attention the necessity of an in-depth investigation of the effect of chitosan on the wound healing process, an aspect which has rarely been addressed in the past [22].

Among chitosan biomaterials, nanofibers appear as a very promising choice due to their easy manipulation, great conformability, semi-permeability for liquid/gas exchange, excellent swelling ability favoring exudate drainage, and good similarity with the extracellular matrix of skin, which facilitates the stimulation of tissue growth [17,18,23]. A plethora of studies dedicated to the investigation of different chitosan-based nanofibers has confirmed the value of chitosan nanofibers, with some reaching the performance required for marketable products for the control of hemorrhages [24–26]. The main barrier which needs to be overcome is the processing of neat chitosan nanofibers, a problematic task due to the difficulty of chitosan electrospinning, which necessitates the use of co-spinning agents, i.e., usually synthetic polymers such as poly (ethylene glycol) and poly (vinyl alcohol) of high molecular weight [4]. In using electrospinning with chitosan to yield defect-free nanofibers, the use of high molecular weight synthetic polymers raises suspicions regarding biodegradability, a negative impact on cells and, ultimately, on tissue regeneration [27,28]. Recent studies have evidenced that by using synthetic polymers as sacrificial matrices, it is possible to obtain neat chitosan nanofibers with excellent mechanical properties, making them more suitable for wound healing [17,18,29–31].

The scope of the present study was to investigate the impact of neat chitosan nanofibers and their composites with different fillers on a series of parameters which are indicators for wound healing processes. To this end, a series of chitosan-based nanofibers were used as wound dressings in burn wound models on rats and their impact on relevant parameters for wound healing was statistically analyzed.

2. Results

2.1. Fiber Characterization

Neat chitosan nanofibers were prepared by electrospinning chitosan/PEO blend fibers, followed by the selective removal of PEO in water. Then, norfloxacin, known for its broad-spectrum antibiotic properties, was loaded into fibers by immersing in ethanol or water to in order to obtain two different degrees of loading, i.e., 4.35% ('high concentration norfloxacin') and 0.94% ('low concentration norfloxacin') (Figure 1). Further, the neat chitosan fibers and NFX loaded ones were reacted at the surface with a bioactive aldehyde B via dynamic imine units to reach an imination degree of 10% which proved a good balance between antimicrobial activity and biocompatibility [17,29].

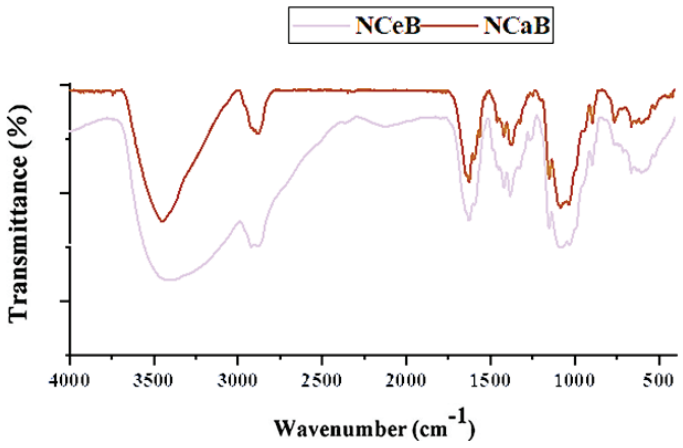

Figure 1. FTIR spectra of the studied fibers.

2.2. Structural Analysis

The FTIR spectra revealed the presence of norfloxacin and the successful imination of the fibers. Furthermore, POM images of the fibers displayed strong birefringence with iridescent colors, characteristic of norfloxacin (Figure 2).

When NFX is dissolved in ethanol, it undergoes crystallization to form unique and strongly birefringent spherulites, which are characterized by their distinct optical properties. These spherulites exhibit a specific appearance under polarized light, making them easily identifiable. However, in the case of the examined fibers, no such spherulite structures were found on their surfaces. This observation indicates that the drug was not crystallizing on the fibers but was instead likely being encapsulated within the interior of the fiber matrix. This encapsulation process suggests a more intimate interaction between the NFX and the fibers, implying that the fibers served as a carrier for the drug, potentially influencing its release and overall bioavailability. Its ultrastructure can be observed in Figure 3.

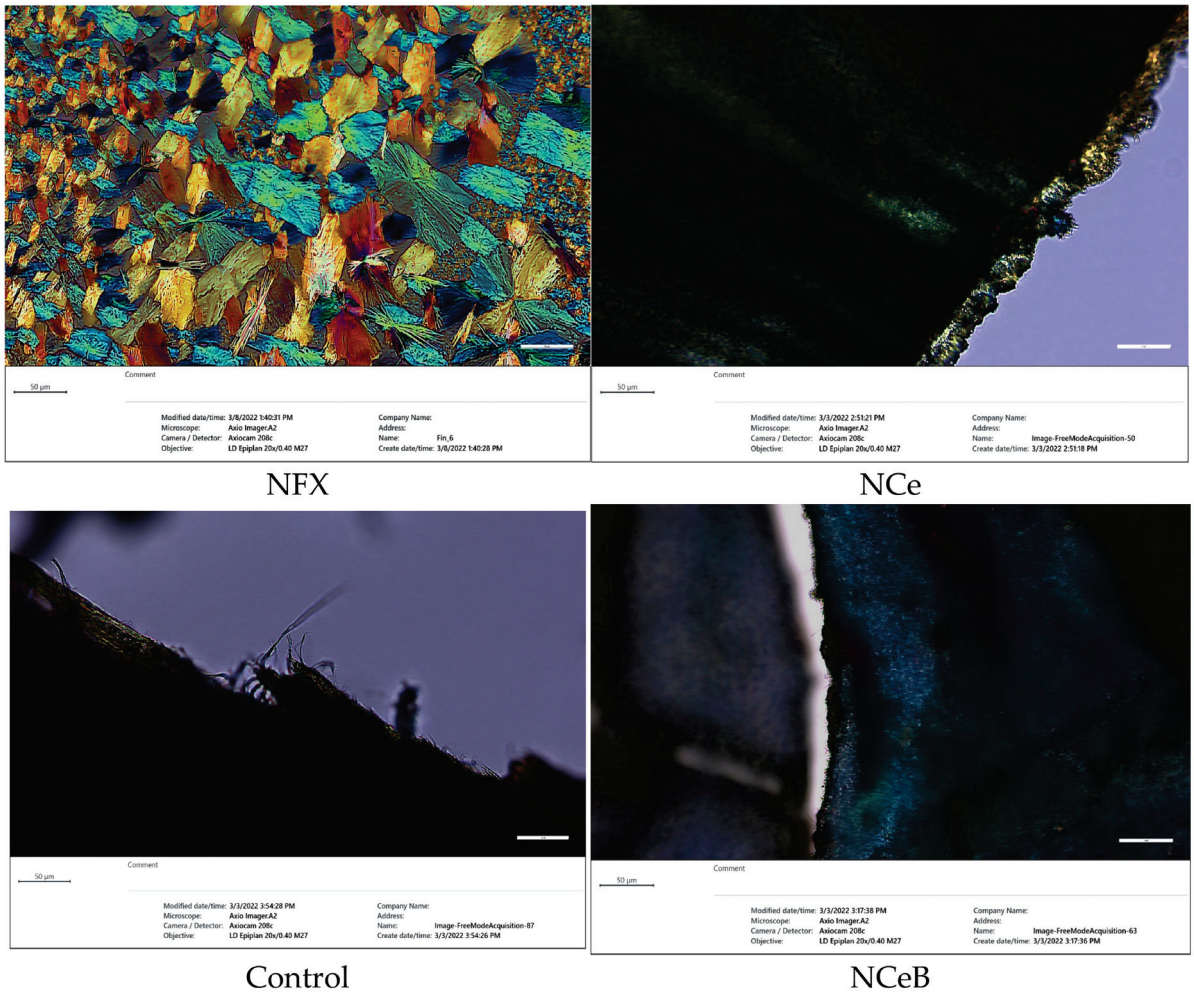

Figure 2. Microphotographs of fibers under polarized light compared with norfloxacin.

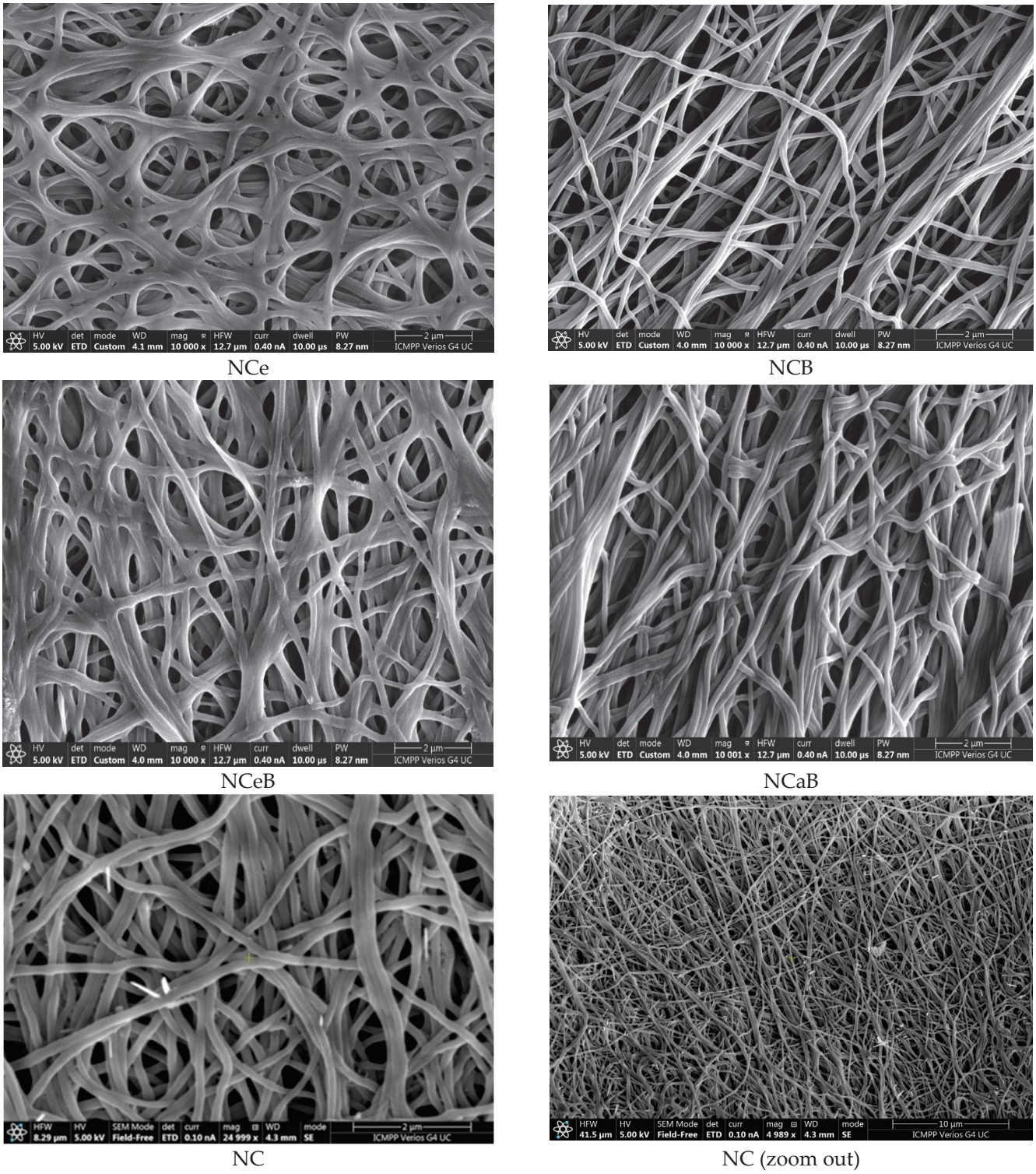

Figure 3. SEM images of the studied fibers.

2.3. Burn Wound Lesion Healing

Immediately after causing the burns, the wounds appeared round (due to the shape of the steel bar used), slightly deepened and of uniform white color, with an area of moderate erythema and oedema. No blistering was observed, and the boundary between the wound and normal skin was clear. One day after inflicting the burn, in the control group, the occurrence of oedema, marginal erythema and a thin crust in the surrounding area was obvious (Figure 4). This crust became thicker and darker afterwards and developed into an

eschar by the 7th day. A substantial increase (* $p < 0.05$) in the area of the burn zone was observed on day 3, followed by contraction of the wound in a time-dependent manner.

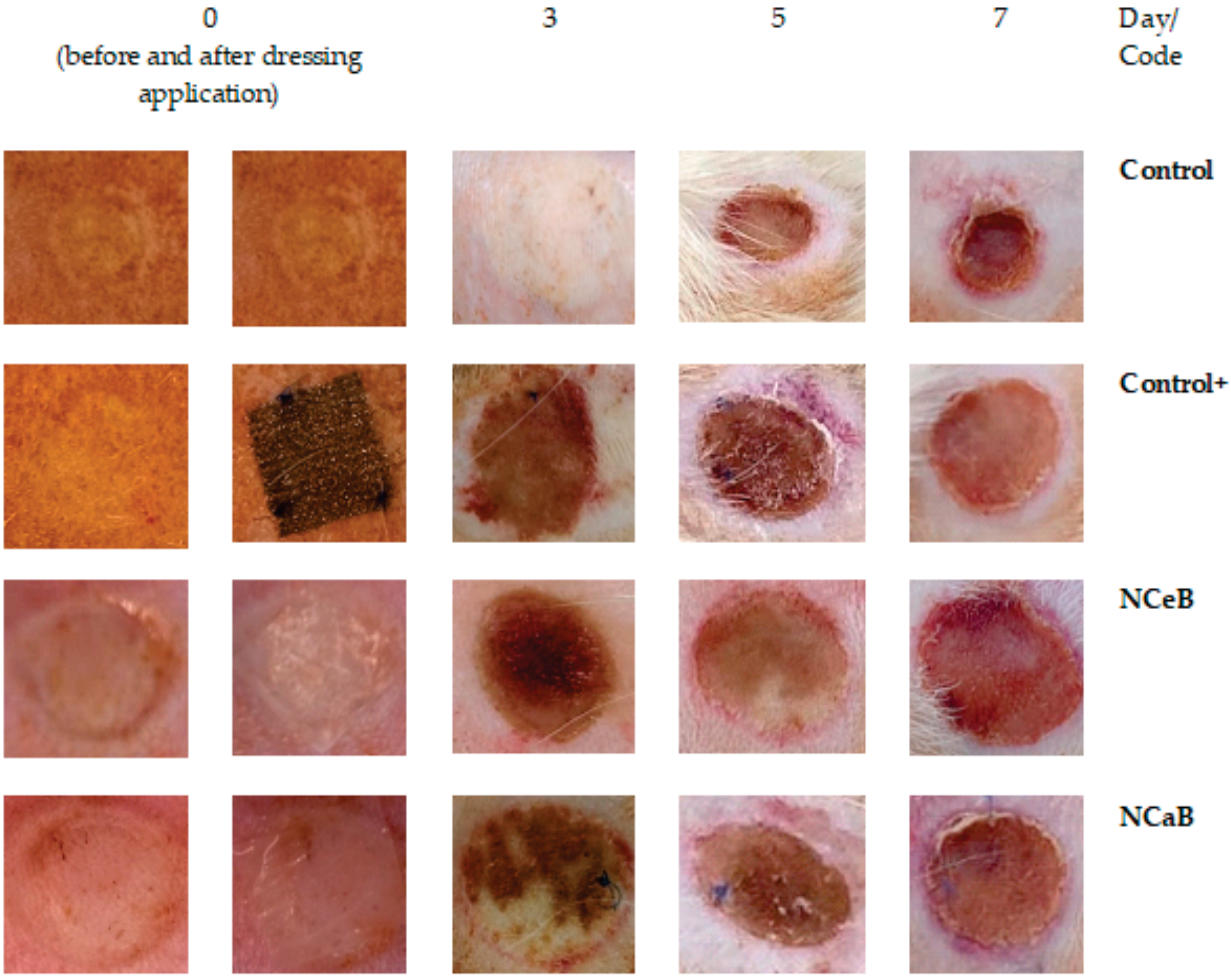

Figure 4. Images of burn wounds collected during the first 7 days after application of the dressing.

2.4. Macroscopical Analysis of the Burn Wound

The application of a commercial dressing (Atrauman® Ag, Hartmann, Heidenheim an der Brenz, Germany) led to a slight increase in wound area up to the fifth day, followed by a decrease to its original diameter by the seventh day. Compared to the control group, the reduction in wound size in the positive control burn group was statistically significant (♦ $p < 0.05$), particularly after five days (Table 1). For the tested fibers, the wounds showed no signs of suppuration and appeared rosy, with well-defined edges. By day seven, small shiny areas, indicative of new epithelial cell formation, were visible, suggesting the onset of tissue regeneration, although the lesions had not yet undergone complete healing.

Table 1. Evolution of wound diameter (cm) during 7 days after dressing application.

Day/Code	Control	Control+	NCeB	NCaB
0	0.968 ± 0.03	0.975 ± 0.01	0.969 ± 0.03	0.976 ± 0.01
3	1.348 ± 0.05 *	1.016 ± 0.03 ♦	1.076 ± 0.01 ♦	1.088 ± 0.01 ♦
5	1.335 ± 0.05 *	0.993 ± 0.01 ♦	1.060 ± 0.03 ♦	1.074 ± 0.01 ♦
7	1.308 ± 0.03 *	0.981 ± 0.01 ♦	1.035 ± 0.01 ♦	1.052 ± 0.03 ♦

* $p < 0.05$ vs. initial moment; ♦ $p < 0.05$ vs. Control.

It is important to note that the fibers treated with aldehyde B affected the progression of burn size similarly to the commercial Atrauman dressing, resulting in a statistically significant reduction in wound size (♦ $p < 0.05$) compared to the control group. This effect was particularly pronounced on day 3 of the experiment, with measurements of 1.035 ± 0.01 mm for NCeB and 1.052 ± 0.03 mm for NCaB, as shown in Table 1.

Table 2 depicts the leucocyte changes by subpopulation and day, in all groups. The studied chitosan formulation were statistically significantly lower than the control + group ($p < 0.05$).

Table 2. Leucocyte count in rats.

Code	Moment of Determination (Day)	Leucocyte Count				
		%				
		PMN	Ly	E	M	B
Control	0	26.6 ± 8.13	69.2 ± 12.37	0.5 ± 0.03	3.5 ± 0.1	0.2 ± 0.03
	3	16.0 ± 6.19 *	79.6 ± 13.25 *	0.4 ± 0.01	3.8 ± 0.05	0.2 ± 0.03
	5	16.8 ± 7.43 *	78.9 ± 11.69 *	0.4 ± 0.01	3.7 ± 0.1	0.2 ± 0.01
	7	18.2 ± 6.38 *	77.3 ± 11.47 *	0.6 ± 0.03	3.7 ± 0.1	0.2 ± 0.01
Control+	0	26.8 ± 6.45	69.0 ± 11.53	0.4 ± 0.03	3.6 ± 0.05	0.2 ± 0.03
	3	26.3 ± 7.37 ♦	69.5 ± 13.19 ♦	0.5 ± 0.03	3.7 ± 0.05	0.2 ± 0.01
	5	26.1 ± 6.29 ♦	69.6 ± 12.55 ♦	0.6 ± 0.01	3.6 ± 0.05	0.2 ± 0.03
	7	26.5 ± 6.11 ♦	68.8 ± 12.43 ♦	0.5 ± 0.03	3.6 ± 0.1	0.2 ± 0.01
NCeB	0	26.8 ± 6.29	68.8 ± 11.35	0.5 ± 0.03	3.7 ± 0.1	0.2 ± 0.03
	3	23.2 ± 6.33	72.5 ± 11.29	0.6 ± 0.01	3.5 ± 0.05	0.2 ± 0.01
	5	23.7 ± 5.51	72.2 ± 11.53	0.4 ± 0.01	3.5 ± 0.05	0.2 ± 0.03
	7	23.7 ± 7.13	72.0 ± 12.41	0.5 ± 0.03	3.6 ± 0.05	0.2 ± 0.01
NCaB	0	26.7 ± 6.67	69.1 ± 10.67	0.5 ± 0.03	3.5 ± 0.1	0.2 ± 0.03
	3	23.0 ± 6.29	72.6 ± 11.55	0.5 ± 0.03	3.7 ± 0.05	0.2 ± 0.01
	5	23.9 ± 6.11	72.0 ± 11.45	0.4 ± 0.03	3.5 ± 0.05	0.2 ± 0.03
	7	24.1 ± 6.39	71.8 ± 11.27	0.4 ± 0.01	3.5 ± 0.05	0.2 ± 0.01

PMN—polymorphonucleates neutrophils, Ly—lymphocytes, E—eosinophils, B—basophils, M—macrophages. * $p < 0.05$ vs. initial moment; ♦ $p < 0.05$ vs. control.

Rat serum cortisol was significantly lower in chitosan groups than in the control group, as seen in Table 3 ($p < 0.05$).

Table 3. The influence of norfloxacin nanofibers administration on serum cortisol levels in rats.

Cortisol (μg/dL)				
Moment	**C**	**C+**	**NCeB**	**NCaB**
0	26.83 ± 2.48	26.67 ± 3.61	26.17 ± 1.60	26.33 ± 2.58
3	54.33 ± 1.51 **	30.50 ± 1.38 ♦	35.67 ± 1.51 ♦	35.33 ± 1.03 ♦
5	53.33 ± 1.86 **	29.17 ± 0.75 ♦	35.17 ± 1.17 ♦	34.67 ± 1.37 ♦
7	52.83 ± 2.14 **	27.83 ± 1.17 ♦	34.83 ± 1.60 ♦	34.33 ± 1.21 ♦

** $p < 0.01$ vs. initial moment; ♦ $p < 0.05$ vs. control group.

SOD enzyme activity is statistically higher in the chitosan groups, as shown in Table 4 ($p < 0.05$).

Table 4. The influence of nanofiber application on SOD activity.

SOD (U/mg Protein)				
Moment	**C**	**C+**	**NCeB**	**NCaB**
0	19.33 ± 1.41	19.33 ± 1.06	19.33 ± 1.33	19.67 ± 0.95
3	11.17 ± 0.68 *	16.5 ± 1.41 ♦	15.50 ± 1.41 ♦	15.50 ± 0.68 ♦
5	10.83 ± 1.06 *	16.33 ± 0.68 ♦	14.33 ± 0.68 ♦	14.67 ± 0.71 ♦
7	10.67 ± 0.68 *	16.17 ± 0.71 ♦	14.17 ± 0.71 ♦	14.17 ± 0.68 ♦

* $p < 0.05$ vs. initial moment; ♦ $p < 0.05$ vs. control.

The impact of the experimental fibers varied based on their composition. The use of chitosan fibers was associated with a rise in cortisol, peaking on day 3 (48.83 ± 2.14 * and 48.83 ± 2.14 *, respectively). Although these values were intermediate between the control and Atrauman groups, they were still statistically significant compared to the control. The slight regulation of cortisol levels by the studied fibers can be attributed to the antioxidant properties of chitosan [32]. In contrast, the nanofibers modified with boronic aldehyde B induced a significant decrease in cortisol levels (34.83 ± 2.04 ♦, 35.33 ± 1.03 ♦, 35.67 ± 1.51 ♦). This was attributed to the strong antioxidant effect induced by the aldehyde B in addition to that of chitosan [33].

In the same trend as SOD, GPx activity is significantly higher in the studied groups than in the control group Table 5 ($p < 0.05$).

Table 5. The influence of nanofibers application on the GPx activity.

GPX (mU/mg Protein)				
Moment	**C**	**C+**	**NCeB**	**NCaB**
0	111.83 ± 20.58	111.67 ± 21.93	112.17 ± 25.58	111.5 ± 25.33
3	87.50 ± 27.53 *	98.50 ± 25.62 ♦	101.67 ± 26.67 ♦	101.50 ± 26.41 ♦
5	87.50 ± 26.82 *	98.17 ± 26.33 ♦	101.83 ± 26.33 ♦	101.50 ± 29.93 ♦
7	87.33 ± 27.17 *	97.67 ± 27.17 ♦	101.50 ± 26.82 ♦	101.33 ± 26.62 ♦

* $p < 0.05$ vs. initial moment; ♦ $p < 0.05$ vs. control.

Lipid peroxidase is another enzyme whose production is triggered by ROS. This enzyme catalyzes the oxidation of fatty acids in cells, leading to the formation of malondialdehyde (MDA), a substance that can be easily measured in blood and is commonly used as a biomarker for oxidative stress [34,35]. Increased free radicals, typical of acute lesions, result in elevated MDA levels. As expected, the control groups exhibited a statistically significant rise in plasma MDA ($p < 0.05$) compared to baseline, peaking on day 3 (43.5 ± 7.27 vs. 32.33 ± 6.21) (Table 6).

Table 6. The influence of fibers application on the MDA activity.

MDA (nmol/g)				
Moment	**C**	**C+**	**NCeB**	**NCaB**
0	32.33 ± 6.21	32.17 ± 7.17	32.5 ± 6.95	32.33 ± 6.62
3	43.5 ± 7.27 *	34.67 ± 5.93 ♦	38.50 ± 6.37 ♦	38.17 ± 6.43 ♦
5	43.17 ± 6.33 *	34.50 ± 6.45 ♦	38.17 ± 7.43 ♦	37.17 ± 6.58 ♦
7	42.83 ± 6.62 *	34.17 ± 6.58 ♦	37.33 ± 6.17 ♦	36.83 ± 5.82 ♦

* $p < 0.05$ vs. initial moment; ♦ $p < 0.05$ vs. control.

In the positive control group, the MDA increase was significantly lower compared to the control group (34.17 ± 6.58 ♦ vs. 42.83 ± 6.62, ♦ $p < 0.05$), with the peak occurring on

day 7, although this increase was not statistically significant compared to the baseline. The fibers' effects varied based on their composition: fibers without B had lower MDA levels compared to the control but still higher than those in the positive control group. In contrast, fibers containing B showed MDA levels like those of the positive control (Table 6).

The complement serum levels were higher in all treated groups than in the control group, as portrayed in Table 7.

Table 7. The influence of fiber application on serum complement activity.

Complement (UCH50)				
Moment	**C**	**C+**	**NCeB**	**NCaB**
0	53.33 ± 8.62	53.67 ± 9.06	53.50 ± 8.45	53.33 ± 8.29
3	39.17 ± 8.21 *	52.17 ± 8.58 ♦	50.50 ± 8.27 ♦	50.67 ± 7.33 ♦
5	39.67 ± 7.39 *	52.50 ± 8.33 ♦	50.57 ± 8.39 ♦	50.50 ± 7.67 ♦
7	39.50 ± 8.42 *	52.67 ± 8.45 ♦	50.83 ± 8.95 ♦	51.17 ± 8.58 ♦

* $p < 0.05$ vs. initial moment; ♦ $p < 0.05$ vs. control.

The capacity of PMN cells to degranulate lytic enzymes that protect against foreign organisms is a critical first line defense feature of the immune system. The recruited macrophages clear wounds of bacterial infections, dead cells and other foreign materials through phagocytosis, which helps control inflammation and initiate tissue remodeling. NBT % serves as an important measure of this capability. In our study, the burns caused a significant increase in NBT % ($p < 0.05$) compared to baseline (14.67 ± 3.42); this was particularly noticeable after 5 days (20.17 ± 4.22) (Table 8).

Table 8. The influence of nanofiber application on NBT %.

NBT (%)				
Moment	**C**	**C+**	**NCeB**	**NCaB**
0	14.67 ± 3.42	14.83 ± 3.39	14.83 ± 3.37	15.17 ± 4.17
3	19.33 ± 4.06 *	15.50 ± 3.44 ♦	17.67 ± 4.33	17.50 ± 3.67
5	20.17 ± 4.22 *	15.50 ± 3.82 ♦	17.67 ± 3.42	17.67 ± 3.58
7	18.67 ± 3.58 *	15.33 ± 3.67 ♦	17.83 ± 3.27	16.50 ± 3.45

* $p < 0.05$ vs. initial moment; ♦ $p < 0.05$ vs. control.

The use of commercial patches led to a minor and statistically insignificant reduction in NBT % compared to baseline but resulted in a significant decrease compared to the control group (♦ $p < 0.05$), especially on day 5 (15.50 ± 3.82 ♦ vs. 20.17 ± 4.22). The studied fibers provided intermediate reductions in this parameter, with values approaching those of the positive control, particularly with the NCaB fibers after 7 days (Table 8).

2.5. Histopathological Evaluation

Two rats from each group were euthanized at 3-, 5- and 7-days post-burn induction to assess the microscopic morphology of the wounds. Following euthanasia, the burn sites along with adjacent healthy skin were excised, processed and examined using a digital histological camera. The examination included all skin layers and evaluated burn depth. Local changes in the burn lesion were analyzed, including the presence of inflammatory reactions, vascular damage, necrosis, granulation tissue, connective tissue and re-epithelialization. The findings are detailed in Table 9 and calculated as a modular score in Table 10, with representative images provided in Figure 5. The data indicate that modifying the fiber surface with boronic aldehyde B significantly improved the adverse effects caused by the burn within the first 3 days compared to both the C and C+ model controls. Additionally, NCeB fibers resulted in nearly complete resolution of these effects by day 7.

Table 9. Histopathologic evaluation of the burns.

Evaluation Criteria	Code			
	Control	Control+	NCeB	NCaB
3 Days				
Intensity of Inflammation				
Congestion	2	2	2	3
Inflammatory oedema	3	2	2	2
Fibrinous exudation	0	0	0	0
Leukocyte infiltrate (neutrophils, macrophages, lymphocytes, histiocytes)	3	4	4	4
Cleansing of the necrosis zone and resorption of the fibrinous matrix	1	2	2	2
Cell differentiation in the wound (endothelial cells, fibroblasts)	1	1	1	1
Fibrillar neogenesis (collagen fibers) and formation of new blood vessels	0	0	0	0
Re-epithelization	0	0	0	0
5 days				
Intensity of Inflammation				
Congestion	3	2	2	2
Inflammatory oedema	2	1	2	2
Fibrinous exudation	1	1	1	1
Leukocyte infiltrate (neutrophils, macrophages, lymphocytes, histiocytes)	4	3	3	3
Cleansing of the necrosis zone and resorption of the fibrinous matrix	1	2	1	1
Cell differentiation in the wound (endothelial cells, fibroblasts)	1	3	1	1
Fibrillar neogenesis (collagen fibers) and formation of new blood vessels.	1	1	1	1
Re-epithelization	0	0	0	0
7 days				
Intensity of Inflammation				
Congestion	1	2	1	1
Inflammatory oedema	0	0	0	0
Fibrinous exudation	0	0	0	0
Leukocyte infiltrate (neutrophils, macrophages, lymphocytes, histiocytes)	2	2	2	3
Cleansing of the necrosis zone and resorption of the fibrinous matrix	0	0	1	1
Cell differentiation in the wound (endothelial cells, fibroblasts)	1	2	2	4
Fibrillar neogenesis (collagen fibers) and formation of new blood vessels.	0	2	1	2
Re-epithelization	0	0	1	1

0—absent 1—very low intensity, 2—low intensity, 3—medium intensity, 4—high intensity Orange: inflammatory phase of healing; Green: proliferative phase; Blue: Remodeling phase.

Table 10. Histological analysis revealed significant differences in tissue regeneration parameters across treatment groups.

Group	Epithelialization Score (0–3)	Inflammation Score (0–3)	Granulation Tissue Score (0–3)
Control	1.0 ± 0.2	2.5 ± 0.3	1.0 ± 0.2
Control+	1.5 ± 0.2	2.0 ± 0.2	1.5 ± 0.3
NCeB	2.5 ± 0.1	1.0 ± 0.1	2.5 ± 0.2
NCaB	2.7 ± 0.1	0.8 ± 0.1	2.7 ± 0.1

ANOVA results indicated significant differences ($p < 0.05$) between treatment groups, highlighting the superior performance of NCeB and NCaB in promoting epithelialization and reducing inflammation.

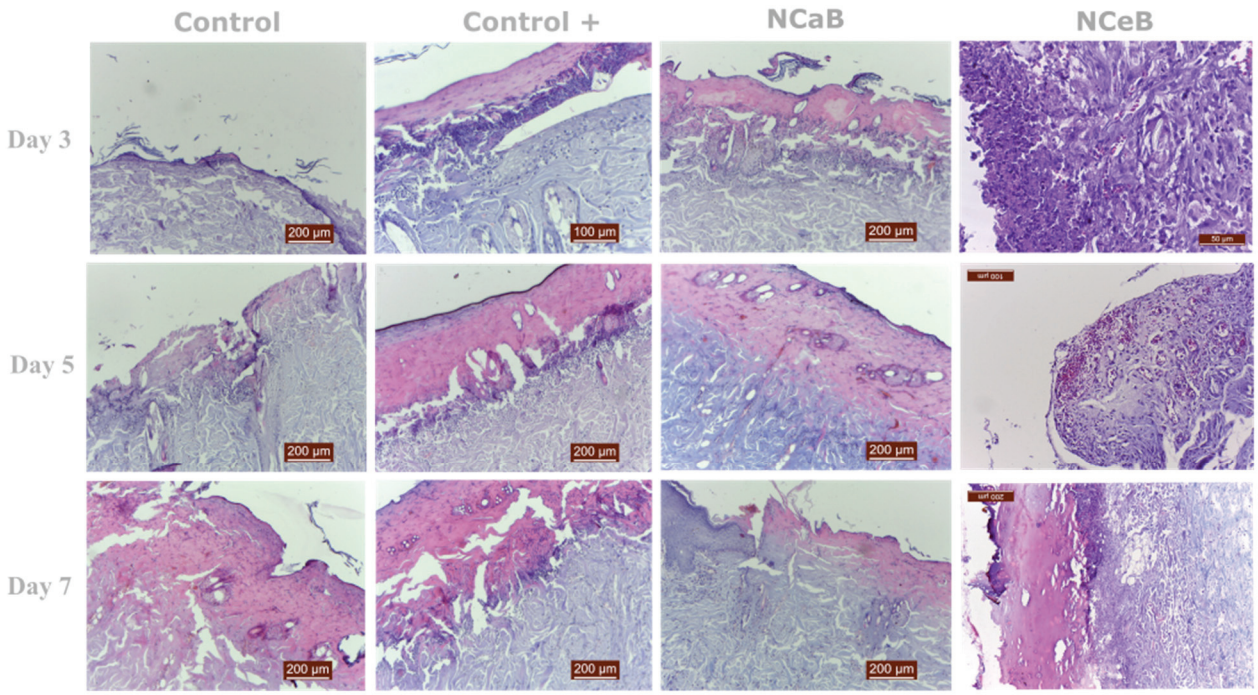

Figure 5. Representative histologic images of burns at 3, 5 and 7 days after the application of the fibers. The sections were prepared at a thickness of 200 µm. The inflammatory cell population is higher in control and control+ groups at all times. NCaB shows a superior cell differentiation at Day 7.

3. Discussions

3.1. Fiber Analysis

Modification of the fiber surface with aldehyde B was intended to endow the fibers with antifungal activity [36,37], complementary to the antibacterial activity of drug, as well as to fix the drug on/into fibers and to achieve a prolonged release effect. The success of this strategy was demonstrated by spectroscopic and microscopic methods, which proved the co-existence of the chitosan, NFX and B in the studied fibers (Figure 1).

3.2. Structural Analysis

However, spherulites, which are characteristic of norfloxacin crystalized from ethanol, were not observed, pointing to an encapsulation into the fibers, most likely in the pores, resulting from PEO removal. The SEM images also pointed to this conclusion, revealing entangled fibers with diameters of ~170 nm and pores ~4 µm, with no crystals on their surface (Figure 3). Thus, FTIR, POM and SEM images confirmed the presence of norfloxacin in the fibers and their imination with aldehyde B. The FTIR spectra of the studied fibers revealed the encapsulation of NFX by the presence of distinctive bands, i.e., carbonyl stretching vibrations at 1636 cm^{-1} and NH quinolone bending at 1618 cm^{-1} [38], and the reaction of aldehyde B with glucosamine of chitosan by the presence of an absorption band at around 1625 cm^{-1}, characteristic of imine bonds, and bands at 1564 cm^{-1} and 760 cm^{-1}, which are specific to vibrations of C=C and B-OH groups [29]. All the bands characteristic of chitosan were present in the spectra of composite chitosan fibers, albeit at slightly shifted to lower/higher wavelengths, suggesting physical interactions between the various components (Figure 1) [39].

3.3. Biochemical Analysis

3.3.1. Inflammatory Studies

For a deeper understanding of the effect of chitosan-based dressings on the wound healing process, a series of relevant parameters were measured at baseline (day 0) and on days 3–7 after dressing application to assess the impact on the hematological profile, immune system and oxidative stress.

The infliction of the wound resulted in a statistically significant (* $p < 0.05$) increase in the percentage of Ly in peripheral blood compared to the moment before injury (69.2 ± 12.37). This was persistent over 7 days, with a maximum on the third day (79.6 ± 13.25 *) (Table 2). This is in line with the inflammation phase of wound healing [40]. Similarly, an increase of the PMN level with a peak of maximum intensity on the third day (26.6 ± 8.13 vs. 16.0 ± 6.19) (* $p < 0.05$) was noticed. PMNs are considered the first line of defense of the innate immune system, with the role of attacking foreign intruders in the body; these followed the known curve of wound healing. Their local and systemic chemotactic action help recruit other immune cells and trigger the healing processes [41].

Clinical studies revealed that for normal wound healing, a robust PMN response must be limited to the acute wound setting [42]. The application of an Atrauman Ag dressing did not produce significant changes in the level of Ly and PMN compared to the initial moment, having statistically significant changes compared to control M (♦ $p < 0.05$) only on day 3.

A comparison of the samples revealed that the alteration of these two parameters was minimal in the case of the samples containing both NFX and B, indicating a synergistic effect. It can be envisaged that the combined antimicrobial activity of NFX and B improved the anti-pathogen barrier properties of the chitosan nanofibers, with the effect of modulating the PMN activity and consequently reducing their oxidative effect on burnt tissues.

Throughout the experiment, no significant differences were observed in the percentages of eosinophils, monocytes or basophils between the chitosan fiber groups and the controls (Table 2). This indicated that the tested dressings did not induce allergic reactions or other pathological conditions [43,44]. This can be also interpreted as a typical wound healing reaction. Furthermore, consistent with previous research, it can be concluded that the application of these dressings did not impair the normal roles of (i) eosinophils in epithelial remodeling [45,46], (ii) monocytes in regulating wound healing through appetite-related hormones [46] or (iii) the restorative functions of basophils [44].

Cortisol levels are a sensitive indicator of wound healing progress, with elevated cortisol associated with increased oxidative stress and slower healing rates [47]. The analysis of cortisol levels throughout the healing process revealed notable trends (Table 3). As expected, the wound caused a statistically significant rise in cortisol compared to baseline ($p < 0.01$), peaking on day 3 (54.33 ± 1.51 vs. 26.83 ± 2.48). The application of the commercial dressing resulted in only a slight increase in cortisol, with a significant reduction compared to the control group (♦ $p < 0.05$), reaching its peak effect on day 7 (27.83 ± 1.17 ♦).

3.3.2. Oxidative Stress Markers

It is well established that redox signaling and oxidative stress are critical regulators of normal wound healing, supporting processes such as haemostasias, inflammation, angiogenesis, granulation tissue formation, wound closure and extracellular matrix maturation [48]. Reactive oxygen species (ROS) play a vital role throughout these phases, with low concentrations promoting cell survival while inhibiting invasive pathogens. However, injuries lead to increased oxidative stress, which depletes enzymatic antioxidants like SOD and GPx, as they are consumed while neutralizing the elevated ROS levels. Consequently, antioxidant supplementation can prevent cellular oxidative damage and enhance recovery.

SOD, an isoenzyme, scavenges superoxide and increases nitric oxide bioavailability, thereby maintaining vascular homeostasis and contractility [48]. SOD also promotes neovascularization, which aids in the repair of the epidermis and dermis. Dysfunction

or reduced levels of SOD can result in severe morphological and cellular defects during wound healing, particularly in older individuals [49]. In acute wounds, SOD activity declines, as it is used to detoxify ROS during the healing process. Thus, SOD levels serve as a key indicator of antioxidant enzyme activity and a measure of the wound healing process.

In the present study, wound formation was accompanied by a significant reduction in SOD levels ($p < 0.05$), falling to almost half of the baseline value (10.67 ± 0.68 vs. 19.33 ± 1.41), with levels progressively decreasing throughout the study (Table 4). The application of the commercial dressing slightly mitigated the decline in SOD, although levels remained significantly lower compared to the initial measurement (* $p < 0.05$) and the control group (♦ $p < 0.05$) at all time points, with the lowest values observed on days 5 (16.33 ± 0.68 ♦ vs. 10.83 ± 1.06) and 7 (16.17 ± 0.71 ♦ vs. 10.67 ± 0.68).

Similarly, the evaluated fibers exhibited nearly identical effects, with those containing boronic aldehyde B showing the closest results to those of the commercial dressing. Nonetheless, the fibers had a less pronounced effect on SOD compared to cortisol, suggesting that while chitosan was more effective at inhibiting ROS, boronic aldehyde B primarily reduced cortisol levels.

GPx is an antioxidant enzyme crucial for maintaining oxidative balance, cellular repair and wound healing across all layers of the epidermis [50]. Since GPx relies on glutathione as an electron donor, reduced glutathione levels in wound lesions inhibit GPx activity. Consequently, monitoring GPx levels is a valuable indicator of wound healing progress. As anticipated, the GPx levels in the control rats decreased significantly over the study period compared to the baseline ($p < 0.05$), reaching their lowest point after 7 days (87.33 ± 27.17 vs. 111.83 ± 20.58).

The use of a commercial dressing notably reduced this decrease (♦ $p < 0.05$), with the lowest value being recorded after 3 days (98.50 ± 25.62). The studied fibers also contributed to reducing the GPx level differences, although the effect varied depending on the composition. Chitosan fibers (especially NCeB) offered only a modest reduction in GPx levels compared to the control, without statistical significance (90.83 ± 26.33 vs. 87.33 ± 27.17 on day 7). However, the presence of B resulted in a significant statistical improvement over the control (101.33 ± 26.62 ♦ vs. 87.33 ± 27.17 on day 7), surpassing the effect of the commercial dressing (Table 5). This underscores the importance of the antioxidant B in supporting effective wound healing.

Normal skin healing involves a complex and delicate interaction between the immune system, keratinocytes and dermal cells [51]. The serum complement system (UCH50) is a crucial component of the immune response [52] and plays a significant role in tissue repair. However, inappropriate activation of this system can lead to impaired wound healing [53,54]. Developing wound dressings that can reduce complement activation is seen as an innovative approach to wound care.

In the control group, a statistically significant decrease in UCH50 was observed compared to baseline, with the most notable drop occurring on day 3 (39.17 ± 8.21 * vs. 53.33 ± 8.62, * $p < 0.05$), indicating inappropriate immune system activity (Table 7). The commercial dressing led to a less pronounced and statistically insignificant reduction. In comparison, fibers without B also reduced UCH50, but their effect was similar to that of the control group. Conversely, fibers containing B achieved UCH50 values comparable to those of the positive group (Table 7).

3.3.3. Limitations

While the preliminary results look promising, there are issues to be addressed in subsequent studies. The short duration of our study was optimal for studying the inflammatory profile, but for long-term effects, we can only extrapolate from the data. A medium term (3 weeks) and long terms (3–6 months) study could have provided a plethora of information regarding the burn scar evolution and its contraction. However, these goals were beyond the scope of the current study. Another limitation was that the animal model, which is a hallmark of burn research, does not translate results directly to the human body.

Rats have loose skin with a dermal muscle ('*panniculus carnosus*'), similar to the facial muscles in human, that increases wound contraction. Furthermore, they have an innate enzyme to synthesize vitamin C, an essential element in collagen synthesis [55,56]. Thirdly, rats' burns are more resilient to infections than humans. Further study on a different model (pig, monkey) could resemble with more precision a human healing response. However, this pilot study has provided the first stepping-stone for advancing our understanding of the potential of the novel chitosan formulation.

Building on these results, we aim to further our research toward determining the medium-term effects of electrospun chitosan and its encapsulation capabilities. These results would add more clarity to the mechanisms involved in its beneficial effects and could pave the way for superior burn wound dressings.

4. Materials and Methods

4.1. Substances

Chitosan (126 kDa, DD = 97%) was prepared by alkaline hydrolysis of low molecular weight chitosan (Aldrich, St. Louis, MO, USA). Norfloxacin (98%), poly (ethylene oxide) (1000 kDa), 2-formylphenylboronic acid (97%), acetic acid (99.89%), ethanol (Aldrich, 98.89%) and sodium hydroxide (95%) were purchased from Aldrich and used as received.

4.2. Chitosan Dressings Preparation

Chitosan/poly (ethylene oxide) (CS/PEO) nanofibers were prepared by electrospinning a CS/PEO (2/1, *w/w*) blend solution in 80% acetic acid with an Inovenso NanoSpinner StarterKit, applying the following conditions: 7 kV, 0.4 mL/h; needle-collector distance: 10 cm; inner diameter of needle: 0.8 mm; collector speed: 800 rpm; 27–28°. Next, the PEO was selectively removed by washing in aqueous solutions and the neat chitosan nanofibers were treated to obtain dressings of various compositions, as follows: (1) The fibers were immersed in a saturated solution of norfloxacin (NFX) in ethanol or water for 24 h before being removed and allowed to dry in a normal atmosphere. (2) The fibers encapsulating NFX and neat chitosan nanofibers were sprayed with a solution of 2-formylphenylboronic acid (B) to reach a 10/1 ratio of glucosamine and aldehyde (aldehyde B). The composition of nanofibers is given in Figure 6. It should be highlighted that the content of aldehyde B was determined by UV-vis [17].

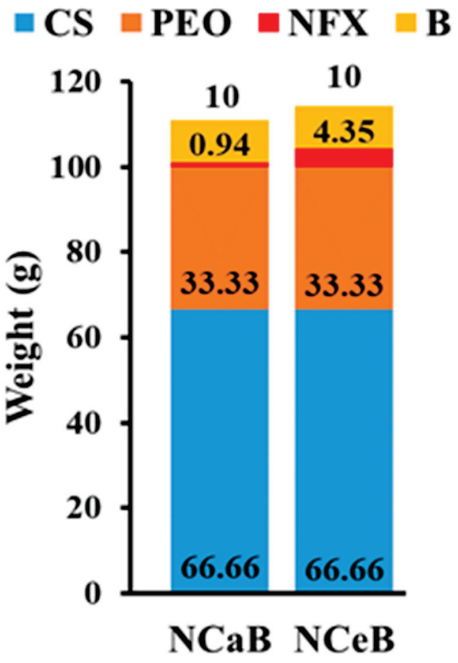

Figure 6. Graphical representation of the fiber composition and the corresponding codes.

4.3. Equipment and Analysis

FTIR spectra of the samples were obtained using a VERTEX 70 FT-IR spectrophotometer (Brucker, Karlsruhe, Germany) in ATR mode. The spectra were measured over the range of 4000 to 600 cm^{-1}, with 32 scans and a resolution of 4 cm^{-1}. Data processing was performed using OPUS 6.5 software. The fiber morphology was monitored with a field emission scanning electron microscope (SEM) EDAX-Quanta 200 (Thermo Fischer Scientific, Waltham, MA, USA), operated at an acceleration voltage of 20 keV and a polarized optical microscope Axio Imager M2 (Zeiss, Jena, Germany) using cross polarizers. The loading degree of norfloxacin into the fibers was monitored by UV-vis spectroscopy on a Cary 60 UV-Vis (Agilent, Santa Clara, CA, USA) by fitting the maximum absorbance at 272 nm on a previously drawn calibration curve, applying the Lambert-Beer law.

4.4. Wound Healing Experiment

The rats were placed in an aseptic medium, anesthetized with isoflurane. Next, the dorsal part was shaved on a surface of approx. 4 cm^2 and then depilated to remove any residual hair which may have hindered the occurrence of a uniform burn wound. The skin was disinfected with 70% ethylic alcohol and allowed to dry and reach room temperature for 3 min. Then, a metal rod with a diameter of 1 cm^2, connected with a thermocouple, was heated at 80 °C in boiling water and then placed on the shaved skin without exerting pressure, supported on its own weight, for 10 s (Figure 7).

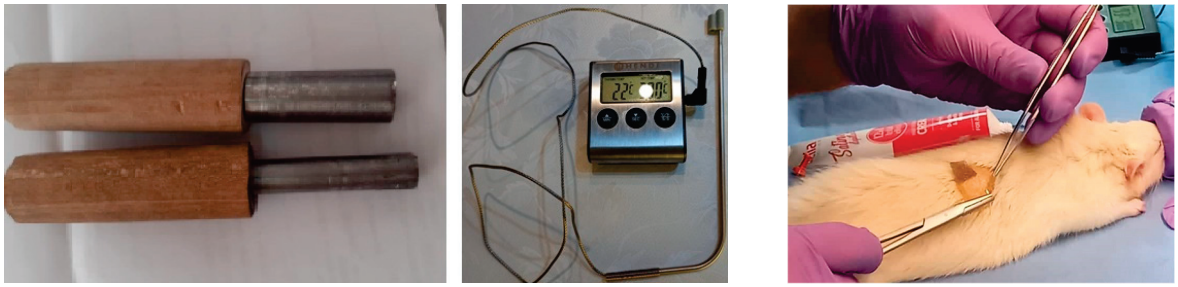

Figure 7. The infliction of burn wound on rats. **Left**: metal contact rods. **Middle**: thermocouple used to confirm the temperature. **Right**: fixing wound dressing on rat burn model skin.

After that, the rats were divided into four groups of six rats each, and each group received the nanofibers mats as follows:

- Group 1 (Control): negative reference, bare wound
- Group 2 (Control+): positive reference, covering the wound with a commercial patch (Atrauman Ag®, Heidenheim, Germany—polyamide fibers impregnated in triglycerides and silver particles)
- Group 3 (NCeB): wound covered with NCeB nanofibers (high concentration norfloxacin, 4.35%)
- Group 4 (NCaB): wound covered with NCaB nanofibers (low concentration norfloxacin, 0.94%)

The dressing was fixed in place as depicted in Figure 8. The rats were monitored for weight fluctuations and any behavioral signs of discomfort or pain, such as scratching, biting, facial expressions or posture, based on the rat grimace scale [36]. After creating the wound, measurements of its diameter were taken with a ruler on days 0, 3, 5 and 7, alongside observations of local morphological features including general appearance, color, consistency, edges, crust formation and detachment, redness, swelling, discharge, bleeding, granulation and any tissue scarring or infections. Photographs were taken after each assessment for comparative analysis. Visual tracking of wound size was conducted by photographing the wound area from a consistent distance of 35 cm using a digital camera with the same lighting and settings on days 0, 3, 5 and 7. A ruler placed beside the wound

provided a reference scale in pixels, allowing wound area calculations through ImageJ software, version 1.8.0.

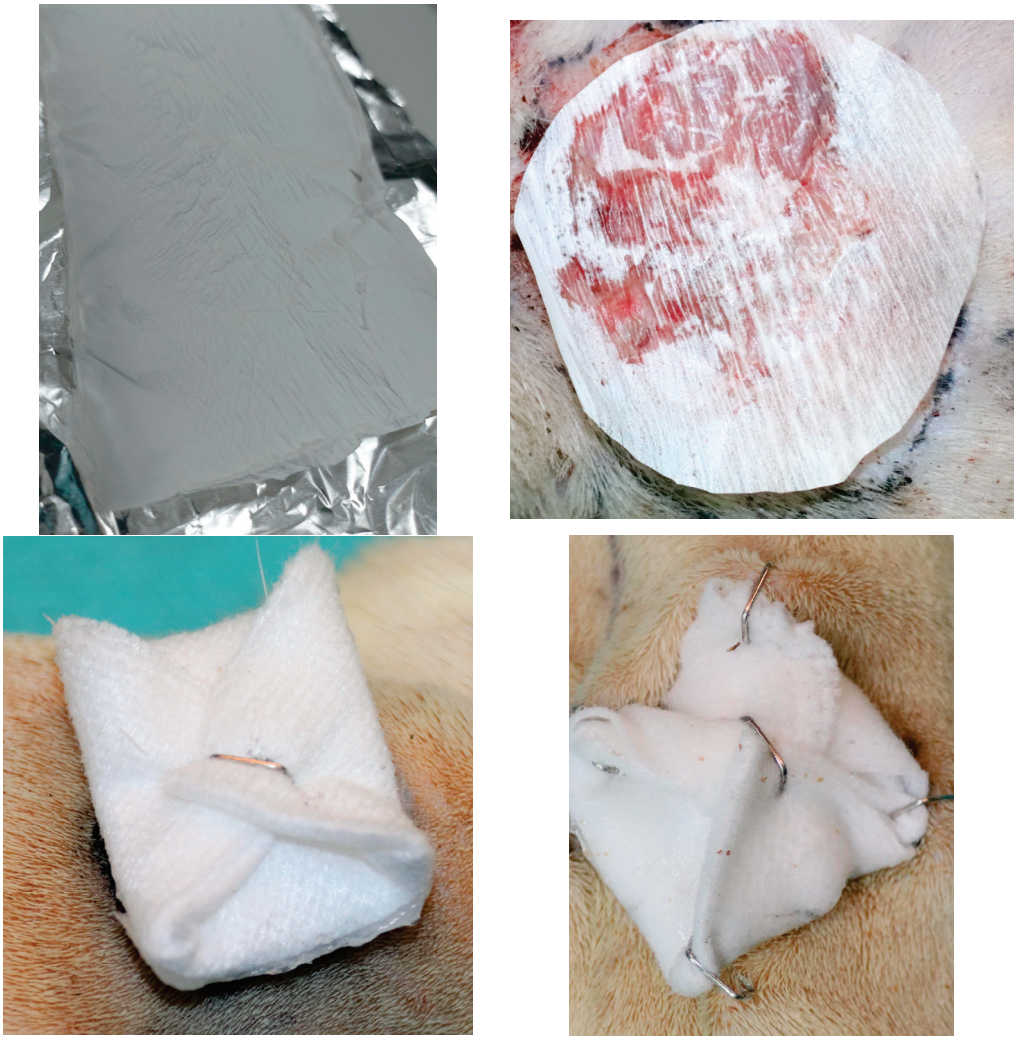

Figure 8. Upper-left: Synthesized electrospun chitosan fiber sheet. **Upper-right**: close-up image of chitosan dressing cut, placed in situ before fixation (surgical marker used to trace wound contour for precise area calculation). **Lower left**: cotton gauze folded to the right size. **Lower right**: Same cotton gauze fixed in four points with surgical staples.

4.5. Blood Markers Examination

Blood samples (0.3–0.5 mL) were collected from the lateral tail vein at two time points: 24 h and 7 days. These samples were analyzed to evaluate the hemodynamic, immune and biochemical profiles. For inflammation studies, the following parameters were measured: number of red blood cells, leukocyte count, cortisol levels, serum complement activity, phagocytic activity of peripheral blood neutrophils (via the NBT test), malondialdehyde (MDA) activity, glutathione peroxidase (GPx) and superoxide dismutase (SOD). Laboratory analyses were performed with the Automated Hematology Analyzer HemaVet 950FS (Drew Scientific, Inc., Boston, MA, USA) and the VITROS 750 XRC analyzer (Alphasoft, Bochum, Germany), using specialized reagents provided by Johnson & Johnson (New Haven, CT, USA).

4.6. Histological Examination

At the end of the experiment, the rats were euthanized with 3% isoflurane anesthesia, and tissues from the implant site were collected. These samples were fixed in Bouin's solution for 24 h and then gradually dehydrated using ethanol baths of increasing concen-

trations (70%, 75%, 80%, 85%, 90%, 96% and absolute ethanol), with each step lasting three hours [33]. Next, samples were clarified in three successive xylene baths, one hour each, and embedded in paraffin through three paraffin baths at 60 °C.

The samples were sectioned at a thickness of 5 µm and stained with hematoxylin-eosin (H&E) following standard procedures: xylene deparaffinization, ethanol hydration, hematoxylin staining, eosin counterstaining, alcohol dehydration, xylene clearing and mounting with Canada balsam [38]. Images were captured using a Nikon E600 Eclipse Ti-E Inverted Microscope (Tokyo, Japan), equipped with NIS Elements Basic Research software (https://www.microscope.healthcare.nikon.com/products/software/nis-elements/nis-elements-basic-research, version June 2023) and a Coolpix 950 digital camera (Nikon, Tokyo, Japan). Figure 9 illustrates the in vivo experimental protocol.

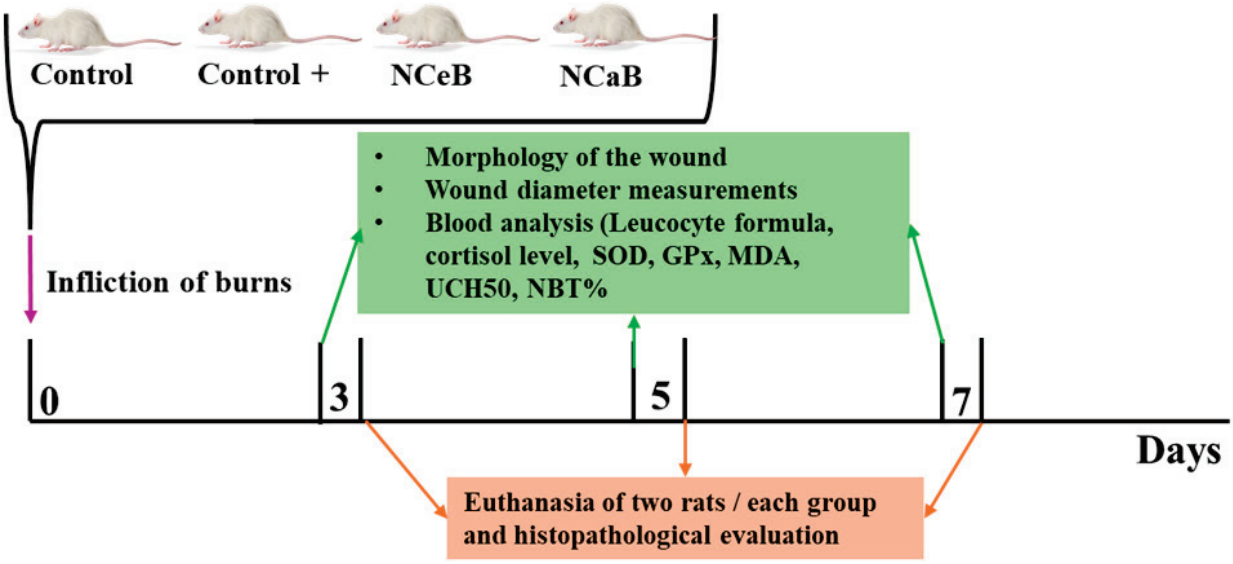

Figure 9. Graphical representation of the in vivo protocol.

4.7. Statistical Processing of Data

Data are presented as the arithmetic mean ± standard deviation (S.D.) for each parameter and substance studied. Statistical analysis was performed using SPSS version 17.0 for Windows, employing one-way ANOVA to assess the significance of differences within each animal group and between the test groups and the control. A *p*-value (probability) of less than 0.05 was considered statistically significant.

4.8. Ethical Aspects of the Research

The experimental protocol was approved by the Research Ethics Committee of UMF "Grigore T. Popa" in Iaşi (Ethical Approval No. 160/04.03.2022) and authorized by the Veterinary Health Directorate (Project Authorization No. 56/19.02.2022). The research methodology adhered fully to the ARRIVE guidelines and to the European legislation on animal welfare (Directive 2010/63/EU of the European Parliament and of the Council of 22 September 2010, on the protection of animals used for scientific purposes).

5. Conclusions

A series of chitosan-based nanofibers were produced by electrospinning using a co-spinning agent as a sacrificial matrix. Norfloxacin antibiotic was embedded into them and their surface was modified with an antioxidant, antifungal aldehyde B. Burn wounds were created on rats with a heated steel rod of 1 cm^2 diameter. The application of the studied dressings produced a statistically significant diminishing of the wound size. This correlated well with a significant a significant increase in MDA and SOD parameters, suggesting that

the antioxidant activity of aldehyde B reduced oxidative stress, favoring wound healing, a result that is consistent with those observed for chitosan-derived compounds.

The statistical insights derived from this study underscore the effectiveness of chitosan-based nanofibers in enhancing wound healing compared to conventional treatments and controls, demonstrating their potential as advanced therapeutic materials for clinical applications in wound management.

Author Contributions: Conceptualization, L.M.-T., C.-G.C. and I.G.; methodology I.G., C.-G.C. and C.C.; software C.-G.C. and C.C.; validation I.G., C.-G.C., D.A. and L.M.-T.; formal analysis A.A., D.A. and S.C.; investigation I.G., C.-G.C., A.A. and S.C.; resources, A.A., S.C., D.A. and S.A.P.; data curation A.A., D.A. and S.C.; writing—original draft preparation C.-G.C., A.A. and S.C.; writing—review and editing, C.-G.C., I.G. and L.M.-T.; visualization, A.A., S.C. and S.A.P.; supervision, L.M.-T. and I.G.; project administration, L.M.-T.; funding acquisition, L.M.-T. All authors have read and agreed to the published version of the manuscript.

Funding: This work was supported by a grant of the Romanian Ministry of Education and Research, CNCS—UEFISCDI, project number PCE2/2021 within PNCDI III and from the European Commission through the project H2020-MSCA-RISE-2019, SWORD-DLV-873123. This work is part of Corneliu George Coman's Ph.D. studies and was co-funded from the "Grigore T. Popa" University of Medicine and Pharmacy Iasi, Romania.

Institutional Review Board Statement: The animal study protocol was approved by the Institutional Ethics Committee of UMF "Grigore T. Popa" in Iaşi (Ethical Approval No. 160/04.03.2022) and authorized by the Veterinary Health Directorate (Project Authorization No. 56/19.02.2022).

Informed Consent Statement: Not applicable.

Data Availability Statement: The original contributions presented in this study are included in the article. Further inquiries can be directed to the corresponding authors.

Conflicts of Interest: The authors state that they have no known financial interests or personal relationships that could have influenced the work presented in this paper.

References

1. Michailidou, G.; Christodoulou, E.; Nanaki, S.; Barmpalexis, P.; Karavas, E.; Vergkizi-Nikolakaki, S.; Bikiaris, D.N. Superhydrophilic and high strength polymeric foam dressings of modified chitosan blends for topical wound delivery of chloramphenicol. *Carbohydr. Polym.* **2019**, *208*, 1–13. [CrossRef] [PubMed]
2. Jayakumar, R.; Prabaharan, M.; Kumar, P.T.S.; Nair, S.V.; Tamura, H. Biomaterials based on chitin and chitosan in wound dressing applications. *Biotechnol. Adv.* **2011**, *29*, 322–337. [CrossRef] [PubMed]
3. Mu, L.; Wu, L.; Wu, S.; Ye, Q.; Zhong, Z. Progress in chitin/chitosan and their derivatives for biomedical applications: Where we stand. *Carbohydr. Polym.* **2024**, *343*, 122233. [CrossRef] [PubMed]
4. Anisiei, A.; Oancea, F.; Marin, L. Electrospinning of chitosan-based nanofibers: From design to prospective applications. *Rev. Chem. Eng.* **2023**, *39*, 31–70. [CrossRef]
5. Marin, L.; Andreica, B.-I.; Anisiei, A.; Cibotaru, S.; Bardosova, M.; Materon, E.M.; Oliveira, O.N. Quaternized chitosan (nano)fibers: A journey from preparation to high performance applications. *Int. J. Biol. Macromol.* **2023**, *242*, 125136. [CrossRef]
6. Che, X.; Zhao, T.; Hu, J.; Yang, K.; Ma, N.; Li, A.; Sun, Q.; Ding, C.; Ding, Q. Application of Chitosan-Based Hydrogel in Promoting Wound Healing: A Review. *Polymers* **2024**, *16*, 344. [CrossRef]
7. Elangwe, C.N.; Morozkina, S.N.; Olekhnovich, R.O.; Krasichkov, A.; Polyakova, V.O.; Uspenskaya, M.V. A Review on Chitosan and Cellulose Hydrogels for Wound Dressings. *Polymers* **2022**, *14*, 5163. [CrossRef]
8. Luo, Y.; Cui, L.; Zou, L.; Zhao, Y.; Chen, L.; Guan, Y.; Zhang, Y. Mechanically strong and on-demand dissoluble chitosan hydrogels for wound dressing applications. *Carbohydr. Polym.* **2022**, *294*, 119774. [CrossRef]
9. Lungu, R.; Paun, M.-A.; Peptanariu, D.; Ailincai, D.; Marin, L.; Nichita, M.-V.; Paun, V.-A.; Paun, V.-P. Biocompatible Chitosan-Based Hydrogels for Bioabsorbable Wound Dressings. *Gels* **2022**, *8*, 107. [CrossRef]
10. Wang, X.; Song, R.; Johnson, M.; Shen, P.; Zhang, N.; Lara-Sáez, I.; Xu, Q.; Wang, W. Chitosan-Based Hydrogels for Infected Wound Treatment. *Macromol. Biosci.* **2023**, *23*, 2300094. [CrossRef]
11. Jin, L.; Yoon, S.-J.; Lee, D.H.; Pyun, Y.C.; Kim, W.Y.; Lee, J.H.; Khang, G.; Chun, H.J.; Yang, D.H. Preparation of Foam Dressings Based on Gelatin, Hyaluronic Acid, and Carboxymethyl Chitosan Containing Fibroblast Growth Factor-7 for Dermal Regeneration. *Polymers* **2021**, *13*, 3279. [CrossRef] [PubMed]
12. Li, Y.; Leng, Q.; Pang, X.; Shi, H.; Liu, Y.; Xiao, S.; Zhao, L.; Zhou, P.; Fu, S. Therapeutic effects of EGF-modified curcumin/chitosan nano-spray on wound healing. *Regen. Biomater.* **2021**, *8*, rbab009. [CrossRef] [PubMed]

13. Tsai, H.-C.; Sheng, C.; Chang, L.-S.; Wen, Z.-H.; Ho, C.-Y.; Chen, C.-M. Chitosan-microencapsulated rhEGF in promoting wound healing. *J. Wound Care* **2021**, *30*, IXi. [CrossRef]
14. Duvnjak Romić, M.D.; Špoljarić, D.; Šegvić Klarić, M.Š.; Cetina-Čižmek, B.; Filipović-Grčić, J.; Hafner, A. Melatonin loaded lipid enriched chitosan microspheres-Hybrid dressing for moderate exuding wounds. *J. Drug Deliv. Sci. Technol.* **2019**, *52*, 431–439. [CrossRef]
15. Amanzadi, B.; Mirzaei, E.; Hassanzadeh, G.; Mahdaviani, P.; Boroumand, S.; Abdollahi, M.; Hosseinabdolghaffari, A.; Majidi, R.F. Chitosan-based layered nanofibers loaded with herbal extract as wound-dressing materials on wound model studies. *Biointerface Res. Appl. Chem.* **2019**, *9*, 3979–3986. [CrossRef]
16. Motasadizadeh, H.; Azizi, S.; Shaabani, A.; Sarvestani, M.G.; Sedghi, R.; Dinarvand, R. Development of PVA/Chitosan-g-Poly (N-vinyl imidazole)/TiO2/curcumin nanofibers as high-performance wound dressing. *Carbohydr. Polym.* **2022**, *296*, 119956. [CrossRef] [PubMed]
17. Ailincai, D.; Cibotaru, S.; Anisiei, A.; Coman, C.G.; Pasca, A.S.; Rosca, I.; Sandu, A.I.; Mititelu-Tartau, L.; Marin, L. Mesoporous chitosan nanofibers loaded with norfloxacin and coated with phenylboronic acid perform as bioabsorbable active dressings to accelerate the healing of burn wounds. *Carbohydr. Polym.* **2023**, *318*, 121135. [CrossRef]
18. Anisiei, A.; Andreica, B.-I.; Mititelu-Tartau, L.; Coman, C.G.; Bilyy, R.; Bila, G.; Rosca, I.; Sandu, A.-I.; Amler, E.; Marin, L. Biodegradable trimethyl chitosan nanofiber mats by electrospinning as bioabsorbable dressings for wound closure and healing. *Int. J. Biol. Macromol.* **2023**, *249*, 126056. [CrossRef]
19. Jungprasertchai, N.; Chuysinuan, P.; Ekabutr, P.; Niamlang, P.; Supaphol, P. Freeze-Dried Carboxymethyl Chitosan/Starch Foam for Use as a Haemostatic Wound Dressing. *J. Polym. Environ.* **2022**, *30*, 1106–1117. [CrossRef]
20. Umar, A.K.; Sriwidodo, S.; Maksum, I.P.; Wathoni, N. Film-Forming Spray of Water-Soluble Chitosan Containing Liposome-Coated Human Epidermal Growth Factor for Wound Healing. *Molecules* **2021**, *26*, 5326. [CrossRef]
21. Valachová, K.; El Meligy, M.A.; Šoltés, L. Hyaluronic acid and chitosan-based electrospun wound dressings: Problems and solutions. *Int. J. Biol. Macromol.* **2022**, *206*, 74–91. [CrossRef] [PubMed]
22. Ji, M.; Li, J.; Wang, Y.; Li, F.; Man, J.; Li, J.; Zhang, C.; Peng, S.; Wang, S. Advances in chitosan-based wound dressings: Modifications, fabrications, applications and prospects. *Carbohydr. Polym.* **2022**, *297*, 120058. [CrossRef] [PubMed]
23. Cui, C.; Sun, S.; Wu, S.; Chen, S.; Ma, J.; Zhou, F. Electrospun chitosan nanofibers for wound healing application. *Eng. Regen.* **2021**, *2*, 82–90. [CrossRef]
24. Feng, P.; Luo, Y.; Ke, C.; Qiu, H.; Wang, W.; Zhu, Y.; Hou, R.; Xu, L.; Wu, S. Chitosan-Based Functional Materials for Skin Wound Repair: Mechanisms and Applications. *Front. Bioeng. Biotechnol.* **2021**, *9*, 650598. [CrossRef]
25. Rajinikanth, B.S.; Rajkumar, D.S.R.; Keerthika, K.; Vijayaragavan, V. Chitosan-Based Biomaterial in Wound Healing: A Review. *Cureus* **2024**, *16*, e55193. [CrossRef] [PubMed]
26. Verma, D.; Okhawilai, M.; Goh, K.L.; Thakur, V.K.; Senthilkumar, N.; Sharma, M.; Uyama, H. Sustainable functionalized chitosan based nano-composites for wound dressings applications: A review. *Environ. Res.* **2023**, *235*, 116580. [CrossRef]
27. Baumann, A.; Tuerck, D.; Prabhu, S.; Dickmann, L.; Sims, J. Pharmacokinetics, metabolism and distribution of PEGs and PEGylated proteins: Quo vadis? *Drug Discov. Today* **2014**, *19*, 1623–1631. [CrossRef]
28. Pathan, S.G.; Fitzgerald, L.M.; Ali, S.M.; Damrauer, S.M.; Bide, M.J.; Nelson, D.W.; Ferran, C.; Phaneuf, T.M.; Phaneuf, M.D. Cytotoxicity associated with electrospun polyvinyl alcohol. *J. Biomed. Mater. Res. B Appl. Biomater.* **2015**, *103*, 1652–1662. [CrossRef]
29. Anisiei, A.; Rosca, I.; Sandu, A.-I.; Bele, A.; Cheng, X.; Marin, L. Imination of Microporous Chitosan Fibers—A Route to Biomaterials with On "Demand Antimicrobial" Activity and Biodegradation for Wound Dressings. *Pharmaceutics* **2022**, *14*, 117. [CrossRef]
30. Lungu, R.; Anisiei, A.; Rosca, I.; Sandu, A.-I.; Ailincai, D.; Marin, L. Double functionalization of chitosan based nanofibers towards biomaterials for wound healing. *React. Funct. Polym.* **2021**, *167*, 105028. [CrossRef]
31. Marin, L.; Dragoi, B.; Olaru, N.; Perju, E.; Coroaba, A.; Doroftei, F.; Scavia, G.; Destri, S.; Zappia, S.; Porzio, W. Nanoporous furfuryl-imine-chitosan fibers as a new pathway towards eco-materials for CO_2 adsorption. *Eur. Polym. J.* **2019**, *120*, 109214. [CrossRef]
32. Gouin, J.-P.; Kiecolt-Glaser, J.K. The Impact of Psychological Stress on Wound Healing: Methods and Mechanisms. *Immunol. Allergy Clin. N. Am.* **2011**, *31*, 81–93. [CrossRef]
33. Xu, Y.Q.; Xing, Y.Y.; Wang, Z.Q.; Yan, S.M.; Shi, B.L. Pre-protective effects of dietary chitosan supplementation against oxidative stress induced by diquat in weaned piglets. *Cell Stress Chaperones* **2018**, *23*, 703–710. [CrossRef] [PubMed]
34. Pasa, S.; Aydın, S.; Kalaycı, S.; Boğa, M.; Atlan, M.; Bingul, M.; Şahin, F.; Temel, H. The synthesis of boronic-imine structured compounds and identification of their anticancer, antimicrobial and antioxidant activities. *J. Pharm. Anal.* **2016**, *6*, 39–48. [CrossRef] [PubMed]
35. Kurahashi, T.; Fujii, J. Roles of Antioxidative Enzymes in Wound Healing. *J. Dev. Biol.* **2015**, *3*, 57–70. [CrossRef]
36. Sotocinal, S.G.; Sorge, R.E.; Zaloum, A.; Tuttle, A.H.; Martin, L.J.; Wieskopf, J.S.; Mapplebeck, J.C.S.; Wei, P.; Zhan, S.; Zhang, S.; et al. The Rat Grimace Scale: A partially automated method for quantifying pain in the laboratory rat via facial expressions. *Mol. Pain* **2011**, *7*, 55. [CrossRef]
37. Borys, K.M.; Wieczorek, D.; Pecura, K.; Lipok, J.; Adamczyk-Woźniak, A. Antifungal activity and tautomeric cyclization equilibria of formylphenylboronic acids. *Bioorg. Chem.* **2019**, *91*, 103081. [CrossRef] [PubMed]

38. Marin, L.; Ailincai, D.; Mares, M.; Paslaru, E.; Cristea, M.; Nica, V.; Simionescu, B.C. Imino-chitosan biopolymeric films. Obtaining, self-assembling, surface and antimicrobial properties. *Carbohydr. Polym.* **2015**, *117*, 762–770. [CrossRef]
39. Sahoo, S.; Chakraborti, C.K.; Behera, P.K.; Mishra, S.C. FTIR and Raman Spectroscopic Investigations of a Norfloxacin/Carbopol934 Polymeric Suspension. *J. Young Pharm.* **2012**, *4*, 138–145. [CrossRef]
40. Branca, C.; D'Angelo, G.; Crupi, C.; Khouzami, K.; Rifici, S.; Ruello, G.; Wanderlingh, U. Role of the OH and NH vibrational groups in polysaccharide-nanocomposite interactions: A FTIR-ATR study on chitosan and chitosan/clay films. *Polymer* **2016**, *99*, 614–622. [CrossRef]
41. Holzer-Geissler, J.C.J.; Schwingenschuh, S.; Zacharias, M.; Einsiedler, J.; Kainz, S.; Reisenegger, P.; Holecek, C.; Hofmann, E.; Wolff-Winiski, B.; Fahrngruber, H.; et al. The Impact of Prolonged Inflammation on Wound Healing. *Biomedicines* **2022**, *10*, 856. [CrossRef] [PubMed]
42. Schönfelder, U.; Abel, M.; Wiegand, C.; Klemm, D.; Elsner, P.; Hipler, U.-C. Influence of selected wound dressings on PMN elastase in chronic wound fluid and their antioxidative potential in vitro. *Biomaterials* **2005**, *26*, 6664–6673. [CrossRef]
43. Wilgus, T.A.; Roy, S.; McDaniel, J.C. Neutrophils and Wound Repair: Positive Actions and Negative Reactions. *Adv. Wound Care* **2013**, *2*, 379–388. [CrossRef] [PubMed]
44. Fulkerson, P.C.; Rothenberg, M.E. Targeting eosinophils in allergy, inflammation and beyond. *Nat. Rev. Drug Discov.* **2013**, *12*, 117–129. [CrossRef] [PubMed]
45. Shibuya, R.; Kim, B.S. Skin-homing basophils and beyond. *Front. Immunol.* **2022**, *13*, 1059098. [CrossRef]
46. Coden, M.E.; Berdnikovs, S. Eosinophils in wound healing and epithelial remodeling: Is coagulation a missing link? *J. Leukoc. Biol.* **2020**, *108*, 93–103. [CrossRef]
47. Kratofil, R.M.; Shim, H.B.; Shim, R.; Lee, W.Y.; Labit, E.; Sinha, S.; Keenan, C.M.; Surewaard, B.G.J.; Noh, J.Y.; Sun, Y.; et al. A monocyte–leptin–angiogenesis pathway critical for repair post-infection. *Nature* **2022**, *609*, 166–173. [CrossRef]
48. Bilgen, F.; Ural, A.; Kurutas, E.B.; Bekerecioglu, M. The effect of oxidative stress and Raftlin levels on wound healing. *Int. Wound J.* **2019**, *16*, 1178–1184. [CrossRef]
49. Fujiwara, T.; Duscher, D.; Rustad, K.C.; Kosaraju, R.; Rodrigues, M.; Whittam, A.J.; Januszyk, M.; Maan, Z.N.; Gurtner, G.C. Extracellular superoxide dismutase deficiency impairs wound healing in advanced age by reducing neovascularization and fibroblast function. *Exp. Dermatol.* **2016**, *25*, 206–211. [CrossRef]
50. Dong, Y.; Wang, Z. ROS-scavenging materials for skin wound healing: Advancements and applications. *Front. Bioeng. Biotechnol.* **2023**, *11*, 1304835. [CrossRef]
51. Gupta, A.; Singh, R.L.; Raghubir, R. Antioxidant status during cutaneous wound healing in immunocompromised rats. *Mol. Cell. Biochem.* **2002**, *241*, 1–7. [CrossRef] [PubMed]
52. Ellis, S.; Lin, E.J.; Tartar, D. Immunology of Wound Healing. *Curr. Dermatol. Rep.* **2018**, *7*, 350–358. [CrossRef] [PubMed]
53. Inglis, J.E.; Radziwon, K.A.; Maniero, G.D. The serum complement system: A simplified laboratory exercise to measure the activity of an important component of the immune system. *Adv. Physiol. Educ.* **2008**, *32*, 317–321. [CrossRef] [PubMed]
54. Cazander, G.; Jukema, G.N.; Nibbering, P.H. Complement Activation and Inhibition in Wound Healing. *Clin. Dev. Immunol.* **2012**, *2012*, 534291. [CrossRef]
55. Narváez-Cuenca, C.-E.; Caicedo-Suárez, A.; Arias-Carmona, L.; Cadavid-Restrepo, G.; Franco-Castañeda, F.-A.; Porras-Villamil, J.-R. Effect of Aloe Vera and Chitosan Coatings on the Shelf Life of Cape Gooseberries (*Physalis peruviana* L.). *Int. J. Biol. Macromol.* **2022**, *213*, 823–830. [CrossRef]
56. Gad, A.A.M.; Sirko, A. L-gulono-γ-lactone Oxidase, the Key Enzyme for L-Ascorbic Acid Biosynthesis. *Curr. Issues Mol. Biol.* **2024**, *46*, 11057–11074. [CrossRef]

International Journal of
Molecular Sciences

MDPI

Article

High-Density Chitosan Induces a Biochemical and Molecular Response in *Coffea arabica* during Infection with *Hemileia vastatrix*

Julio César López-Velázquez [1], Soledad García-Morales [2], Gloria Paola López-Sánchez [3], Mayra Itzcalotzin Montero-Cortés [4], Alberto Uc-Várguez [5] and Joaquín Alejandro Qui-Zapata [1,*]

[1] Biotecnología Vegetal, Centro de Investigación y Asistencia en Tecnología y Diseño del Estado de Jalisco A.C., Camino Arenero 1227, El Bajío, Zapopan 45019, Mexico; jucelopez_al@ciatej.edu.mx
[2] Biotecnología Vegetal, CONAHCYT-Centro de Investigación y Asistencia en Tecnología y Diseño del Estado de Jalisco A.C., Camino Arenero 1227, El Bajío, Zapopan 45019, Mexico; smorales@ciatej.mx
[3] Escuela de Ingeniería y Ciencias, Tecnológico de Monterrey, General Ramón Corona 2514, Nuevo México, Zapopan 45201, Mexico; paola.lsibt@gmail.com
[4] Instituto Tecnológico de Tlajomulco/TecNM, Km. 10 Carretera Tlajomulco-San Miguel Cuyutlán, Tlajomulco de Zúñiga 45640, Mexico; mayra.mc@tlajomulco.tecnm.mx
[5] Subsede Sureste, Centro de Investigación y Asistencia en Tecnología y Diseño del Estado de Jalisco A.C., Tablaje Catastral 31264 Km 5.5 Carretera Sierra Papacal-Chuburna, Mérida 97302, Mexico; auc@ciatej.mx
* Correspondence: jqui@ciatej.mx; Tel.: +52-(33)-3345-5200 (ext. 1707)

Abstract: The coffee industry faces coffee leaf rust caused by *Hemileia vastratix*, which is considered the most devastating disease of the crop, as it reduces the photosynthetic rate and limits productivity. The use of plant resistance inducers, such as chitosan, is an alternative for the control of the disease by inducing the synthesis of phytoalexins, as well as the activation of resistance genes. Previously, the effect of chitosan from different sources and physicochemical properties was studied; however, its mechanisms of action have not been fully elucidated. In this work, the ability of food-grade high-density chitosan (0.01% and 0.05%) to control the infection caused by the pathogen was evaluated. Subsequently, the effect of high-density chitosan (0.05%) on the induction of pathogenesis-related gene expression (*GLUC*, *POX*, *PAL*, *NPR1*, and *CAT*), the enzymatic activity of pathogenesis-related proteins (GLUC, POX, SOD, PPO, and APX), and phytoalexin production were evaluated. The results showed that 0.05% chitosan increased the activity and gene expression of *ß-1,3 glucanases* and induced a differentiated response in enzymes related to the antioxidant system of plants. In addition, a correlation was observed between the activities of polyphenol oxidase and the production of phytoalexin, which allowed an effective defense response in coffee plants.

Keywords: *Hemileia vastatrix*; *Coffea arabica*; chitosan; NPR1; coffee rust

1. Introduction

Coffee is classified as one of the agricultural products with the highest economic value worldwide [1]. In Mexico, coffee growing is an important economic activity, positioning it as the eleventh largest producer country in the world, with an estimated production of 900,215 tons in 2020 [2]. However, there are increasing threats to coffee production due to pests, diseases, and adverse climatic conditions. Among these limitations in coffee production, the most devastating disease is coffee leaf rust caused by *Hemileia vastatrix*. Under favorable conditions for the pathogen, it can cause defoliation of up to 50% and losses between 30 and 50% in production yield [3]. Resistant varieties and the application of agrochemicals, mainly copper-based, are used to control the disease [4]. Despite the release of some resistant cultivars in recent years, the rust continues to negatively affect production and undermine the income of producers due to the appearance of new strains and new outbreaks of the disease [5]. The use of agrochemicals continues to be the most widely used option for its control, although their use has several drawbacks, including

their cost, toxicity, harmful effect on the environment, and the development of resistance, which makes their use difficult in urban areas and traditional low-scale crops. This makes it necessary and a priority to search for ecological and safe alternatives in the agricultural sector [6]. Among these alternatives, the use of elicitors has been explored, whose purpose is to activate the defense response of plants with the application of low concentrations and are characterized by being of natural or synthetic origin [7]; in coffee plants, the use of these molecules has been documented with positive effects [8–10].

Recently, research has been reported on the role of chitosan as a plant defense inducer in *Coffea arabica* for the control of coffee rust [11]. The mechanism of action of chitosan as an elicitor has been described for some plants, although not completely in coffee. Chitosan is recognized by plasma membrane receptors and induces the transcription of defense-related genes, which is reflected in the synthesis of proteins and metabolites of interest. It has been documented that chitosan increases transcriptional levels of β-1,3 glucanases, chitinases, PR1, Pti5, and WRKY26, phenylalanine ammonium lyase (PAL), resveratrol synthase, as well as the antioxidant enzyme system. In addition, it regulates stomata opening and stimulates the generation of reactive oxygen species (ROS) and energy production [12,13]. However, there are different chitosans on the market that vary in price, purity, source, and process of obtaining them, which leads to different physicochemical properties, and the response in plants can also vary.

In a study conducted by López-Velázquez et al. [11], the effect of the physicochemical properties of commercial chitosans of low and medium molecular weight, as well as practical (Sigma-Aldrich) and high density (food grade) chitosan was used. The results of this work showed that the viscosity of chitosan is an important parameter due to adherence to the plant, whereas molecular weight and degree of acetylation did not show differential effects. In addition, it was observed that chitosan influences the plant defense system, increasing the activity levels of β-1,3 glucanases and peroxidases. The biological effectiveness of coffee rust of chitosans from different methods of production, such as conventional chemical (practical grade) and biotechnological (enzymatic process), has also been evaluated [14]. The best protection response was observed with the chitosan obtained by the chemical method, presenting a higher level of PR enzyme activity (β-1,3 glucanases and peroxidases) in plants treated with chitosan and the pathogen. Both practical-grade chitosan and high-density chitosan showed higher protection against coffee rust [11]. However, practical grade chitosan has been extensively studied and is characterized by higher purity but also higher cost, which could discourage its use. However, high-density chitosan, although of lower purity, can be purchased at a lower price and is readily available, facilitating its use in agriculture.

The defense response induced by practical-grade chitosan has already been reported for coffee [11], although the biochemical and molecular response of this induced resistance remains to be described in more detail. In addition, it is necessary to verify whether the effect of defense induction in other chitosans is maintained or equivalent to that induced by practical grade chitosan. In this work, the biological effectiveness of two concentrations of high-density (food-grade) chitosan as an elicitor in the protection against coffee rust was evaluated. The concentration that induced the highest protection against rust was selected to identify the biochemically and molecularly induced defense mechanism triggered in coffee plants susceptible to *H. vastatrix*.

2. Results

2.1. Biological Effectiveness Test

The disease occurred in all treatments inoculated with *H. vastatrix*. However, the severity of the infection was different for each treatment. Plants in the control treatment (C) showed no signs of the disease, no defoliation occurred during the experiment, and no colonization of the pathogen was verified by microscopy (Figure 1). The treatment inoculated with the pathogen (H) showed 100% disease incidence, and the area under the disease progress curve (AUDPC) value was 102 (Table 1). In all cases where the disease was

observed, the plants showed the characteristic symptoms of coffee rust, defoliation, leaves with chlorosis, and the appearance of yellow or orange spots on the leaves (Figure 1a,b). On the other hand, in the treatments that were inoculated with the pathogen and treated with high-density chitosan 0.01% (Q1) and 0.05% (Q5), although they presented 100% disease incidence, the severity of infection was lower in treatment Q5 (Table 1). Microscopy tests showed that the mycelium of the pathogen was present in both treatments, although, in the Q5 treatment, cell death was also observed in the infected tissue (Figure 1c).

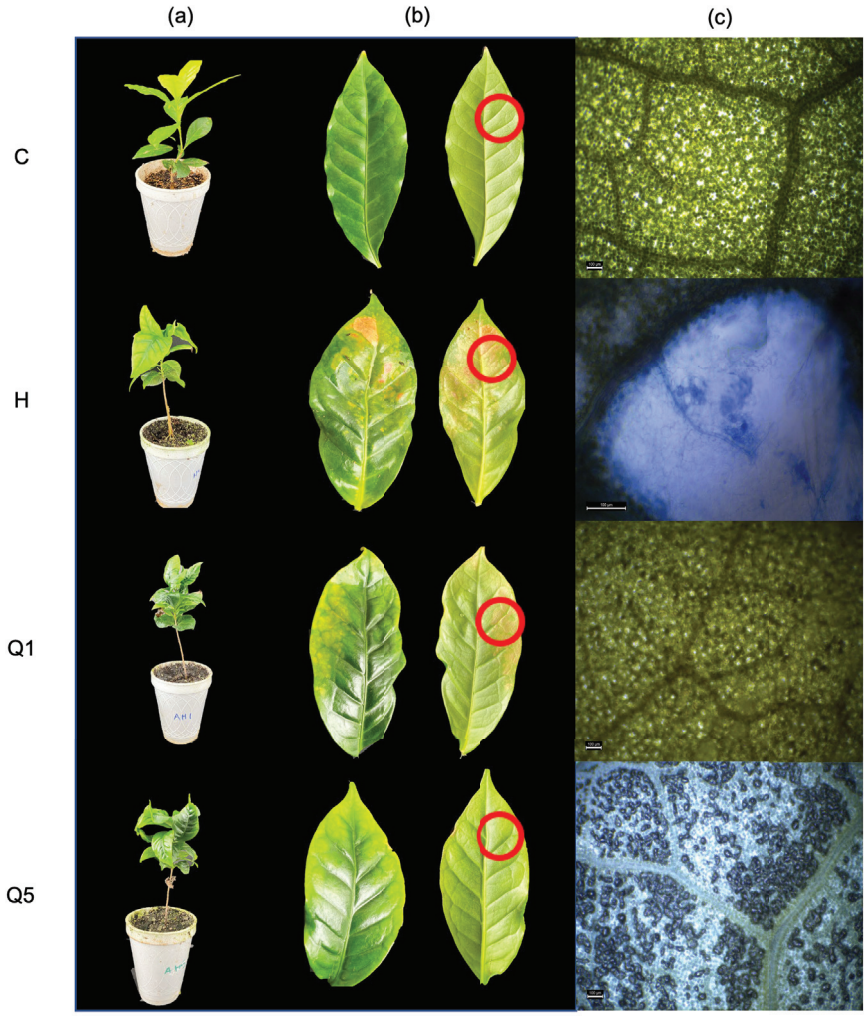

Figure 1. Biological effectiveness test 90 days after inoculation. (**a**) Biological effectiveness test, (**b**) disease leaves, and (**c**) presence of pathogen. (C) Plants without treatment, (H) plants inoculated with *Hemileia vastatrix*, (Q1) plants sprayed with 0.01% high-density chitosan and inoculated with *H. vastatrix*, and (Q5) plants sprayed with 0.05% high-density chitosan and inoculated with *H. vastatrix*. The red circles indicate the area of the leaf where the pathogen was observed.

Table 1. Disease parameters evaluated.

Treatment	Disease Incidence (%)	AUDPC (au)
C	0	0.0 ± 0.0 c
H	100	102 ± 14.3 a
Q1	100	40.0 ± 20.6 b
Q5	100	25.0 ± 11.66 b

The treatments correspond to: (C) plants without treatment, (H) plants inoculated with *Hemileia vastatrix*, (Q1) plants sprayed with 0.01% high-density chitosan and inoculated with *H. vastatrix*, and (Q5) plants sprayed with 0.05% high-density chitosan and inoculated with *H. vastatrix*. Values presented are means with standard deviation. Values with different letters show statistically significant differences at the 95% LSD confidence level ($p < 0.05$). au: Arbitrary units.

2.2. PR-Protein Activity and Phytoalexin Accumulation

For the evaluation of the defense mechanisms induced by chitosan, a concentration of 0.05% was chosen. The activity of enzymes related to pathogenesis (PR) and plant defense, such as β-1,3 glucanases, peroxidases, superoxide dismutase, ascorbate peroxidase, and polyphenol oxidase, was evaluated, as well as the accumulation of phytoalexins through the content of total phenolic compounds. For β-1,3-glucanase activity, it was observed that plants inoculated with the pathogen (H) presented a significant decrease in activity starting at 12 h after inoculation with the pathogen that was maintained until 24 h (Figure 2a). An increase in the level of the control was observed at 48 h and a significant decrease at 72 h.

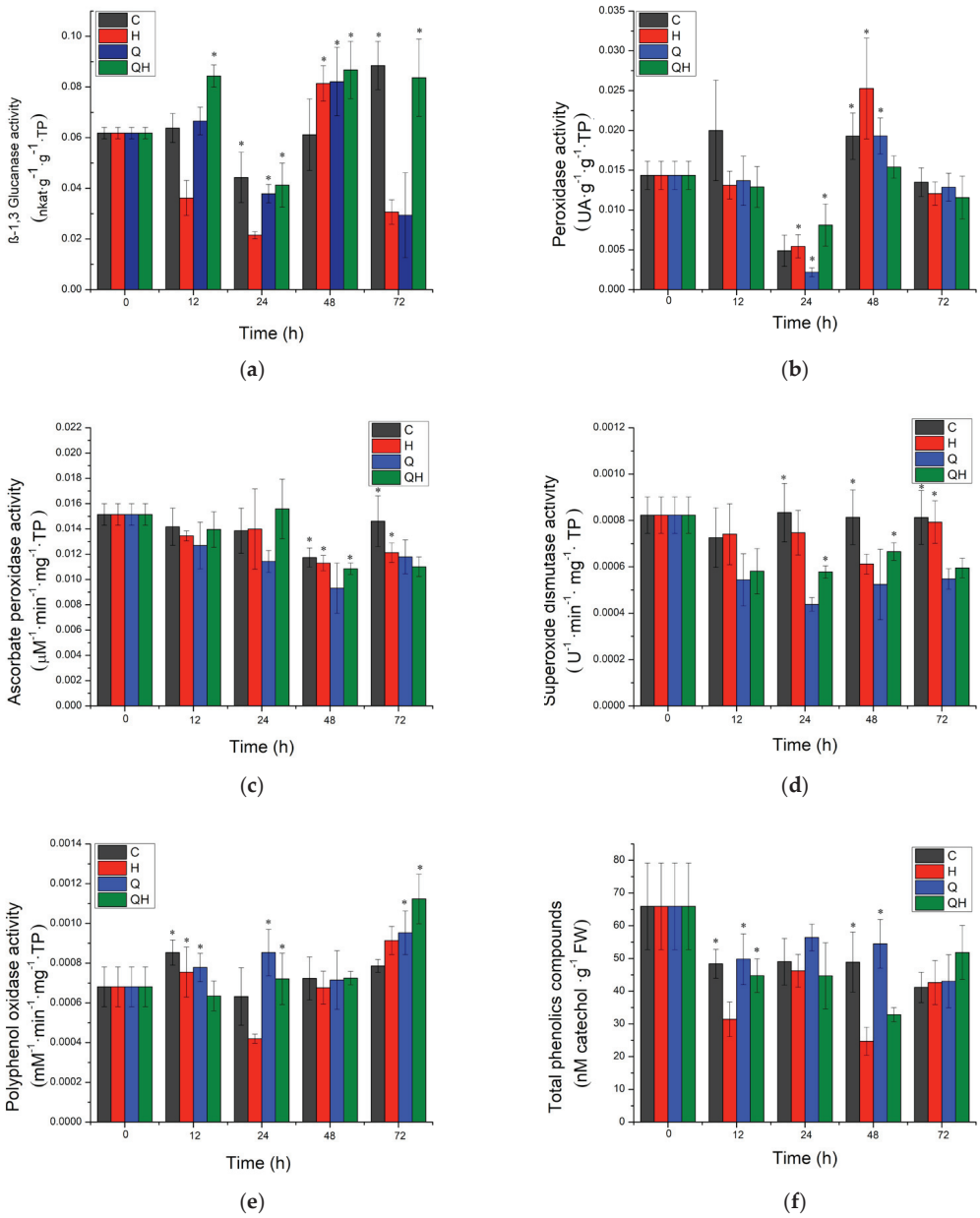

Figure 2. PR protein activity of (**a**) β-1,3 glucanase, (**b**) peroxidase, (**c**) ascorbate peroxidase, (**d**) superoxide dismutase, and (**e**) polyphenol oxidase. Phytoalexin accumulation of (**f**) total phenolics compounds. (C) Plants without treatment, (H) plants inoculated with *Hemileia vastatrix*, (Q) plants sprayed with 0.05% food chitosan, and (QH) plants sprayed with 0.05% food chitosan and inoculated with *H. vastatrix*. Values presented are means with standard deviation. Values with asterisks show statistically significant differences at the 95% LSD confidence level ($p < 0.05$).

For plants inoculated with the pathogen and treated with chitosan (QH), a significantly differentiated response to infected plants was observed; at 12 h, a significant increase in activity was observed, decreasing to the level of the control at 24 h. After 48 h, a significant increase in activity was observed and then a decrease to the level of the control at 72 h. The response induced by chitosan in coffee plants for β-1,3-glucanase activity was always higher than that present in infected plants (H) (Figure 2a).

Regarding the group of enzymes with peroxidase activity, plants inoculated with the pathogen (H) did not show a significant difference with the control at times evaluated (Figure 2b). For plants inoculated with the pathogen and treated with chitosan (QH), a significantly different response to infected plants was only observed up to 48 h after inoculation with the pathogen. A decrease in activity was observed at 48 h and returned to the level of the control at 72 h (Figure 2b).

For ascorbate peroxidase activity, it was observed that plants inoculated with the pathogen (H) did not show a significant difference with the control at the times evaluated (Figure 2c). For plants inoculated with the pathogen and treated with chitosan (QH), only a significantly different response to infected plants was observed up to 72 h after inoculation with the pathogen, with a decrease in activity (Figure 2c).

On the other hand, for superoxide dismutase activity, it was observed that plants inoculated with the pathogen (H) presented a significant decrease in activity at 48 h after pathogen inoculation, although there was an increase in activity to the level of the control at 72 h (Figure 2d). For plants inoculated with the pathogen and treated with chitosan (QH), a significantly different response to infected plants was observed; at 24 h, a significant decrease in activity was observed, which increased to the level of the control at 48 h. At 72 h, a significant decrease in activity was again observed (Figure 2d).

Regarding the activity of the polyphenol oxidase enzyme (Figure 2e), it was observed that plants inoculated with the pathogen (H) showed a significant decrease in activity at 24 h after pathogen inoculation, although there was an increase in activity at the pathogen level at 48 h and a significant increase at 72 h (Figure 2e). For plants inoculated with the pathogen and treated with chitosan (QH), a significantly differentiated response to infected plants was observed; at 12 h, a significant decrease in activity was observed, which increased to the level of the control at 24 h and was maintained at 48 h. At 72 h, a significant increase in activity was again observed at the level of the pathogen (Figure 2e). At 72 h, a significant increase in activity was again observed (Figure 2d). The chitosan-induced response in coffee plants for polyphenol oxidase activity was early and higher than that observed in infected plants (H) (Figure 2e).

Finally, the accumulation of phytoalexins was evaluated with the quantification of total phenolic compounds, which are related to the capacity of the plant to stop infection against pathogens. It was observed that plants inoculated with the pathogen (H) showed a significant decrease from 12 h after pathogen inoculation, although there was an increase in activity at the pathogen level at 24 h. A significant decrease was observed at 48 h and again an increase to the level of the control at 72 h (Figure 2f). For the plants inoculated with the pathogen and treated with chitosan (QH), there were no significant differences with the control at 12 and 24 h. It was not until 48 h that the content decreased, although to a lesser extent than in infected plants, and an increase in the level of the control was observed at 72 h (Figure 2d). The response induced by chitosan in coffee plants for the content of total phenolic compounds was greater than that observed in infected plants (H) (Figure 2f).

2.3. Quantitative Analysis of Defense-Related Gene Expression by Real-Time PCR

Normalization of the reference genes used showed the following values: GADPH: 0.1726; actin: 0.1000, 14.3.3, and 0.1219, and the actin gene was chosen as the internal control gene. Gene expression of genes encoding proteins related to plant pathogenesis and protection was also determined. In the relative expression of the β-1,3-glucanase gene (Figure 3a), it was observed that plants inoculated with the pathogen (H) presented a significant increase in expression 12 h after inoculation with the pathogen and subsequently

a significant decrease in its expression at 24 h that was maintained at 48 h. For plants inoculated with the pathogen and treated with chitosan (QH), a lower level of expression was observed than in infected plants at 12 h. However, after 24 h, a significant increase in the level of expression was observed, which decreased significantly, although in a greater proportion than the other treatments up to 48 h, and was maintained up to 48 h.

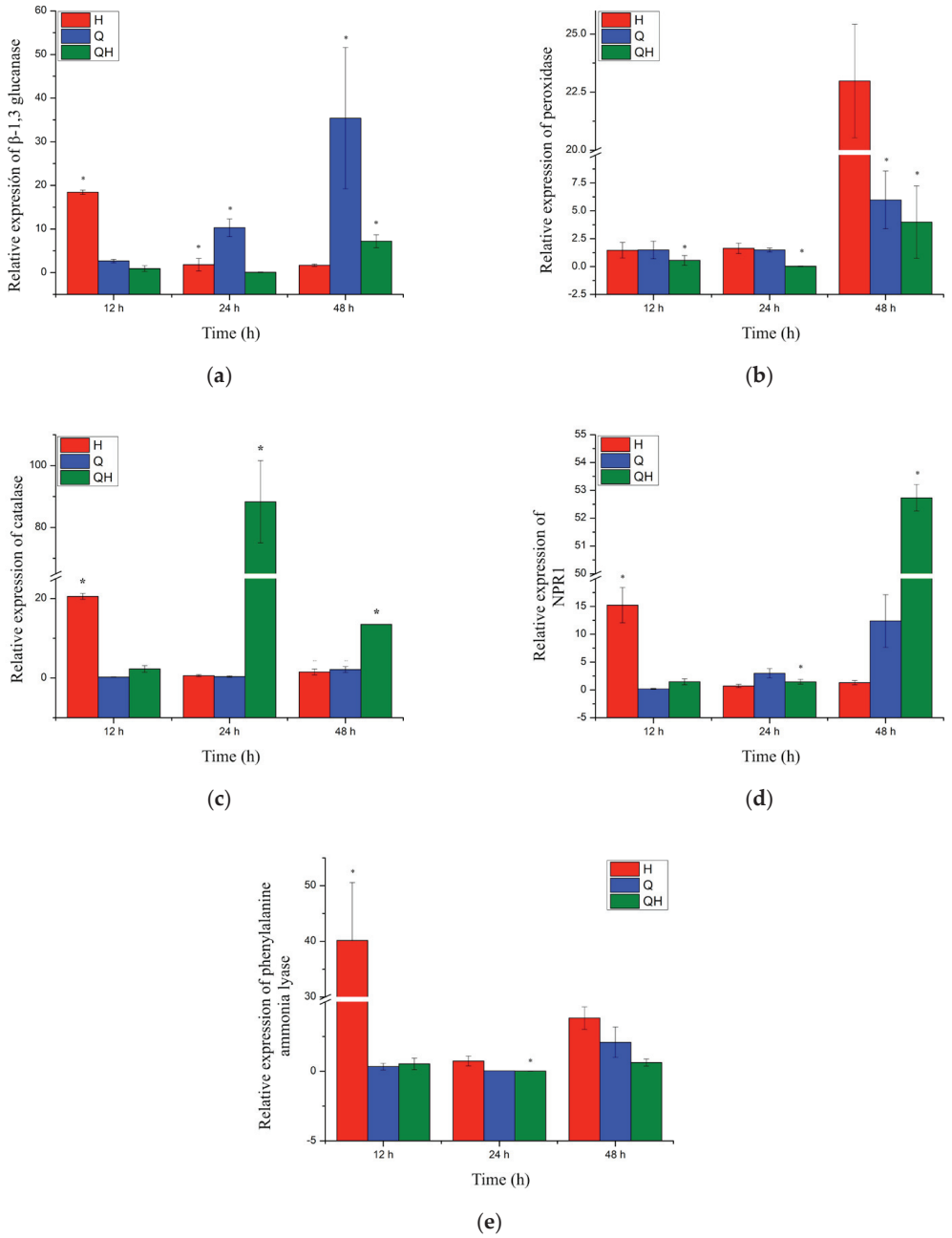

Figure 3. Relative expression of genes (**a**) *β-1,3 glucanase*, (**b**) *peroxidase*, (**c**) *catalase*, (**d**) *NPR1*, (**e**) and *phenilalanine ammonia lyase*. (H) Plants inoculated with *Hemileia vastatrix*, (Q) plants sprayed with 0.05% food chitosan, and (QH) plants sprayed with 0.05% food chitosan and inoculated with *H. vastatrix*. Values presented are means with standard deviation. Values with asterisks show statistically significant differences at the 95% LSD confidence level ($p < 0.05$). Plants without treatment were used as a baseline.

Peroxidase gene expression (Figure 3b) did not show significant differences with respect to the control at the times evaluated in plants inoculated with the pathogen (H). For plants inoculated with the pathogen and treated with chitosan (QH), a high level of

expression was observed with respect to infected plants from 12 h, although it decreased at 24 h (seven-fold) and reached the same level of expression as the control at 48 h.

Regarding catalase gene expression (Figure 3c), it was observed that plants inoculated with the pathogen (H) showed a significant increase at 12 h after pathogen inoculation. Expression levels decreased at 24 h and remained at the level of the control at 48 h. For plants inoculated with the pathogen and treated with chitosan (QH), a level of expression was observed at the level of the control at 12 h, increasing at 24 h and a higher level of expression at 48 h with respect to infected plants (Figure 3c).

Likewise, the expression coding for NPR1 was evaluated (Figure 3d), and it was observed that plants inoculated with the pathogen (H) presented a significant increase at 12 h after pathogen inoculation (15-fold). However, expression levels decreased significantly to the level of the control at 24 h and remained at this level at 48 h. For plants inoculated with the pathogen and treated with chitosan (QH), a level of expression was observed at the level of the control at 12 h, increasing at 24 h (12-fold) and a higher level of expression at 48 h (52-fold) with respect to infected plants (Figure 3d).

Finally, in the evaluation of phenylalanine ammonium lyase (PAL) expression (Figure 3e), it was observed that plants inoculated with the pathogen (H) showed a significant increase at 12 h (40-fold) after pathogen inoculation. However, expression levels decreased significantly to the level of the control at 24 h and remained at this level at 48 h. For plants inoculated with the pathogen and treated with chitosan (QH), expression levels were observed at the control level at 12 h, increasing at 24 h (4-fold) and returning to the control level at 48 h (Figure 3d).

3. Discussion

There is a great diversity of chitosans on the market, with different origins and methods of obtaining them, from conventional chemical processes for the deacetylation of chitin to enzymatic and green transformation processes. This diversity has been found to confer differentiated properties, and in the case of its effect as a plant defense inducer, it may be greater or lesser depending on its physicochemical characteristics [11] or method of obtaining [14]. However, an important point to consider is that, depending on its nature and purity, the costs of chitosan can be variable. In this work, we chose to use high-density food-grade chitosan that has a lower cost with respect to other chitosans, which could facilitate its adoption as a control product for coffee rust, with a lower impact on the cost of production. In this study, it was observed that the food-grade chitosan maintained its control effect for coffee rust and plant defense induction, equivalent to that previously described with a practical-grade chitosan, the most widely used and described.

The effectiveness of chitosan in the present study is evident by demonstrating that the amount of disease estimated in terms of severity was lower for treatments Q1 and Q5, compared to the control treatment with an amount of disease of 25, 40, and 102, respectively. In addition, a notorious vegetative development proves the protective ability of chitosan to induce the immune system of plants as an effective agent in activating plant defense [15]. Chitosan has been shown to stimulate plant growth and defense hormones, such as jasmonic acid and salicylic acid, at low concentrations [16]. In this work, it was also possible to observe the induction of cell death in leaves infected with *H. vastatrix* at the highest concentration of chitosan (Q5).

There are similar studies in *Coffea arabica*, with Soares-Leal et al. [17] using copper and silver nanoparticles. In turn, Fajardo-Franco et al. [18] used biofungicides against yellow rust and Plaza-Pérez et al. [19] applied boron, zinc, and manganese for the same purpose.

In this work, the changes related to the induction of plant defense at the biochemical and molecular level were investigated. The function of a plant defense inducer was facilitated through a phenomenon called priming, where molecules are used that act as response modifiers that can lead to a more intense, faster, earlier, or more sensitive defense response compared to plants that are exposed to the same stress condition, as mentioned by Tugizimana et al. [20].

During the induction of the effective defense response, specialized defense mechanisms are triggered that have the function of preventing the establishment of the pathogen in the plant tissue. Pathogenesis-related proteins (PRs) are overexpressed under stress conditions or following pathogen attack. These responses are controlled by two signaling pathways, jasmonic acid (JA) and salicylic acid (SA), which have specific protein groups; for JA, one can cite plant defensin, thionin, and chitinase B. For the SA pathway, it is NPR1 which is considered the central regulator of defense responses in a large number of plants and involves both systemic acquired resistance (SAR) and induced systemic resistance (ISR) [15]. Chitosan is recognized to activate the transcription of the gene encoding *NPR1*. In a study carried out by Gangireddygari et al. [21], it was found that gene expression levels by foliar application of chitosan on pepper increased, and, in turn, upregulated genes such as *PAL*, *polyphenol oxidase* (*PPO*), and *superoxide dismutase* (*SOD*), keeping infection caused by a virus (CMV) limited. These results correlate with the results obtained in this work, where an increase in the transcriptional levels of *NPR1* was observed. With the application of chitosan (HQ), higher levels of expression were observed compared to other treatments at 48 and 72 h. It is worth mentioning that the NPR1 protein is found at basal levels in the nucleus and cytoplasm [12]. Prior to pathogen infection, the SA concentration is low, and NPR1 is inactivated through disulfide bonds. However, upon infection, the SA content increases and NPR1 switches to an active state and is transferred to the nucleus to regulate gene expression [12].

On the other hand, when a fungal infection occurs in plants and when chitosan is applied, genes related to the defense response are activated, among which are the enzymes β-1,3 glucanases and chitinases of the GH19 family (classes I, II, IV, VI, and VII) [14]. A correlation was observed with the results obtained between gene expression and enzyme activity of β-1,3 glucanases, where an increase in enzyme activities was observed at 12, 48, and 72 h in plants treated with chitosan and inoculated with *H. vastatrix* (QH); this response was observed more than 100 times in comparison with infected plants (H). For the gene expression assay, it was observed that chitosan had an increase from 12 h and remained elevated until 48 h, when it reached its maximum expression. In turn, this behavior is similar to that observed by Jogaiah et al. [15], who observed that cucumber plants increased the activity of these enzymes from 6 to 48 h after being inoculated with *Erysiphe cichoracearuma*. Additionally, Liu et al. [22] reported that chitosan induced *glucanase* gene expression in potatoes against *Alternaria tenuissima* and maintained their high levels compared to their controls. It is worth mentioning that β-1,3 glucanases are considered the best characterized pathogenesis-related proteins, which could directly hydrolyze the cell walls of phytopathogenic fungi, thus releasing β-1,3 glucan compounds and chitin oligosaccharides that stimulate host defense responses [23]. Therefore, it was suggested that the induction of this enzyme activity had an effect during the invasion of the pathogen in coffee plants since an increase in the activity of these enzymes and a decrease in the severity of the infection were observed, which would indicate that the enzymes were able to hydrolyze cellular parts of the pathogen [24].

During the pathogenesis process of different fungi, the production and accumulation of molecules that have different functions in the response process of the plant to the pathogen attack are triggered. Among these molecules, ROS have different functions in the plant defense response process, and they can act as second messengers that generate a response locally, including cell wall strengthening, protein cross-linking, and the hypersensitive response (HR), which can include the induction of programmed cell death (PCD) [25]. However, these molecules can also damage proteins and lipids and cause alterations in host DNA, necessitating the induction of enzymatic and non-enzymatic control mechanisms to prevent this damage [26]. Within all this cellular machinery are peroxidases which are enzymes that play a role in a wide range of physiological and developmental processes; they are involved in the generation and detoxification of hydrogen peroxide (H_2O_2), being antioxidants, and they are an important initial defense adapted by plants to cope with the effects of biotic and abiotic stresses [27]. The variation in the level of peroxidase activity is

related to the type of elicitor, as not all resistance inducers increase the level of peroxidases compared to other levels of protection. It was reported by Fischer [28] that in some cases, peroxidase activity levels remained low or null, a behavior like that obtained in this study, where it was observed that *peroxidase* gene expression levels initially remained high during the first days of infection by the pathogen. However, both expression levels and enzyme activity decreased as time progressed (Figures 2c and 3b). A similar behavior was obtained in the study by Luján-Hidalgo et al. [29] in coffee, where peroxidase activity decreased after infection, which was associated with a beneficial response to avoid infection and was related to its responsibility in reinforcing the cell wall of the plant. In the study by Varghese et al. [30], they observed the same trend in ginger, where chitosan did not present an increase in peroxidase activity; however, the accumulation of lignin, one of the polymers associated with cell wall strengthening, was observed.

In addition, there are specific peroxidases that face pathogen invasion and can be induced by chitosan, including SOD, which is the first enzyme in the ROS detoxification process, reacting with O_2^{-2} superoxide radicals to produce H_2O_2 [31]. In this work, this group of enzymes had similar kinetics to peroxidases; they remained stable during the first evaluation times, and at 72 h, there was a decrease in activity (Figure 2d). In the same sense, APX, which catalyzes the reaction to convert H_2O_2 into H_2O and O_2, showed a similar response, although at 12 h, it had high activity, which decreased as time passed. For CAT, a tetrameric enzyme for ROS detoxification that converts H_2O_2 to H_2O and is the first enzyme to act in the presence of oxidative stress [31], the results showed increased gene expression throughout the times evaluated. These results agree with those reported by López-Velázquez et al. [14], where CAT activity increased with the application of chitosan, and SOD remained without significant changes. The study conducted by Zhang et al. [32] reported that chitosan had an important effect on the activation of the antioxidant system of plants since enzyme activity was favored, suggesting that chitosan regulates in favor of the plant defense system and its metabolic activation for metabolite synthesis.

However, the decrease in peroxidase activity may be related to redirection to other defense mechanisms, e.g., the induction of PCD and oxidative burst, and effective defense mechanisms against biotrophic pathogens such as coffee rust [25]. Biotrophic fungi, as part of their basic pathogenesis mechanisms, present fungal effectors that inhibit PCD induction, including inducers of antioxidant mechanisms aimed at cutting the role as signal molecules of ROS and defensive processes associated with their proliferation [33]. Although not explored in this work, it raises the prospect for future work to explore the role of cell wall strengthening, PCD induction, and ROS accumulation in resistance to rust infection in the coffee plant.

On the other hand, phenolic compounds contribute to maintaining overall plant health by regulating a wide range of functions, such as protection against pathogens, chelation of heavy metals, and prevention against oxidative stress. They provide mechanical strength to the cell, forming lignin and suberin, two important constituents of the cell wall [34]. In this study, the content of phenolic compounds had a better effect compared to plants infected with *H. vastatrix* (H), which, unlike the other treatments evaluated, decreased. In the work carried out by Guo et al. [35], it was observed that chitosan induced the accumulation of total phenolic compounds; however, the content of these compounds was lower compared to the control, as in this case. Peian et al. [35] reported an increase in the content of total phenolic compounds in strawberry and grape berries that were treated with chitosan when exposed to *Botrytis cinerea*.

Phenolic compounds are generated from the shikimic acid pathway and are precursors of phenylpropanoids through the activity of the PAL enzyme, where phenylalanine undergoes deamination and becomes a precursor of flavonoids, lignin, and other defense compounds [36]. In this work, *PAL* gene expression was monitored with respect to infected plants (H); the expression increased 5-fold at 12 h and almost 45-fold at 24 h, reaching its maximum expression at 48 h, which was related to what was observed in the content of total phenolic compounds. Comparing the results with Godana et al. [36], PAL activity

was favored at 2 days when the grapes were treated with chitosan and inoculated with *Pichia anomala*, after which the activity decreased, suggesting that there would be a production of total phenolic compounds. Another important aspect is the relationship with polyphenol oxidase activity, which is an enzyme that catalyzes the oxidation of phenolic compounds into highly reactive quinones, which help plants defend themselves against pathogens [22]. The results showed that enzyme activity was favored with chitosan application (QH) compared to infected plants (H), and a directly proportional relationship was found with the accumulation of total phenolic compounds. Chitosan also plays a fundamental role in the induction of enzymatic activity, as observed in the work of Liu et al. [22], where it increased the levels of this activity in potatoes. In addition, it also plays a role in the thickening of the plant cell wall, which serves as a physical barrier to prevent colonization by pathogens [28]. A similar effect was found in the study by Ahmad et al. [37], where PPO activity was induced by chitosan and was associated with a beneficial response in the control of citrus diseases, and the amount of total phenolic compounds was increased.

In this study, it was observed that food-grade chitosan was able to induce effective protection against *H. vastatrix* infection in coffee of an intensity equivalent to that of practical-grade chitosan. Chitosan was able to induce a differentiated defense response with respect to rust-infected plants. It significantly increased the activity of β-1,3 glucanases. Antioxidant enzyme activity was also different from that observed in rust-infected coffee plants. However, it was observed that most of them presented lower activity than that observed in infected plants, which could be related to the role acquired by ROS in triggering an effective defense response against coffee rust or by directing these molecules to the strengthening of the cell wall. It was able to induce the production and accumulation of phytoalexins by inducing the expression of *PAL* and *PPO* genes and the content of total phenolic compounds. However, the nature of these compounds and their role in the effective defense mechanism against rust remains to be defined. Finally, chitosan was able to induce *NPR1* gene expression, indicating its role in the SA signaling pathway and in the dissemination of an effective systemic defense response. From these results, a better understanding of the effective defense mechanisms induced by chitosan in the protection against *H. vastatrix* infection in coffee plants was obtained. It is important to consider the evaluation of the role of chitosan in cell wall strengthening, PCD induction, and ROS accumulation in resistance to rust infection in coffee plants.

4. Materials and Methods

4.1. Plant Material

Coffee fruits (*Coffea arabica* var. Typica) were collected in the locality of Tlajomulco de Zúñiga, Jalisco, Mexico. The fruits were pulped, and the seeds were recovered. The seeds were washed with water and disinfected with 3% (*v*/*v*) sodium hypochlorite for 20 min. They were then placed in a drying oven (Drying, DH6-9145A, Xi'an, China) at 30 °C ± 2 °C for 48 h. Subsequently, seeds were germinated in a mixture of peat moss with vermiculite (5:2) in germination trays, which were placed in an incubation room at 26 °C ± 2 °C, with a photoperiod of 16 h light/8 h dark. Plants were fertilized every week with macro- and micronutrients and were used for experiments at the age of 6 months [38].

4.2. Biological Material

Uredinospores of the phytopathogenic fungus *H. vastatrix* were collected from plants with rust symptoms in the municipality of Ejutla, Jalisco, Mexico. The spores were recovered and resuspended in distilled water with 0.05% (*v*/*v*) tween 20 (Sigma-Aldrich, Poole, UK). The solution was adjusted to a concentration of 1×10^5 uredinospores/mL and sprayed on the underside of the leaves. The plants were watered, covered with a polyethylene bag, and kept in darkness for 72 h in an incubation room at 26 °C ± 2 °C [39]. After 72 h, the plants were kept in a 16/8 light/dark photoperiod at 26 °C ± 2 °C.

4.3. High-Density Chitosan Solution

A 1% (*w*/*v*) solution of high-density food-grade chitosan (America Alimentos, Guadalajara, Jalisco, Mexico) was prepared. The chitosan was dissolved in a 0.4 M acetic acid solution (Fermont, Guadalajara, Jalisco, Mexico) with 2 M sodium acetate (Sigma-Aldrich, St. Louis, MO, USA). Finally, a 0.01% and 0.05% dilution of chitosan was performed with distilled water.

4.4. Biological Effectiveness Test with Food-Grade Chitosan

The plants were distributed in four treatments with ten plants each: control plants treated with distilled water (C), plants inoculated with *H. vastatrix* (H), plants treated with 0.01% food-grade chitosan and inoculated with the pathogen (Q1), and plants treated with 0.05% food grade chitosan and inoculated with the pathogen (Q5). Treatments C and H were sprayed with an atomizer with 3 mL of distilled water, and treatments Q1 and Q5 with 3 mL of food-grade chitosan on all leaves. Seven days after water and chitosan application, plants were inoculated with 3 mL of *H. vastatrix* urediniospore suspension. The plants were kept in an incubation room at 26 °C ± 2 °C and were monitored for 90 days (40, 60, and 90 days after inoculation) to observe the development of the disease, taking as a reference Technical Data Sheet 40, Coffee Rust, SENASICA [40]. The experiment was carried out in December 2021 and March 2022.

4.4.1. Disease Incidence

The plants were observed at 40, 60, and 90 days after inoculation, and disease incidence was calculated according to Equation (1). Each treatment had 10 plants [41].

$$\text{Disease incidence } (\%) = \frac{NIP}{TIP}\,(100), \tag{1}$$

where *NIP* corresponds to the number of infected plants, and *TIP* corresponds to the total number of infected plants assessed.

4.4.2. Area under the Disease Progress Curve (AUDPC)

Data were collected on the severity of infection at 40, 60, and 90 days after inoculation, and the area under the disease progress curve was determined according to Equation (2) [42].

$$\text{AUDPC} = \sum_{i=1}^{n}\left[\frac{y_i + y_{i+1}}{2}\right](x_i - x_{i-1}) \tag{2}$$

where AUDPC is the area under disease progress curve, y_i is the percentage of visible infectes area (y_i/100) at the *i*-th observation, x_i—day of the *i*-th observation, and *n* the total number of observations.

4.4.3. Observation of the Presence of Pathogen in the Plant Tissue

Leaf samples were taken 90 days after inoculation with the pathogen. Leaves were washed with distilled water to remove particles prior to staining and placed in 50 mL conical tubes. The samples were bleached with 1.7 M KOH at 50 °C for 30 min. Subsequently, they were washed with sterile distilled water twice and 0.5 M hydrogen peroxide at 50 °C for 15 min. Finally, they were stained with 0. 05% (*w*/*v*) in lactoglycerol (lactic acid: glycerol: water; 1:1:1:1, *v*/*v*) at 50 °C for 30 min. Excess dye was removed with lactoglycerol and observed under an optical microscope (Olympus model BH-2, Tokyo, Japan) [43].

4.5. Enzymatic Activity Evaluation Related to the Pathogenesis and Accumulation of Phytoalexins

Leaves were sampled before inoculation (0 h) and 12, 24, 48, and 72 h after inoculation with the pathogen. Leaves were frozen in liquid nitrogen and stored at −80 °C until processing. In total, 200 mg of fresh tissue was weighed and macerated in liquid nitrogen in a mortar with 1% polyvinylpyrrolidone. For the determination of enzymes with

superoxide dismutase and ascorbate peroxidase activity, the pulverized tissue was mixed with potassium phosphate buffer pH 7.8, 0.1 mM EDTA, and 10 mM ascorbic acid, and then centrifuged at 13,000× *g* for 25 min at 4 °C. For the determination of β-1,3 glucanase, peroxidase, and polyphenol oxidase activity, the tissue was resuspended in potassium phosphate buffer pH 7.0 and 0.1 mM EDTA, then centrifuged at 13,000× *g* for 25 min at 4 °C [8]. To determine phytoalexins, 0.1 g of tissue was resuspended in 500 µL of 80% methanol [11]. On each sampling day, 3 plants were taken for the corresponding evaluation, and each test was performed in triplicate. For all assays, 200 uL of sample were used and read in a 96-well microplate.

4.5.1. β-1,3 Glucanase Activity

β-1,3 glucanase activity was determined with the colorimetric method for the detection of reducing sugars DNS (3,5-Dinitrosalicylic acid), quantification was determined with a calibration curve with glucose, and activity was reported in nkat per g of total protein (nkat·g^{-1}·g^{-1} PT) [11]. The read was carried out in a spectrophotometer (Thermo Fisher Scientific, Multiskan Go FI-01620, Vantaa, Finland).

4.5.2. Peroxidase Activity

Perioxidase activity determination was carried out with the guaiacol oxidation method. The variation of one absorbance unit per minute was defined as one unit of peroxidase activity (1 AU) and was expressed per gram of total protein (UA·g^{-1} PT) [11]. The read was carried out in a spectrophotometer (Thermo Fisher Scientific, Multiskan Go FI-01620, Vantaa, Finland).

4.5.3. Superoxide Dismutase Activity

Superoxide dismutase activity was evaluated by the ability of the SOD enzyme to inhibit the photoreduction of nitro blue tetrazolium (NBT) prepared in an incubation medium composed of 50 mM potassium phosphate, pH 7.8, 14 mM methionine, 0.1 µM EDTA, 75 µM NBT, 2 µM riboflavin, and plant extract, then incubated for 7 min with a 30 W fluorescent lamp and read at 560 nm in a spectrophotometer (Thermo Fisher Scientific, Multiskan Go FI-01620, Vantaa, Finland). One unit of SOD is considered the amount of enzyme capable of being inhibited by 50% NBT photoreduction under assay conditions. The units were reported in U^{-1}·min^{-1}·mg^{-1}·TP [8].

4.5.4. Ascorbate Peroxidase Activity

Twenty µL of the plant extract were added to 200 µL of 100 mM potassium phosphate solution at pH 7.0, 0.5 mM ascorbic acid, 0.1 mM hydrogen peroxide, and water. The activity was determined by consuming H_2O_2 at 290 nm for 1 min at 25 °C in a spectrophotometer (Thermo Fisher Scientific, Multiskan Go FI-01620, Vantaa, Finland). The molar extinction coefficient of 1.4 mM·cm^{-1} was used to calculate APX activity, and the units were reported in μM^{-1}·min^{-1}·mg^{-1}·TP [8].

4.5.5. Polyphenol Oxidase Activity

Twenty µL of the plant extract were added to 200 µL of 70 mM potassium phosphate solution at pH 7.0 and 20 mM catechol. Then, it was incubated at 30 °C for 10 min. Absorbance was measured at 410 nm in a spectrophotometer (Thermo Fisher Scientific, Multiskan Go FI-01620, Vantaa, Finland). The molar extinction coefficient of 1.235 mM·cm^{-1} was used to calculate the PPO activity, and the units were reported in mM^{-1}·min^{-1}·mg^{-1}·TP [8].

4.5.6. Protein Quantification

Protein quantification was performed using the Bradford method described by Kruger [44], using bovine albumin for the calibration curve. The read was carried out in a spectrophotometer (Thermo Fisher Scientific, Multiskan Go FI-01620, Vantaa, Finland).

4.5.7. Phytoalexin Accumulation

Phytoalexin accumulation was performed by quantification of total phenolic compounds by Folin–Ciocalteu's method and a catechol curve was used at known concentrations. The accumulation of phenolic compounds was reported in nM catecol·mg^{-1} FW [11]. The read was carried out in a spectrophotometer (Thermo Fisher Scientific, Multiskan Go FI-01620, Vantaa, Finland).

4.6. Quantitative Analysis of Defense-Related Gene Expression by Real-Time PCR

The plants were distributed in four treatments: control plants treated with distilled water (C), plants inoculated with *H. vastatrix* (H), plants treated with 0.05% high-density chitosan (Q), and plants treated with 0.05% high-density chitosan and inoculated with the pathogen (QH). Three mL of distilled water were sprayed in treatments C and H, and 3 mL of high-density chitosan in treatments Q and QH. Seven days after the application of water or chitosan, 3 mL were inoculated with the suspension of urediniospores of *H. vastatrix*. Plants were kept in an incubation room at 26 °C ± 2 °C, and leaf samples were taken at 12, 24, and 48 h after inoculation with the pathogen [9]. On each sampling day, 3 plants were taken for the corresponding evaluation, and each test was performed in duplicate.

4.6.1. Primers Design

Primers coding for the genes *peroxidase* (*POX*), *catalase* (*CAT*), *ß-1,3-glucanase* (*GLU*), and *phenylalanine ammonia lyase* (*PAL*) were designed. The genomic sequences were obtained from the Phytozome repository. Subsequently, the OligoAnalyzer Tool from IDT and Primer-BLAST from NCBI were used. Additionally, *glyceraldehyde-3-phosphate dehydrogenase* (*GADPH*), *actin 8*, and *14-3-3* primers were designed as constitutive controls. Table 2 shows the characteristics of each pair of oligonucleotides. The stability of the primers was determined according to the method of Vandesompele et al. [45].

Table 2. Oligonucleotides.

Genes	Oligonucleotide Sequences (5′-3′)	Size (pb)	Accession Number
Peroxidase (POX)	FW: GTGGATGCGGAGTACCTGAA RV: AACCGTTTGGACCTCCAGTT	153	evm.TU.Scaffold_618.242
Catalase (CAT)	FW: GATGCACCCAATTCCTTCTGC RV: CCCAGCGACAGATAAAGCG	140	evm.TU.Scaffold_2256.195
ß-1,3 glucanase	FW: GGGTGACCCTACAAAAGCCA RV: GGCCTGGAGGAAAGGTTCAT	121	evm.TU.Scaffold_517.1
Phenylalanine ammonia lyase (PAL)	FW: CTTGTGAGGGGAGAGTTGGG RV: GGTAGGTGGCTCTTGTCAGC	112	evm.TU.Scaffold_618.1114
NPR1	FW: TTGGTTATGAGGCTGCTGCT RV: GGCTTTAGATGCTGCAAGGC	138	evm.model.Scaffold_523.152
GAPDH	FW: CCCTTGGGGTGAAACTGGAG RV: AACATGGGTGCATCCTTGCT	138	evm.model.Scaffold_608.230
Actin 8	FW: ATTAGCTCGACAAGACGCCC RV: CTCACGTTCCATGTGTTGCG	142	evm.model.Scaffold_315.601
14-3-3	FW: GCTGAGTTCAAAACTGGGGCTG RV: ATTGGGTGTGTTGGAGCCAG	110	evm.model.Scaffold_2421.275

4.6.2. RNA Extraction and cDNA Synthesis

The TRIzol extraction protocol (Invitrogen, Carlsbad, CA, USA) was used with some modifications) [46]. In total, 200 mg of sample were macerated with liquid nitrogen, and 1 mL of TRIzol was added for 5 min. The samples were centrifuged at 11,000× *g* for 15 min at 4 °C, the supernatant was removed, and 500 µL chloroform (Sigma-Aldrich, Dorset, UK) were added, shaken for 20 min at −20 °C, then centrifuged at 11,000× *g* for 15 min at 4 °C. the supernatant was removed, 500 µL chloroform (Sigma-Aldrich, Dorset, UK). Subsequently, the supernatant was recovered, and 500 µL of isopropanol (Sigma-Aldrich, Dorset, UK) were added, left to stand for 2 h at −80 °C, and centrifuged at 11,000× *g* for 15 min at 4 °C, after which the supernatant was removed. Three washes were performed with 75% ethanol (Sigma-Aldrich, St. Louis, MO, USA), and the pel-

let was dried and resuspended in 20 µL of RNAse-free water. RNA was quantified at 260 nm and migrated on 0.8% agarose gel. For cDNA synthesis, the Maxima H Minus First Strand cDNA Synthesis kit (Thermo Fisher Scientific Baltics UAB, Vilnius, Lithuania) was used. Synthesis was performed according to the manufacturer's instructions, starting from 100 ng of total RNA.

4.6.3. RT qPCR

RT qPCR analyses were performed on a Step-One Real-Time PCR System thermal cycler (Applied Biosystems, Life Technologies, San Francisco, CA, USA) using SYBR Green as the detection system. The reaction conditions were 2 min at 50 °C, 10 min at 60 °C, followed by 40 cycles of 15 s at 95 °C, and 1 min at 60 °C, ending the cycle with 15 s at 95 °C. The reaction was carried out with 50 ng of cDNA, 0.2 µL of each primer, and 7.5 µL of SYBR green PCR Master Mix (Invitrogen, St. Louis, MO, USA) and RNAse-free water. For the evaluation of each gene, three biological samples with two technical replicates were performed. Relative quantification (RQ) was performed using the ddCT method [47].

$$\text{RQ} = 2^{-\text{ddCT}};\ \text{ddCT} = [(\text{CT gene of interest} - \text{CT constitutive gene})\ \text{treated plant} - (\text{CT gene of interest} - \text{CT constitutive gene})\ \text{untreated control plant}]. \quad (3)$$

4.7. Statistical Analysis

One-way analysis of variance (ANOVA) was performed using Minitab 19.2020.2.0 software, followed by a separation of means through the LSD test, with a significance level of 95%.

5. Conclusions

The application of 0.05% high-density food-grade chitosan significantly reduced the severity of *H. vastatrix* infection by increasing the activity and gene expression of *β-1,3 glucanases*. In addition, a differentiated response was found in enzymes related to the antioxidant system of plants. Additionally, a correlation was observed between the activities of the enzyme polyphenol oxidase and the production of total phenolic compounds that allowed an effective defense response in coffee plants.

Author Contributions: Conceptualization, J.C.L.-V., J.A.Q.-Z. and S.G.-M.; Methodology, J.A.Q.-Z., J.C.L.-V. and S.G.-M.; Software, G.P.L.-S., J.C.L.-V. and S.G.-M.; Validation, J.A.Q.-Z. and S.G.-M.; Formal analysis, J.A.Q.-Z. and S.G.-M.; Investigation, J.C.L.-V., G.P.L.-S. and J.A.Q.-Z.; Resources, J.A.Q.-Z.; Data curation, J.A.Q.-Z., J.C.L.-V. and S.G.-M.; Writing—original draft preparation, J.C.L.-V. and J.A.Q.-Z.; Writing—review and editing, J.A.Q.-Z., S.G.-M., M.I.M.-C. and A.U.-V.; Visualization, A.U.-V. and M.I.M.-C.; Supervision, J.A.Q.-Z.; Project administration, J.A.Q.-Z.; Funding acquisition, J.A.Q.-Z. All authors have read and agreed to the published version of the manuscript.

Funding: This research was supported by the project "Estrategias multidisciplinarias para incrementar el valor agregado de las cadenas productivas de café, frijol, mango, agave mezcalero y productos acuícolas (tilapia) en la región pacífico sur a través de la ciencia, tecnología e innovación" grant number FORDECYT 292474.

Institutional Review Board Statement: Not applicable.

Informed Consent Statement: Not applicable.

Data Availability Statement: The data presented in this study are available on request from the corresponding author.

Acknowledgments: The first author is grateful to the Consejo Nacional de Humanidades, Ciencias y Tecnologías, for grant 783189 for a scholarship for a Ph.D. in Biotechnological Innovation. We also thank Onofre Jiménez Contreras for the facilities for the collection of coffee berries and Jorge González Zárate for the facilities for the collection of *H. vastatrix*.

Conflicts of Interest: The authors declare no conflict of interest.

References

1. King, H. Trading the Soft Commodity Markets, Investopedia. Available online: https://www.investopedia.com/articles/optioninvestor/07/soft_market.asp (accessed on 19 May 2023).
2. ASERCA. Panorama Agropecuario Semanal de Café. Available online: https://info.aserca.gob.mx/panorama/semanal.asp?de=cafe (accessed on 19 May 2023).
3. Salcedo-Sarmiento, S.; Aucique-Pérez, C.E.; Silveira, P.R.; Colmán, A.A.; Silva, A.L.; Corrêa-Mansur, P.S.; Rodrigues, F.A.; Evans, H.C.; Barreto, R.W. Elucidating the interactions between the rust *Hemileia vastatrix* and a *Calonectria mycoparasite* and the coffee plant. *iScience* **2021**, *24*, 102352. [CrossRef] [PubMed]
4. Gichuru, E.; Alwora, G.; Gimase, J.; Kathurima, C. Coffee Leaf Rust (*Hemileia vastatrix*) in Kenya—A Review. *Agronomy* **2021**, *11*, 2590. [CrossRef]
5. Barka, G.D.; Caixeta, E.T.; Ferreira, S.S.; Zambolim, L. In silico guided structural and functional analysis of genes with potential involvement in resistance to coffee leaf rust: A functional marker based approach. *PLoS ONE* **2020**, *15*, e0222747. [CrossRef] [PubMed]
6. Zheng, F.; Chen, L.; Zhang, P.; Zhou, J.; Lu, X.; Tian, W. Carbohydrate polymers exhibit great potential as effective elicitors in organic agriculture: A review. *Carbohydr. Polym.* **2020**, *230*, 115637. [CrossRef] [PubMed]
7. Gorni, P.H.; Pacheco, A.C.; Lima-Moro, A.; Silva, J.F.A.; Moreli, R.R.; de Miranda, G.R.; Pelegrini, J.M.; Zaniboni, C.; Spera, K.D.; Junior, J.L.B.; et al. Elicitation Improves the Leaf Area, Enzymatic Activities, Antioxidant Activity and Content of Secondary Metabolites in *Achillea millefolium* L. Grown in the Field. *J. Plant Growth Regul.* **2021**, *40*, 1652–1666. [CrossRef]
8. Andrade-Monteiro, A.C.; Vilela-de Resende, M.L.; Teixeira-Valente, T.C.; Ribeiro-Junior, P.M.; Foresti-Pereira, V.; Rodrigues-da Costa, J.; Gourlat-da Silva, J.A. Manganese Phosphite in Coffee Defence against *Hemileia vastatrix*, the Coffee Rust Fungus: Biochemical and Molecular Analyses. *J. Phytopathol.* **2016**, *164*, 1043–1053. [CrossRef]
9. Budzinki, I.G.F.; Camargo, P.O.; Lemos, S.M.C.; Guyot, R.; Calzado, N.F.; Ivamoto-Suzuki, S.T.; Domingues, D.S. Transcriptomic alterations in roots of two contrasting *Coffea arabica* cultivars after hexanoic acid priming. *Front. Genet.* **2022**, *13*, 925811. [CrossRef]
10. Pereira-Silva, P.D.F.; Vilela-De Resende, M.L.; Reichel, T.; De Lima-Santos, M.; Dos Santos-Botelho, D.M.; Batista-Ferreira, E.; Chagas-Freitas, N. Potassium Phosphite Activates Components Associated with Constitutive Defense Responses in *Coffea arabica* Cultivars. *Mol. Biotechnol.* **2023**, *65*, 1777–1795. [CrossRef]
11. López-Velázquez, J.C.; Haro-González, J.N.; García-Morales, S.; Espinosa-Andrews, H.; Navarro-López, D.E.; Montero-Cortés, M.I.; Qui-Zapata, J.A. Evaluation of the Physicochemical Properties of Chitosans in Inducing the Defense Response of *Coffea arabica* against the Fungus *Hemileia vastatrix*. *Polymers* **2021**, *13*, 1940. [CrossRef]
12. Zheng, K.; Lu, J.; Li, J.; Yu, Y.; Zhang, J.; He, Z.; Ismail, O.M.; Wu, J.; Xie, X.; Li, X.; et al. Efficiency of chitosan application against *Phytophthora infestans* and the activation of defence mechanisms in potato. *Int. J. Biol. Macromol.* **2021**, *182*, 1670–1680. [CrossRef]
13. Sofi, K.G.; Metzger, C.; Riemann, M.; Nick, P. Chitosan triggers actin remodelling and activation of defence genes that is repressed by calcium influx in grapevine cells. *Plant Sci.* **2023**, *326*, 111527. [CrossRef] [PubMed]
14. López-Velázquez, J.C.; García-Morales, S.; Espinosa-Andrews, H.; Montero-Cortés, M.I.; Qui-Zapata, J.A. Control de la roya del café utilizando moléculas de quitosanos de diferentes orígenes. In Proceedings of the XLIII Encuentro Nacional de la AMIDIQ, Puerto Vallarta, México, 23–26 August 2022.
15. Jogaiah, S.; Satapute, P.; De Britto, S.; Konappa, N.; Udayashankar, A.C. Exogenous priming of chitosan induces upregulation of phytohormones and resistance against cucumber powdery mildew disease is correlated with localized biosynthesis of defense enzymes. *Int. J. Biol. Macromol.* **2020**, *162*, 1825–1838. [CrossRef] [PubMed]
16. Suarez-Fernandez, M.; Marhuenda-Egea, F.C.; Lopez-Moya, F.; Arnao, M.B.; Cabrera-Escribano, F.; Nueda, M.J.; Gunsé, B.; Lopez-Llorca, L.V. Chitosan Induces Plant Hormones and Defenses in Tomato Root Exudates. *Front. Plant Sci.* **2020**, *11*, 572087. [CrossRef] [PubMed]
17. Soares-Leal, F.D.; Santos-Neto, H.; Lopes-Pinheiro, I.C.; Marques-Oliveira, J.; Alexandre-Pozza, A.A.; Ampélio-Pozza, E. Copper and silver nanoparticles control coffee rust: Decrease the quantity of sprayed active ingredients and is an alternative for sustainable coffee production. *Eur. J. Plant Pathol.* **2023**, *1*, 1–13. [CrossRef]
18. Fajardo-Franco, M.L.; Aguilar-Tlatelpa, M.; Guzmán-Plazola, R.A. Biofungicides evaluation in two coffee cultivars for *Hemileia vastatrix* control. *RMF* **2020**, *38*, 293–306. [CrossRef]
19. Plaza-Pérez, C.D.; Ampélio-Pozza, E.; Alexandre-Pozza, A.A.; Elmer, W.H.; Bastos-Pereira, A.; Gomes-Guimarães, D.D.S.; Andrade-Monteiro, A.C.; Vilela-De Resende, M.L. Boron, zinc and manganese suppress rust on coffee plants grown in a nutrient solution. *Eur. J. Plant Pathol.* **2020**, *156*, 727–738. [CrossRef]
20. Tugizimana, F.; Mhlongo, M.I.; Piater, L.A.; Dubery, I.A. Metabolomics in Plant Priming Research: The Way Forward? *Int. J. Mol. Sci.* **2018**, *19*, 1759. [CrossRef]
21. Gangireddygari, V.S.R.; Chung, B.N.; Cho, I.S.; Yoon, J.Y. Inhibitory Effect of Chitosan and Phosphate Cross-linked Chitosan against Cucumber Mosaic Virus and Pepper Mild Mottle Virus. *Plant Pathol. J.* **2021**, *37*, 632–640. [CrossRef]
22. Liu, J.; Zhang, X.; Kennedy, J.F.; Jiang, M.; Cai, Q.; Wu, X. Chitosan induces resistance to tuber rot in stored potato caused by *Alternaria tenuissima*. *Int. J. Biol. Macromol.* **2019**, *140*, 851–857. [CrossRef]
23. Liu, Y.; Wisniewski, M.; Kennedy, J.F.; Jiang, Y.; Tang, J.; Liu, J. Chitosan and oligochitosan enhance ginger (*Zingiber officinale Roscoe*) resistance to rhizome rot caused by *Fusarium oxysporum* in storage. *Carbohydr. Polym.* **2016**, *151*, 474–479. [CrossRef]

24. Samarah, N.H.; AL-Quraan, N.A.; Massad, R.S.; Welbaum, G.E. Treatment of bell pepper (*Capsicum annuum* L.) seeds with chitosan increases chitinase and glucanase activities and enhances emergence in a standard cold test. *Sci. Hortic.* **2020**, *269*, 109393. [CrossRef]
25. Khan, M.; Ali, S.; Al Azzawi, T.N.I.; Saqib, S.; Ullah, F.; Ayaz, A.; Zaman, W. The Key Roles of ROS and RNS as a Signaling Molecule in Plant–Microbe Interactions. *Antioxidants* **2023**, *12*, 268. [CrossRef]
26. Al-Mokadem, A.Z.; Alnaggar, A.E.A.M.; Mancy, A.G.; Sofy, A.R.; Sofy, M.R.; Mohamed, A.K.S.H.; Abou Ghazala, M.M.A.; El-Zabalawy, K.M.; Salem, N.F.G.; Elnosary, M.E.; et al. Foliar Application of Chitosan and Phosphorus Alleviate the Potato virus Y-Induced Resistance by Modulation of the Reactive Oxygen Species, Antioxidant Defense System Activity and Gene Expression in Potato. *Agronomy* **2022**, *12*, 3064. [CrossRef]
27. Kidwai, M.; Ahmad, I.Z.; Chakrabarty, D. Class III peroxidase: An indispensable enzyme for biotic/abiotic stress tolerance and a potent candidate for crop improvement. *Plant Cell Rep.* **2020**, *39*, 1381–1393. [CrossRef]
28. Fischer, I.H.; Morales, J.V.P.; da Silva, L.M.; de Almeida Bertani, R.M.; Deus, A.C.F.; Pascholati, S.F. Activity of Phosphites and Chitosan on Biochemical Responses and Target Spot Control in Cucumber Plants. *Gesunde Pflanz.* **2023**, *75*, 825–835. [CrossRef]
29. Luján-Hidalgo, M.C.; Jiménez-Aguilar, L.A.; Ruiz-Lau, N.; Reyes-Zambrano, S.J.; Gutiérrez-Miceli, F.A. Cambios bioquímicos en respuesta al ataque de roya en plantaciones de café. *Polibotánica* **2020**, *49*, 149–160. [CrossRef]
30. Varghese, L.; Thomas, G. Chitosan triggers tolerance to *Pythium myriotylum* infection in ginger (*Zingiber officinale*) by modulating multiple defense signaling pathways. *Physiol. Mol. Plant Pathol.* **2023**, *125*, 101983. [CrossRef]
31. Hasanuzzaman, M.; Bhuyan, M.H.M.; Zulfiqar, F.; Raza, A.; Mohsin, S.; Mahmud, J.A.; Fujita, M.; Fotopoulos, V. Reactive Oxygen Species and Antioxidant Defense in Plants under Abiotic Stress: Revisiting the Crucial Role of a Universal Defense Regulator. *Antioxidants* **2020**, *9*, 681. [CrossRef] [PubMed]
32. Zhang, Z.; Zhao, P.; Zhang, P.; Su, L.; Jia, H.; Wei, X.; Fang, J.; Jia, H. Integrative transcriptomics and metabolomics data exploring the effect of chitosan on postharvest grape resistance to *Botrytis cinerea*. *Postharvest Biol. Technol.* **2020**, *167*, 111248. [CrossRef]
33. Mapuranga, J.; Zhang, N.; Zhang, L.; Chang, J.; Yang, W. Infection Strategies and Pathogenicity of Biotrophic Plant Fungal Pathogens. *Front. Microbiol.* **2022**, *13*, 799396. [CrossRef]
34. Guo, Y.; Zhou, J.; Zhang, J.; Zhang, S. Chitosan combined with sodium silicate treatment induces resistance against rot caused by *Alternaria alternata* in postharvest jujube fruit. *J. Phytopathol.* **2019**, *167*, 451–460. [CrossRef]
35. Zhang, P.; Jia, H.; Gong, P.; Ehsan, S.; Pang, Q.; Dong, T.; Li, T.; Jin, H.; Fang, J. Chitosan induces jasmonic acid production leading to resistance of ripened fruit against *Botrytis cinerea* infection. *Food Chem.* **2021**, *337*, 127772. [CrossRef]
36. Godana, E.A.; Yang, Q.; Zhao, L.; Zhang, X.; Liu, J.; Zhang, H. Pichia anomala Induced With Chitosan Triggers Defense Response of Table Grapes Against Post-harvest Blue Mold Disease. *Front. Microbiol.* **2021**, *12*, 704519. [CrossRef] [PubMed]
37. Ahmad, B.; Suleiman, S.; Ahmad, M. Induction of Biochemical Changes in Santa Teriza Lime Leaves by Chitosan Application Influence Citrus Leaf Miner Damage. *Am. J. Plant Sci.* **2022**, *13*, 403–415. [CrossRef]
38. Mesén, F.; Jiménez, L.D. Producción de Clones de Café Por Miniestacas. Available online: https://repositorio.catie.ac.cr/bitstream/handle/11554/8176/Produccion_de_clones_de_cafe.pdf?sequence=1&isAllowed=y (accessed on 22 May 2023).
39. Ferreira-Possa, K.; Gourlat-Silva, J.A.; Vilela-Resende, M.L.; Tenente, R.; Pinheiro, C.; Chaves, I.; Planchon, S.; Andrade-Monteiro, A.C.; Renaut, J.; Figueiredo-Carvalho, M.A.; et al. Primary Metabolism Is Distinctly Modulated by Plant Resistance Inducers in *Coffea arabica* Leaves Infected by *Hemileia vastatrix*. *Front. Plant Sci.* **2020**, *11*, 309. [CrossRef] [PubMed]
40. SENASICA. Roya del Cafeto. *Hemileia vastatrix* Berkeley & Broome Ficha Técnica No. 40. Available online: http://www.cesavep.org/descargas/RDC/Ficha_Tecnica_Roya_del_cafeto.pdf (accessed on 22 May 2023).
41. Edy, N.; Anshary, A.; Basir-Cyio, M.M.; Lakani, I.; Kadir, S.R.A.; Mahmud, S. Incidence and Severity of Ganoderma Rot Disease in Tropical Land-use Systems and Their Virulence to Palm Oil. *Plant Pathol. J.* **2020**, *19*, 98–105. [CrossRef]
42. Bocianowski, J.; Tratwal, A.; Nowosad, K. Genotype by environment interaction for area under the disease-progress curve (AUDPC) value in spring barley using additive main effects and multiplicative interaction model. *Australas. Plant Pathol.* **2020**, *49*, 525–529. [CrossRef]
43. López-Velázquez, J.C.; Rodríguez-Rodríguez, R.; Espinosa-Andrews, H.; Qui-Zapata, J.A.; García-Morales, S.; Navarro-López, D.E.; Luna-Bárcenas, G.; Vassallo-Brigneti, E.C.; García-Carvajal, Z.Y. Gelatin–chitosan–PVA hydrogels and their application in agriculture. *J. Chem. Technol. Biotechnol.* **2019**, *94*, 3495–3504. [CrossRef]
44. Kruger, N.J. The Bradford Method for Protein Quantitation. In *The Protein Protocols Handbook*, 3rd ed.; Walker, J.M., Ed.; Springer Protocols Handbooks; Humana Press: Totowa, NJ, USA, 2009; Volume 1, pp. 17–24. [CrossRef]
45. Vandesompele, J.; De Preter, K.; Pattyn, F.; Poppe, B.; Van Roy, N.; De Paepe, A.; Speleman, F. Accurate normalization of real-time quantitative RT-PCR data by geometric averaging of multiple internal control genes. *Genome Biol.* **2002**, *3*, 1–12. [CrossRef]
46. Meng, L.; Feldman, L. A rapid TRIzol-based two-step method for DNA-free RNA extraction from *Arabidopsis siliques* and dry seeds. *Biotechnol. J.* **2010**, *5*, 183–186. [CrossRef]
47. Schmittgen, T.D.; Livak, K.J. Analyzing real-time PCR data by the comparative CT method. *Nat. Protoc.* **2008**, *3*, 1101–1108. [CrossRef] [PubMed]

MDPI AG
Grosspeteranlage 5
4052 Basel
Switzerland
Tel.: +41 61 683 77 34

International Journal of Molecular Sciences Editorial Office
E-mail: ijms@mdpi.com
www.mdpi.com/journal/ijms

Academic Open
Access Publishing

mdpi.com

ISBN 978-3-7258-5424-0